THE UNIVERSITY OF SYDNEY

The University of Sydney

Electronic Spectra of Aromatic Hydrocarbons: A Deductive Approach to the Diffuse Interstellar Bands

Author: *Gerard Dean O'Connor*

Supervisor: *Prof. Timothy W. Schmidt*

A thesis submitted in fulfilment of the requirements for the degree of Doctor of Philosophy

at

The Faculty of Science

of

The University of Sydney

November 9, 2015

Declaration of Authorship

I, Gerard D. O'Connor, declare that this thesis titled, 'Electronic Spectra of Aromatic Hydrocarbons: A Deductive Approach to the Diffuse Interstellar Bands' and the work presented in it are my own. I confirm that:

- This work was done wholly while in candidature for a research degree at this University.
- No part of this thesis has previously been submitted for a degree or any other qualification at this University or any other institution.
- Where I have consulted the published work of others, this is always clearly attributed.
- Where I have quoted from the work of others, the source is always given. With the exception of such quotations, this thesis is entirely my own work.
- Where the thesis is based on work done by myself jointly with others, I have made clear exactly what was done by others and what I have contributed myself.
- Editorial advice, proof reading and consolation was provided by my research supervisor, Prof. Timothy W. Schmidt. No other editorial assistance was obtained in the preparation of this thesis.

Gerard Dean O'Connor
November 9, 2015

"Once you eliminate the impossible, whatever remains, no matter how improbable, must be the truth"

Sir Arthur Conan Doyle

"Because it is there"

George Mallory

Abstract

Electronic Spectra of Aromatic Hydrocarbons: A Deductive Approach to the Diffuse Interstellar Bands

by Gerard D. O'Connor

The diffuse interstellar bands are a series of more than 500 interstellar absorption features, the carriers of which have remained unidentified since 1919.

In order to determine which aromatic chemical species are likely to be carriers of the diffuse interstellar bands, trends observed in the spectroscopic features of polycyclic aromatic hydrocarbon (PAH) species with chromophores ranging from 6 to 17 carbon atoms are considered. These trends are explored for PAHs with differing charge states and multiplicities, for multiple electronic transitions.

Previously unreported electronic transitions of the neutral radicals 1-naphthylmethyl, 2-napthylmethyl, 9-methylanthracene and 1-pyrenylmethyl as well as the 9-methylanthracenium$^+$ and phenalenium$^+$ radical cations and the closed-shell neutral molecule 1H-phenalene were recorded. The consideration of these experimental spectra in light of theoretical results in a synergistic understanding of the electronic and spectroscopic properties of these molecules that experiments or theory in isolation cannot achieve.

The $D_1 \leftarrow D_0$ transitions of small PAH resonance stabilized radicals (RSRs) are shown to be unlikely to be responsible for the DIBs, due to their weak transition intensities and pronounced vibronic structure. The spectroscopic properties of larger PAH RSRs were empirically extrapolated from experimental and computational trends, showing that these larger molecules are also unlikely to be responsible for the diffuse interstellar bands. The vibronic structures of these molecules were assigned. These assignments were guided by TD-B3LYP methods as well as Franck-Condon and Herzberg-Teller simulations.

As the $D_1 \leftarrow D_0$ transitions of PAH RSRs are weak, techniques were developed to obtain the gas-phase spectra of more intense electronic transitions to higher excited-states by double-resonance spectroscopy. Several strong transitions were observed, which were then assigned using *ab-initio* and TD-DFT computational methods (including TD-B3LYP, TD-CAM-B3LYP and TD-M06). These transitions are also dismissed as potential carriers of the DIBs due to the extremely broad spectral features they produced.

The spectra of PAH radical cations were observed through the resonant photodissociation of weakly bound van der Waals complexes. The recorded spectra covered a range from the mid infrared to the ultraviolet, with one such spectrum showing features of seven distinct electronic transitions. These electronic transitions were assigned based with the assistance of X-MCQDPT2 calculations. The vibronic spectra of the $D_1 \leftarrow D_0$ transition of the 9-methylanthracene$^+$ radical cation was also assigned, and the intensity pattern was modelled as a combined Franck-Condon *pseudo*-Jahn-Teller system.

Molecules based on the phenalenyl motif were examined spectroscopically and theoretically, giving an overview of the effects of symmetry, multiplicity, charge and heteroatomic substitution on the spectroscopic properties of aromatic molecules.

As a result of the work presented, several classes of PAH can now be dismissed as possible carriers of the DIBs. Further avenues of research have been suggested. The role of this work as part of the ongoing search for the carriers of the DIBs will be discussed.

Acknowledgements

First and foremost, I would like to thank my supervisor, Prof. Timothy Schmidt. The first time I met Tim, he went above-and-beyond helping me negotiate the bureaucratic minefield required for me to re-enter university as an Honours student. Most people would react differently when a bus-driver (in uniform) arrives at their office door with a less-than-stellar set of academic transcripts. Since then, Tim's energy and enthusiasm have been infectious, and his patience and wisdom have been greatly appreciated (particularly in the last few months). I'd also like to thank my associate supervisor Prof. Scott Kable. He was a helpful source of advice, but I would mainly like to thank him for his role in bringing together the people and equipment that made for such a productive, and entertaining, working environment.

To all the people from the group formerly known as the Laser Spectroscopy Group, I thank you for all of your comradeship, support, interest and senses of humour. I especially want to thank Klaas Nauta, Tyler Troy and Nahid Chalyavi for all that they taught me, Olha Krechkivska for assistance in the latter years of my PhD, and Callan Wilcox and Mitchell Quinn for their friendship, calming presence and frequent assistance in the lab.

One of the things that I most enjoyed about the last few years has been the opportunity to interact with the wider molecular spectroscopy community. I especially want to thank Michael McCarthy and Evan Bieske for letting me loose in their labs, as well as Kyle Crabtree, Oscar Martinez Jr, Vik Dryza and Julian Sanelli for getting me involved, and for showing me how everything worked. I'd also like to thank John F. Stanton and Scott Reid for all that I have learnt from them and for the many fun times. And to all those whom I have met at conferences, I thank you. The excitement of joining this quirky little community is what kept the fires burning on the darkest of days.

I would not have been able to continue to pursue this work without the understanding of my (less-scientific) co-workers at Sydney Buses and FKG Nyngan and I would like to thank all my co-workers for keeping me honest. I'd also like to thank my parents and family for all of their encouragement, from my school days onward.

To all of my friends in Sydney, and especially those from the Engineering Revue, I thank you. Over the past few years you have also become my family. This is particularly true for my former house mates Paddy and Danya, and my best friends Laura and Dave, who have all gone above-and-beyond in keeping me somewhat social and at least functionally sane in recent years.

And to my wonderful wife Natasha, who has completely changed my life, I thank-you for continuing to love and support me. You make me the person I want to be, without actually trying.

And to everyone else, **Thanks**.

Contents

List of Figures

List of Tables

Chapter 1

Introduction

1.1 Astronomical Chemistry and Spectroscopy

With the notable exception of data acquired by space probe exploration of the solar system's moons, planets and comets, as well as the terrestrial examination of meteorites, all knowledge of extraterrestrial chemistry has thus far been obtained through the analysis of astronomical spectra. This limitation in knowledge of the chemical species which compose our galaxy fundamentally restricts our understanding of the nature of chemistry beyond the solar-system. While much work has been done to model the chemical processes that transform atoms produced in stellar nuclear-synthesis[1] into the molecules of the interstellar medium (ISM),[2–8] and then into planetary systems,[9–14] these models must always be tested against our understanding of the reactants involved in extraterrestrial chemistry and the environment in which it occurs.

The Milky Way galaxy is rich in organic molecules. Carbon is formed as part of the carbon-nitrogen-oxygen (CNO)-cycle of stars on the asymptotic giant branch (AGB).[1,15] This carbon is then released into the ISM by either the formation of a planetary nebulae or through a supernova.[16] Extreme AGB stars, protoplanetary nebulae and planetary nebula all exhibit the spectroscopic signatures of organic molecules.[15,17,18] These molecules enrich the ISM and lead to the formation of diffuse clouds.[15]

As the density increases through the aggregation of diffuse, translucent and then molecular-clouds,[16] these molecules conglomerate to form organic nanoparticles and carbon dust.[19] These molecules are then present during the formation of planetary disks and are fundamental to the rich organic chemistry we observe in the solar system. This rich chemistry is

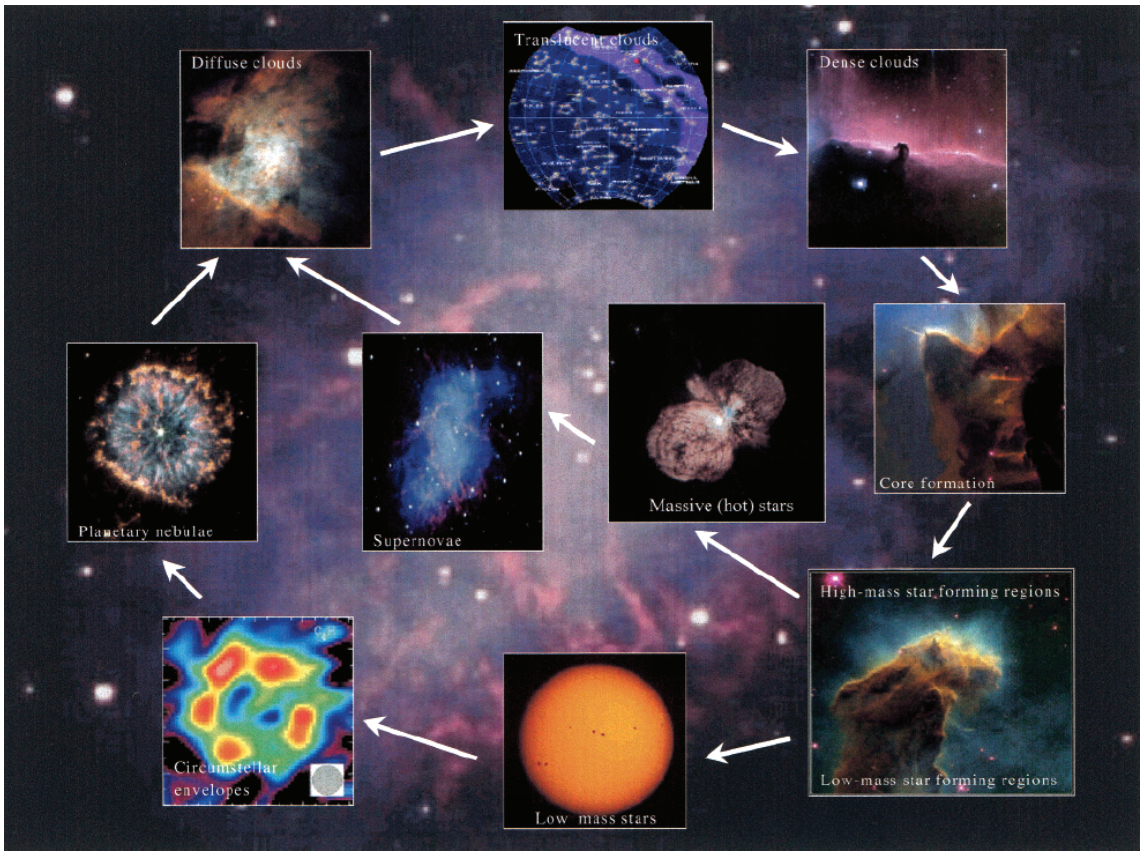

Figure 1.1: Cycle of matter in the interstellar medium: Diffuse clouds containing organic molecules condense to form translucent clouds, molecular clouds, core formations, star-forming regions and planetary systems. Supernovae, circumstellar envelopes, and planetary nebulae then release enriched matter back into the ISM. Image from a review paper by Ralf Kaiser.[16]

demonstrated by the abundance of organic molecules such as those found in meteorites,[20] and on Earth.[18,21,22] Remnants of the interstellar environment in which the solar system formed can be observed in comets.[21] Indeed, it has been suggested that pre-biotic organic molecules delivered to earth by early cometary impacts may have introduced precursors to the molecules now found in living organisms.[23–25] Much of this knowledge of the chemistry has come from the combination of astronomical and laboratory spectroscopy.

1.1.1 The Sun and Other Stars

Astronomical spectra were first observed during Sir Isaac Newton's early work on the nature of light, in which he used glass prisms to refract the light of the sun.[26] Dark features were observed in this solar spectrum, first by William Hyde Wollaston in 1802,[27] then by Joseph von Fraunhofer in 1815.[28] Fraunhofer made detailed measurements of the wavelength of 574 dark spectral lines, similar to those observed in Figure 1.2. Fraunhofer noted that

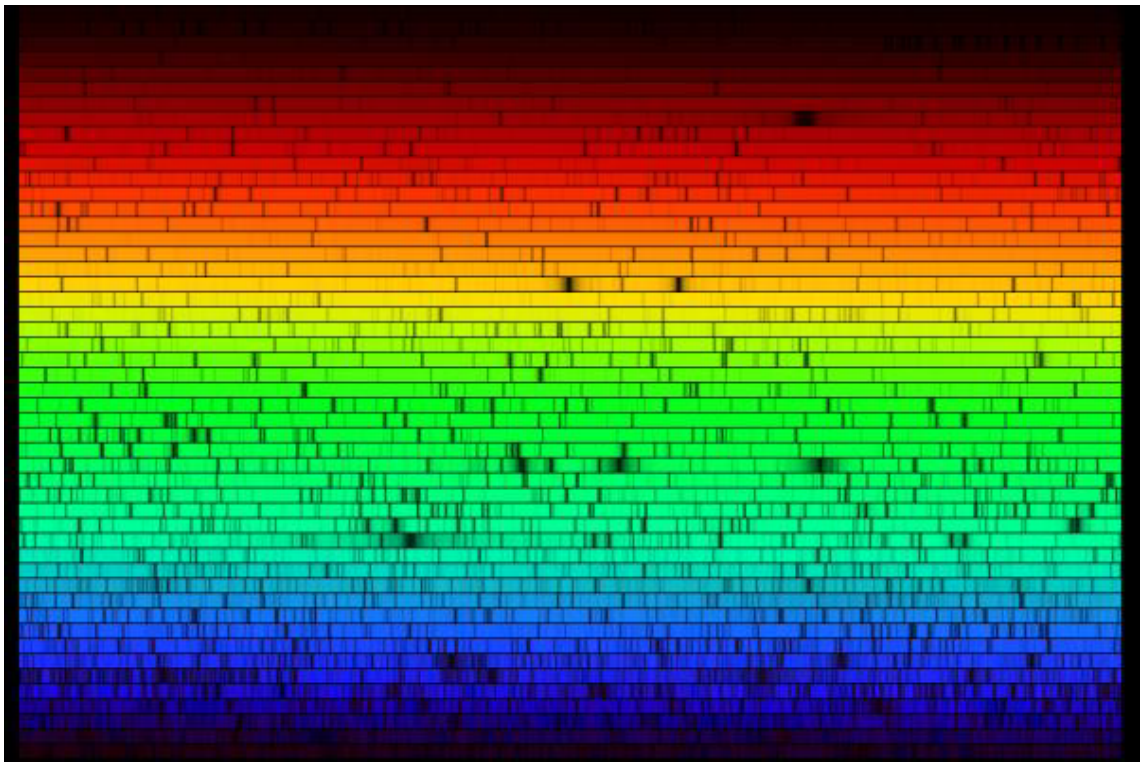

Figure 1.2: The Solar absorption spectrum. This image was created from a digital atlas observed with the Fourier Transform Spectrometer at the McMath-Pierce Solar Facility at the National Solar Observatory on Kitt Peak, near Tucson, Arizona. Absorption features such as these were first reported by Wollaston[27] and Fraunhofer.[28] Credit and Copyright: N.A.Sharp, NOAO/NSO/Kitt Peak FTS/AURA/NSF. Image available at *http* : *//apod.nasa.gov/apod/ap*000815*.html*

that the same pattern of dark lines were observed in the spectrum of Venus, which we now know to be reflected sunlight. Fraunhofer also observed dark lines in the spectrum of the bright fixed star Sirius. However, these lines had a distinctly different intensity pattern. Indeed, Fraunhofer observed only three strong lines in the spectrum of Sirius, one in the green, two in the blue.[29] In 1823, Fraunhofer also reported the spectrum of Castor, Pollux, Capella, Betelgeuse and Procyon, all featuring their own distinct pattern (with Betelgeuse being especially rich in dark lines).[29,30]

It was Gustav Kirchhoff and Robert Bunsen that first observed that these dark lines corresponded to bright emission lines observed in the flame spectra of specific chemical elements, correctly postulating that the dark lines in the solar spectrum were due to the absorption by these same elements, and as such these elements exist in the solar atmosphere.[31–33] Since then the analysis of stellar spectra, both atomic and molecular in origin, has allowed deeper insight into the chemistry of the photospheres of stars and the nature of stars themselves.[34,35]

1.1.2 The Solar System

In addition to the Earth and the Sun, the other bodies of the solar system have also long drawn the interest of astronomical spectroscopists. One early example is the observation that a complex set of bright emission features observed in flames by Wollaston,[27] then independantly recorded in detail by Swan (after whom the bands are named),[36] were matched with bright emission features observed by Huggins in the the spectrum of a comet.[37] The carrier of this spectrum was a strong topic of debate for some time, with the primary candidates being either the diatomic carbon molecule (C_2) or acetylene (C_2H_2).[38,39] However, the Swan emission bands did not correspond to observed acetylene gas absorption measurements,[40] and improved modelling of the rotational structure in these bands led to the increasing acceptance that C_2 was the likely carrier of the Swan bands.[40–42] As such, the assignment of C_2 is one of the earliest examples of a molecular carrier of an extraterrestrial spectrum being assigned by the fitting of an experimental laboratory spectrum to a theoretical model. Emission and absorption bands of C_2 are now observed throughout the galaxy.[43–46]

The atmospheres of the planets and moons of the Solar System have also been widely examined by astronomical chemists. Early observations of the chemical composition of planetary atmospheres were made via radio-astronomy, in the centimetre and millimetre range,[47–50] IR astronomy,[51] and optical astronomy.[52,53] Remote observation of planetary spectra continues to be a rich source of information on the molecular composition of a wide variety of environments. From this we have learned that that the atmospheres of the solar system contain complex chemical systems.[54–56]

The understanding of the chemistry of planetary atmospheres has more recently been enhanced by the exploration undertaken by space probes since the latter half of the last century. These probes have not only added to the vast bank of spectroscopic information available,[57–60] but have enabled planetary atmospheres to be sampled by techniques such as mass-spectrometry,[61–67] which has allowed us to gain insight into the processes that govern the chemistry of these environments.[54–56]

The large Saturnian satellite, Titan, has attracted significant interest in the astronomical chemistry community. Kuiper, by recording optical spectra, confirmed that Titan has an atmosphere in which he detected molecules such as methane and ammonia.[68] Since then, Titan has been visited by the Voyager space probes[69–76] as well as the Cassini-Huygens probe.[64,66,67,77,78] These probes determined that the atmosphere of Titan, while consisting mostly of N_2, has a complex chemistry of organic compounds including aromatic

Figure 1.3: Image of Saturns moon Titan, obtained on the Cassini space-probe, showing an atmospheric haze containing small particles of organic molecules. Image Credit: NASA/JPL/Space Science Institute. Availible at *http* : *//www.nasa.gov/mission_pages/cassini/media/cassini* − 072904.*html*

species such as benzene.[79,80] This has led to a number of laboratory-based and theoretical studies aimed at understanding the chemical processes leading to this rich mixture of molecules.[55,56,81–91]

In recent years, an increasingly vast array of molecular spectra is now being observed in exoplanets.[12–14,92] Many of the exoplanets that have been observed have conditions unlike any of those observed in the solar-system, such as the hot super-earths.[14,93,94] Understanding the chemistry of these distant atmospheres has the potential to be one of the frontiers of astronomical spectroscopy in the 21st century.

1.2 The Interstellar Medium (ISM)

It is now known that the interstellar medium (ISM) of a spiral galaxy is far from an empty void. Stars larger than approximately 0.4 solar masses end their life as either planetary nebulae[1] or supernovae.[95,96] Supernovae, as well as the processes that lead to the formation of planetary nebulae, enrich the ISM with atoms such as carbon, nitrogen and oxygen, from which form the molecules which interstellar chemistry is based.

To understand the chemical processes which form interstellar molecules, several models for interstellar chemistry have been introduced. These models, such as the 'UMIST Gas-Phase Chemical Network' of Millar and co-workers[4] and the 'New Standard Model' of Herbst and co-workers[3] are based on known properties of the ISM. These properties include the

Table 1.1: A list of molecules identified in the ISM and circumstellar shells as of June 2015, available from The Cologne Database for Molecular Spectroscopy (CDMS).[6–8] Carbon chains as long as $HC_{11}N$ have been observed in molecular clouds by millimetre-wave spectroscopy. Underlined species have been observed due to their vibration-rotation spectra in the infrared. C_2 has only been observed by electronic spectroscopy, in the optical region.

No. of atoms	Molecular Formulae
2	AlF AlCl **C_2** CH CH^+ CN CO CO^+ CP CS CSi HCl H_2 KCl NH NO NS NaCl OH PN SO SO^+ SiN SiO SiS HF SH FeO? O_2 CF^+ SiH PO AlO OH^+ CN^- SH^+ HCl^+ TiO ArH+ NO^+?
3	C_3 C_2H C_2O C_2S CH_2 HCN HCO HCO^+ HCS^+ HOC^+ H_2O H_2S HNC HNO MgCN MgNC N_2H^+ N_2O NaCN OCS SO_2 *c*-SiC_2 CO_2 NH_2 H_3^+ AlNC SiCN SiNC HCP CCP AlOH H_2O^+ H_2Cl^+ KCN FeCN HO_2 TiO_2 C_2N Si_2C
4	*c*-C_3H *l*-C_3H C_3N C_3O C_3S C_2H_2 HCCN HCNH$^+$ HNCO HNCS $HOCO^+$ H_2CO H_2CN H_2CS H_3O^+ NH_3 SiC_3 CH_3 C_3N^- PH_3 HCNO HOCN HSCN H_2O_2 C_3H^+ HMgNC HCCO
5	C_5 C_4H C_4Si *l*-C_3H_2 *c*-C_3H_2 CH_2CN CH_4 HC_3N HC_2NC HCOOH H_2CNH H_2C_2O H_2NCN HNC_3 SiH_4 H_2COH^+ CH_4^- HC(O)CN HNCNH CH_3O NH_4^+ H_2NCO^+
6	C_5H C_5O C_2H_4 CH_3CN CH_3NC CH_3OH CH_3SH HC_3NH^+ HC_2CHO $HCONH_2$ *l*-HC_4H? *l*-H_2C_4 C_5N *l*-HC_4H *c*-H_2C_3O C_5N^- HNCHCN
7	C_6H C_6H^- CH_2CHCN CH_3C_2H HC_5N CH_3CHO NH_2CH_3 *c*-C_2H_4O H_2CCHOH C_6H^-
8	CH_3C_3N $HCOOCH_3$ CH_3COOH C_7H H_2C_6 CH_2OHCHO *l*-HC_6H? CH_2CHCHO? CH_2CCHCN H_2NCH_2CN CH_3CHNH
9	CH_3C_4H CH_3CH_2CN $(CH_3)_2O$ CH_3CH_2OH HC_7N C_8H CH_3CONH_3 C_8H^- C_3H_6 CH_3CH_2SH?
10	CH_3C_5N? $(CH_3)_2CO$ NH_2CH_2COOH? $(CH_2OH)_2$? CH_3CH_2CHO
11	HC_9N CH_3C_6H C_2H_5OCHO CH_3OCOCH_3
12	*c*-C_6H_6 *n*-C_3H_7CN *i*-C_3H_7CN
13	$HC_{11}N$
60	C_{60}
70	C_{70}

abundance of currently identified molecules, molecular temperature (obtained by observing rotational band profiles of interstellar molecules), vacuum ultraviolet (VUV) flux, estimated density and the theoretical ratio of heavy atoms to hydrogen atoms in the galactic plane based on the abundance of observable species.[2]

The accuracy of these models is therefore limited by the knowledge of the relative abundance of interstellar molecules. This can be improved by assigning interstellar spectral features to known carriers. To assign the carrier of an interstellar band, they must be compared with spectra obtained in a simulated interstellar environment. This requires the spectrum of the chemical species to be recorded in the gas phase at low temperature and under high vacuum.[97] Techniques which allow these measurements, particularly in the visible region of the spectrum, will be discussed in Chapter 3. Spectral information on

interstellar molecules has been detected across many regions of the electromagnetic spectrum. Currently more than 180 molecules have been detected in the interstellar medium or circumstellar shells.[6–8] These are listed in Table 1.1.

Millimetre-wave and radio-wave astronomy have successfully identified numerous interstellar molecules,[98] as can be observed in Table 1.1.[6–8] Molecules with permanent dipole moments can lose rotational energy by emitting photons in the radio and millimetre range. It is a major advantage of this technique that rotational spectroscopy also gives the exact vibrationally averaged geometry of the molecule, allowing unambiguous assignment of observed spectra.[99]

The molecules responsible for astronomical millimetre-wave features can be identified by comparison with laboratory millimetre-wave spectra, where much work has been done. In particular, Thaddeus, McCarthy and co-workers at the Harvard-Smithsonian Center for Astrophysics have recorded the laboratory spectra of over 50 molecules of interest to interstellar chemistry[98,100–104]. Molecules with larger dipole moments are easier to identify from their microwave spectra. This method of identification is therefore responsible for the large number of asymmetric carbon chains, including carbon chain cations and anions, identified in the ISM as shown in Table 1.1. Molecules as large as $HC_{11}N$ have been identified by these techniques.[105]

The quality of astronomical rotational spectra has improved significantly in recent years. Spectroscopic information of numerous astronomical environments has recently been reported by the Atacama Large Millimeter/Submillimeter Array (ALMA).[106–108] Additionally, work continues towards the construction of the Australian Square Kilometer Array Pathfinder (ASKAP). With more than 50 times the sensitivity of the previous generation of radio telescopes, ASKAP is expected to greatly increase the pool of information available to interstellar chemistry, and radio astronomy in general.[109]

Another area of astronomy which has yielded information about molecules in the ISM is infra-red (IR) astronomy. Until recently, much of the IR region was inaccessible to astronomy due to water vapour in the Earth's atmosphere.[97] This did not prevent observations in the far IR region of the electromagnetic spectrum. Some interstellar molecules have been identified by far IR astronomy, including Hinkle, Bernath and Keady's identification of the C_3 and C_5 molecules.[110,111]

In recent years, orbital IR telescopes such as COBE[112], ISO[17] and the Spitzer Space Telescope have allowed access to previously inaccessible regions of the IR spectrum. This has led to the further identification of interstellar molecules, such as the discovery by the

Spitzer Space Telescope of C_{60} and C_{70} fullerenes in the circumstellar shell of a planetary nebula,[113] and their subsequent discovery in other astronomical environments.[114–116]

1.2.1 Electronic Transitions of Interstellar Molecules.

Some of the earliest molecules detected in the ISM were assigned based on optical spectroscopy. As mentioned previously, C_2 has been observed in various astronomical environments.[43–46] Another optically observed interstellar molecule that has attracted significant interest is SiC_2. Unidentified bands in the blue and green regions of the visible spectrum of N-type stars, that also showed strong carbon lines, were first observed in 1926.[117,118] In 1956 Kleman, using a graphite oven charged with Silica, proved that the carrier of these "Merrill-Sanford bands" was a molecule containing only silicon and carbon.[119] The structure of this molecule was originally considered to be a linear molecule with the formula SiC_2, analogous of the C_3 molecule.[120–122] However, detailed analysis of the rotationally resolved jet-cooled spectrum of these bands by Michalopoulos proved that this molecule in fact has a triangular structure in both the ground and excited state.[123] SiC_2 continues to be of significant interest to astronomy.[124] Recently Steglich and Maier recorded the most complete excitation spectra of the Merrill-Sanford system of SiC_2 so far published.[125]

Many of the interstellar spectral features observed in the visible spectrum remain unidentified. Two such sources of unidentified visible features include the Red-Rectangle bands (RRBs), a series of emission features observed in the biconical protoplanatary nebular the Red-Rectangle,[126,127] and the diffuse interstellar bands (DIBs), a series of absorption features attributed to molecules in the ISM. Interstellar spectra with no assigned carriers is not unique to the visible region, with prominent unidentified features also observed by millimetre-wave astronomy (such as the anomalous microwave emission (AME))[128,129] and IR (such as the unidentified infrared emission (UIR)).[130,131]

Given that the molecules creating these features are unknown, the models describing interstellar chemistry are based on an incomplete picture of the ISM. To better understand interstellar chemistry, it is therefore necessary to identify the molecules responsible for these unidentified spectral features. This study was aimed at making a contribution towards the ongoing efforts to identify the carriers of the DIBs.

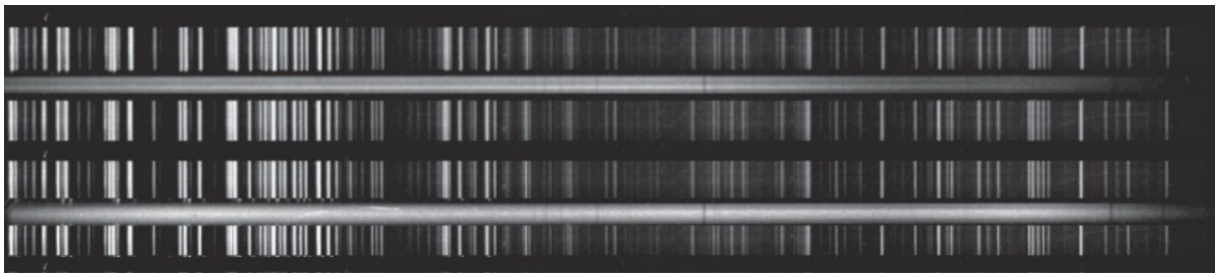

Figure 1.4: Images of two plates of ζ-Persei obtained by Mary Lea Heger at Lick Observatory in 1919. Heger's measurements, made using these plates in 1920, contain the first documented record of the DIBs. Image from McCall and Griffin (2013)[137]

1.3 The Diffuse Interstellar Bands (DIBs)

The carriers of the DIBs, a series of more than 500 interstellar absorption features in the visible and NIR attributed to the ISM, have remained unidentified since the bands were first observed almost a century ago.[132,133] In 1934 Merrill confirmed that some anomalous spectral absorption features, reported by Mary Lea Heger in 1919,[134,135] remained stationary with respect to the oscillating stellar spectral features of binary stars.[136] The plates on which Mary Lea Heger's spectra is recorded is shown in Figure 1.4. Since these stationary absorption features could not be carried by the moving stellar source, it was hypothesised that the additional absorption features belonged to chemical species existing in the space between the stars and the Earth. The identity of the carriers of these absorption features remains the longest unsolved mystery in astronomy.[132] A simulated DIB spectrum is presented in Figure 1.5.

Numerous theories regarding the possible identities of the DIB carriers have been suggested, including ultracold solid oxygen, metastable H_2, MgO grains and contaminated hydrogen clusters.[133,138] However, the majority of proposals are carbonaceous molecules.[133] There are numerous reasons for this. Firstly, due to the abundance of the DIBs it is often assumed that the carriers of the DIBs are most likely formed from the most abundant reactive interstellar elements, hydrogen, carbon, oxygen and nitrogen.[139] Also, there is an acknowledged shortfall between the interstellar carbon accounted for by observed species relative to the expected abundance of carbon in the ISM.[140] Another reason that organic molecules are hypothesised to exist in diffuse clouds is due to their known importance to the interstellar cycle of matter and the formation of planetary systems such as our own. If the DIBs are indeed carried by organic species, as seems likely, understanding the processes by which these molecules form would prove a valuable insight into the chemistry of carbon in the ISM.

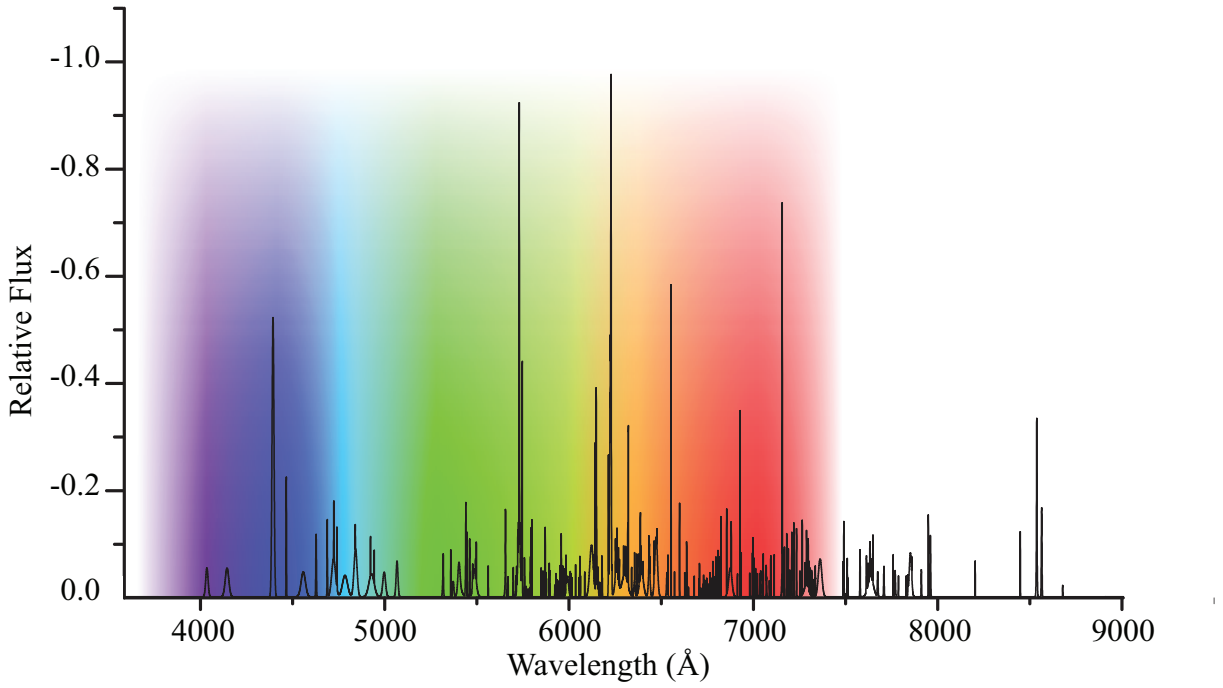

Figure 1.5: Simulated spectrum of the diffuse interstellar bands. Reproduced from the DIB catalogue of Jenniskens *et al.*[141–143]

The number of DIBs observed in the ISM now exceeds 500.[137,144,145] It has been shown that the intensities of the DIBs are not correlated,[146] which suggests the DIBs each have a unique carrier. Therefore, the number of DIB carriers outnumber the number of identified interstellar molecules, shown in Table 1.1, by approximately three-to-one. Snow and McCall have argued that "once the DIB carriers are known and their chemistry understood, the DIBs may represent a powerful multidimensional probe of the physical conditions (temperature, density, radiation field, etc.) in diffuse clouds."[139] This makes identifying the carriers of the DIBs an important astrophysical building block, as well as a curious puzzle to solve.

1.3.1 Properties of DIB Carriers

Molecules that can be considered as plausible candidates as carriers of the DIBs must have certain properties. Initially, the molecule in question must absorb in the same spectral region as the observed DIBs. Figures 1.5 and 1.6 both show that the DIBs are observed exclusively in the visible and NIR regions, and therefore only chemical species that have electronic transitions of the appropriate energy need be considered.

Additionally, the band profiles of potential carrier transitions, observed at low-temperature in simulated astronomical conditions, must match that observed in the DIBs. Figure 1.6

shows the full-width-at-half-maximum (FWHM) of the confirmed DIBs observed in the spectrum of HD183143 by Hobbs *et. al.* (2009).[145] It can be seen that the FWHM of all observed DIBs appear in a range between 0.42 Å (λ5840.7 Å) and 22.56 Å (λ4428.8 AA). However the vast majority of the observed bands have a FWHM of approximately one Å. The limitations of band widths are further discussed in Chapters 5, 6 and 7. With the exception of the broad lorentzian DIBs, the profiles of most DIBs are attributed to rotational structure. The profiles of some of these DIBs, such as the λ6614 Å DIB, show a broad red tail. It has been suggested by Oka *et. al.* that these features are the result of large polar carriers with population in many high-J levels, due to radiative pumping by dust emission.[147] However, Bernstein *et. al.* have shown that these structures can be described by a simple bi-modal distribution, suggesting the convolution of two overlapping DIBs.[148]

Matching of the band profile of a DIB is just as important as matching the energy. With such a large number of DIBs observed in the visible/NIR, coincidental matches in energy are to be expected. It is also important that the transition being suggested as a carrier of a DIB is the only strong transition for that molecule in the visible spectrum, as any additional intense structure would also have to be observed in the DIBs. As the intensities of the DIBs have been shown to be uncorrelated, this is unlikely.[146]

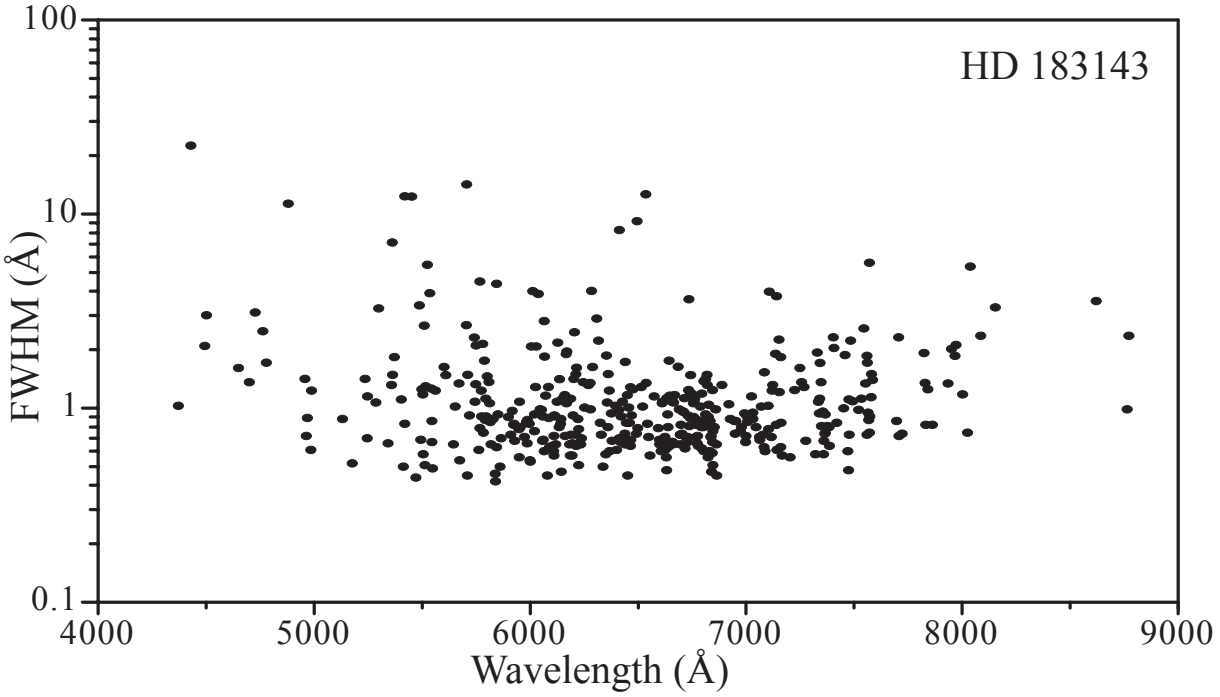

Figure 1.6: Log-linear scatter plot of FWHM (Å) and Wavelength (Å) of confirmed DIBs in the spectrum of HD183143.[145] Data obtained through *http : //dibdata.org/*

An additional limitation on the possible assignment of DIBs is the intensity of the proposed carrier transition. Modelling of organic DIB carriers assumes that the observed transitions have an oscillator strength $f = 10^{-2}$.[140] While transitions stronger than this will still be valid carriers with lower column densities, carrier transitions with oscillator strength significantly lower than $f = 10^{-2}$ would require significantly higher abundances than expected by current models. The expected abundance of carbon in diffuse clouds makes this unlikely.

Potential DIB carriers must also be able to survive the harsh radiation environment of the ISM. It is believed that most DIB carriers exist in the diffuse atomic clouds (where hydrogen is primarily in its atomic form, rather than its diatomic molecular form),[139] although some also appear to be present in the lower radiation diffuse molecular clouds.[139] This has led to the suggestion that many DIB carriers may be ionised.[149]

The carbon-chain hypothesis was first put forward by Douglas in 1977,[150] and has since then been thoroughly investigated, primarily by the group of J. P. Maier of The University of Basel.[151–154] There have been some promising coincidences between observed and measured spectral features, notably C_7^-, l-$C_3H_2^-$ and C_3H_2,[155–157] but these identifications have, in each case, been refuted by further evidence.[158,159]

However this work will focus on the hypothesis that polycylic aromatic hydrocarbons (PAHs) may be carriers of DIBs.

1.3.2 Polycyclic Aromatic Hydrocarbon (PAH) Hypothesis

PAHs are networks of sp^2 hybridized carbon atoms, whose "dangling bonds" are passivated with hydrogen. In the limit of large system size, one arrives at graphene,[160] which has no band gap. The smallest PAH is naphthalene, a white crystalline material which absorbs in the UV.[161] PAHs serve as theoretical benchmarks for larger carbon networks and graphene nano-particles. Some PAHs have found technological applications in solar energy and molecular electronics.[162,163] PAHs are also important pollutants in Earth's atmosphere, as they are produced in combustion reactions.[164,165]

The existence of PAHs in the ISM was first invoked to explain the ultraviolet extinction curve.[166,167] Further evidence for interstellar PAHs came from in the form of the IR astronomy.[130,131] In the mid-1980s it was observed that star-forming regions and carbon rich nebula exhibit IR emission features ranging from 3.3 μm to 11 μm (the UIRs), appearing to be consistent vibrational modes of aromatic molecules, such as PAHs.[130,131] These modes include the 3.3 μm C-H stretching mode, the 6.2 and 7.7 μm C-C stretching modes as well

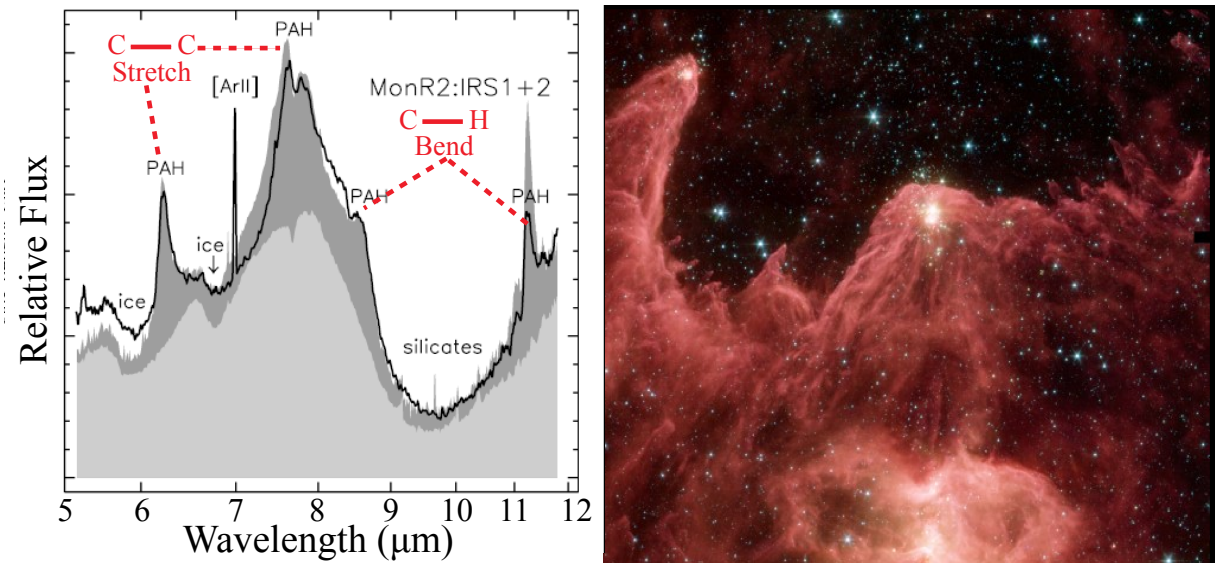

Figure 1.7: Left: IR Spectra of embedded protostar Mon R2:IRS 1 showing emission corresponding to known PAH vibrational modes. Adapted from spectrum published by Spoon *et al.*[170]; **Right**: False colour IR image of W5 region. The red in this image corresponds to the vibrational modes of PAHs. Image: NASA/JPL-Caltech/Harvard-Smithsonian CfA/ESA/STScI

as the 8.6 and 11.3 μm C-H bending modes. These bands have been labeled in Figure 1.7. In recent years, sources of this IR emission have received much attention from the COBE[112], ISO[17] and Spitzer orbital IR space telescopes. These studies provide strong evidence for the widespread abundance of PAHs in the ISM. However the exact structure of the PAHs responsible remains unclear. Indeed, it has recently been suggested that the UIRs are better fit by combined aromatic-aliphatic molecules.[168,169]

As PAHs are suspected to already be present in the ISM, because of the UIRs, it was hypothesized by several groups that the PAH family might be responsible for the DIBs, in neutral, ionic, radical or closed-shell form.[171–173] PAHs have several additional features that made them appear to be good candidates for the carriers of the DIBs. Larger PAHs are predicted to be able survive the harsh radiation field of the diffuse interstellar medium.[174] They are primarily made up of carbon and hydrogen, which are abundant in the ISM, and as such could exist in the column densities required to produce the absorption intensities observed in the DIBs.[140,174] Finally, some PAHs have strong transitions in the visible part of the spectrum.[174]

As mentioned previously, proposed DIB carriers must absorb in the visible or NIR. A simple Hückel picture is sufficient to determine which PAHs are likely to have visible transitions. The classes of PAH, in terms of oxidation state and multiplicity, are described in terms of simple Hückel fronter orbitals in Figure 1.8.

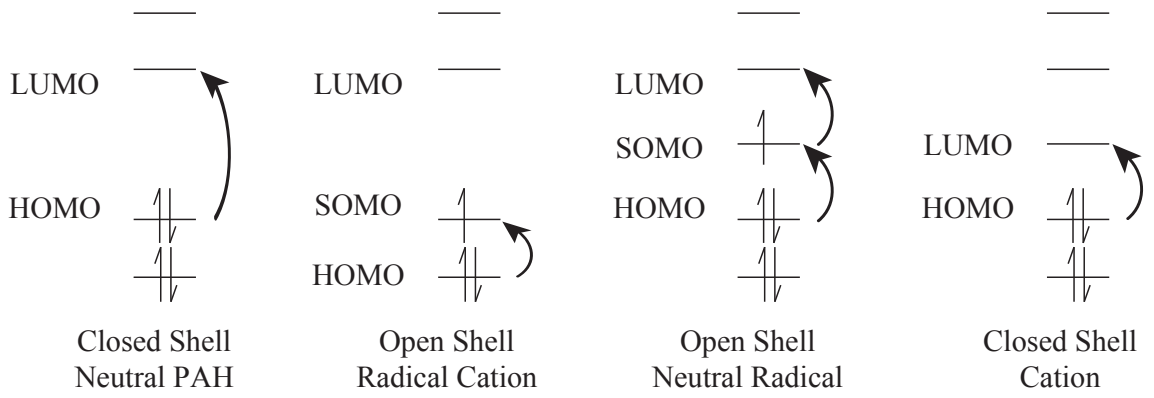

Figure 1.8: Fronter orbitals of typical ground state electronic structure of PAHs, as prediced by the Hückel model. PAHs can be devided into classes based on mulitplicity and charge. The single electron transitions likely to contribute to the first electronic excited state are indicated by the black curled arrows

Most spectroscopic studies on the band gaps and vibrational frequencies of PAHs have focussed on the closed-shell species, which are often commercially available,[161,175] or readily synthesized.[176] The $S_1 \leftarrow S_0$ transition of a neutral closed-shell PAHs is primarily due to single electron transitions that are energetically similar to a transition from the highest occupied molecular orbital (HOMO) to the lowest unoccupied molecular orbital (LUMO), shown in the leftmost diagram of Figure 1.8. For small PAHs, the $S_1 \leftarrow S_0$ transitions correspond to absorptions in the UV spectrum, and as such these molecules cannot be carriers of the DIBs. Only relatively large neutral closed shell PAHs, such as tetracene ($C_{18}H_{12}$)[177] and Hexa-*peri*-hexabenzocoronene ($C_{42}H_{18}$)[176] absorb in the spectral regions relevant to the DIBs. The $S_1 \leftarrow S_0$ transitions of closed shell PAHs will be examined further in Chapter 7.

Ionising these molecules creates radical cations. These resonance stabilised radical cation species generally have weak IR $D_1 \leftarrow D_0$ transitions, with stronger visible $D_2 \leftarrow D_0$ transitions. These strong visible transitions have been suggested as carriers of the DIBs. However the D_2 higher excited state of these cations is generally short lived, resulting in transitions that are significantly lifetime broadened. These lifetime broadened state have lorentzian profiles, and it is possible that a strong transition to a short-lived state may be responsible for the broad lorenzian DIB at $\lambda 4428.8\,\text{Å}$, as well of some of the other broad DIBs. Indeed, several PAH radical cations have been proposed as carriers of the DIBs.[178–180] However, these assignments have been shown to be inconsistent with further observation.[181,182] These transitions will be examined further in Chapters 6 and 7.

The $D_1 \leftarrow D_0$ transitions of medium sized neutral PAH resonance stabilised radicals (RSRs) absorb in the visible and NIR spectrum. These PAH RSRs have been considered

possible products of interstellar photofragmentation,[183–185] and have been the focus of several recent studies.[183,185–203]

Visible and NIR transitions of many aromatic species have now been observed in the gas phase under simulated astronomical conditions (high vacuum, low temperature),[204] including the $S_1 \leftarrow S_0$ transitions of large closed-shell neutral species,[176] $D_2 \leftarrow D_0$ transitions of radical cations,[205,206] the $D_1 \leftarrow D_0$ transitions of neutral radicals[183,185–203] and recently the $S_1 \leftarrow S_0$ transitions of closed shell cations.[207–209] All have been dismissed as potential carriers of the DIBs.

1.4 Focus of This Work

This work aims to build on the work of previous studies, by looking for trends in the spectroscopic properties of aromatic molecules of a particular multiplicity and of a particular charge. The interpretation of these trends will be guided by theoretical analysis of the spectra in question, understanding the changing nature of excited states as examined by techniques ranging from the conceptually simple Hückel level of theory through to the application of modern excited state computational chemistry. The trends observed will include excitation energy, excited state lifetime, electronic transition intensities, Franck-Condon[210,211] and Herzberg-Teller[212] vibronic intensities and the spectroscopic width of observed bands. These trends will be extrapolated from experimentally examining excited states of varying energy, symmetry, energy-gap and density-of-states for aromatic chromophores ranging from 6-17 carbon atoms. These trends will be extrapolated to larger aromatic chromophores. This was done to determine which of the previously considered classes of PAH can be dismissed as plausible carriers of the DIBs, and which aromatic species may still be plausible carriers based on existing evidence.

Chapter 2 will outline the computational and theoretical techniques used in this work and how they can, in conjunction with experimental results, lead to an understanding of the spectral properties of similar transitions. Chapter 2 will also outline the effectiveness of computational chemistry tools that will be used to assign the spectra obtained in this study. Chapter 3 will outline the experimental techniques and equipment used to acquire spectra in this work.

Chapter 4 examines the $D_1 \leftarrow D_0$ transitions of neutral PAH RSRs by recording the $D_1 \leftarrow D_0$ excitation spectra of 9-anthracenylmethyl (9-AnMe) and 1-pyrenylmethyl (1-PyMe), the largest neutral radicals yet observed in the gas-phase. Computational chemistry

methods are used to assist in the assignment of the recorded spectra. Chapter 4 then compares the recorded spectra with previously recorded spectra of smaller PAH RSRs to extrapolate the spectral properties of larger molecules of this type. Chapter 4 also introduces a means of improving the accuracy of time-dependant density functional theory (TD-DFT) electronic transition energies through empirical correction.

Chapter 5 looks at transitions to higher-excited states of neutral PAH RSRs through double-resonance techniques. The transitions viewed are those with calculated oscillator strength greater than $f = 10^{-2}$, in line with astronomical modelling.[140] Further theoretical methods are introduced to empirically enhance the calculation of excited state energies. A new R2C2PI after internal conversion technique is demonstrated, thanks to a serendipitous near match between the ionisation energy of 9-AnMe and the output of an ArF excimer laser.

Chapter 6 explores the spectral properties of radical cations by examining the photodissociation spectrum of argon tagged 9-methylanthracenium$^+$ cation (Ar$\cdots$9-MeAn$^+$) for the spectral range from 8000 cm^{-1} to 44444 cm^{-1}. Eight distinct electronic transitions are observed and assigned in this region based on ab-initio methods previously developed in Chapter 5. The vibronic structure of the weak $D_1 \leftarrow D_0$ transition of Ar$\cdots$9-MeAn$^+$ was assigned, and the highly vibronic structure of the unreported $D_1 \leftarrow D_0$ transition of anthracenium$^+$ will be discussed.

Chapter 7 looks at molecules based on the phenalenyl motif. Phenalenyl is stable as a neutral radical, a cation and an anion. The phenalenyl radical and its cation are discussed, in conjunction with new theoretical results, regarding their unusual electronic structure and possible interstellar importance. In Chapter 7, the $S_1 \leftarrow S_0$ spectrum of the closed shell neutral, 1H-phenalene, is also reported and the possible astronomical relevance of larger closed shell PAH molecules are discussed. Chapter 7 also reports three visible electronic transitions of the 1H-phenalenium$^+$ radical cation and these are assigned. The nitrogen heterocycles, 1-azaphenalene and 9b-azaphenalene are explored theoretically and the astronomical relevance of nitrogen containing PAHs (PANHs) is discussed.

Chapter 8 reflects on the results of the previous chapters and the methodologies introduced. Classes of molecules requiring further analysis are discussed and further experiments are suggested. Several classes of PAH are dismissed as potential carriers of the DIBs.

Overall, this work aims to set out a methodology by which future proposed carriers of the DIBs may be considered, and potentially eliminated, based on trends observed in spectroscopically related molecular species. If these methods fail to eliminate suggested

molecules, further measurements may be warranted. However such deductive methods rely on having proposed carriers to test, and in this regard experimental spectroscopists remain dependant on the insight and imagination of their colleagues in astrophysics and theoretical chemistry.

Chapter 2

Computational Methods

Spectroscopy, in isolation, is a powerful tool for the detection and identification of known chemical species. For example, the carriers of many of the stellar absorption features observed by Fraunhofer[28] were identified by Kirchhoff and Bunsen through the simple process of recording the flame spectra of known samples, and comparing these spectra with those observed astronomically, with little understanding of the nature of the atoms producing the spectra.[31–33] This direct comparison of astronomical spectra with known laboratory spectra is still a fundamental component of interstellar spectroscopy.

However, the usefulness of spectroscopy in understanding the physico-chemical and energetic properties of molecules is greatly enhanced when complemented with theoretical analysis of the spectrum. Therefore, knowing what photon energy a molecule can absorb can be practically useful. However, greater theoretical understanding is required to understand the quantum mechanical processes responsible for these absorptions. This has led to a symbiotic development in the understanding of molecular spectra and theoretical quantum mechanics.

It was the spectra of atoms, in particular hydrogen, that led Niels Bohr to add the quantisation of energy levels[213,214] to Rutherford's model.[215] This model, based on the earlier work of Max Planck,[216] gave rise to the earliest form of atomic quantum theory. This basic model was eventually expanded and generalised, resulting in the Schrödinger equation that is the basis of today's molecular electronic structure theory.[217]

2.1 Molecular Electronic Structure Theory

Molecular electronic structure theory is governed by the non-relativistic time-independent Schrödinger equation. This equation, in its simplest form, can be expressed

$$\hat{H}\Psi_i = \varepsilon_i \Psi_i \tag{2.1}$$

All states of the system are described by the wavefunctions Ψ_i. These wavefunctions are eigenfunctions of the hamiltonian operator, $\hat{H}$. The eigenvalues ε_i of this equation correspond to the total energies of the states.[217]

All observable properties of the system are described by the wavefunctions of that system. With the appropriate operator, $\hat{Q}$, the expectation value $\langle q \rangle_i$ for observable Q can be obtained by the equation;

$$\langle q \rangle_i = \frac{\int \Psi_i^* \hat{Q} \Psi_i d\tau}{\int \Psi_i^* \Psi_i d\tau} \tag{2.2}$$

Written in Dirac notation, this is simplified as;

$$\langle q \rangle_i = \frac{\langle i|\hat{Q}|i\rangle}{\langle i|i\rangle} \tag{2.3}$$

For molecular systems total energy can be given as the sum of the kinetic energies (corresponding to operators $\hat{T}$) and potential energies (corresponding to operators $\hat{V}$) of the nuclei, N, and the electrons, e. The full hamiltonian for Equation 2.1 can be written as;

$$\hat{H} = \hat{T}_N + \hat{T}_e + \hat{V}_{Ne} + \hat{V}_{NN} + \hat{V}_{ee} \tag{2.4}$$

In this equation, $\hat{T}_N$ is the nuclear kinetic energy operator and $\hat{T}_e$ is the electronic kinetic energy operator. $\hat{V}_{Ne}$ is the operator corresponding to coulomb attraction between the electrons and the nuclei. $\hat{V}_{NN}$ and $\hat{V}_{ee}$ respectively correspond to the nuclear and electronic coulomb repulsion terms.

This equation governs molecular electronic structure theory and could, in theory, be used to predict all observable properties for a molecule. Unfortunately, this equation can only be solved analytically for the hydrogen atom. For larger molecules, approximations have to be made to determine the wavefunctions and energy eigenvalues of the Schrödinger equation. Different computational methods use different approximations to solve the Schrödinger equation. As such, the answers obtained provide different insights into the internal structure of molecules.

2.1.1 The Variational principle

As the exact vibronic wavefunctions and energies of a molecule cannot be determined analytically, they must be approximated. The approximate wave function,Ψ_{trial}, may be written as a linear combination of the linearly independant eigenstates, Ψ_0,Ψ_1..., with coefficients c_i;

$$\Psi_{trial} = \sum_i c_i \Psi_i \tag{2.5}$$

The energy of the approximate wavefunction, ε_{trial} is defined by its energy expectation value (Equation 2.3).

$$\varepsilon_{trial} = \frac{\sum_i c_i^2 \langle i|\hat{H}|i\rangle}{\sum_i c_i^2 \langle i|i\rangle} \geq \varepsilon_0 \tag{2.6}$$

As the energy is minimised with respect to each c_i coefficient, the energy approaches that of the true ground state. As such, the calculated energy represents an upper bound to the true ground state energy of the system.[218] By this technique, approximate numerical solutions of the Schrödinger equation can be calculated.

2.1.2 The Adiabatic Born-Oppenheimer Approximation

The adiabatic Born-Oppenheimer approximation provides the framework for much of our understanding of molecular quantum mechanics. It is implicitly used by all electronic structure codes. This approximation assumes that electrons instantly adapt to the position of the nuclei,[219] adopting a wavefunction, ψ_e which obeys the electronic Schrödinger equation

$$\hat{H}_e \psi_e(\mathbf{q};\mathbf{Q}) = \varepsilon(\mathbf{Q})\psi_e(\mathbf{q};\mathbf{Q}) \tag{2.7}$$

where

$$\hat{H}_e = \hat{T}_e + \hat{V}_{Ne} + \hat{V}_{ee} + \hat{V}_{NN}. \tag{2.8}$$

Under this approximation the wavefunction of electrons, $\psi_e(\mathbf{q};\mathbf{Q})$, depend only parametrically on nuclear positions, $\mathbf{Q}$. By plotting the potential energy, $\varepsilon(\mathbf{Q})$, for each geometry $\mathbf{Q}$ the solutions obtained from this hamiltonian can be used to plot the potential energy surface for the molecule.

The full vibronic wavefunction is written as a product of the electronic wavefunction and the vibrational wavefunction,

$$\begin{aligned}\Psi(\mathbf{q},\mathbf{Q}) &= \psi_e(\mathbf{q};\mathbf{Q})\psi_v(\mathbf{Q}) \\ &= |e\rangle|v\rangle. \end{aligned} \tag{2.9}$$

The adiabatic approximation, that the electrons spontaneously adapt to changes in the nuclear position, has the computational advantage of diagonalising the electronic potential operator in the matrix representation of the hamiltonian. For three electronic states, the hamiltonian may be written

$$\hat{H} = \begin{pmatrix} T_{11} & T_{12} & T_{13} \\ T_{21} & T_{22} & T_{23} \\ T_{31} & T_{32} & T_{33} \end{pmatrix} + \begin{pmatrix} V_{11} & 0 & 0 \\ 0 & V_{22} & 0 \\ 0 & 0 & V_{33} \end{pmatrix} \tag{2.10}$$

where $\langle v_i|\varepsilon(\mathbf{Q})|v_j\rangle$ from Equation 2.7, and the elements T_{ij} of the nuclear kinetic energy operator are of the form

$$\begin{aligned}\langle e_i|\langle v_i|\hat{T}_N|v_j\rangle|e_j\rangle &= \sum_n \frac{-\hbar^2}{2M_n}\left\langle e_i\left|\left\langle v_i\left|\frac{\partial^2}{\partial Q_n^2}\right|v_j\right\rangle\right|e_j\right\rangle \\ &= \sum_n \frac{-\hbar^2}{2M_n}\left[\langle e_i|e_j\rangle\left\langle v_i\left|\frac{\partial^2}{\partial Q_n^2}\right|v_j\right\rangle + \left\langle e_i\left|\frac{\partial^2}{\partial Q_n^2}\right|e_j\right\rangle\langle v_i|v_j\rangle\right. \\ &\quad \left. +2\left\langle e_i\left|\frac{\partial}{\partial Q_n}\right|e_j\right\rangle\left\langle v_i\left|\frac{\partial}{\partial Q_n}\right|v_j\right\rangle\right]. \end{aligned} \tag{2.11}$$

The first term gives the nuclear kinetic energy while the second and third terms in Equation 2.11, the derivative couplings, describe how motion in a nuclear coordinate mixes electronic states.

If derivative coupling between the electronic states is negligible, the nuclear kinetic energy operator can be approximated by a diagonalised matrix,

$$\hat{H} = \begin{pmatrix} T_{11} & 0 & 0 \\ 0 & T_{22} & 0 \\ 0 & 0 & T_{33} \end{pmatrix} + \begin{pmatrix} V_{11} & 0 & 0 \\ 0 & V_{22} & 0 \\ 0 & 0 & V_{33} \end{pmatrix}. \tag{2.12}$$

While this approximation holds for most systems, it breaks down in systems with strong derivative coupling between electronic states, rendering the Born-Oppenheimer approximation invalid. For example, if the coupling exists between electronic states 2 and 3, the

hamiltonian becomes;

$$\hat{H} = \begin{pmatrix} T_{11} & 0 & 0 \\ 0 & T_{22} & T_{23} \\ 0 & T_{32} & T_{33} \end{pmatrix} + \begin{pmatrix} V_{11} & 0 & 0 \\ 0 & V_{22} & 0 \\ 0 & 0 & V_{33} \end{pmatrix} \tag{2.13}$$

In situations with this strong coupling, the off diagonal terms introduced makes solving Equation 2.13 extremely difficult. One approach to obtaining computational solutions for such systems is to use the diabatic, rather than adiabatic, representation. Here a unitary transformation decouples the electronic states with respect to the nuclear kinetic energy operator. In an infinite electronic basis, this is equivalent to the crude Born-Oppenheimer approximation, where the electrons in the molecule being examined are insensitive to the positions of the nuclei. This is at the expense of coupling the electronic energy states;

$$\hat{H} = \begin{pmatrix} T_{11} & 0 & 0 \\ 0 & T_{22} & 0 \\ 0 & 0 & T_{33} \end{pmatrix} + \begin{pmatrix} V_{11} & 0 & 0 \\ 0 & V_{22} & V_{23} \\ 0 & V_{23} & V_{33} \end{pmatrix} \tag{2.14}$$

Such strong coupling is observed in the D_{3h} symmetric phenalenyl radical, which was the focus of the author's undergraduate honours thesis as well as a subsequent paper.[201,220] This molecule will be briefly discussed in Chapter 7.

By their nature, electronic structure codes diagonalize the electronic energy at the specified geometry, and thus operate with in the framework of the adiabatic Born-Oppenheimer approximation. This approximation holds for the majority of molecules examined in this work. Two computational chemistry packages were used in this study: GAUSSIAN09[221] and FIREFLY[222]. The approximations used by these programs, and the theoretical methods they invoke, are outlined later in this this chapter.

2.2 Computational Methods

2.2.1 *Ab-initio* methods

Ab-initio, literally meaning "from the beginning" in Latin, was a description of computational methods first used by Parr *et. al.* in 1950.[223] It has come to mean quantum mechanical methods derived from first principles. These methods seek to find ways of

simplifying a quantum chemical problem, allowing the Schrödinger equation for the simplified system to be solved or approximately solved. Such methods include Hartree-Fock, perturbation theory and multi-reference methods, as well as methods that combine these. The methods used in this work are outlined below.

2.2.1.1 Restricted [Open shell] Hartree Fock (RHF/ROHF) - Self Consistent Field (SCF) Method

To create the wavefunctions of the molecular orbitals, required for later use in configuration interaction equations, RHF/ROHF-SCF calculations were performed using the FIREFLY package.[222] The RHF technique is applicable to closed-shell molecules, whereas ROHF has been adapted for radicals. These methods use an average field approximation to model electron-electron interactions. Each of the N electrons is described as moving in the average field of the other $N-1$ electrons.

The N-electron wavefunction is first given as a Hartree product of one electron wavefunctions;

$$\Phi(1,2,...,N) = \phi_1(1)\phi_2(2)...\phi_N(N) \tag{2.15}$$

where $i \equiv \mathbf{q}_i$. The spin-orbitals, $\{\phi_i\}_{i=1}^{N}$, representing molecular orbitals with up or down spin electrons, are formed from a linear combination of atomic basis functions, $\{\chi\}$;

$$\phi_i = \sum_k c_{ki}\chi_k, \tag{2.16}$$

these, in turn, being represented by a sum over gaussian primitives in fixed ratios.

The overall wavefunction is the normalised and antisymmetrised Hartree product, known as a Slater determinant;

$$\Phi(1,2,\ldots,n)| = \frac{1}{\sqrt{N!}} \begin{vmatrix} \phi_1(1) & \phi_2(1) & \cdots & \phi_N(1) \\ \phi_1(2) & \phi_2(2) & \cdots & \phi_N(2) \\ \vdots & \vdots & \ddots & \vdots \\ \phi_1(n) & \phi_2(N) & \cdots & \phi_N(N) \end{vmatrix} \tag{2.17}$$

where $\phi_i(j)$ indicates electron j occupies spin-orbital i. As such, the exchange of two electrons results in a change of sign of the Slater determinant, thus obeying Fermi-Dirac statistics and the Pauli exclusion principle.

The average field approximation is based on the assumption that the spin orbital wavefunctions of the other $N-1$ electrons are known. As this is generally not true, an initial wavefunction, approximating the true wavefunction, needs to be chosen.

To obtain an initial guess for the wavefunction, the electron-electron potential, V_{ee}, is ignored and the HF equations are solved for each spin orbital. These equations are determined variationally from the Schrödinger equation[224] and the one-electron hamiltonian is written as;

$$\hat{F}_i\phi_i(i) = \left\{\hat{h}_i + \sum_j (\hat{J}_j - \hat{K}_j)\right\}\phi_i(i) = \varepsilon_i\phi_i(i) \tag{2.18}$$

The $\hat{h}_i$ contains the $\hat{T}_e$ and $\hat{V}_{Ne}$ terms from Equation 2.4, which are determined explicitly for electron i. The repulsion from other electrons, V_{ee}, is contained in the coulomb ($\hat{J}_j$) and exchange ($\hat{K}_j$) operators.[225,226]

These equations can be solved numerically for each term in the Slater determinant (Equation 2.17) as one and two electron integrals.

The initial guess wavefunctions can be determined by omitting the ($\hat{J}_j$) and ($\hat{K}_j$) operators and solving Equation 2.18 for all the electrons. ($\hat{J}_j$) and ($\hat{K}_j$) can then be determined from these wavefunctions to obtain new wavefunctions for the electron spin-orbitals. These new wavefunctions are then used to determine new values for the ($\hat{J}_j$) and ($\hat{K}_j$) operators. This process continues until the wavefunctions produced by Equation 2.18 match those input into the equation, within a pre-set convergence criteria. This way, the minimum energy wavefunctions can be determined.

2.2.1.2 Configuration Interaction (CI)

CI calculations introduce additional configurations (in the form of Slater determinants) that allow electrons to avoid each other. Because of this, CI calculations include the instantaneous interactions between electrons that were omitted from the RHF/ROHF calculations. These additional configurations are formed by exciting electrons from the single RHF/ROHF Slater determinant into unoccupied spin orbitals. Electron excitation operators, $\hat{C}$, are chosen to match the symmetry of the original Slater determinant. The overall wavefunction is the linear combination of the Slater determinants resulting from these excitations. This is shown as Equation 2.19. The coefficients in this equation are chosen to minimise the energy of the system, in accordance with the variational principle outlined in Section 2.1.1

$$\Psi_{CI} = a_0\Psi_{HF} + \sum_{i,a} a_i\hat{C}_i^a\Psi_{HF} + \sum_{ij,ab} a_{ij}\hat{C}_{ij}^{ab}\Psi_{HF} + \dots \tag{2.19}$$

where $\hat{C}_i^a$ is the single excitation operator that excites the electron occupying orbital i into the unoccupied orbital a. Similarly, $\hat{C}_{ij}^{ab}$ is a double excitation operator. A full CI calculation includes such operators up to order N. While a full CI calculation allows for all symmetry-allowed transitions, this form of calculation is unfeasible for systems as large as the PAHs studied in later chapters.

2.2.1.3 Second Order Extended Multi-Configuration Quasi-Degenerate Perturbation Theory (X-MCQDPT2)

Alexander Granovsky's X-MCQDPT method is exclusively available through the FIREFLY computational chemistry program.[227] It is a multi-state multi-reference perturbation theory (MS-MR-PT) method. As the name suggests, these methods calculate the energies of several electronic states, by improving on multi-reference techniques using perturbation theory. Other techniques of this type include second-order complete active space perturbation theory (CASPT2) and second-order n-electron valence state perturbation theory (NEVPT2). A comparison of various earlier MR-PT methods was published by Chaudhuri *et. al.*[228] which, along with Granovsky's paper,[227] gives a good and highly detailed account of the differences between these techniques and their relative strengths and weaknesses. This section will focus largely on MS-MR-PT methods in general, and how X-MCQDPT2 was used in this work.

Multi-reference techniques simplify the full CI calculation by using an active space. The active space is a selection of frontier orbitals. Ideally, excitations within the active space will result in the electronic configurations most strongly contributing to the excited states being examined. By limiting the possible configurations to electronic excitations within these orbitals the number of Slater determinants required is reduced dramatically, allowing excited-state calculations to be performed on large molecules.

An inherent compromise exists in this method. By increasing the size of the active space, the excited-states under examination can be more accurately modelled at the cost of increased computing time and system complexity. The inverse is also true; computational requirements can be reduced at the cost of accuracy by reducing the size of the active space. In the end, the appropriate choice of active space depends on the molecule being studied and the detail required from the results.

Perturbation theory is a mathematical theory whereby an approximate solution to a problem is determined by exactly solving a related problem and adding a series of perturbations to approximate the behaviour of the desired solution.

Perturbation theory is generally presented in the form of a power series. In general it can be written in the form

$$A = A_0 + \epsilon^1 A_1 + \epsilon^2 A_2 + ... \tag{2.20}$$

As ϵ is small, the higher order terms become progressively smaller.

An approximation by second-order perturbation theory has the general form

$$A = A_0 + \epsilon^1 A_1 + \epsilon^2 A_2 \tag{2.21}$$

The second-order perturbation theory enhancement used in the X-MCQDPT2 technique is based on second-order Møller–Plesset perturbation theory (MP2).[229] MP2 is a relatively inexpensive method for improving the accuracy of *ab-initio* techniques, such as Hartree-Fock and multi-reference methods. It was original developed as a means of adding electron correlation effects to Hartree-Fock methods.

In this work, X-MCQDPT2 calculations were performed to calculate vertical electronic transition energies, T_v, and transition dipole moments, μ_0. These values are explained later in this chapter. The X-MCQDPT2 technique was applied to RHF/ROHF orbitals that were also calculated in Firefly[222] with the same basis set. The geometries used for the RHF/ROHF and X-MCQDPT2 calculations were optimised using the B3LYP/6-311++G(d,p) level of theory. The X-MCQDPT2 calculations in Chapter 5 were performed by Professor Timothy Schmidt. Based on the apparent success of this technique in calculating energies and intensities of higher electronic excited states, X-MCQDPT2 calculations were also performed by the author, the results of which are presented in Chapters 6 and 7. CASPT2, another MS-MR-PT method, was used in calculations provided by Dr George Bacskay and are included in Chapter 4.

2.2.2 Density Functional Theory (DFT)

In this study, DFT calculations were performed to determine equilibrium geometries and to perform normal mode analysis. These calculations were run using the Gaussian09 computational chemistry package.

DFT is based on the Hohenberg-Kohn theorem which states that the ground state electronic properties of a system can be uniquely described by its electron density.[230] The energy of this system can be expressed, in terms of electron density $\rho(\mathbf{r})$, by the equation;

$$E[\rho] = E_T[\rho] + E_{Ne}[\rho] + E_J[\rho] + E_{xc}[\rho] \tag{2.22}$$

In Kohn-Sham (KS) DFT, the charge density of N electrons is formulated in terms of spin orbitals;

$$\rho(\mathbf{r}) = \sum_{i=1}^{N} |\phi_i(\mathbf{r})|^2 \tag{2.23}$$

E_T, the kinetic energy, can then be determined based on these orbitals,

$$E_T = \sum_{i=1}^{N} \langle \phi_i | \hat{T}_e | \phi_i \rangle \tag{2.24}$$

These KS orbitals $\{\phi_i\}_{i=1}^{N}$ are obtained via the variational principle described in Section 2.1.1. The KS energy operator can then be defined;

$$\hat{F}_{KS}\phi_i = \epsilon_i \phi_i \tag{2.25}$$

$$\hat{F}_{KS} = \hat{T}_e + \upsilon(\mathbf{r}) + J(\mathbf{r}) + \upsilon_{xc}(\mathbf{r}) \tag{2.26}$$

where $\upsilon(\mathbf{r})$ is the nuclear attraction term, $J(\mathbf{r})$ is the coulomb repulsion term and $\upsilon_{xc}(\mathbf{r})$ is the exchange-correlation correction term. The exchange-correlation term cannot be analytically determined and must be approximated. These approximations are generally derived by fitting parameters that are derived from accurate experimental data or numerical calculations. DFT is therefore a semi-empirical technique.

This work makes use of three differently parametrised hybrid DFT methods, B3LYP[231,232] CAM-B3LYP[233] and M06.[234] Calculations using these DFT techniques were undertaken in the GAUSSIAN09 computational chemistry package.[221]

2.2.2.1 Time-Dependent Density Functional Theory (TD-DFT)

Density functional methods, such as B3LYP, are extremely efficient at calculating ground-state properties. However, a similar formulation for calculating excited-state properties

requires a theoretical treatment derived from the time-dependent Schrödinger equation.

$$\hat{H}(t)|\Psi(t)\rangle = i\frac{\partial}{\partial t}|\Psi(t)\rangle \tag{2.27}$$

Properties requiring time-dependent treatment include atomic and nuclear scattering,[235] the dynamical response of inhomogeneous metallic systems,[236] and any excited-state property of an electronically excited molecular system.

The generalised time-dependant formulation of KS DFT was developed by Runge and Gross in 1984.[236] In addition to the initial publication of Runge and Gross that explains in detail the methodology on which the theory is based,[236] there are a number of excellent review articles outlining the development, formalism and applications of the Runge-Gross equation and TD-DFT in general.

A non-exhaustive list of these review articles include the works of

- Gross and Kohn (1990);[237]
- Onida, Reining and Rubio (2002);[238]
- Chelikowsky, Kronik and Vasiliev (2003);[239]
- Rosa, Ricciardi, Gritsenko and Baerends (2004);[240]
- Dreuw and Head-Gordon (2005);[241]
- Barone, Improta and Rega (2008);[242]
- Jacquemin, Wathelet, Perpéte, and Adamo (2009);[243]
- Casida (2009);[244]
- van Faasen and Burke (2009);[245]
- Jacquemin, Mennucci and Adamo (2011);[246]
- Marques, Maitra, Nogueira, Gross and Rubino (2012);[247]
- Adamo and Jacquemin (2013).[248]

TD-DFT has been shown to be a useful tool when calculating excited-state transition energies, geometries and vibrational frequencies, as well as simulating the intensities of electronic and vibronic transitions. It can be applied to numerous DFT functionals, including the B3LYP (TD-B3LYP), CAM-B3LYP (TD-CAM-B3LYP) and M06 (TD-M06) functionals used in this work. These applications of TD-DFT will be discussed below.

2.3 Calculation of Molecular Properties

2.3.1 Optimised Geometry

Geometry optimisation is the process by which the minimum energy geometry of a molecule is iteratively determined for a specified electronic energy level. Quantum chemical software achieves this by adjusting the geometry of the molecule until a stationary point on the potential surface is found. This can be performed using a wide range of *ab-initio*, DFT (for ground states) and TD-DFT (for excited states) levels of theory.

All geometry optimisations in this work were undertaken using the GAUSSIAN09[221] suite of software. The default algorithm used by GAUSSIAN09 for minimizations (optimizations to a local minimum) is the Berny algorithm[249] using GEDIIS[250] in redundant internal coordinates.[221,251–257] This algorithm uses the forces acting on the atoms of a given structure, together with the second derivative matrix (called the Hessian matrix), to predict energetically more favourable structures and thus optimize the molecular structure towards the next local minimum on the potential energy surface.[258] As it is computationally expensive to explicitly calculate the Hessian at each point, the calculation approximates the Hessian, initially using a simple valence force field, then updating this estimate using energies and first-derivatives for each new point along the optimisation pathway.

This process, like all optimisation process, will find the nearest minimum. It is therefore important to have a good estimate of the starting geometry to avoid optimising to a local minimum, as opposed to the true optimised geometry.

All ground state geometry optimisations were undertaken using DFT, with B3LYP, CAM-B3LYP and M06 all used. All excited state geometries reported in this work were calculated using TD-B3LYP.

2.3.2 Electronic Transition Energy and Intensity

The following properties can be calculated by quantum chemical software programs using a range of *ab-initio* and TD-DFT methods. The energy difference they refer to is displayed in Figure 2.1.

The vertical excitation energy (T_v) is the difference in energy between the ground electronic state and the excited electronic state at the optimised geometry of the ground-state. This ignores differences in geometry and zero-point energy between the ground state and the

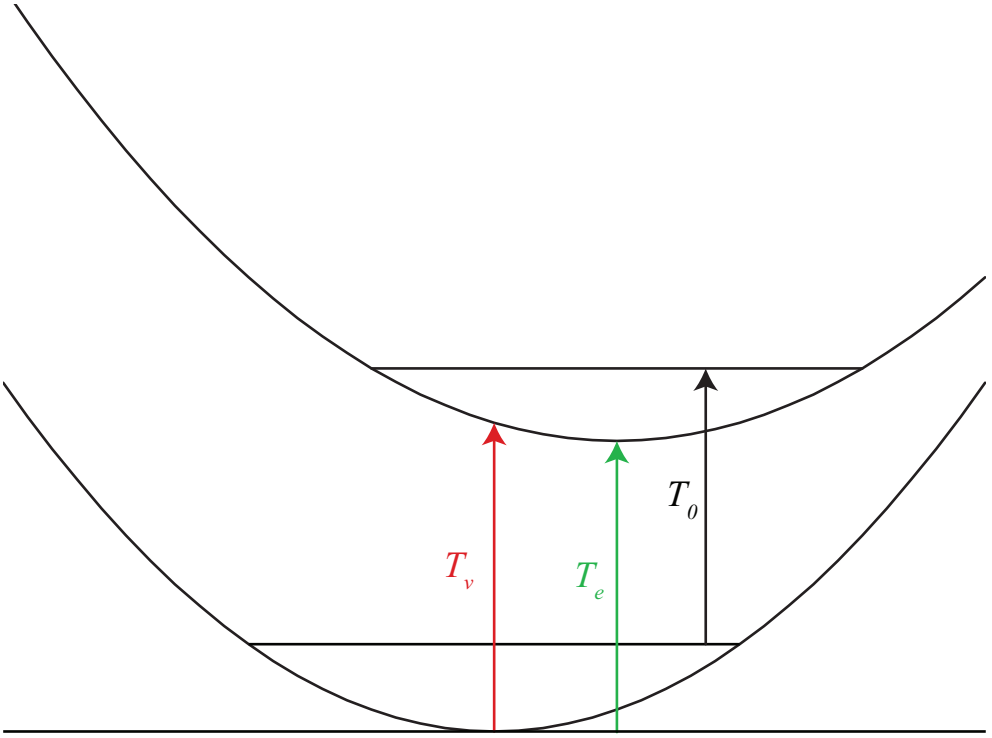

Figure 2.1: Energy level diagram showing the deffinition of T_v: the vertical excitation energy; T_e: the adiabatic excitation energy; and T_0: the zero-point corrected excitation energy

excited state. This estimate of the electronic transition energy is the least computationally demanding, as optimising ground state geometries is significantly less expensive than optimising excited state geometries. While this is the value that least represents the observed electronic excitation energy, this inexpensive measure of electronic excitation energy can be an excellent method of predicting electronic transition energies, especially when corrected by empirical scaling.[185] This will be discussed further in Chapter 4.

An improvement on this value is the adiabatic transition energy (T_e). This involves calculating the difference in energy between the geometry optimised ground-state and the geometry optimised excited-state. This calculation therefore implicitly includes the geometry change of the molecule upon excitation.

Calculation of zero-point energy further improves this calculation, giving the zero-point-corrected transition energy (T_0). Indeed, it is T_0 which is directly experimentally measured when an electronic origin band is observed.

Through studies of the specific heat of hydrogen, Einstein and Stern concluded that the vibrational energy of a molecular vibration has energy

$$\epsilon = \frac{h\nu}{e^{\frac{h\nu}{kT}}} + \frac{h\nu}{2} \tag{2.28}$$

Table 2.1: TD-B3LYP/6-311++G(d,p) calculated $S_1 \leftarrow S_0$ transition energies of benzene. Calculations were run on same computer system (Silica cluster of the High-Performance Computing Facility at The University of Sydney) with same number of processors (four).† - Estimated position of forbidden electronic origin transition, from Stephenson *et al.*[261]

Method	CPU time (hours)	E_{calc} (eV)	$E_{experiment}$† (eV)	Δ_E (eV)
T_v	1.7	5.48	4.72	0.76
T_e	5.3	5.34	4.72	0.62
T_0	191.5	5.18	4.72	0.46

where h is Planck's constant, ν is the fundamental frequency of the vibrational normal mode, k is the Boltzmann constant and T is the vibrational temperature in Kelvin.[259]

It follows from Equation 2.28 that at absolute zero, the energy of a vibrational mode can be given as $\epsilon = 1/2h\nu$. This is the zero-point energy, which is a consequence of the Heisenberg uncertainty principle.[260]

The zero-point energy for each electronic state can be calculated as the sum of the zero-point vibrational energies,

$$ZPE = \sum_{1 \leq n \leq 3N-6} \frac{h\nu_n}{2} \tag{2.29}$$

where n is a vibrational normal mode, and N is the number of atoms.

Calculation of excited-state frequencies, which involves explicitly calculating the Hessian of the excited-state geometry for each vibrational mode, is extremely expensive. These calculations are discussed later in this chapter. As a result, calculation of T_0 has significantly greater expense than calculation of T_v or T_e.

As an example, T_v, T_e and T_0 were calculated for the $S_0 \leftarrow S_1$ transition of benzene at the TD-B3LYP/6-311++G(d,p) level of theory, and this data is tabulated in Table 2.1. Barnes *et al* performed similar calculations on a large number of small radical species with a large number of functional and basis sets, and finds similar trends.[262]

As you would expect, with an error of 0.46 eV, the calculated value for T_0 is closest to the experimentally measured value of T_0. However, this comes at significantly increased expense, with the calculation taking more than 100 times longer to run.

While the raw value of T_v overestimates the electronic transition energy of benzene by 0.76 eV, this calculation is far more cost effective to run. It is shown in Chapters 4, 5 and

7 that by empirically correcting affordable TD-DFT T_v values, experimental values of T_0 can be estimated cheaply with an accuracy better than 0.2 eV.

2.3.3 Normal Mode Analysis

A normal mode of a vibrating system is a pattern of motion in which all parts of the system move sinusoidally with the same frequency and with a fixed phase relation. All possible resonant vibrations of the system can be described in terms of its normal modes.

All possible motions and forces for an N atom system can be described in terms $3N$ cartesian co-ordinates $\{x_j\}$. By Newton's second law, a single cartesian co-ordinate x_i of an atom with mass m_i is described by the equation

$$m_i\ddot{x}_i = \sum_j^{3N} \frac{\partial^2 V}{\partial x_i \partial x_j} x_j = 0 \tag{2.30}$$

This system can be described in terms of the mass weighted co-ordinates $\{y_i\}$ where $y_i = \sqrt{m_i}x_i$. If we substitute these co-ordinates into Equation 2.30 and apply the chain rule, this is reduced to

$$\ddot{y}_i + \sum_j^{3N} \frac{\partial^2 V}{\partial y_i \partial y_j} y_j = 0 \tag{2.31}$$

As the motion is sinusoidal,

$$y_i = y_0 \sin(\omega t) \tag{2.32}$$

$\ddot{y}_i$ has the form

$$\ddot{y}_i = -\omega^2 y_i \tag{2.33}$$

If we then define $\boldsymbol{G}$ as the matrix with elements $G_{ij} = \partial^2 V / \partial y_i \partial y_j$, Equation 2.31 can be represented as an eigenfunction equation

$$\boldsymbol{G}\boldsymbol{y} = \omega^2 \boldsymbol{y} \tag{2.34}$$

Upon diagonalising matrix $\boldsymbol{G}$, the eigenvalues of this system are the mass-weighted normal co-originates. Computational chemistry programs calculate the $3N$ vibrational normal modes by diagonalising this matrix. Of the $3N$ normal modes produced, six will be redundant in a non-linear molecule giving a total of $3N - 6$ vibrational normal modes.

2.3.4 Harmonic Frequencies of Vibrational Normal Modes

As a first order approximation, normal modes frequencies, the starting point for any vibronic assignment, can be estimated using the simple harmonic oscillator model. This assumes that the vibration can be modelled as a spring which obeys Hooke's law,

$$F = -kQ \tag{2.35}$$

where k is the force constant of the vibrational mode and Q is the displacement from the equilibrium geometry.

In classical mechanics, Newton's second law of motion means this can be re-written in terms of a reduced-mass μ

$$F = \mu \frac{d^2Q}{dt} \tag{2.36}$$

Combining Equations 2.35 and 2.36 and solving gives the harmonic frequency

$$\nu = \frac{1}{2\pi}\sqrt{\frac{k}{\mu}} \tag{2.37}$$

where force constant k is the second derivative of the potential energy V,

$$k = \frac{\partial^2 V}{\partial Q^2} \tag{2.38}$$

In this harmonic model, the potential V is quadratic. Solving the Schrödinger equation for this model gives the quantum harmonic oscillator

$$\varepsilon_n = \hbar\left(n + \frac{1}{2}\right)\sqrt{\frac{k}{\mu}} \tag{2.39}$$

This approximation requires vibrational energy potentials to be approximately parabolic in shape. Molecular vibrations that obey this simple harmonic model are referred to as harmonic and, as can be seen in Equation 2.39, energy levels of a particular vibration are evenly spaced.

Computationally, this means that the fundamental vibration of a normal mode ($n = 1$) may be estimated from the second derivative of the potential energy surface at the equilibrium geometry.

In this work, harmonic vibrational energy levels are calculated using B3LYP (for the ground state) and TD-B3LYP (for the excited state). These calculations are performed using the GAUSSIAN09[221] software package. Calculating normal mode frequencies on the ground state is relatively inexpensive, taking minutes to calculate after the geometry has been optimised. As mentioned previously calculating the second derivative of the excited state potentials is extremely expensive. However, due to the accuracy of the calculation for harmonic vibrational modes, it is nonetheless used in Chapters 4,6 and 7. These calculations also allow for Frank-Condon and Herzberg-Teller intensities to be simulated, and these calculations will be discussed later in this chapter.

Vibrational modes are not always well represented by the simple harmonic oscillator model. In these cases, anharmonic vibrational frequencies can be calculated by solving the Schrödinger equation for the relevant potential energy surface. This was done in Chapters 4 and 7 by first constructing a potential energy surface using a series of single point TD-B3LYP calculations and then solving the 1-dimensional Schrödinger equation variationally using in-house code provided by Prof. Timothy Schmidt. This method of determining anharmonic frequencies is outlined in more detail in Chapter 4.

2.3.5 Vibronic Transition Intensities

Since it was originally postulated in 1926, the Franck-Condon principal has been a starting point for determining the intensity of vibronic transitions.[210,211]

The IUPAC gold book defines the Frank-Condon principal as follows:

- Classically, the Franck–Condon principle is the approximation that an electronic transition is most likely to occur without changes in the positions of the nuclei in the molecular entity and its environment. The resulting state is called a Franck–Condon state, and the transition involved, a vertical transition. The quantum mechanical formulation of this principle is that the intensity of a vibronic transition is proportional to the square of the overlap integral between the vibrational wavefunctions of the two states that are involved in the transition.[264]

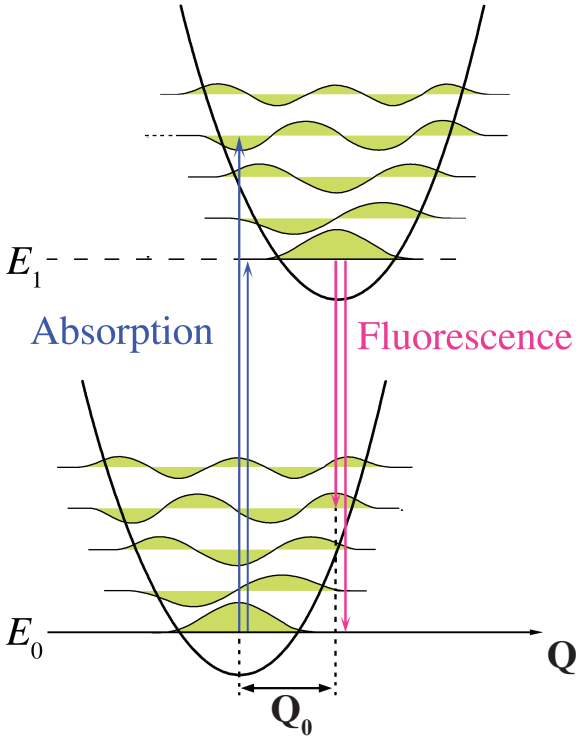

Figure 2.2: Energy level diagram for transitions between electronic states. Available at http://commons.wikimedia.org/wiki/File:Phonon-energy-diagram.png under the the Creative Commons Attribution-Share Alike 2.5 Generic license. Created by Mark Somoza based on figures in: J. Friedrich and D. Haarer (1984).[263] Image modified by the author to remove non-relevent labels.

This is demonstrated in Figure 2.2. In this figure, there is very little overlap between the vibrationally unexcited wavefunctions of E_0 and E_1, and as such the $E_1 \leftarrow E_0$ electronic origin absorption band is likely to be weak. Instead the intensity is likely to be found in the band corresponding to a transition from the vibrationless E_0 to $n = 3$ in E_0.

Under the Franck-Condon approximation the transition moment, $\boldsymbol{\mu}$, for a transition between two vibrational states is a constant, μ_e, throughout the vibrational co-ordinate $\mathbf{Q}$.

As such

$$\mu(\mathbf{Q}) = \boldsymbol{\mu}_e \tag{2.40}$$

And the Franck-Condon transition moment between vibrational states ϕ'_v and ϕ''_v is

$$\mu_{FC} = \mu_e \int \phi'_v \phi''_v d\mathbf{Q} \tag{2.41}$$

Therefore, the Franck-Condon approximation holds for any system where the transition moment is independent of the vibrational co-ordinate. This will not be the case where there is significant coupling between the observed vibronic transition and other electronic transitions.

In particular, a vibronic transition may gain intensity if distortion along the vibrational co-ordinate increases the coupling with a stronger, higher energy electronic transition. This causes the vibronic mode to be coupled to the stronger electronic state, introducing a vibrational co-ordinate dependence to the transition dipole moment. While in many cases this component can be ignored, it may become the dominant contribution where transitions have weak Franck-Condon intensity, such as the forbidden $1^1B_{2u} \leftarrow X^1A_{1g}$ transition of benzene, or where the vibronic coupling is strong. These effects were first discussed by Herzberg and Teller in 1933[212] and intensity induced by the dependence of $\mu(\boldsymbol{Q})$ on the nuclear co-ordinate is known as the Herzberg-Teller effect.[265] The Herzberg-Teller effect is alternatively described in terms of intensity "stealing" from vibronic interaction or as a strong dependence of $\mu(\boldsymbol{Q})$ on the nuclear co-ordinate. This is two ways of describing the same physical effect.[265]

By considering a partial linear-dependence on the nuclear co-ordinate, a more general form of the transition moment can be written

$$\mu(\boldsymbol{Q}) = \mu_e + \sum_{i}^{3N-6} \alpha_i \mathbf{Q_i} \tag{2.42}$$

where μ_e is the Franck-Condon component and $\sum \alpha_i \vec{R}_i$ is the first order Herzberg-Teller term.

The quantum-mechanical application of this combined theorem comes from applying the transition dipole moment operator for multiple charges

$$\hat{\mu} = \sum q_i Q_i \tag{2.43}$$

to the electronic potential component of the time-dependant Schrödinger equation for the transition from state $|i\rangle$ to state $|f\rangle$

$$\langle f|\hat{V}(t)|i\rangle = \langle f|E(t)\cdot\hat{\mu}|i\rangle = E(t)\langle f|\hat{\mu}|i\rangle \tag{2.44}$$

Expanding out of Bra-Ket notation

$$\langle f|\hat{\mu}|i\rangle = \iint \Phi'_v(\boldsymbol{Q})\Phi'_e(\boldsymbol{q},\boldsymbol{Q})\hat{\mu}\Phi''_e(\boldsymbol{q},\boldsymbol{Q})\Phi''_v(\boldsymbol{Q})\cdot \mathrm{d}\boldsymbol{Q}\cdot \mathrm{d}\boldsymbol{q} \tag{2.45}$$

where Φ''_v and Φ'_v are the nuclear state wavefunctions for initial and final state respectively whereas Φ''_e and Φ'_e are the electronic state wavefunctions for initial and final state respectively

By integrating over the electron co-ordinate $\boldsymbol{q}$, Equation 2.45 can be reduced to

$$\langle f|\hat{\mu}|i\rangle = \int \phi'_v(\boldsymbol{Q})\mu(\boldsymbol{Q})\ \phi''_v(\boldsymbol{Q}) \cdot \mathrm{d}\boldsymbol{Q} \tag{2.46}$$

By applying this to the Franck-Condon and Herzberg-Teller results of Equation 2.42 we can calculate a combined Franck-Condon and first-order Herzberg Teller transition dipole moment

$$\mu_{FCHT} = \mu_e \int \phi'_v \phi''_v \cdot \mathrm{d}\boldsymbol{Q} + \sum_i^{3N-6} \alpha_i \int \phi'_v \boldsymbol{Q} \phi''_v \cdot \mathrm{d}\boldsymbol{Q} \tag{2.47}$$

The effect of the Herzberg-Teller on the selection rules of vibrational transitions is the result of the linear dependence on the nuclear co-ordinates. In Franck-Condon transitions, vertical transitions are preferred due to the greater overlap of the vibrational wavefunctions. As such, for a molecule with little geometry change between the ground and excited state (such as most of the aromatic molecules observed in this study), for an allowed electronic transition, the electronic origin transition can be expected to be dominant.

However, in Herzberg-Teller transitions, the wavefunction of the fundamental ground state is perturbed by the linear transition dipole moment. The strongest overlap upon excitation in these cases tends to favour an increase in one-quanta of the Herzberg-Teller active mode.

This change in selection rules is even more profound in emission. Dispersing emission from one-quantum of a Herzberg-Teller mode will show emission to two-quanta of that mode and to the vibrational ground state, with the emission to the two-quanta mode being twice as intense. Such behaviours were observed in the authors honours thesis.[220] However, the excited states observed in this study were not observed in fluorescence, as they mostly had short excited state lifetimes and correspondingly weak fluorescence yields.

2.3.6 Simulating Intensities in Gaussian09

The Gaussian09 package has the ability to simulate TD-DFT intensities of vibronic transitions. This can be done at both the Frank-Condon level of theory (FC simulation) as well as the combined Franck-Condon/ first-order Herzberg-Teller levels of theory (FCHT simulation). These calculations require initial calculation of TD-DFT excited state frequencies (in this study, TD-B3LYP is used). The ground state normal modes are calculated as part

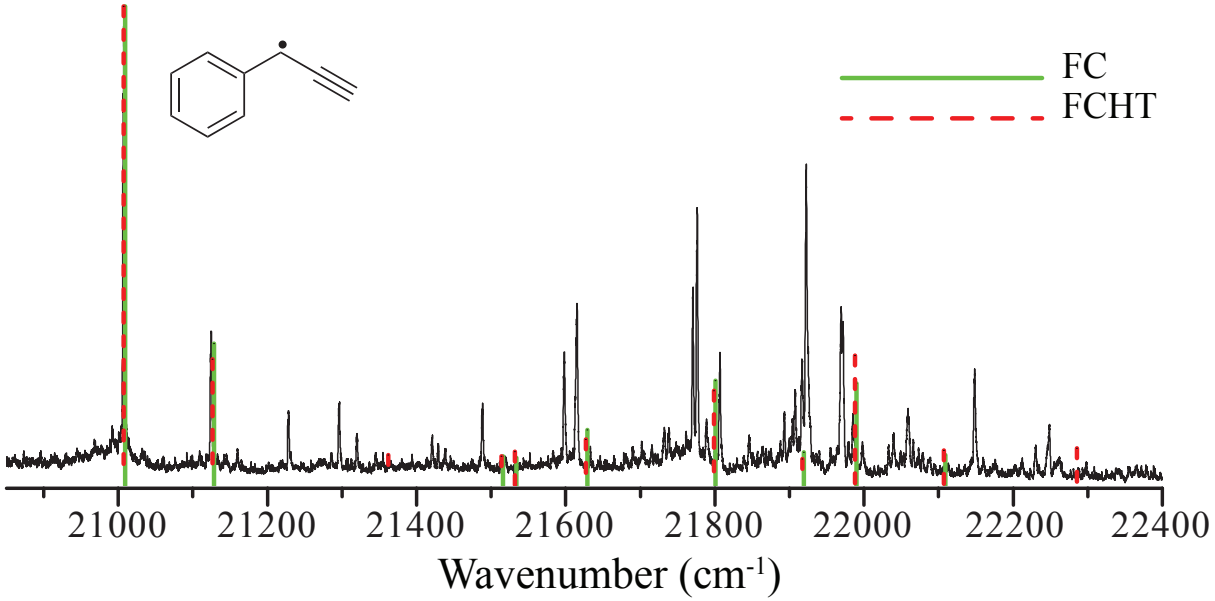

Figure 2.3: Black: $D_1 \leftarrow D_0$ LIF excitation spectrum of 1-PPr.[193] Green solid: TD-B3LYP/6-311++G(d,p) FC simulation of $D_1 \leftarrow D_0$ spectrum of 1-PPr. Scaled to match origin. Red dashed:TD-B3LYP/6-311++G(d,p) FCHT simulation of $D_1 \leftarrow D_0$ spectrum of 1-PPr. Scaled to match origin.

of the simulation and the excited state excitation spectrum is then output. The simulation can be set up with user-defined peak widths. However, in this study only the stick spectrum was used.

To gauge the accuracy of of the FC and FCHT simulations, the previously assigned gas-phase spectra of several molecules were simulated. FC and FCHT spectra were simulated for the $D_1 \leftarrow D_0$ transitions of 1-phenylpropargyl (1-PPr),[193,266] 1-naphthylmethyl (1-NpMe) and 2-naphthylmethyl (2-NpMe) radicals.[183] These simulations were performed at the TD-B3LYP level of theory with a 6-311++G(d,p) basis set.

2.3.6.1 1-Phenylpropargyl (1-PPr)

In Figure 2.3, FC and FCHT stick-spectra for the $D_1 \leftarrow D_0$ transition of 1-PPr are shown overlaying the corresponding gas-phase laser-induced fluorescence (LIF) spectrum.[193]

It can be seen in Figure 2.3 that for the $D_1 \leftarrow D_0$ transition of 1-PPr the FC and FCHT simulations give almost identically the same intensity pattern, suggesting that the Franck-Condon approximation dominates the simulated intensities for this transition. The relative intensity of the origin band and the first vibrational band located at 117 cm^{-1} appears well simulated by both FC and FCHT. The remaining vibrational structure is simulated to be significantly weaker than than what is observed. However, Figure 2.4 shows that the

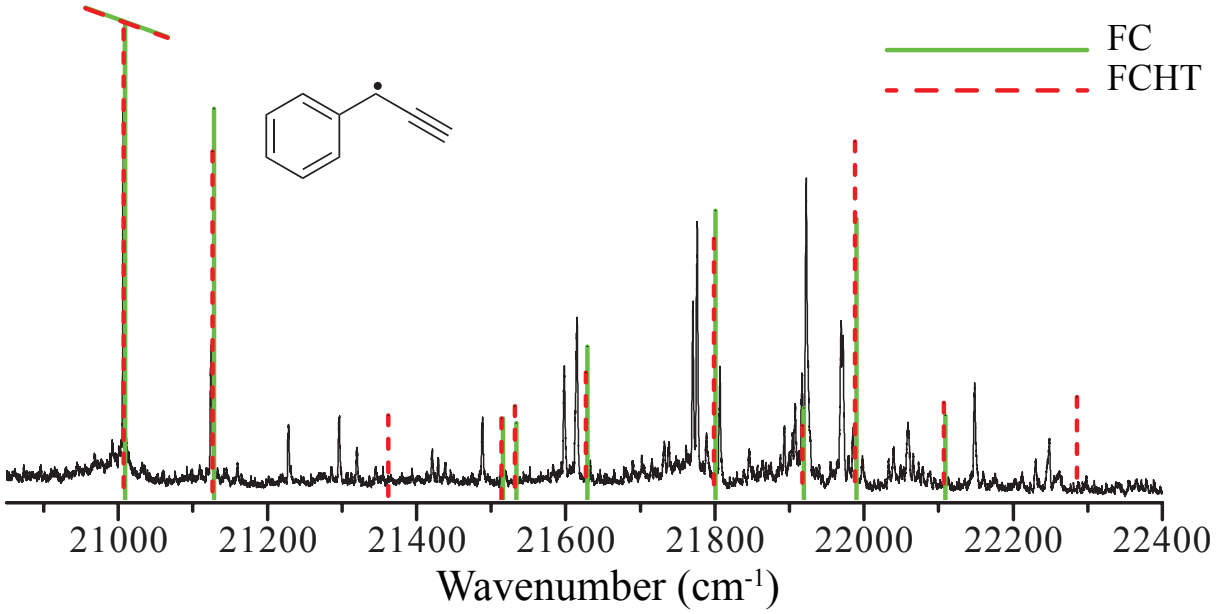

Figure 2.4: Black: $D_1 \leftarrow D_0$ LIF excitation spectrum of 1-PPr.[193] Green solid: TD-B3LYP/6-311++G(d,p) FC simulation of $D_1 \leftarrow D_0$ spectrum of 1-PPr. Scaled to show relitive intensity of vibronic transitions. Red dashed:TD-B3LYP/6-311++G(d,p) FCHT simulation of $D_1 \leftarrow D_0$ spectrum of 1-PPr. Scaled to show relative intensity of vibronic transitions.

transitions of these bands are well fit relative to each other, possibly suggesting saturation of the observed spectrum. It is curious that the relative intensities of the transitions at 21924 cm^{-1} and 21972 cm^{-1} appear to be reversed in the simulations. However, overall, there is good agreement between the simulated and observed spectra.

2.3.6.2 1-Naphthylmethyl (1-NpMe)

Figure 2.5 shows FC and FCHT stick-spectra for the $D_1 \leftarrow D_0$ transition of 1-NpMe is shown overlaying the corresponding gas-phase R2C2PI spectrum.[183]

It can be seen from Figure 2.5 that most of the intense peaks in the observed spectrum are not predicted to have significant intensity in the FC simulation. The FCHT simulation however does an excellent job of simulating the observed intense vibronic transitions, suggesting that Herzberg-Teller coupling is partially responsible for the intensity of many of these transitions. In particular the three large bands at 17697 cm^{-1}, 17730 cm^{-1} and 17787 cm^{-1} are not predicted to have significant intensity by the FC simulation but are predicted to be strong by the FCHT simulation. This Herzberg-Teller intensity is caused by coupling to a significantly stronger, higher-energy electronic transition. This stronger transition to a higher excited state is a feature of odd-alternate hydrocarbon radicals, such

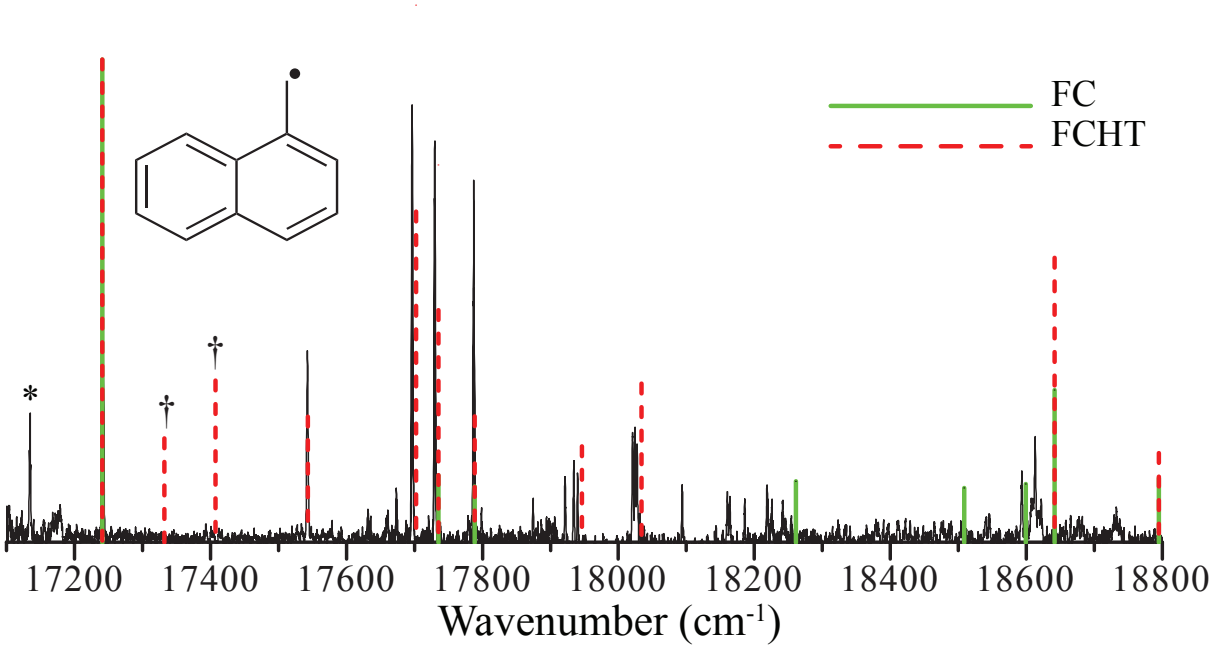

Figure 2.5: Black: $D_1 \leftarrow D_0$ R2C2PI excitation spectrum of 1-NpMe.[183] Green solid: TD-B3LYP/6-311++G(d,p) FC simulation of $D_1 \leftarrow D_0$ spectrum of 1-NpMe. Scaled to match origin intensity. Red dashed:TD-B3LYP/6-311++G(d,p) FCHT simulation of $D_1 \leftarrow D_0$ spectrum of 1-NpMe. Scaled to match origin intensity. * - $D_1 \leftarrow D_0$ electronic origin of 2-NpMe (see Figure 2.6) † - single-quantum out-of-plane modes (simulated but not observed).

as 1-NpMe. These stronger transitions to higher excited states are examined in detail in Chapter 5.

The FCHT simulation reports intensity in single-quantum of several low-frequency out of plane modes. However none of these transitions are observed in the R2C2PI spectrum. It can therefore be concluded that the FCHT simulation has significantly overstated the effect of Herzberg-Teller coupling on these modes.

2.3.6.3 2-Naphthylmethyl (2-NpMe)

In Figure 2.6, FC and FCHT stick-spectra for the $D_1 \leftarrow D_0$ transition of 2-NpMe are displayed with the corresponding gas-phase R2C2PI spectrum.[183]

Both the FC and FCHT do a poor job simulating the 2-NpMe R2C2PI spectrum shown in Figure 2.6, despite the success of these techniques in simulating the spectrum of the similar 1-NpMe. It can therefore be concluded that, while a useful tool in the assignment of vibronic spectra, these simulations cannot reliably reproduce experimental spectra in all instances. However, this technique is used extensively in this work to aid in the assignment and understanding of observed vibronic spectra, and proves particularly useful

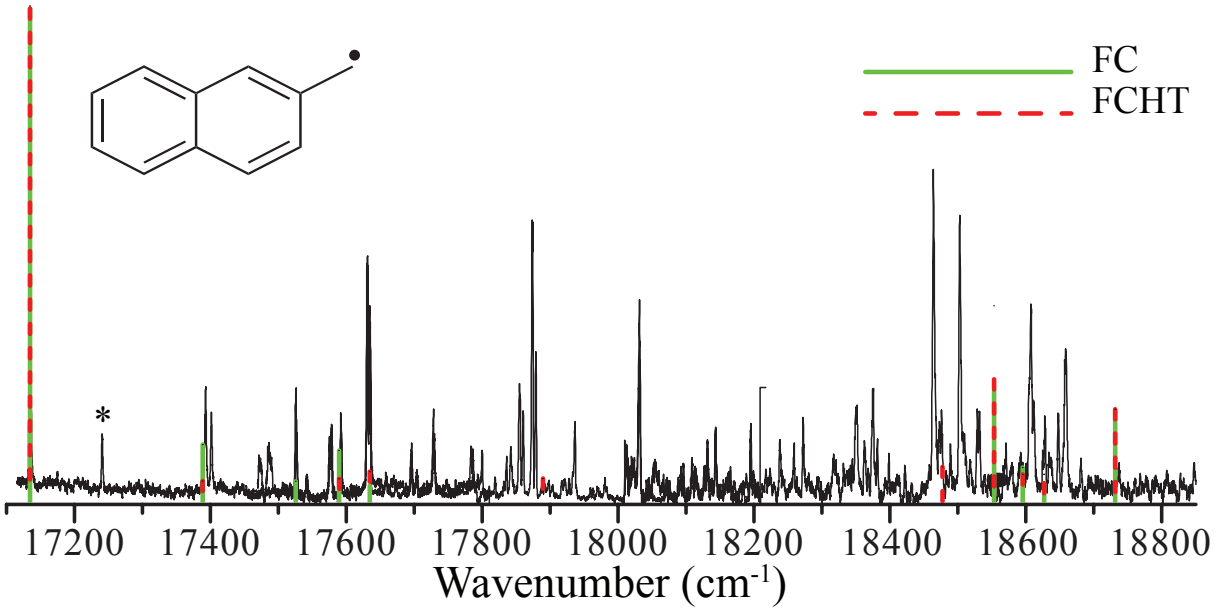

Figure 2.6: Black: $D_1 \leftarrow D_0$ R2C2PI excitation spectrum of 2-NpMe.[183] Green solid: TD-B3LYP/6-311++G(d,p) FC simulation of $D_1 \leftarrow D_0$ spectrum of 2-NpMe. Scaled to match origin intensity. Red dashed:TD-B3LYP/6-311++G(d,p) FCHT simulation of $D_1 \leftarrow D_0$ spectrum of 2-NpMe. Scaled to match origin intensity. * - $D_1 \leftarrow D_0$ electronic origin of 1-NpMe (see Figure 2.5).

in the assignment of highly congested spectra where several possible assignments, based on frequency, present themselves.

2.4 Conclusions

Several efficient and affordable *ab-initio*, DFT and TD-DFT techniques are available to the modern experimental spectroscopist. These techniques are especially well suited to the understanding and assignment of jet-cooled gas-phase spectra, as the calculation of solvation effects and vibrational hot-band spectra are unnecessary.

Modern computational power has also made these techniques far more accessible than they have previously been. While, for speed and convenience, many of the calculations reported in this work were performed on the Silica cluster of the High-Performance Computer Facility at The University of Sydney, several calculation were performed on a typical modern laptop personal computer. With the relative ease of use of computational chemistry programs such as GAUSSIAN09[221] and FIREFLY[222], the tools available for the calculation of chemical properties are vast.

It it important to point out that the computational methods described here all have limited accuracy and rely on assumptions that must be tested. In that knowledge, this work attempts to develop methods of using experimental data to determine not only the accuracy of these computational methods, but to find trends which allow greater accuracy in the interpretation of these results.

By understanding the quantum-mechanical source of spectral properties, trends in these properties can be extrapolated for the transitions of larger molecules of similar multiplicity and charge. It is these trends that this work uses to determine, for any sized chromophore, if a class of aromatic hydrocarbon is likely to have optical transitions relevant to interstellar spectroscopy, particularly the DIBs.

Chapter 3

Experimental Techniques and Apparatus

The basis of this work is experimental spectra of aromatic molecules, radicals and ions recorded in simulated astronomical conditions. The experimental techniques and apparatus used to record these spectra are outlined in this chapter.

3.1 Vacuum Techniques

All spectra recorded in this work were recorded in a low pressure environment, in the laboratory. This has several benefits. Firstly, many of the molecules observed in this work (such as resonance stabilised radicals) are commonly thought of as reaction intermediates, meaning they are highly reactive but physically stable.[267] As such, in a vacuum, these species will not spontaneously decompose, but they will react under collisions with all but the most inert chemical species, including reactions with similar/identical species. While short lived in the atmosphere, and indeed most collisional environments, these molecular species are potentially relevant to interstellar spectroscopy, as they are stable in the interstellar vacuum. Indeed, many such species have already been observed in the ISM, as shown in Table 1.1.

To observe these reaction intermediates, they must be isolated from all but the most inert species. They must also be separated from other, identical, reaction intermediates to prevent dimerisation.

One means of overcoming this is matrix isolation spectroscopy, whereby molecules are trapped in a cold, inert medium.[268–272] However spectra recorded under these conditions will be affected by the presence of the matrix, as it will unevenly stabilise molecules in different energetic states or environments. This most-commonly results in a matrix red-shift, as the excited states of the molecule of interest interact more strongly with the matrix medium, however blue-shifts can also occur. A similar, but smaller, matrix shift is observed in the spectra of molecules in weakly-bonded van der Waals complexes, such as those observed by photodissociation spectroscopy in Chapters 6 and 7.

If laboratory spectra are to be directly compared to astronomical spectra, they must be recorded under simulated astronomical conditions. The density in the ISM varies from $\sim 10^{-4}$ atoms/cm^3 in the hot ionised medium to $\sim 10^{6}$ atoms/cm^3 in molecular clouds.[273] As a result, these molecules are effectively isolated.

While our achievable laboratory densities are somewhat higher than those found in diffuse clouds, on the order of $\sim 10^{6}$ atoms/cm^3, molecules at these densities are also effectively isolated on laboratory timescales. This is also the case for the molecules observed in the molecular beam experiments outlined in this chapter.

Astronomical molecules are also observed at low temperature, with the temperature of the cold neutral medium ranging from 50 K to 100 K.[273] Recording molecular spectra at low temperatures also has the advantage of drastically simplifying the observed spectra. By cooling molecules so that, prior to excitation, all molecules are in the vibrational and electronic ground state, the observed spectrum is free of vibronic hot bands, greatly simplifying assignment of the observed spectra. Indeed, with the exception of broadening due to methyl-rotor internal rotation and van der Waals modes, no vibrational hot band structure is observed in any of the spectra reported in this work.

One common method of isolating and cooling molecules under simulated astronomical conditions is through the production of a molecular beam through a supersonic free-jet expansion.

3.1.1 Supersonic Free-Jet Expansion

The concept of cooling and isolating molecules in a supersonic free-jet expansion dates back to Kantrowitz and Grey in 1951, who suggested the technique as means of improving the intensity of molecular beams by precollimating the molecules through a narrow slit as they enter the vacuum chamber from the high pressure source,[274] a technique which was soon

experimentally verified.[275] A free-jet expansion is created by separating a high-pressure gas sample from an evacuated low-pressure region with a small nozzle-orifice.[267] The expansion rapidly cools the translational degrees of freedom and the cold bath of translationally-cold gas initially acts to cool the other degrees of freedom.[276] As the expansion continues, the density of the jet reduces and the rate of collisions rapidly reduces to zero. In the absence of collisions, energy can no longer flow from the internal degrees of freedom and intermolecular reactions are quenched.[276] As such, the cooled isolated molecules are effectively "frozen" in the jet. For a more detailed description of the physical processes of the supersonic free-jet expansion and its application to modern gas-phase spectroscopy, the author recommends the review articles of Donald H. Levy[276,277] and Terry A. Miller[267] due to the accessibility of their language.

All experiments in this work create a supersonic free-jet expansion through the use of essentially the same experimental setup. The high-pressure gas region in these experiments had a pressure, known as the backing pressure, in a range varying from $2 - 8\,\text{bar}$ (optimised to enhance signal). The operating pressure of the evacuated low-pressure region (the source chambers of the spectrometers outlined later in this chapter) had a typical operating pressure on the order of $10^{-4}\,\text{Torr}$. The nozzle used in these experiments was a Parker Hannifin General Valve Series 9 pulsed solenoid nozzle controlled by a Parker Hannifin General Valve Iota One nozzle driver. The valve opening time was optimised to enhance signal while preserving the integrity of the vacuum.

All experiments in this work involved the use of argon as an inert buffer-gas to limit the potential for intermolecular reactions in the cooling phase of the free-jet expansion. The argon buffer gas was also used to form weakly-bound van der Waals complexes with the aromatic hydrocarbon cations analysed in the photodissociation experiments outlined later in this chapter.

While stable molecules in the initial supersonic free-jet expansion can be of spectroscopic interest, such as the 1H-phenalene molecule studied in Chapter 7, reactive intermediate species being studied must be created in the jet. Neutral radicals observed in the REMPI-TOF spectrometer were created using a pulsed discharge nozzle (PDN), whereas positively-charged weakly-bound van der Waals complexes observed in the photodissociation spectrometer were created *via* electron-bombardment.

3.1.2 Pulsed Discharge Nozzle (PDN)

It has already been outlined that one benefit of producing a molecular beam in a supersonic free-jet expansion is that the isolated cold molecules produced by this method, similar to molecules in an interstellar environment, allow laboratory spectra to be compared with astronomical spectra of molecules observed in the ISM. This low temperature, high vacuum environment is similarly ideal for the study of highly reactive species. The challenges involved with studying highly reactive species is a process that begins with their production. To overcome their transient nature, the reactive species studied must be isolated immediately following their creation.

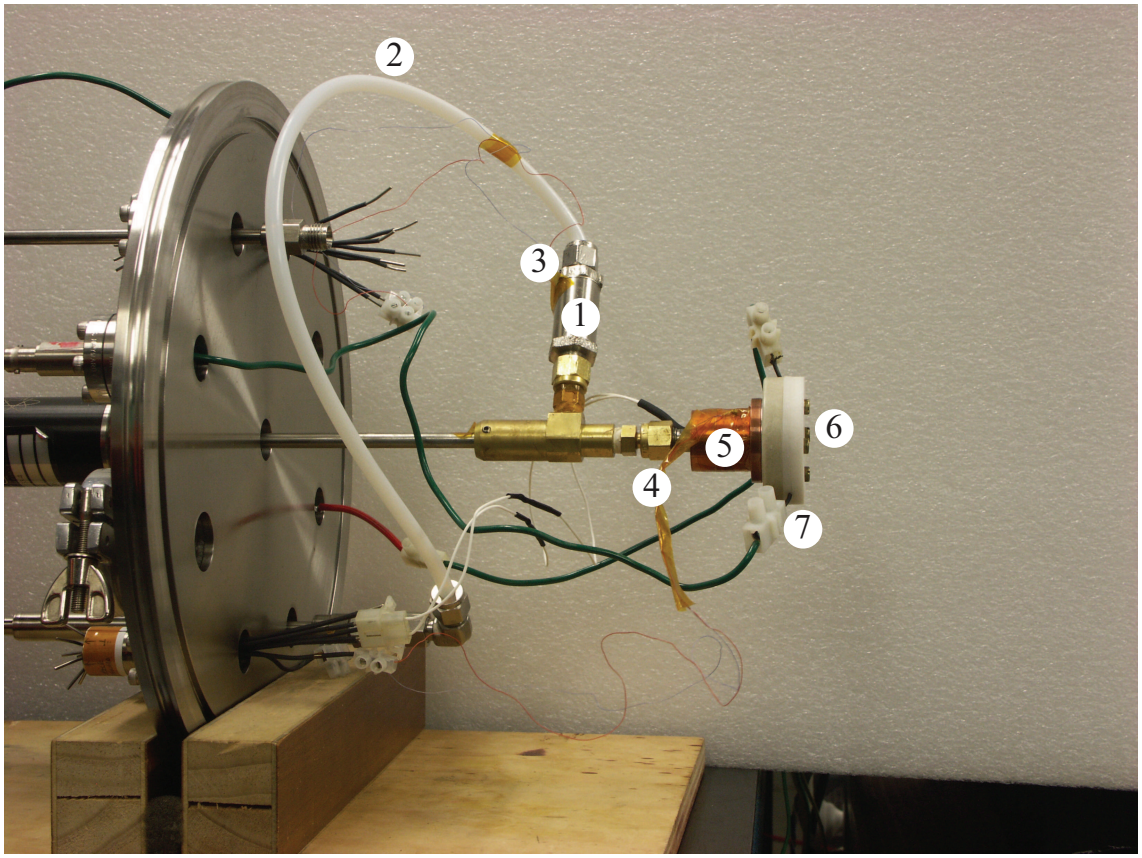

Figure 3.1: Picture of flange, sample holder and PDN assembly without heating wire. 1) Sample holder; 2) Backing gas connecting hose; 3) Sample chamber thermocouple wire; 4) PDN thermocouple wire; 5) General Valve series 9 pulsed solenoid valve; 6) Electrodes and Teflon® spacers; 7) High voltage connection to discharge electrodes. The assembly shown belongs to an LIF chamber. The REMPI-TOF assembly is largely identical, the primary difference is that the PDN is mounted to an adjustible translation stage, which is used to align the molecular beam with the skimmer.

One way to accomplish this is to use a pulsed high-voltage discharge to break molecular bonds during the initial, cooling phase of the free-jet expansion. The reaction-intermediates formed in the jet are subsequently cooled by supersonic expansion. Further reaction is

quenched as the species formed are isolated by the continued expansion of the molecular beam.[266,267,278]. This technique for creating highly reactive species by combining a pulsed supersonic free-jet expansion with a high voltage discharge was first developed by Schlachta *et al.*[279] and has since become an indispensable tool for the gas phase spectroscopy of highly reactive species.

PDNs have become one of the primary tools in the study of neutral radicals, such as those examined in Chapters 4 and 5. There are many different ways that an electric discharge may form a radical. Two possible methods are hydrogen abstraction or addition. In the case of hydrogen abstraction, highly reactive discharge products abstract peripheral hydrogens, producing PAH radicals. Hydrogen addition may also occur. In this process hydrogen atoms, cleaved from other molecules in the discharge, are added to an unsaturated precursor molecule. Both of these processes have been shown to be enhanced by trace amounts of H_2O.[280]

The importance of H_2O in catalysing these discharge reactions was demonstrated within our group in a paper by Krechkivska *et. al.*.[280] In this paper it was shown that a discharge of fully duterated benzene (C_6D_6), produced the radical C_6D_6H, with no trace of the C_6D_7 radical formed. Additionally, if benzene (C_6H_6) was discharged with trace amounts of D_2O the C_6H_6D radical was formed. This suggests that these reactions are, in fact, driven by fragmented water molecules. This occurs because water reacts with metastable argon (formed in the discharge) with a cross section exceeding 100 Å to yield H atoms and OH radicals.[281]

It is also worth noting that a high voltage discharge has sufficient energy to break several bonds in a molecule. As such, multiple radical products can be formed. For example, an electrical discharge containing 1-hexyne has been observed by Schmidt and co-workers to produce the C_2, C_3, 1-phenylpropargyl (1-PPr) radical as well as the *trans*- and *cis*-1-vinylpropargyl radicals.[193,266,282] It is also possible to produce the same species from different precursors. For example, 1-PPr has been observed in discharges of benzene, toluene, 1-phenylpropyne, 3-phenylpropyne and 1-hexyne.[282,283]

The PDN used in these experiments is similar to that used by Ohshima and Endo.[284] It combines the commercially available General Valve series 9, mentioned previously, with stainless steel electrodes separated from each other and from the valve body, with Teflon® insulating spacers. The current supplied to the electrodes is regulated by an adjustable high voltage source and a variable resistor, and is pulsed by a Behlke GHTS-30 high-voltage pulser. The parent molecules were seeded into the argon buffer-gas by suspending the sample in glass-wool in a chamber, behind the nozzle, in the high-pressure

gas lines. If vapour pressure was insufficient at room temperature, the sample chamber and PDN were heated. If heating was used, the PDN was maintained at a temperature higher than the sample chamber to prevent condensation in the nozzle, interfering with its operation and changing the molecular beam conditions. Temperature of the sample chamber and the PDN were monitored by T-type thermocouples.

Figure 3.1 shows the features of the sample chamber, heating, and pulsed discharge nozzle (PDN) assembly, with the heating wire removed. The photo comes from a laser induced fluorescence chamber. The REMPI-TOF assembly is effectively identical to that shown, with the addition of an adjustable translation stage on which the PDN is mounted, which is used to align the molecular beam with the skimmer. The assembly is mounted to a removable flange that makes up one wall of the vacuum chamber. It contains electrical feed-through connections (including high voltage connections for the discharge), and gas fittings with isolation taps. With this setup, systems inside the vacuum chamber can be controlled externally without venting the vacuum chamber. This configuration also allowed for these systems to be removed together, allowing easy maintenance and sample replacement, without having to dismantle systems inside the chamber. Similar setups were used for all experiments using the REMPI-TOF spectrometer.

3.1.3 Electron Bombardment/Electrospray

The photodissociation spectrometer outlined later in this chapter creates charged, weakly-bound, van der Waals complexes by bombarding the pulsed supersonic free-jet expansion with high energy electrons ($\sim 500\,\mathrm{eV}$), sourced from two hot-filaments. The electron beam ionizes molecules in the jet, creating a cool plasma which lends itself to the creation of charged clusters.[285] The cations observed in this work resulted from ionisation of a stable parent molecule. The radical-cations formed were then stabilised by forming a weakly-bound van der Waals complex with a neighbouring atom before being cooled and isolated by the supersonic free-jet expansion.

3.2 Jet-Cooled Action Spectroscopy Techniques

Once the molecules have been cooled and isolated in the supersonic free-jet expansion, they can be interrogated with photon sources. However, with the exception of traditional reflection/transmission measurements, the absorption of a photon is not directly observed

but rather inferred through the observation of a secondary event. Due to the low density of molecules in a free-jet, an insignificant amount of light is absorbed by molecules in the jet for a reduction in transmitted light to be measured. One means of directly observing photon absorption in a jet is through increasing the photon pathlength by using a high-finesse optical cavity. Resonant absorption is then observed by a decay in the ring-down time of the cavity (this technique is known as cavity ring down spectroscopy).[286] Otherwise, jet-cooled spectroscopy relies on the detection of a secondary event, or action, which occurs following excitation of the molecule.

One of the most common forms of action spectroscopy is laser-induced fluorescence (LIF), whereby photons emitted from excited molecules are detected after the excited molecule undergoes fluorescence. This is an extremely useful technique, as in addition to providing observable evidence of resonant photo-excitation, dispersing this fluorescence emission can be analysed to provide ground-state vibrational frequencies. As mentioned in Chapter 2, ground-state frequencies can be calculated more accurately and inexpensively than excited state frequencies. As such, ground-state frequencies are computationally cheaper to assign. The intensity pattern of a dispersed band can also give information about whether the excited mode is Herzberg-Teller active (as described in Chapter 2). Also, by recording the decay-rate of fluorescence over time, excited-state lifetimes can be measured. Unfortunately, LIF techniques are only viable when the excited-state being observed has a strong fluorescence yield. The excited-states observed in this work all have relativity weak fluorescent yields, due primarily to their short excited state lifetimes (the excited states decay *via* internal-conversion rather that fluorescing), making them unsuitable for study by LIF spectroscopy.

Three forms of action spectroscopy are used in this work, resonance-enhanced multi-photon ionisation (REMPI) spectroscopy, double-resonance spectroscopy and resonant photodissociation spectroscopy. Double-reasonance spectroscopy is outlined in Chapter 5. REMPI and resonant photodissociation techniques are outlined in the remainder of this chapter.

3.2.1 Resonance-Enhanced Multi-Photon Ionisation (REMPI) Spectroscopy

Two REMPI schemes are used in this work, resonant 2-photon ionisation (R2PI) and resonant 2-colour 2-photon ionisation (R2C2PI). Both involve photoionisation of a molecule following resonant excitation of that molecule to an excited state.

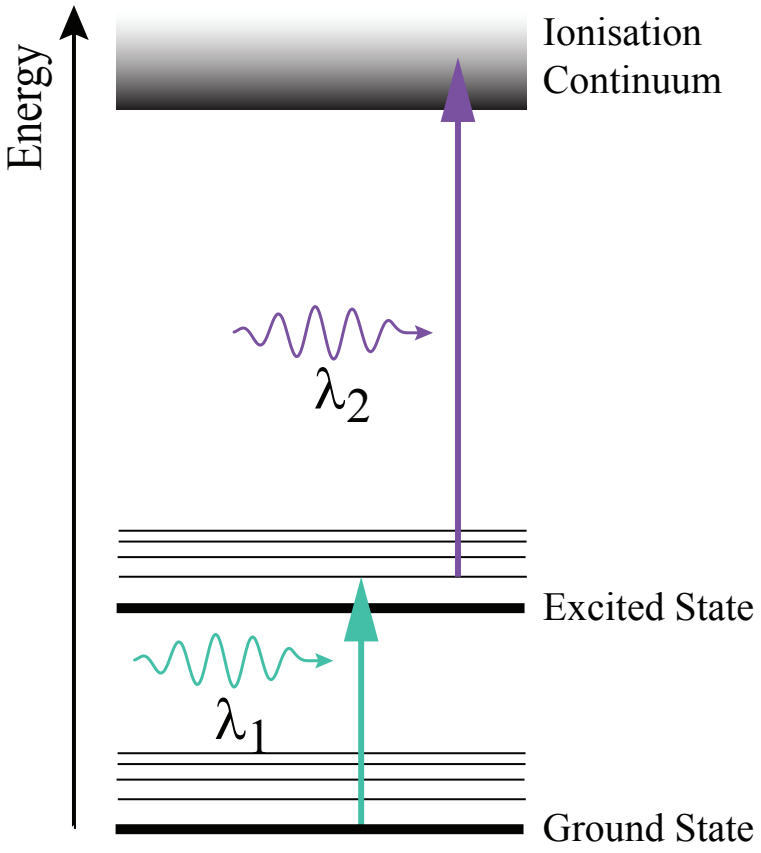

Figure 3.2: Schematic energy level diagram of R2C2PI. The excitation photon (λ_1) is absorbed by a molecule, which is resonantly excited from a ground state energy level to an excited state energy level. As less energy is now required to ionise the molecule, it is now possible for the molecule to be ionised by the ionisation photon (λ_2).

R2C2PI is a technique by which jet-cooled molecules are first excited by a tunable laser before subsequent ionisation by a second, typically UV, laser. The UV frequency is chosen such that a single photon does not have sufficient energy to ionise the molecule from the ground state. If the tunable excitation photon (λ_1) is not resonant with a transition, relatively few ions are created. Some ions may be formed by the non-resonant absorption of two or more UV photons and this is observed as relatively minor background signal. When photons from the tunable excitation laser resonantly excites the molecule, that molecule may then be ionised by subsequent absorption of an additional UV ionisation photon (λ_2). This increases the number of ions produced by orders of magnitude. The R2C2PI technique is depicted schematically in Figure 3.2 and is used in Chapters 4, 5 and 7. If the photon energy of the excitation laser is energetically sufficient to ionise the molecule from the excited state, then a second ionisation laser is not required. This one laser, two photon method is the R2PI that is also utilised in Chapter 7.

By combining these REMPI schemes with a time of flight mass-spectrometer, the mass

of the ions created can be determined. Ions created are accelerated by a fixed potential up a flight tube and are detected by a multi-channel plate ion detector. The mass of the ions created can be determined by the time delay between the ionisation laser pulse and detection of the ions. To obtain the excitation spectrum, the tunable laser is scanned while recording the ion flux of the relevant mass signal. Within the Laser Spectroscopy Group of The University of Sydney (now the Molecular Photonics Laboratories at UNSW), this combined REMPI/time-of-flight (REMPI-TOF) method has allowed the accurate identification of many previously unidentified discharge products and allowed for the observation of excitation spectra that would be difficult or impossible by other means.[176,183,185,193,199,201,202,280,287,288]

The time-of-flight mass spectrometer is similar to that described by Wiley and McLaren.[289] It features a linear flight tube mounted perpendicular to the molecular beam and the laser beam path. As such, the ions are formed with an initial momentum (in the direction of the flight tube) of approximately zero.[289] If all ions were formed at exactly the same time, in the same location and with zero momentum in the direction of the flight-tube, then ions with the same m/z would reach the detector at the same time. In reality some spread exists due to the initial spacial and kinetic energy distribution, with the greatest limitation in resolution due to the volume of the interaction area.

This is partially compensated for by the inherent spatial focusing of Wiley/McLaren time-of-flight mass spectrometers. On formation, the ions are guided towards the flight tube by an electric-field of $\sim 200\,\mathrm{V}$. This was provided by a repeller plate, with a static potential of $\sim 2200\,\mathrm{V}$, and an extractor grid with a static potential of $\sim 2000\,\mathrm{V}$. After passing through the extraction grid, the ions are then accelerated by an $\sim 2000\,\mathrm{V}$ electric field provided by the potential difference between the extractor grid and an earthed electric field grid at the entrance of the field free flight tube. The ions then drift until they enter the multi-channel plate (MCP) detector at the far end of the flight tube. Ions formed further from the detector spend more time in the accelerator. As they are accelerated to higher velocities, they have shorter drift times, ideally allowing them to arrive at the detector concurrently with ions formed closed to the detector.[289,290]

The time-of-flight of an ion with charge z and mass m in a Wiley/Mclaren time-of-flight spectrometer can be calculated as follows. If d is the length of the acceleration region (with field E_d) and D is the length of the field free region, an ion formed in the extraction region

(with field E_s) a distance s from the extractor plate will have a flight time

$$\tau = 1.02\left(\frac{m}{2zsE_s + 2zdE_d}\right)^{1/2}\left(2s\left(\frac{sE_s + dE_d}{sE_2}\right)^{1/2} + \frac{2d\left(\frac{sE_s+dE_d}{sE_2}\right)^{1/2}}{\left(\frac{sE_s+dE_d}{sE_2}\right)^{1/2}+1} + D\right).^{289} \quad (3.1)$$

The main advantage of the Wiley/Mclaren time-of-flight mass spectrometer over other methods of mass-spectrometry is that it allows the mass spectrum to be recorded rapidly (in a matter of microseconds, depending on the mass being monitored). It can therefore record the mass spectrum produced by every shot of the ionisation laser in a REMPI set-up, allowing changes in the mass-spectrum to be monitored as the wavelength of the tunable excitation laser is scanned. This is the basis of the REMPI-TOF technique.

The mass-resolution inherent in REMPI-TOF spectroscopy is especially powerful when combined with a PDN. An inherent difficulty in analysing the spectra obtained from discharge spectroscopy is that multiple species are often produced. While it is possible to maximise the production of a particular radical, it is impossible to guarantee the exclusive formation of the species of interest. Mass-resolution, in conjunction with theoretical analysis of the recorded spectrum, is one means by which the actual species responsible for observed transitions can be determined. Additionally, by increasing the flux of ionising photons, a mass-spectrum of the discharge may be observed due to non-resonant ionisation of the species present.

All R2C2PI and R2PI spectra reported in this work, in Chapters 4, 5 and 7, were recorded in the REMPI-TOF spectrometer, shown in Figure 3.3, which at the time of the experiments was located at the Laser Spectroscopy Laboratory of the School of Chemistry of the University of Sydney. The REMPI-TOF spectrometer was constructed in house[291] and consists of two differentially pumped chambers, connected by a 2 mm skimmer. The larger source chamber contains the sample chamber and PDN assembly, mounted to a removable flange. Vacuum for the source chamber was provided by a VARIAN VHS-250 oil vapour diffusion pump backed with an ALCATEL 2033 rotary vane pump. With the nozzle driver turned off, this provided a vacuum in the order of 10^{-7} Torr; operating pressures in the source chamber were generally below 10^{-4} Torr, depending on backing pressure and nozzle opening time. The source chamber is connected by the 2 mm skimmer to the extraction chamber. The extraction chamber has three fused-silica windows which allow entry of the probing laser beams. It also contains the electric field grids and is connected to the flight tube, the top of which contains a dual MCP.

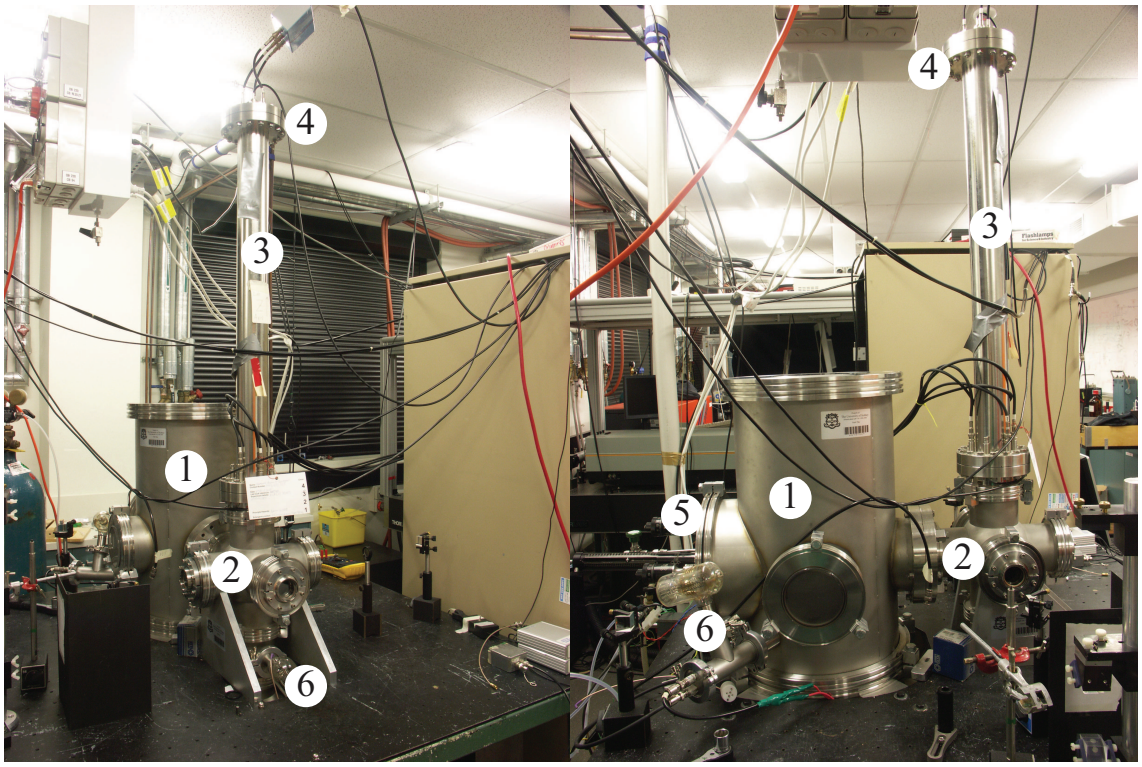

Figure 3.3: Front and side view of REMPI-TOF chamber. 1) Source chamber; 2) Extraction chamber 3) Flight tube; 4) Multichannel plate ion detector; 5) Removable flange holding sample chamber and PDN assembly; 6) Vacuum ion gauges.

Vacuum for the extraction chamber was provided by a Pfeiffer Balzers TPH330 turbomolecular pump backed by an Alcatel 2012A rotary vane pump. Operating vacuum for the extraction chamber was in the 10^{-7} Torr range during the experiments. The pressure of both the source and extraction chamber were monitored with Duniway T-KF40 ionisation gauge heads, monitored with Varian 843 ion gauge controllers.

The R2C2PI experiments carried out in Chapters 4, 5 and 7 proceeded as follows. A molecular beam was initially produced by a supersonic free-jet expansion from a PDN, the core of which is passed through the 2 mm diameter skimmer. This ensures only the coldest molecules at the core of the beam enter the extraction chamber.

After entering the electric field grids, the neutral molecules were excited by a Nd:YAG pumped tunable dye-laser, which was scanned when recording excitation spectra. Excited molecules were then ionised by a second source: either from the frequency doubled output of a Nd:YAG pumped dye-laser (tunable to a maximum energy of 206 nm), the fourth harmonic of a Nd:YAG laser (266 nm), a XeF excimer laser (248 nm) or an ArF excimer laser (193 nm). The Nd:YAG lasers had a fixed operating frequency of either 10 Hz or 20 Hz, whereas the ArF excimer laser could be fired at either of these frequencies. The

choice of ionisation source depended on the energy required, the timing accuracy needed (excimers often have a significant timing jitter than can cause noise in R2C2PI spectra of excited states with lifetimes less than $\sim 20\,\text{ns}$) and the availability of the sources at the time of the experiment.

Signal was collected on a LECROY 9354TM digital storage sampling oscilloscope. The oscilloscope was triggered by the same pulse that triggered the ionisation laser. Timing control during this experiment was provided by two HIGHLAND TECHNOLOGY T560 digital delay generators, controlled by in-house software written in LABVIEW by Dr Tyler Troy as part of his doctoral thesis.[184] The experiment was run at 10 Hz or 20 Hz, depending on the lasers used for the experiment.

The procedure for the R2PI spectrum recorded in Chapter 7 was identical to that for the R2C2PI experiments, except both excitation and ionisation photons were provided by the frequency doubled output of the same Nd:YAG pumped tunable dye-laser.

3.2.2 Resonant Photodissociation Spectroscopy and Argon-Tagging

Resonant photodissociation spectroscopy is a form of action spectroscopy that can be undertaken when a molecule or cluster of molecules dissociates after being resonantly excited. This can then be detected through mass spectroscopy by the appearance of lower m/z fragment molecules, the reduction in the ion flux of the initial ions/clusters or a change in ratio of the m/z flux between the parent and fragment molecules. The method used in this work observes resonant photodissociation of weakly bound van der Waals complexes by the appearance of fragment ions.

The resonant photodissociation spectra recorded in Chapters 6 and 7 were undertaken at The University of Melbourne with the assistance of the Bieske group of the School of Chemistry. The photodissociation spectrometer is depicted in Figure 3.4. It consists of a supersonic free-jet expansion source (similar to the REMPI-TOF apparatus previously discussed) and tandem quadrupole mass filters, separated by an octupole interaction region. Ion fragments generated are detected by an MCP.

The photodissociation spectrometer has been described previously in a review article by Wild and Bieske[285] and since then in several experimental papers.[207,292–318]

The photodissociation spectrometer used in these experiments has been successful in obtaining spectra of a large number of weakly bound van der Waals complexes, including several argon/nitrogen-tagged resonance-stabilised cationic species. These include a number of

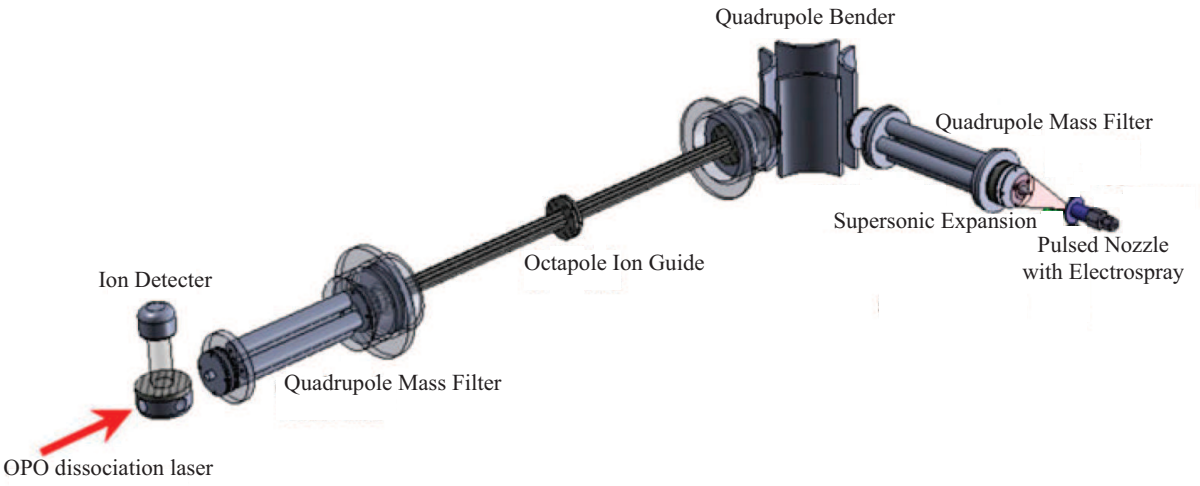

Figure 3.4: Digram of the photodissociation spectrometer located in The University of Melbourne. Image taken from Dryza and Bieske (2013),[292] image and labels of ion-source adjusted to reflect experimental setup used in this work.

resonance stabilised hydrocarbon cations such as benzylium$^+$,[207] 1,3-cyclopentadienium$^+$[316] and indeneium$^+$[315] as well as argon/nitrogen tagged cations containing nitrogen heterocycles such as quinolinium$^+$,[313] isoquinolinium$^+$,[313] N-pyridinium$^+$,[317] and indolium$^+$.[318]

The photodissociation experiments in Chapters 6 and 7 proceeded as follows. Argon containing trace amounts of the neutral parent molecule was introduced into the source chamber as a pulsed supersonic free-jet expansion. Vacuum for this chamber was provided by an oil-vapour diffusion pump.[319] The free-jet was bombarded by $\sim 500\,\text{eV}$ electrons, accelerated from two hot filaments, in the cooling region of the free-jet expansion. This created a cool plasma in which charged molecular complexes of the ionised parent molecules and argon were formed. The charged clusters then passed through a skimmer into a quadrupole mass filter,[320] where the complex of interest ($\text{PAH}^+ \cdots \text{Ar}$) was mass-selected, and clusters of other m/z ratios were ejected from the molecular beam. The quadrapole was differentially pumped by a turbomolecular pump[321] and a liquid nitrogen cold-trap.[322]

The mass-selected complexes then passed through a quadrupole bender, ejecting neutrals from the molecular beam. The bender was differentially pumped by a large turbomolecular pump.[321]

The mass selected $\text{PAH}^+ \cdots \text{Ar}$ clusters then entered an octupole ion guide,[323] collimating the beam of charged clusters. The octupole region was also differentially pumped by a turbomolecular pump[321] and a liquid-nitrogen cold trap.[322] Operating pressures in this region were generally on the order of $10^{-8}\,\text{Torr}$, which was necessary to minimise collisional

dissociation of the $PAH^+ \cdots Ar$ clusters, which is a source of unwanted background signal. In the octupole region, the $PAH^+ \cdots Ar$ clusters were interrogated by photons from an OPOTek Vibrant optical parametric oscillator. If the $PAH^+ \cdots Ar$ absorbed a photon, the weakly bound cluster dissociated producing the bare aromatic cation (PAH^+) and an argon atom. The PAH^+ were then selected by a second quadrupole mass filter,[320] before the cations were detected by a multichannel plate ion detector.

The $PAH^+ \cdots Ar$ cluster has similar spectroscopic properties to the bare PAH^+ cation. This 'argon-tagging' technique has been used in the past to record the spectra of PAH cations in near gas-phase conditions.[205,207,315,316,324] While these spectra cannot be directly compared to interstellar spectra due to a small solvent shift, spectra of this kind can be used to determine if the transition observed represents a feasible assignment for interstellar transitions. It is also possible to quantify the solvent shift by examining the shift of larger clusters (Ar_2,Ar_3,...) and extrapolating back to the bare molecule.[205,324]

3.3 Conclusions

The principle, on which all techniques outlined in this chapter are based, is that when the absorption of photons results in a detectable event, that event can be used as the basis of action spectroscopy. This chapter offers only a brief outline of the experimental techniques used in this paper and their potential. Specific adaptations of the methods used in this work will be outlined in Chapters 4, 5, 6 and 7 and additional action spectroscopy methods will be briefly outlined in Chapter 8.

Chapter 4

$D_1 \leftarrow D_0$ Transitions of Benzylic Resonance Stabilised Polycyclic Aromatic Hydrocarbon Radicals

4.1 Author's Note

The work published in this chapter has been, in part, published in *The Journal of Physical Chemistry A*.[185]

- G. D. O'Connor, G. B. Bacskay, G. V. G. Woodhouse, T. P. Troy, K. Nauta, and T. W. Schmidt: "Excitation Spectra of Large Jet-Cooled Polycyclic Aromatic Hydrocarbon Radicals: 9-Anthracenylmethyl ($C_{15}H_{11}$) and 1-Pyrenylmethyl ($C_{17}H_{11}$)". *J. Phys. Chem. A*, 117(50),13899–13907 (2013)[185]

Ab-initio calculations performed by Dr George B. Bacskay of the University of Sydney School of Chemistry as part of this paper have been included for completeness. These contributions are acknowledged within the chapter.

4.2 Introduction

As mentioned in chapter 1, the harsh radiation environment of the interstellar medium (ISM) could feasibly lead to the formation of benzylic type polycyclic aromatic hydrocarbons (PAHs) through the photodissociation of large amorphous hydrogenated carbon

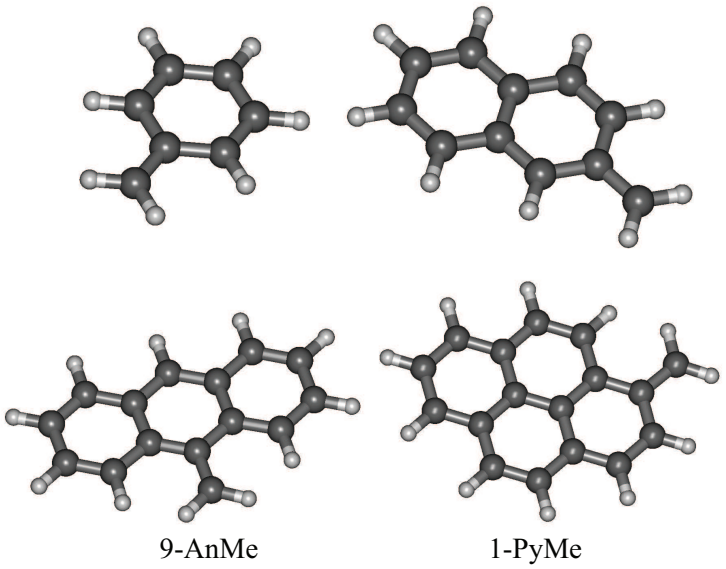

Figure 4.1: Structures of benzyl radical (top left), and benzannulated analogs: 2-naphthylmethyl (top right); 9-anthracenylmethyl (bottom left); and 1-pyrenylmethyl (bottom right).

networks, which are a postulated form of interstellar carbon.[5,168] Most spectroscopic studies on the band gaps and vibrational frequencies of PAHs have focussed on the neutral closed-shell species, which are often commercially available,[161,175] or readily synthesized.[176] There are fewer studies on PAHs with unpaired electrons.

Though not a PAH, the benzyl radical is the prototypical aromatic radical, where the unpaired electron is delocalized throughout the conjugated π-system. Radicals featuring this delocalization are known as resonance-stabilized radicals (RSRs). The benzyl radical has been the subject of extensive theoretical and experimental examination,[187–192,325–327] and is calculated to exhibit a radical stabilization energy (RSE) of 60 kJ/mol.[328] That is to say, breaking a C–H bond in the methyl group of toluene requires 60 kJ/mol less energy than in methane (the methyl radical is defined as having a RSE of 0). From this, one can predict that the C–C bond of 1,2-diphenylethane would be weakened by 2×60 kJ/mol. As such, benzyl-type radicals may be preferentially formed through the break-up of large amorphous hydrogenated carbon networks.

Of the larger benzylic radicals, only the naphthylmethyl radicals have been studied in the gas phase by laser spectroscopy prior to this work.[183] The larger radicals, based on the anthracene and pyrene frameworks, are the subjects of the present study. The structures of these radicals are shown in Figure 4.1.

In this chapter, a combination of experiment and theory are used to obtain the excitation wavelengths of the $D_1 \leftarrow D_0$ transitions of the 9-anthracenylmethyl (9-AnMe) and

1-pyrenylmethyl (1-PyMe) radicals, pictured in Figure 4.1, and then identify them using the mass-resolved R2C2PI technique, coupled to a PDN supersonic expansion source, as described in Chapter 3. The spectra are discussed in the context of unidentified astronomical spectral features, and predictions are made for the absorption positions of still larger benzannulated benzyl radicals (BBRs).

4.3 Theoretical Methods

The quantum chemical calculations of ground-state and excited-state geometries and frequencies of 9-AnMe and 1-PyMe were carried out using DFT and TD-DFT, utilizing the B3LYP functional[231,232] and the 6-311++G(d,p) basis set.

This data is supplemented by complete active space self-consistent field (CASSCF) theory calculations,[329] performed by Dr George B. Bacskay of the School of Chemistry at The University of Sydney. The CASSCF calculations were performed using an active space of 7 active electrons in 7 active orbitals. The 6-31G(d) basis[330] was used in the CASSCF calculations for 9-AnMe, but for technical reasons the H basis in the 1-PyMe was reduced to the minimal STO-3G set.[331] (Analogous calculations on 9-AnMe have demonstrated that the effect of such simplification in the basis results in negligibly small changes in the geometries, frequencies and relative energies.)

The excitation energies were obtained both at the TD-B3LYP/6-311++G(d,p) and complete active space second order perturbation (CASPT2) level of theory,[332–334] with an active space of 11 electrons in 11 orbitals, in conjunction with the 6-311G(d) and 6-31G bases on the C and H atoms respectively. The CASPT2 values were again provided by Dr George B. Bacskay of the School of Chemistry at the University of Sydney.

Excited-state potential energy surfaces of 9-AnMe were constructed by computing single point TD-B3LYP excited-state energies at geometries distorted by application of the appropriate excited-state vibrational coordinates. The calculated points were then fit with a cubic spline, allowing the variational calculation of (anharmonic) vibrational states.

The B3LYP and TD-B3LYP calculations were carried out using the Gaussian09[221] suite of software. The Dalton program[335] was used to obtain CASSCF geometries and frequencies, while the CASPT2 calculations were carried out using MOLPRO.[336]

4.4 Experimental Methods

4.4.1 Excitation Spectra

Mass-resolved R2C2PI was used to record the $D_1 \leftarrow D_0$ excitation spectra reported in this chapter. The apparatus used is described in detail in Chapter 3 and has been described previously.[183,200,201,282,287,337] It combines the REMPI-TOF apparatus and the PDN described in detail in Chapter 3. The specific setup used for the experiments reported in this chapter are summarised here.

Argon, seeded with traces of commercially available 9-methylanthracene or 1-methylpyrene, was expanded into a vacuum chamber through a PDN.[284] Discharge conditions were optimized separately for 9-AnMe and 1-PyMe radical production. For 9-AnMe radicals, 9-methylanthracene was seeded into 4 bar of argon at 368 K before being supersonically expanded into a vacuum and passed through the two electrodes of the PDN. A potential of -800 V, in series with an 18 kΩ resistor and pulsed for a duration of 80 μs, was applied to the inner electrode at a time coincident with the 230 μs gas pulse. For 1-PyMe radical production, 1-methylpyrene was seeded into 9 bar of argon at 343 K before being supersonically expanded into a vacuum and passed through the two electrodes of the PDN. A potential of -1100 V, in series with an 18 kΩ resistor, pulsed for a duration of 70 μs, was applied to the inner electrode at a time coincident with the 170 μs gas pulse. The radical-containing plasma was then cooled by supersonic expansion. The coolest part of the jet passed through a 2 mm skimmer into the differentially-pumped interrogation region, between the electrostatic grids of a time-of-flight mass-spectrometer.

In the interrogation region, the radicals were first excited by a Nd:YAG-pumped dye laser and then subsequently ionized. For 9-AnMe, ionization photons were produced by the 193 nm (6.4 eV) output of a small ArF excimer laser, whereas 1-PyMe ionization photons were produced by a frequency doubled Nd:YAG-pumped dye laser containing Exalite 417, producing 206 nm (6.0 eV) photons. Resulting cations were accelerated by a +2.4 kV potential along a time-of-flight tube before being detected by a tandem multi-channel plate. Ion signal, corresponding to the appropriate mass/charge ratio (m/z 191 for 9-AnMe, m/z 215 for 1-PyMe), was plotted against excitation wavelength to obtain the final spectrum.

Table 4.1: $D_n \leftarrow D_0$ vertical electronic transition energies, T_n, and oscillator strengths, f, of 9-AnMe and 1-PyMe radical, calculated at the TD-B3LYP/6-311++G(d,p) level of theory. The symmetry of the transition moment is given as $\Gamma_{\mu_{n0}}$.

	9-AnMe			1-PyMe		
n	$\Gamma_{\mu_{n0}}$	T_n (eV)	f	$\Gamma_{\mu_{n0}}$	T_n (eV)	f
1	A_1	1.95	0.0003	A'	1.96	0.0011
2	A_1	2.76	0.0889	A'	2.61	0.0015
3	B_2	2.8	0.0006	A'	2.86	0.2499
4	A_1	3.13	0.0032	A'	3.06	0.0164
5	B_2	3.2	0.0013	A'	3.15	0.0499
6	B_2	3.39	0.1319	A'	3.2	0.0174
7	B_2	3.63	0.0696	A'	3.5	0.0982
8	B_2	3.87	0.0009	A'	3.7	0.0022

4.4.1.1 Hole-Burning

Hole-burning depletion, an application of double-resonance depletion, can be used to determine if bands belong to the same species and share a common state. Double-resonance depletion will be discussed in greater detail in Chapter 5.

Hole-burning depletion was undertaken through the addition of a Nd:YAG-pumped dye laser pulse, 100 ns prior to the excitation and ionization laser pulses. Due to low signal-to-noise, hole-burning depletions were obtained by subsequent one minute acquisitions at fixed frequencies, alternating between activation and deactivation of the depletion laser.

4.5 Excitation Energies (TD-DFT and CASPT2)

The TD-B3LYP/6-311++G(d,p) excitation energies for 9-AnMe and 1-PyMe are reported in Table 4.1. These species are odd-alternant RSRs, where the carbons can be labelled alternatively α or β in such a way that no neighbouring carbon has the same label. As odd-alternant RSRs, the $D_1 \leftarrow D_0$ transitions of BBRs are expected to be dominated by the combination of two single-electron transitions: from the highest-occupied molecular orbital (HOMO) to the singly-occupied molecular orbital (SOMO); and from the SOMO to the lowest-unoccupied molecular orbital (LUMO)[338]. In the $D_1 \leftarrow D_0$ transition, the transition moments of these single-electron transitions interfere destructively, resulting in a relatively weak transition. A stronger, higher-energy, transition occurs when the transition moments of the same two single-electron transitions interfere constructively. This stronger transition occurs at a higher energy (Table 4.1).

Table 4.2: TD-B3LYP $D_1 \leftarrow D_0$ transition energies of BBRs, calculated with a 6-311++G(d,p) basis, compared to experimental values. Corrected TD-B3LYP values obtained by linear fit of benzyl, 1-PPr, 1-NpMe and 2-NpMe radicals calculated and experimental values (See Table 4.2). 9-AnMe and 1-PyMe not included in this fit.

TD-B3LYP/6-311++G(d,p)					
Mode	Formula	$E\,(eV)$	$E^{corrected}\,(eV)$	Experimental (eV)	Δ_E (eV)
benzyl	C_7H_7	3.17	2.74	2.74[189]	0.00
1-PPr	C_9H_7	3.01	2.60	2.60[193]	0.00
1-NpMe	$C_{11}H_9$	2.50	2.16	2.14[183]	-0.02
2-NpMe	$C_{11}H_9$	2.43	2.10	2.12[183]	0.02
9-AnMe	$C_{17}H_{11}$	1.95	1.69	1.71	0.02
1-PyMe	$C_{15}H_{11}$	1.96	1.70	1.66	-0.04

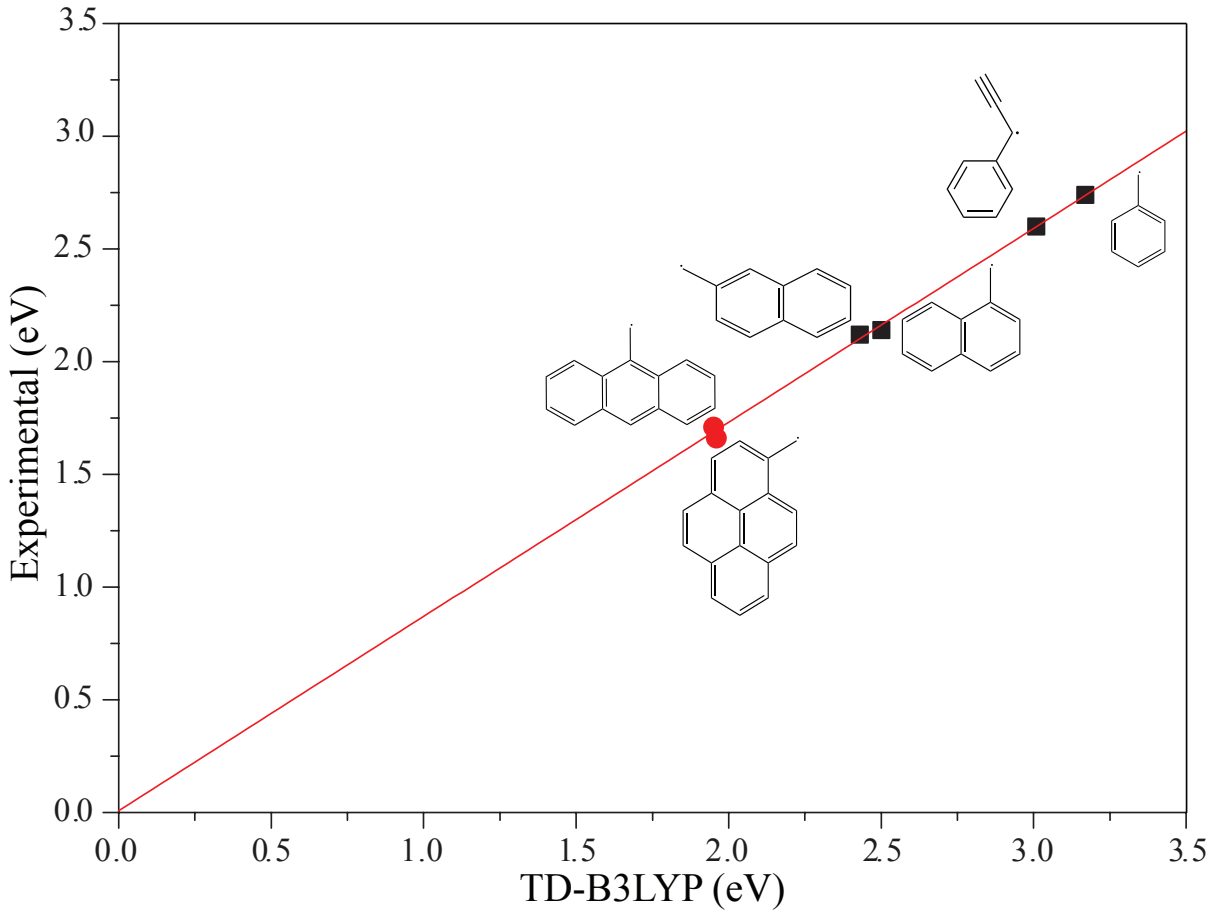

Figure 4.2: Correlation of experimental and vertical TD-B3LYP/6-311++G(d,p) $D_1 \leftarrow D_0$ electronic excitation energies. Experimental values for benzyl[189], 1-NpMe and 2-NpMe radicals[183] are from literature. The experimental excitation energy for the 9-AnMe and 1-PyMe radicals are from data reported in this chapter. The line, $0.861T_{TD-B3LYP} + 0.008$, is a fit through the square black data points

Table 4.3: TD-B3LYP $D_1 \leftarrow D_0$ transition energies of BBRs, calculated with a 6-311++G(d,p) basis, compared to experimental values. Corrected TD-B3LYP values obtained by linear fit of benzyl, 1-PPr, 1-NpMe, 2-NpMe, 9-AnMe and 1-PyMe calculated and experimental values (See Table 4.2).

TD-B3LYP/6-311++G(d,p)					
Mode	Formula	$E\,(eV)$	$E^{corrected}\,(eV)$	Experimental (eV)	Δ_E (eV)
benzyl	C_7H_7	3.17	2.76	2.74[189]	-0.02
1-PPr	C_9H_7	3.01	2.62	2.6[193]	-0.02
1-NpMe	$C_{11}H_9$	2.50	2.18	2.14[183]	-0.04
2-NpMe	$C_{11}H_9$	2.43	2.11	2.12[183]	0.01
9-AnMe	$C_{17}H_{11}$	1.95	1.70	1.71	0.01
1-PyMe	$C_{15}H_{11}$	1.96	1.71	1.66	-0.05
2-PerMe	$C_{21}H_{13}$	1.67	1.46		
6-AnanMe	$C_{23}H_{13}$	1.63	1.42		

Table 4.4: TD-CAM-B3LYP $D_1 \leftarrow D_0$ transition energies of BBRs, calculated with a 6-311++G(d,p) basis, compared to experimental values. Corrected TD-CAM-B3LYP values obtained by linear fit of benzyl, 1-PPr, 1-NpMe, 2-NpMe, 9-AnMe and 1-PyMe calculated and experimental values (See Table 4.2).

TD-CAM-B3LYP/6-311++G(d,p)					
Mode	Formula	$E\,(eV)$	$E^{corrected}\,(eV)$	Experimental (eV)	Δ_E (eV)
benzyl	C_7H_7	3.52	2.81	2.74[189]	-0.07
1-PPr	C_9H_7	3.19	2.51	2.60[193]	0.09
1-NpMe	$C_{11}H_9$	2.77	2.14	2.14[183]	0.00
2-NpMe	$C_{11}H_9$	2.80	2.16	2.12[183]	-0.04
9-AnMe	$C_{17}H_{11}$	2.33	1.74	1.71	-0.03
1-PyMe	$C_{15}H_{11}$	2.24	1.66	1.66	0.00
2-PerMe	$C_{21}H_{13}$	1.78	1.25		
6-AnanMe	$C_{23}H_{13}$	2.05	1.49		

4.6 Results and Discussion

As demonstrated in Chapter 2, the TD-B3LYP/6-311++G(d,p) method has been shown to overestimate $D_1 \leftarrow D_0$ transition energies of RSRs. A comparison between calculated and experimental values for benzylic PAH radicals suggests that this error may occur in a systematic way.

In Figure 4.2, experimental $D_1 \leftarrow D_0$ excitation energies of RSRs previously analysed under jet-cooled conditions, benzyl,[189] 1-phenylpropargyl (1-PPr),[193] 1-naphthylmethyl (1-NpMe) and 2-naphthylmethyl (2-NpMe) radicals,[183] were plotted against the presently calculated TD-B3LYP values. A linear fit of these data results in an empirical correction to the calculated excitation energies. 1-PPr is not strictly a BBR, however this combined aromatic/olefinic RSR appears to fall follow the same trend as the observed small benzylic RSRs.

Table 4.5: TD-M06 $D_1 \leftarrow D_0$ transition energies of BBRs, calculated with a 6-311++G(d,p) basis, compared to experimental values. Corrected TD-M06 values obtained by linear fit of benzyl, 1-PPr, 1-NpMe, 2-NpMe, 9-AnMe and 1-PyMe calculated and experimental values (See Table 4.2).

TD-M06/6-311++G(d,p)					
Mode	Formula	$E\,(eV)$	$E^{corrected}\,(eV)$	Experimental (eV)	Δ_E (eV)
benzyl	C_7H_7	3.17	2.74	2.74[189]	0.00
1-PPr	C_9H_7	3.02	2.60	2.60[193]	0.00
1-NpMe	$C_{11}H_9$	2.53	2.15	2.14[183]	-0.01
2-NpMe	$C_{11}H_9$	2.48	2.10	2.12[183]	0.02
9-AnMe	$C_{17}H_{11}$	2.05	1.7	1.71	0.01
1-PyMe	$C_{15}H_{11}$	2.01	1.67	1.66	-0.01
2-PerMe	$C_{21}H_{13}$	1.69	1.37		
6-AnanMe	$C_{23}H_{13}$	1.73	1.41		

Table 4.6: Adiabatic ($T_e^{TD-B3LPY}$) and zero-point energy corrected ($T_0^{TD-B3LYP}$) TD-B3LYP $D_1 \leftarrow D_0$ transition energies of BBRs, calculated with a 6-311++G(d,p) basis, compared to experimental values. Corrected $T_0^{TD-B3LYP}$ values obtained by linear fit of benzyl, 1-PPr, 1-NpMe and 2-NpMe calculated and experimental values (See Table 4.2). 9-AnMe and 1-PyMe not included in this fit.

TD-B3LYP/6-311++G(d,p)						
Mode	Formula	$T_e\,(eV)$	$T_0\,(eV)$	$T_0^{corrected}\,(eV)$	Experimental (eV)	Δ_E (eV)
benzyl	C_7H_7	3.00	2.91	2.69	2.74[189]	0.05
1-PPr	C_9H_7	2.86	2.31	2.24	2.60[193]	0.36
1-NpMe	$C_{11}H_9$	2.38	2.26	2.21	2.14[183]	-0.07
2-NpMe	$C_{11}H_9$	2.31	2.75	2.57	2.12[183]	-0.45
9-AnMe	$C_{17}H_{11}$	1.90	1.85	1.91	1.71	-0.20
1-PyMe	$C_{15}H_{11}$	1.89	1.84	1.90	1.66	-0.24

This line, with formula $T_{exp} = 0.861 T_{TD-B3LYP} + 0.008$ and an R^2 value of 0.997, was used to estimate the $D_1 \leftarrow D_0$ transition energies of 9-AnMe and 1-PyMe. From the respective $T_{TD-B3LYP}$ energies of 1.95 eV and 1.96 eV, the expected origin band positions for these radicals are calculated to lie near 1.69 eV, or 730 nm. This formula makes predictions for the known radical excitation energies with errors of 0.02 eV, and so we could not necessarily expect the predictions for 9-AnMe and 1-PyMe to be better than this. The corrected TD-B3LYP values are tabulated in Table 4.2.

Inclusion of 9-AnMe and 1-PyMe in the fit (from the data reported in this chapter) has little effect on the linear fit, giving a line of $T_{exp} = 0.867 T_{TD-B3LYP} + 0.008$ with the same 0.997 R^2 value. Using this fit, the $D_1 \leftarrow D_0$ transition energy for each molecule in this study was calculated. The results for this improved fit are tabulated in Table 4.3.

Similar experimental-theoretical correlation was observed when comparing experimental

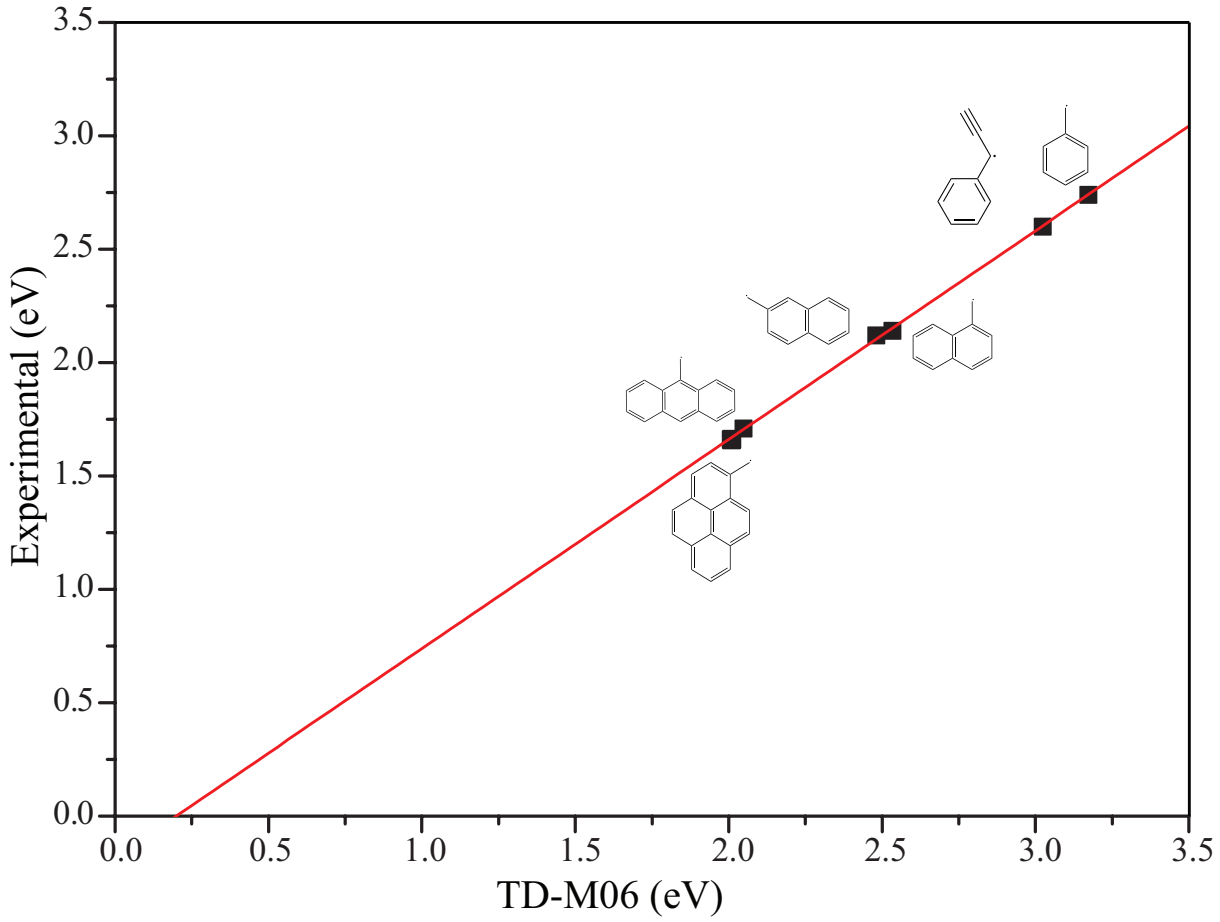

Figure 4.3: Correlation of experimental and TD-M06/6-311++G(d,p) $D_1 \leftarrow D_0$ vertical electronic excitation energies. Experimental values for benzyl,[189] 1-PPr,[193] 1-NpMe and 2-NpMe radicals[183] are from literature. The experimental excitation energy for the 9-AnMe and 1-PyMe radicals are from data reported in this chapter. The red line, $0.92T_{TD-M06} - 0.180$ is fit through the data points

energies with vertical excitation energies calculated by TD-M06 (Figure 4.3) and TD-CAM-B3LYP (Figure 4.4). The CAM-TD-B3LYP calculated and corrected values are tabulated in Table 4.4, and the TD-M06 data is tabulated in Table 4.5. TD-M06 gave the best correlation, with $R^2 = 0.999$, at slightly increased cost. TD-CAM-B3LYP also performed well, with $R^2 = 0.985$.

In an attempt to further refine this technique, TD-B3LYP zero-point corrected adiabatic excitation energies (T_0) were calculated for all molecules used in the previous fit. The comparison between T_0 and experiment, shown in Figure 4.5, and tabulated in Table 4.6 gives a fit line of $T_{exp} = 0.739T_0^{TD-B3LYP} - 0.537$. This gives no significant improvement over the empirically corrected vertical TD-B3LYP values. Indeed this results in a lower correlation between calculated and observed results, with an R^2 value of 0.951 and a maximum ΔE of 0.45 eV as seen in Table 4.6. Additionally, these calculations involve a significantly increased cost. As such, further predictions of the electronic excitation energies of RSRs were instead based on the calculated vertical excitation energies.

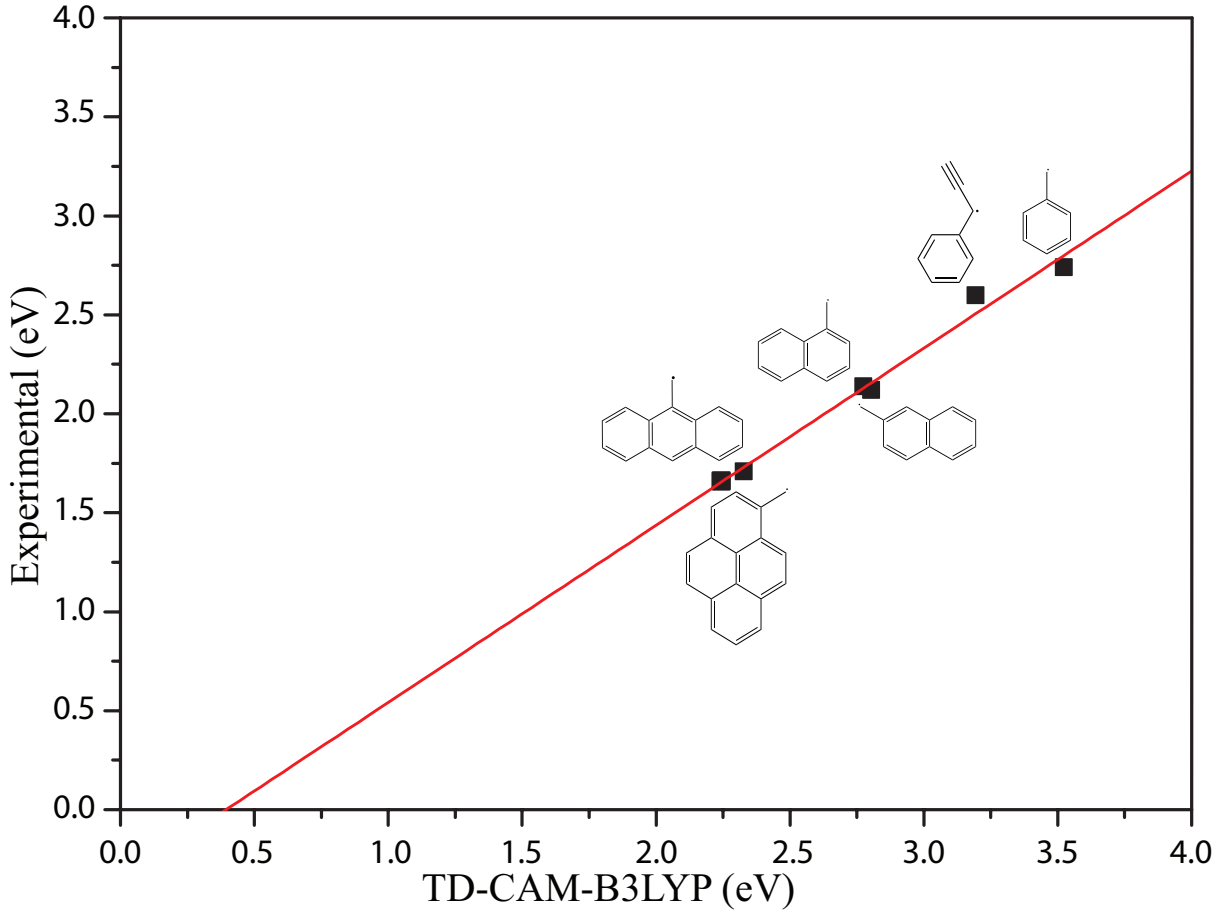

Figure 4.4: Correlation of experimental and TD-CAM-B3LYP/6-311++G(d,p) $D_1 \leftarrow D_0$ vertical electronic excitation energies. Experimental values for benzyl,[189] 1-PPr,[193] 1-NpMe and 2-NpMe radicals[183] are from literature. The experimental excitation energy for the 9-AnMe and 1-PyMe radicals are from data reported in this chapter. The red line, $0.895T_{TD-CAM-B3LYP} - 0.353$ is fit through the data points

The computed $D_1 \leftarrow D_0$ excitation energies (adiabatic and zero-point corrected) are listed in Table 4.7 along with the experimental values. While TD-B3LYP overestimates the excitation energies of 9-AnMe and 1-PyMe respectively by $\sim 1200\,\mathrm{cm}^{-1}$, the scaled TD-DFT values are within $\sim 250\,\mathrm{cm}^{-1}$ of experiment. By contrast, the *ab initio* CASPT2 method under- and overestimates these energies by $\sim 1000\,\mathrm{cm}^{-1}$. As found in previous work on related smaller molecule, both theoretical approaches provide acceptable estimates of the excitation energies, especially when empirical scaling and offset is applied.[183,200]

This work suggests the best value method for predicting the $D_1 \leftarrow D_0$ transition energy of RSRs is through empirical correction to TD-DFT vertical excitation energy. This proved effective for the three functionals tested, TD-B3LYP, TD-CAM-B3LYP and TD-M06, with TD-M06 giving slightly higher accuracy and TD-B3LYP the slightly cheaper option.

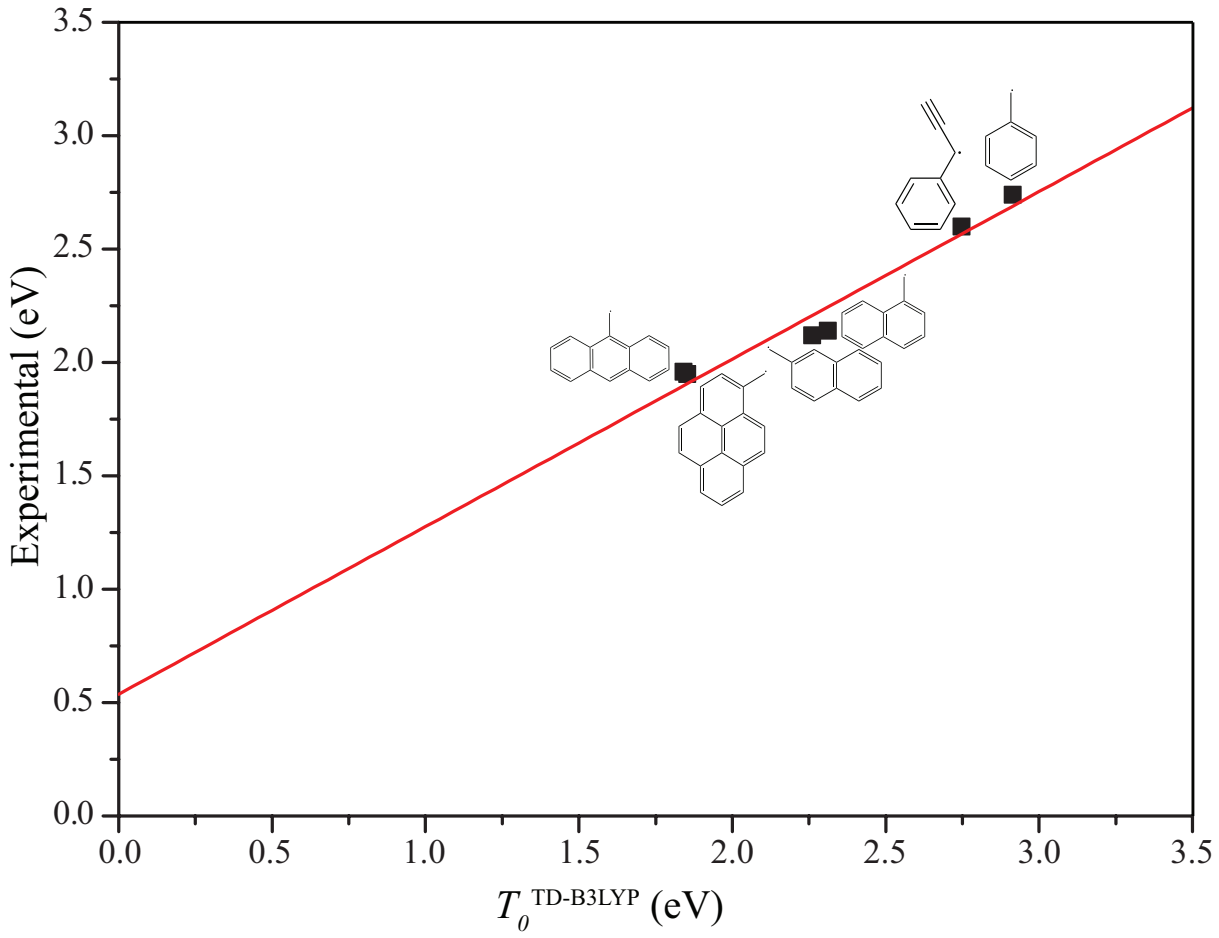

Figure 4.5: Correlation of experimental and TD-B3LYP/6-311++G(d,p) $D_1 \leftarrow D_0$ zero-point corrected adiabatic electronic excitation energies. Experimental values for benzyl,[189] 1-PPr,[193] 1-NpMe and 2-NpMe radicals[183] are from literature. The experimental excitation energy for the 9-AnMe and 1-PyMe radicals are from data reported in this chapter. The red line, $T_{exp} = 0.73T_0^{TD-B3LYP} - 0.537$ is fit through the data points

Table 4.7: 9-AnMe and 1-PyMe $D_1 \leftarrow D_0$ excitation energies (cm^{-1}).

	9-AnMe		1-PyMe	
Method	T_e	T_0	T_e	T_0
CASPT2	13375	12698	14638	14227
TD-B3LYP	15232	14945	15204	14854
Scaled DFT[a]	-	13611	-	13681
Experiment	-	13757	-	13417

a See Figure 4.2

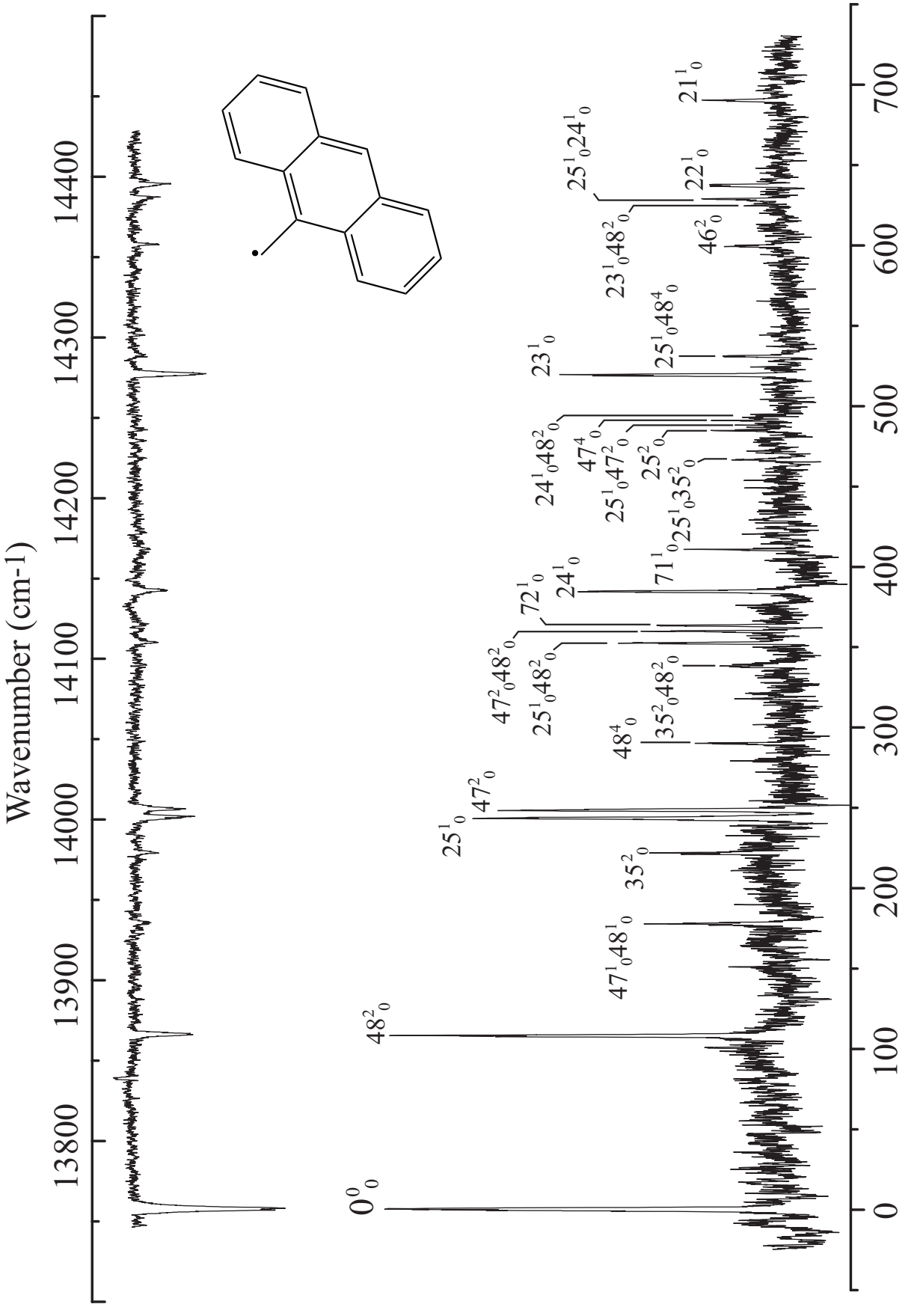

Figure 4.6: R2C2PI spectrum of a m/z 191 product of an electrical discharge containing 9-methylanthracene, assigned to 9-anthracenylmethyl radical (structure shown). Top: Lower power spectrum, revealing more accurate relative intensities but less defined peak positions due to a higher averaging level.

4.6.1 9-Anthracenylmethyl (9-AnMe) Radical Spectrum

Figure 4.6 shows the R2C2PI spectrum obtained in the region $12850 - 14500\,\mathrm{cm}^{-1}$ by monitoring the m/z 191 mass channel, using 9-methylanthracene as a precursor. Hydrogen abstraction in a discharge has been observed previously to generate many RSRs,[183,201] and thus it is here proposed that the spectrum obtained is due to 9-AnMe.

As shown in Table 4.7, the CASPT2 calculated value for T_0 is $1059\,\mathrm{cm}^{-1}$ smaller than the observed origin transition, while the empirically scaled TD-B3LYP value is just $167\,\mathrm{cm}^{-1}$ less than the observed transition. The agreement between the calculated excitation energies, the structure of the precursor, and the observed m/z of the spectral carrier all support an assignment of the observed spectrum to the 9-AnMe radical.

4.6.1.1 9-AnMe Spectral Assignments

The 9-AnMe radical is of C_{2v} symmetry, and assignments of vibrational modes have been made using the labelling conventions commonly used for this point group. The $D_1 \leftarrow D_0$ transition of 9-AnMe is calculated to be of A_1 symmetry ($B_1 \leftarrow B_1$), and thus vibrational levels with total a_1 symmetry are Franck-Condon allowed, whereas transitions to vibrational states of b_2 and b_1 symmetry are only allowed through vibronic coupling. The electronic origin band is therefore Franck-Condon allowed and the strong band observed at $13757\,\mathrm{cm}^{-1}$ is assigned thus ($0^0{}_0$). The energies of the additional vibronic bands are reported relative to this band.

The TD-B3LYP D_1 excited-state frequencies for 9-AnMe are tabulated in Table 4.8. The 72 vibrational modes are labelled in the Mulliken convention in the C_{2v} point group, showing 25 a_1, 10 a_2, 13 b_1 and 24 b_2 vibrational modes. It is expected that several modes, especially out-of-plane bending, may exhibit anharmonicity, and thus 1-dimensional scans of these coordinates were performed. Calculated anharmonic frequencies for several modes are listed in Table 4.9.

The TD-B3LYP/6-311++G(d,p) excited-state harmonic frequencies of a_1 symmetry, ν_{21-25}, correspond well to the observed relative frequencies of strong absorption features, with a maximum disagreement of just $12\,\mathrm{cm}^{-1}$ (Table 4.10). However, the large band, observed at $+108\,\mathrm{cm}^{-1}$, is significantly lower than the lowest frequency a_1 mode (ν_{25}). It is possible that multiple isomers could be generated by a discharge, as seen previously.[183] To explore this possibility, spectral hole-burning was used to confirm that the $+108\,\mathrm{cm}^{-1}$ band is due to the same molecule as the putative origin and the strongest low-frequency bands. Indeed,

Table 4.8: TD-B3LYP/6-311++G(d,p) D_1 harmonic excited-state frequencies (cm^{-1}) of 9-AnMe and 1-PyMe radicals.

9-AnMe						1-PyMe					
Mode	Γ	Freq.	Mode	Γ	Freq.	Mode	Γ	Freq.	Mode	Γ	Freq.
1	a_1	3217	36	b_1	965	1	a'	3258	40	a'	971
2	a_1	3194	37	b_1	925	2	a'	3203	41	a'	899
3	a_1	3190	38	b_1	874	3	a'	3187	42	a'	821
4	a_1	3173	39	b_1	829	4	a'	3180	43	a'	779
5	a_1	3166	40	b_1	770	5	a'	3178	44	a'	715
6	a_1	3160	41	b_1	733	6	a'	3176	45	a'	684
7	a_1	1610	42	b_1	710	7	a'	3168	46	a'	595
8	a_1	1608	43	b_1	593	8	a'	3164	47	a'	537
9	a_1	1566	44	b_1	511	9	a'	3163	48	a'	520
10	a_1	1514	45	b_1	380	10	a'	3162	49	a'	490
11	a_1	1470	46	b_1	295	11	a'	3160	50	a'	447
12	a_1	1435	47	b_1	123	12	a'	1692	51	a'	414
13	a_1	1371	48	b_1	44	13	a'	1606	52	a'	391
14	a_1	1301	49	b_2	3281	14	a'	1563	53	a'	285
15	a_1	1285	50	b_2	3210	15	a'	1563	54	a''	966
16	a_1	1195	51	b_2	3190	16	a'	1534	55	a''	956
17	a_1	1171	52	b_2	3173	17	a'	1522	56	a''	944
18	a_1	1113	53	b_2	3164	18	a'	1503	57	a''	931
19	a_1	1062	54	b_2	1556	19	a'	1497	58	a''	852
20	a_1	877	55	b_2	1548	20	a'	1470	59	a''	834
21	a_1	702	56	b_2	1506	21	a'	1444	60	a''	816
22	a_1	641	57	b_2	1462	22	a'	1439	61	a''	788
23	a_1	527	58	b_2	1424	23	a'	1411	62	a''	775
24	a_1	387	59	b_2	1365	24	a'	1397	63	a''	748
25	a_1	246	60	b_2	1323	25	a'	1369	64	a''	724
26	a_2	966	61	b_2	1267	26	a'	1333	65	a''	697
27	a_2	920	62	b_2	1196	27	a'	1325	66	a''	666
28	a_2	843	63	b_2	1178	28	a'	1286	67	a''	592
29	a_2	739	64	b_2	1114	29	a'	1264	68	a''	550
30	a_2	730	65	b_2	1093	30	a'	1236	69	a''	500
31	a_2	517	66	b_2	1036	31	a'	1229	70	a''	482
32	a_2	479	67	b_2	907	32	a'	1209	71	a''	450
33	a_2	326	68	b_2	822	33	a'	1188	72	a''	403
34	a_2	231	69	b_2	612	34	a'	1164	73	a''	289
35	a_2	98	70	b_2	563	35	a'	1162	74	a''	256
			71	b_2	421	36	a'	1136	75	a''	200
			72	b_2	374	37	a'	1127	76	a''	171
						38	a'	1087	77	a''	105
						39	a'	993	78	a''	74

Table 4.9: Anharmonic frequencies of 9-AnMe in the D_1 excited-state computed at the TD-B3LYP/6-311++G(d,p) level of theory from scans of the potential energy surface.

ν	Γ_ν	$v = 1$	$v = 2$
21	a_1	702	1404
22	a_1	642	1283
23	a_1	387	1020
24	a_1	387	774
25	a_1	248	496
35	a_2	106	220
46	b_1	297	595
47	b_1	130	265
48	b_1	58	126
71	b_2	419	841
72	b_2	374	753

the strong band in question, as well as the band labelled $25^1{}_0$ in Figure 4.6, were verified to belong to the same molecule as the origin, as seen in Figure 4.7.

Combinations of even-numbered quanta of a_2, b_1 or b_2 modes will also have a total symmetry of a_1, and these possible assignments were considered. Due to potentially significant anharmonicity of the out-of-plane a_2 and b_1 modes, calculated anharmonic frequencies were used for the remainder of the assignment.

The band observed at $+108\,\mathrm{cm}^{-1}$ is assigned as two quanta of the lowest frequency b_1 mode, $2\nu_{48}$, with a calculated anharmonic excited-state frequency of $126\,\mathrm{cm}^{-1}$. Similar two-quanta b_1 assignments can be made for the bands at $+249\,\mathrm{cm}^{-1}$ ($2\nu_{47}$) and $+600\,\mathrm{cm}^{-1}$ ($2\nu_{46}$). The band with relative frequency $+221\,\mathrm{cm}^{-1}$ can be assigned to two quanta of the lowest-frequency a_2 mode, $2\nu_{35}$.

The band observed with a relative frequency of $+178\,\mathrm{cm}^{-1}$ may be assigned to the combination band $47^1{}_0 48^1{}_0$. From anharmonic calculations of single quanta of these modes, the band is calculated to appear at $188\,\mathrm{cm}^{-1}$. But, given that the energies of both $2\nu_{47}$ and $2\nu_{48}$ are overestimated by 16 and $18\,\mathrm{cm}^{-1}$, respectively, an error of $10\,\mathrm{cm}^{-1}$ is not excessive.

Due to the appreciable intensity of the bands assigned to modes $2\nu_{48}$ and ν_{25}, it is expected that combination bands featuring these modes may have observable intensities. Further assignments are made to combination bands containing either $2\nu_{48}$ or ν_{25}, with the relative frequencies estimated from already-assigned bands. Small differences between the expected and observed frequencies are observed, but are generally within a few cm^{-1} (Table 4.10).

The bands observed at $+364\,\mathrm{cm}^{-1}$ and $+411\,\mathrm{cm}^{-1}$ do not correspond to the calculated anharmonic frequency of any mode, or combination of modes, with total symmetry a_1.

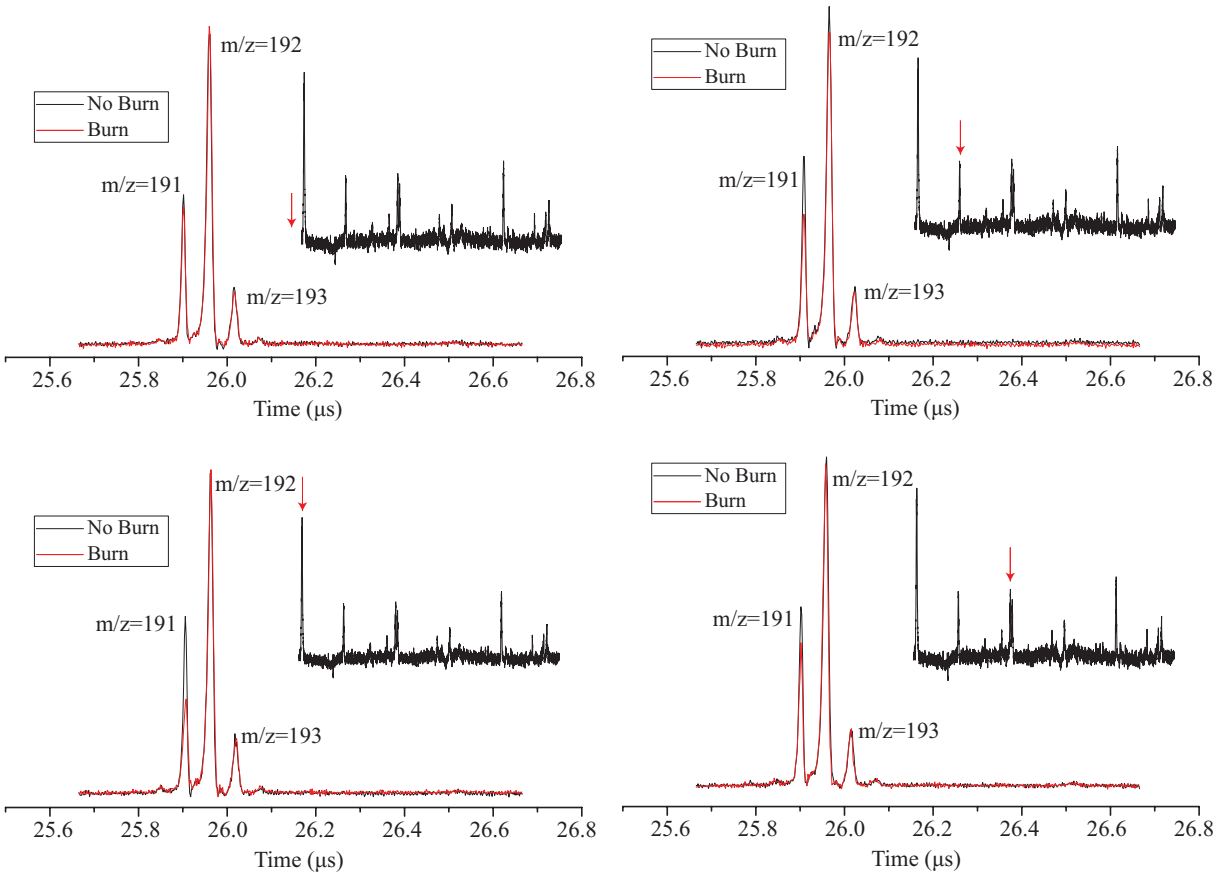

Figure 4.7: View of TOF trace showing effect of application of hole-burning laser. Probe laser resonant with origin transition of the $D_1 \leftarrow D_0$ transition of 9-AnMe ($13757\,\mathrm{cm}^{-1}$). Frequency of hole-burning laser indicated by red arrow. Top left box shows that no depletion is observed when the hole-burning laser is not resonant with any observed transition. The other segments show depletion when the laser is resonant with the origin, 25^1_0 and 48^2_0.

However, vibronic coupling with higher B_2 electronic transitions could allow single quanta of b_2 modes to be observed. Good agreement between calculated anharmonic excited-state frequencies for b_2 modes ν_{72} and ν_{71} with bands observed at relative frequencies $+364\,\mathrm{cm}^{-1}$ and $+411\,\mathrm{cm}^{-1}$ support this conjecture. As seen in Table 4.1, TD-B3LYP predicts several strong transitions of B_2 symmetry. The $D_6 \leftarrow D_0$ B_2 transition, which TD-B3LYP calculates as 1.44 eV above the reported $D_1 \leftarrow D_0$ transition, is calculated to be more than 400 times as intense as the observed transition. This is because the $D_1 \leftarrow D_0$ transitions of PAH RSRs are rather weak, as will be discussed in Chapter 5.

With good correspondence between calculated frequencies and the observed spectrum, as seen in Table 4.10, the assignment of this spectrum to 9-AnMe is well supported.

Table 4.10: Assignment of observed vibrational frequencies of 9-AnMe radical in the D_1 excited state and comparison with computed harmonic and anharmonic frequencies obtained at the TD-B3LYP/6-311++G(d,p) level of theory. The starred frequencies are tentative observed values based on partially resolved bands. Expected frequencies (Σ_{obs}) of combination bands are the sum of the observed component frequencies.

	Assignment	Observed	Harmonic	Anharmonic	$\Delta_{anh.}$	Σ_{obs}	$\Delta_{exp.}$
a_1	ν_{25}	244	246	248	+4		
modes	ν_{24}	385	387	387	+2		
	ν_{23}	519	527	510	-9		
	ν_{22}	637	641	642	+5		
	ν_{21}	690	702	702	+12		
b_1	$2\nu_{48}$	108	88	126	+18		
modes	$2\nu_{47}$	249	246	265	+16		
	$2\nu_{46}$	600	590	595	-5		
	$4\nu_{48}$	290	176	281	-9		
a_2 modes	$2\nu_{35}$	221	196	220	-1		
b_2	ν_{72}	364	374	374	+10		
modes	ν_{71}	411	421	419	+8		
combination	$\nu_{47}\nu_{48}$	178	167	188	+10		
bands	$2\nu_{35}2\nu_{48}$	338	284	346	+8	329	-9
	$2\nu_{47}2\nu_{48}$	360	334	391	+31	357	-3
	$\nu_{25}2\nu_{48}$	353	334	374	+21	352	-1
	$\nu_{25}2\nu_{35}$	467	442	468	+1	465	-2
	$\nu_{25}2\nu_{47}$	*488	492	513	+25	493	+5
	$\nu_{25}\nu_{24}$	629	633	635	+6	629	0
	$\nu_{25}4\nu_{48}$	531	422	529	-2	534	+3
	$\nu_{24}2\nu_{48}$	*493	475	513	+20	493	0
	$\nu_{23}2\nu_{48}$	*628	615	636	+8	627	-1

4.6.2 1-Pyrenylmethyl (1-PyMe) Radical Spectrum

4.6.2.1 1-PyMe Spectral Assignments

Figure 4.8 shows the R2C2PI excitation spectrum obtained in the region 12800−15800 cm^{-1} by monitoring the m/z 215 mass channel for a discharge containing 1-methylpyrene. It is expected that the spectrum is due to 1-PyMe, formed from 1-methylpyrene by hydrogen abstraction, in a similar manner to 9-AnMe. The $D_1 \leftarrow D_0$ transition of 1-PyMe is calculated to have in-plane A' symmetry ($A'' \leftarrow A''$). Vibrational modes of a' symmetry are therefore Frank-Condon allowed and the electronic origin band is allowed and expected. The lowest frequency band at 13417 cm^{-1} is assigned thus. This assignment is in good agreement with the $D_1 \leftarrow D_0$ transition energy calculated by both CASPT2 (14228 cm^{-1}) and scaled TD-B3LYP/6-311++G(d,p) (13660 cm^{-1}).

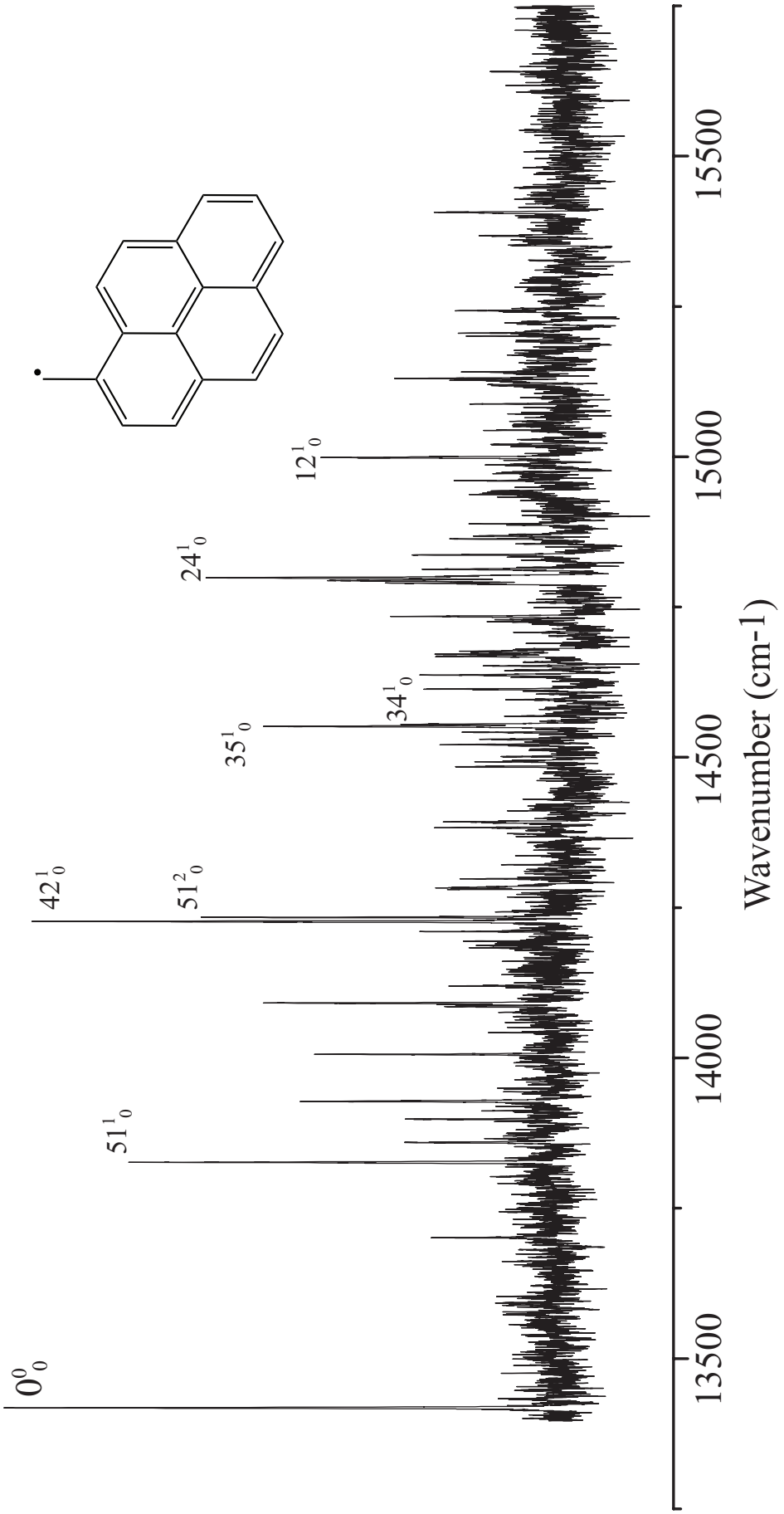

Figure 4.8: R2C2PI spectrum of 1-methylpyrene discharge recorded for m/z 215. Spectrum assigned to 1-pyrenylmethyl radical (structure shown).

Table 4.11: Assigned vibronic bands of 1-PyMe radical. Calculated values obtained at the TD-B3LYP/6-311++G(d,p) level of theory

Assignment	Γ	Calc.	Obs.	Δ_{c-o}
ν_{53}	a'	285	283	+2
ν_{51}	a'	414	408	+6
ν_{50}	a'	447	441	+8
ν_{49}	a'	490	480	+10
ν_{48}	a'	520	509	+11
ν_{46}	a'	595	588	+7
ν_{45}	a'	684	673	+11
ν_{44}	a'	715	702	+13
ν_{42}	a'	821	809	+12
ν_{35}	a'	1162	1134	+28
ν_{34}	a'	1164	1137	+27
ν_{24}	a'	1397	1380	+17
ν_{12}	a'	1692	1714	-22
$2\nu_{51}$	a'	828	816	+12

While it might at first be surprising that the 1-PyMe radical, with a larger chromophore, absorbs at an energy so similar to 9-AnMe, this is easily rationalized in terms of the electronic structure arising from a radical site interacting with the peripheral π system of the PAH. Both anthracene and pyrene possess a periphery with 14 C–C bonds, rendering them aromatic according to Hückel's rule.[339] As such, if the PAHs are considered to be perturbed cyclic systems, then, in the spirit of Hückel's rule, they would be expected to absorb at similar energies. As such, it is unsurprising that the radicals built on these chromophores also absorb at similar energies.

The TD-B3LYP D_1 excited-state frequencies for 1-PyMe are also tabulated in Table 4.8. The 78 vibrational modes are labelled in Mulliken convention in C_s symmetry, showing 53 a' and 25 a'' vibrational modes.

The assignment of the 1-PyMe vibronic structure is focused on low frequency modes with vibrational energies below 900 cm^{-1}, assignment of higher-frequency bands being complicated by multiple valid assignments fitting observed bands. All peaks in this region show good agreement with the calculated TD-B3LYP harmonic excited-state frequencies of a' vibrational modes (Table 4.11). These assignments are displayed in Figure 4.8 and listed in Table 4.11. The band $2\nu_{51}$ is the only two-quanta assignment. The higher-frequency bands with the highest intensity were also assigned.

Spectra of the origin and ν_{42}, obtained with low pulse energies (500 μJ), show that the band assigned to ν_{42} has $\sim 80\%$ the intensity of the origin band. The FC and FCHT stick spectrum shown in Figure 4.10 was used to guide the assignment of these higher energy

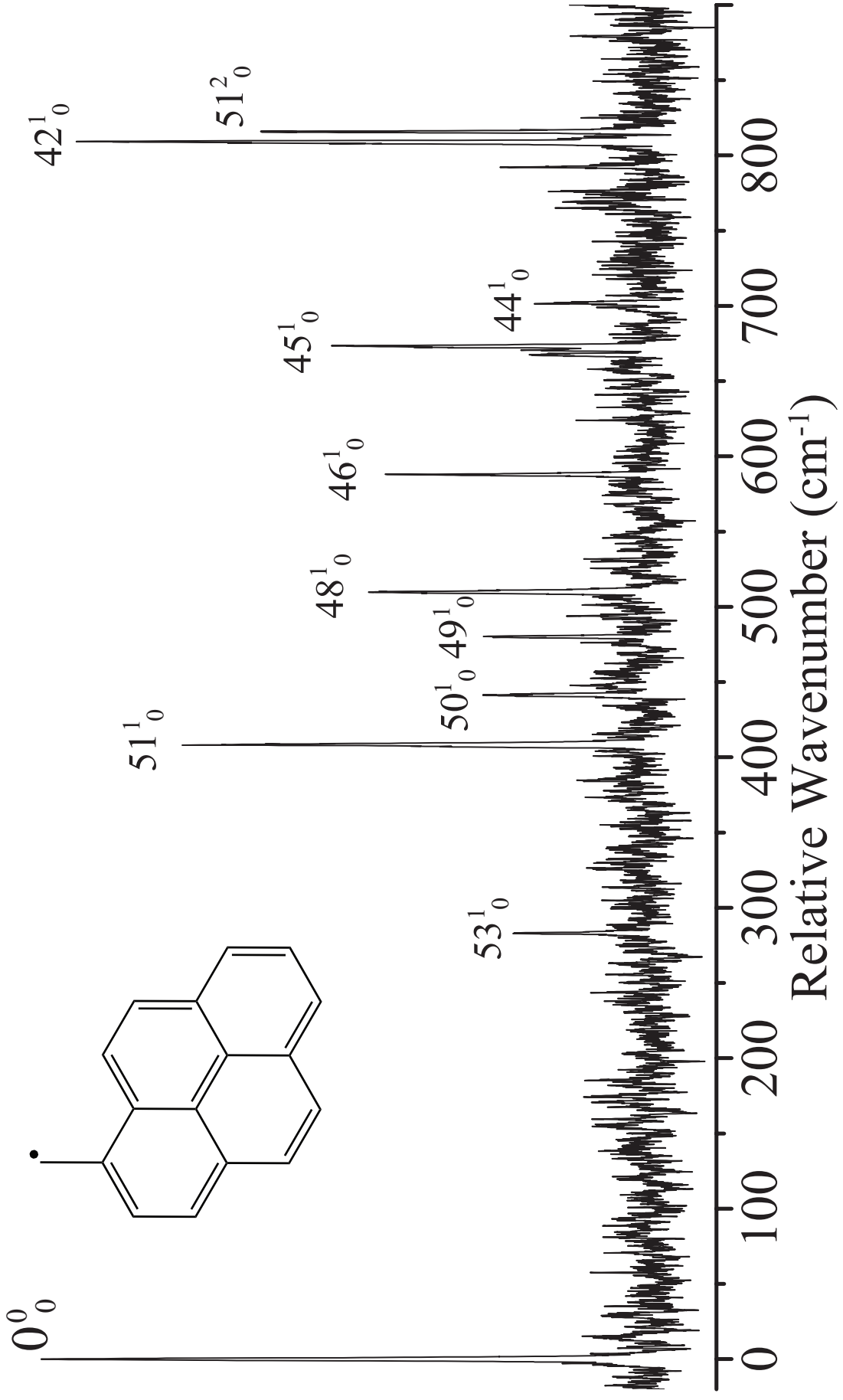

Figure 4.9: Assigned low frequency bands of 1-PyMe

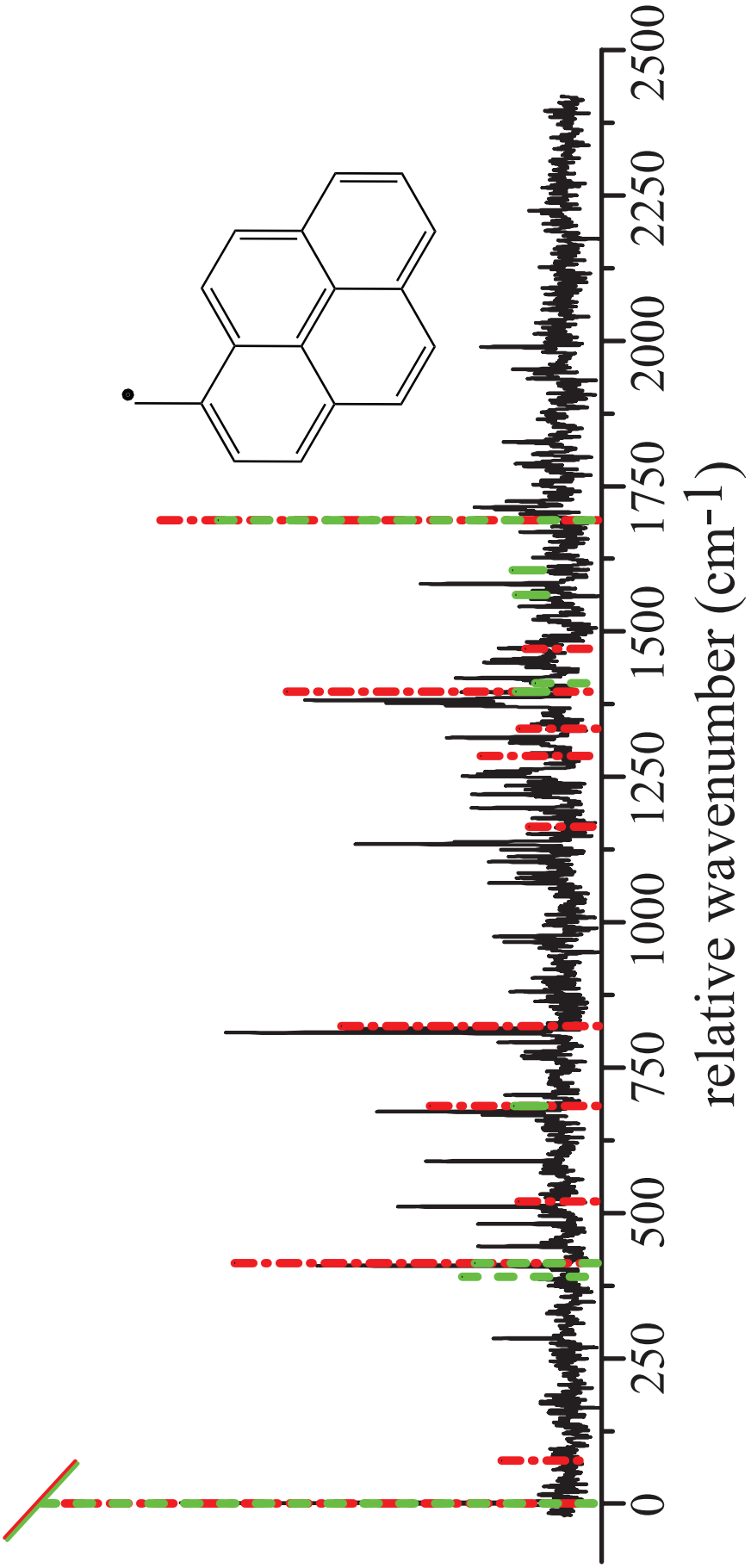

Figure 4.10: Comparison between FC siumlated stick spectra of 1-PyMe (Green), FCHT simulated stick spectrum of 1-PyMe (Red) and R2C2PI spectrum of 1-PyMe (black). Simulated origin bands truncated at aproximatly 0.25 predicted intensity.

bands. Both FC and FCHT simulations predict origin bands approximately four times stronger than the observed spectra, suggesting that even the low-power scans may have still been somewhat saturated. There is good general agreement between the intensity pattern of the FCHT spectrum and the strong vibronic structures observed in the R2C2PI spectrum. Many of these transitions are not observed in the FC spectrum, suggesting strong Herzberg-Teller coupling to a stronger electronic transition. Indeed, the $D_3 \leftarrow D_0$ transition is calculated to be several orders of magnitude more intense that the observed $D_1 \leftarrow D_0$ transition shown in Table 4.1, and is of the correct symmetry to vibronically couple.

4.6.3 Excited-State Lifetime

The excited-state lifetime can be obtained by recording R2C2PI signal as a function of the delay time between the excitation and ionization lasers. The intensity pattern created by this technique contains two components: a gaussian component caused by the temporal resolution of the two lasers and an exponential decay component caused by the decaying excited-state. This convolution can be fit to the equation

$$A \exp\left(\frac{-(t-\tau_d)^2}{w^2}\right) * \exp\left(\frac{-t}{\tau_r}\right) \tag{4.1}$$

where A is a scaling constant, t is time, τ_d is the time when the lasers are temporally overlapped, w is the width of the gaussian, and τ_r is the exponential decay lifetime of the excited state. Fitting this equation to the high resolution ionisation lifetime scan of 9-AnMe, shown in Figure 4.11, gives a convolved laser width w of 5.1 ns and a D_1 excited state lifetime $\tau_r = 4.0\,\text{ns} \pm 0.5\,\text{ns}$.

The transient also exhibits a long-lived component, maintaining a low intensity for more than a microsecond. The slight positive slope of the long lived component is due to a minor misalignment of the lasers, with more excited molecules able to drift into the ionisation beam after the longer delay. The long-lived signal is due to ionization directly from the highly vibrationally-excited ground state, accessed by internal conversion.

The transient was recorded with an ionization photon energy of 6.42 eV. The B3LYP/6-311++G(d,p) vertical ionization energy (IE) of 9-AnMe was calculated to be 6.32 eV. However, previous work by Troy *et. al.* has shown that this method underestimates IEs by about 0.08 eV.[200] This suggests that single-photon ionization would be possible from

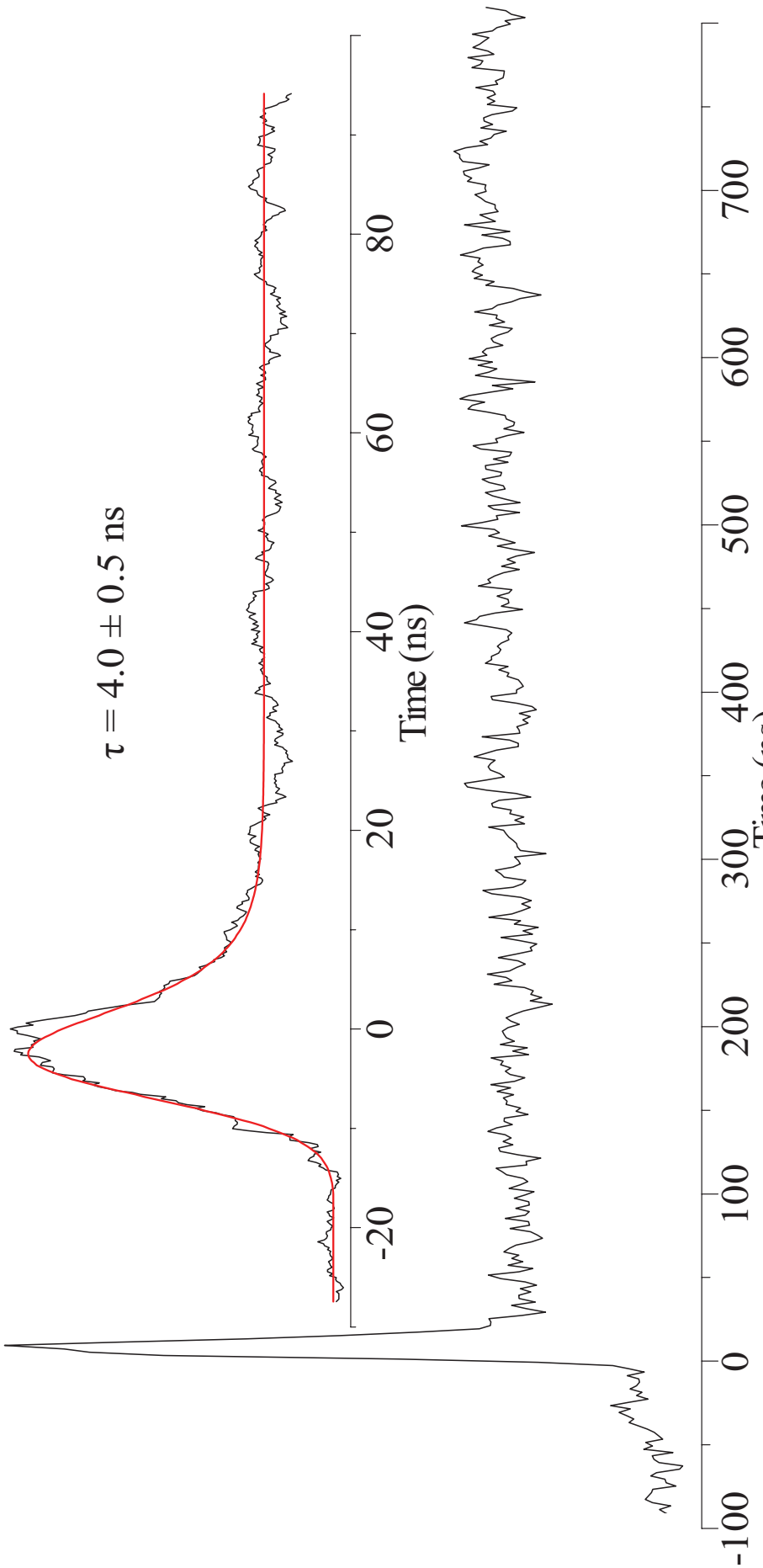

Figure 4.11: Ionization lifetime scan of 9-AnMe showing D_1 excited-state lifetime of < 5 ns (High resolution insert). The long lived component is likely caused by ionization from the vibrationally excited ground-state following internal conversion.

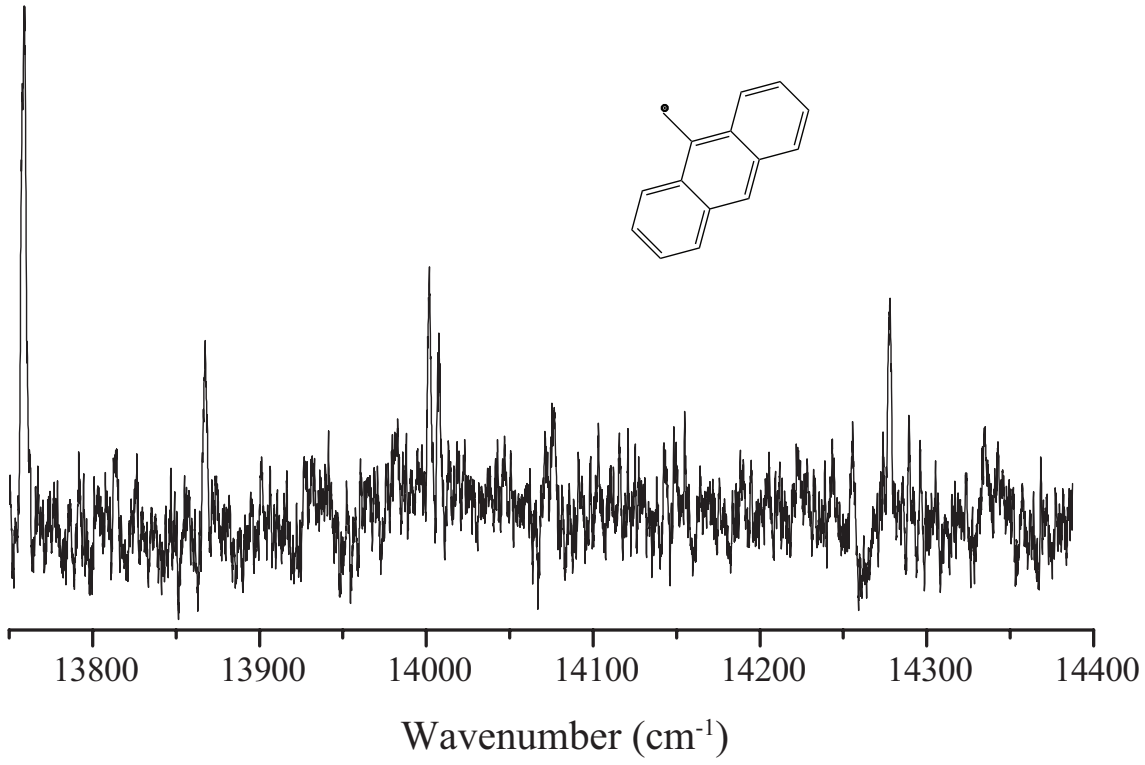

Figure 4.12: 9-AnMe $D_1 \leftarrow D_0$ excitation spectrum recorded using R2C2PI after internal conversion. Excited molecules are ionised after internal conversion to the vibrationally excited D_0 ground state. This signal is independent of the lifetime of the D_1 excited state as shown in in Figure 4.11.

the cold ground state. However, this is not observed, and thus we conclude that the IE is slightly above the ionization laser energy, IE $\gtrsim 6.42\,\text{eV}$.

Initial decay from the excited state will be through internal conversion to any energetically equivalent vibrational state of the ground state. From these highly excited vibrational states, a strong Frank-Condon overlap with equivalent vibrational state in the ground state of the 9-anthracenylmethylium (9-AnMe$^+$) cation is likely. As such, if these states are energetically accessible, ionisation can occur. A comparison between ground state frequencies of the 9-AnMe radical and the 9-AnMe$^+$ cation, calculated using the B3LYP method, is shown in Table 4.12. It can be seen that many combinations of these vibrational modes will have lower frequencies in the cation than in the radical. Thus, the hypothesis that this long lived component is caused by ionisation after internal conversion appears to be sound.

The long lived component is wavelength dependant and it is possible to re-record the $D_1 \leftarrow D_0$ excitation spectrum at long delay times, as shown in Figure 4.12. A feature of this long lived component of the signal is that it is independent of the lifetime of the

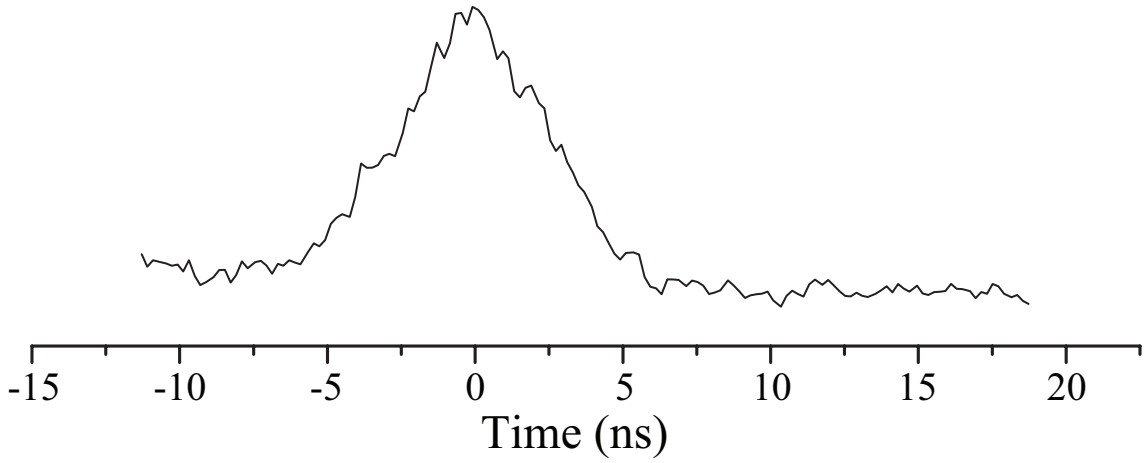

Figure 4.13: Ionisation lifetime scan of 1-PyMe, showing a D_1 lifetime of less than 1 ns. The exact value is below the resolution of this measurement

excited state. This is exploited in the R2C2PI after internal conversion technique, used to record a higher excited state of the 9-AnMe radical in Chapter 5.

The lifetime of the excited state of 1-PyMe was found to be below the resolution of this technique. The lifetime scan of 1-PyMe is shown in Figure 4.13.

4.6.4 Larger Radicals

Due to the relatively low computational cost of TD-B3LYP/6-311++G(d,p), the $D_1 \leftarrow D_0$ transition of even larger BBR systems may be determined. By adding the present data for 9-AnMe and 1-PyMe to the analysis put forward in Figure 4.2, a refined scaling formula of $T_{exp} = 0.867 T_{TD-B3LYP} - 0.008$ is obtained. From this, the larger radicals, 2-perylenylmethyl (2-PerMe) and 6-anthanthrenylmethyl (6-AnanMe) (structures displayed in Figure 4.14), which are calculated to absorb at 1.67 eV and 1.63 eV, are predicted to absorb at 1.44 eV and 1.41 eV respectively ($\sim$ 870 nm). The largest error for this fit in the data set is 0.03 eV, which gives a sense of the expected accuracy in the prediction.

4.6.5 Comparison with Astronomical spectra

The 9-AnMe radical spectrum was compared with astronomical spectra known to contain DIBs,[144,145] made available online by the Apache Point Observatory Diffuse Interstellar Band collaboration (*dibdata.org/*). A high resolution spectrum of the 13757 cm^{-1} origin band was recorded with 0.01 Å step size. A gaussian fit to this band yielded a band centre of 7266.99 Å (air) and a full-width at half-maximum (FWHM) of 0.79 Å. This does not

Table 4.12: Comparrison of ground-state B3LYP/6-31++1G(d,p) harmonic frequencies, in cm^{-1}, of 9-AnMe and 9-AnMe$^+$. Modes with a lower harmonic frequency in the cationic species highlighted in red

Mode	Γ	9-AnMe	9-AnMe$^+$	Δ	Mode	Γ	9-AnMe	9-AnMe$^+$	Δ
1	a_1	3203	3218	15	36	b_1	1008	1045	37
2	a_1	3185	3210	25	37	b_1	988	1037	50
3	a_1	3172	3190	18	38	b_1	904	1032	128
4	a_1	3166	3182	16	39	b_1	872	996	124
5	a_1	3158	3178	20	40	b_1	851	913	62
6	a_1	3152	3162	10	41	b_1	788	799	11
7	a_1	1641	1654	13	42	b_1	749	755	5
8	a_1	1583	1631	48	43	b_1	629	617	-13
9	a_1	1564	1588	24	44	b_1	537	513	-25
10	a_1	1512	1537	25	45	b_1	414	407	-7
11	a_1	1496	1506	10	46	b_1	303	314	11
12	a_1	1426	1470	44	47	b_1	127	122	-5
13	a_1	1350	1391	41	48	b_1	19	-30	-48
14	a_1	1322	1336	14	49	b_2	3255	3265	10
15	a_1	1237	1319	81	50	b_2	3199	3216	17
16	a_1	1220	1234	14	51	b_2	3184	3209	25
17	a_1	1180	1209	29	52	b_2	3167	3189	23
18	a_1	1137	1145	7	53	b_2	3154	3181	28
19	a_1	1053	1062	9	54	b_2	1626	1630	4
20	a_1	893	894	2	55	b_2	1582	1597	15
21	a_1	716	716	0	56	b_2	1546	1564	19
22	a_1	672	677	5	57	b_2	1485	1493	8
23	a_1	551	544	-8	58	b_2	1443	1468	26
24	a_1	382	390	9	59	b_2	1371	1390	19
25	a_1	255	253	-1	60	b_2	1350	1374	24
26	a_2	1008	1046	38	61	b_2	1283	1299	16
27	a_2	984	1019	35	62	b_2	1233	1250	17
28	a_2	884	911	27	63	b_2	1205	1227	23
29	a_2	779	801	23	64	b_2	1132	1138	7
30	a_2	755	757	2	65	b_2	1110	1115	5
31	a_2	596	626	29	66	b_2	1044	1051	7
32	a_2	512	492	-21	67	b_2	925	926	1
33	a_2	433	433	0	68	b_2	825	826	1
34	a_2	240	231	-9	69	b_2	637	635	-2
35	a_2	104	98	-6	70	b_2	583	580	-3
					71	b_2	434	433	-1
					72	b_2	384	377	-7

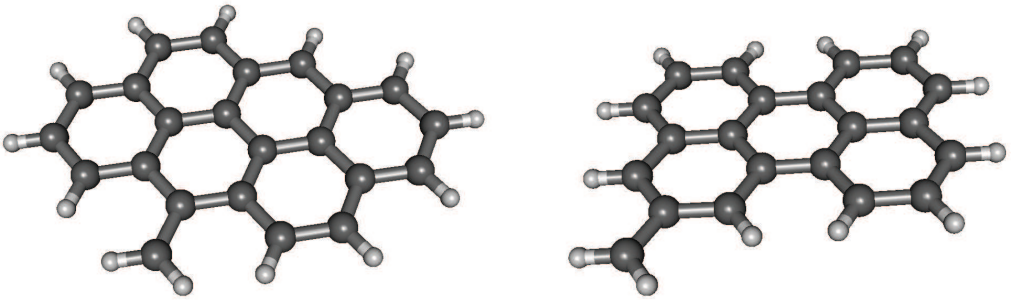

Figure 4.14: Structure of the 6-anthanthrenylmethyl (6-AnanMe) [left] and 2-perylenylmethyl (2-PerMe) [right] radicals

match any reported DIB, the nearest known feature being observed at 7268.53 Å in the spectrum of HD 183143.[145]

The 1-PyMe radical's 13417 cm^{-1} origin band was similarly compared with astronomical spectra, giving a band centre in air of 7451.11 Å and a FWHM of 0.89 Å. This overlaps the 7451.46 Å DIB, which has a reported FWHM of 1.00 Å, also observed in the spectrum of HD 183143.[145] However, the vibronic band assigned to ν_{42} (7027.02 Å, FWHM 1.40 Å) with $\sim$ 80% of the origin intensity, does not match any reported DIB. Indeed, as all but two DIBs have been shown to be uncorrelated,[146] only spectra dominated by a single transition represent potential DIB carriers.

The $D_1 \leftarrow D_0$ transitions of odd-alternant hydrocarbon radicals, such as BBRs, have been shown previously to be of low intensity. The energetically degenerate single electron transitions into and out of the singly-occupied molecular orbital destructively interfere, resulting in a weak transition. The low intensity of the $D_1 \leftarrow D_0$ transitions of RSRs may explain why none of these transitions have yet been observed as DIBs. Additionally, coupling to the intense higher-energy transition is likely responsible for the strong vibronic coupling observed in 1-PyMe. This vibronic coupling is likely to be stronger in larger BBRs as the difference between the weak and strong electronic transition energies decrease. This suggests that these BBRs are unlikely to be DIB carriers.

4.7 Conclusion

The excitation spectra of the 9-AnMe and 1-PyMe radicals have been observed for the first time. They were identified through a combination of R2C2PI spectroscopy and quantum-chemical calculations. The $D_1 \leftarrow D_0$ spectra have been assigned through a combination of TD-B3LYP methods, including anharmonic calculations and FCHT simulations. Both spectra showed evidence of significant Herzberg-Teller coupling.

Using the TD-B3LYP/6-311++G(d,p) method in conjunction with empirical scaling, the $D_1 \leftarrow D_0$ excitation energies of 9-AnMe and 1-PyMe were predicted to an accuracy of $\sim 250\,\mathrm{cm}^{-1}$. This scaling represents an improvement in the predictive capability of the TD-B3LYP/6-311++G(d,p) method by a factor of ~ 5. Empirical scaling was similarly effective when applied to TD-CAM-B3LYP/6-311++G(d,p) and TD-M06/6-311++G(d,p) calculations. Scaled TD-M06 vertical excitation frequencies gave the most accurate prediction of experimental excitation energies, albeit at slightly increased cost when compared to TD-B3LYP. For both these molecules the scaled TD-DFT approach, as proposed in this work, has also outperformed the CASPT2 calculations. Further application of this scaling predicts absorption positions for the larger 2-PerMe and 6-AnanMe radicals in the near-infrared (NIR) region.

The $D_1 \leftarrow D_0$ transition of the 9-AnMe radical was not found to match any DIB, and the strongly vibronic intensity pattern of 1-PyMe excludes it as a DIB carrier. The very low IEs of these species imply that their dominant ionization state in the ISM may be cationic. Obtaining gas-phase spectra of these cations is an experimental challenge, and these closed-shell cationic species will be discussed in Chapter 7.

Chapter 5

Higher Excited States of Neutral Resonance Stabilised Radicals

5.1 Author's Note

The work published in this chapter has been, in part, published in *Molecular Physics*.[340]

- G. D. O'Connor, G. V. G. Woodhouse, T. P. Troy, and T. W. Schmidt. "Double-resonance spectroscopy of radicals: higher electronic excited states of 1- and 2-naphthylmethyl, 1-phenylpropargyl and 9-anthracenylmethyl". *Mol. Phys.*, Preprint: 1–10, (2015)[340]

Ab-initio calculations performed by Prof. Timothy Schmidt of the School of Chemistry at UNSW, as part of this paper, have been included for completeness. The 1-PPr double resonance spectrum was recorded by Gabrielle V.G. Woodhouse as part of her undergraduate honours thesis,[341] with the authors assistance. These contributions are acknowledged within the chapter.

5.2 Introduction

As mentioned in Chapter 4, The $D_1 \leftarrow D_0$ transitions of neutral, aromatic RSRs have similar widths to DIBs, and lie in the visible part of the electromagnetic spectrum.[183,287] However, none have been observed in the ISM. One possible reason for this, despite the

evidence that aromatic species should be present,[130,131,171–173] is the low oscillator strengths of their $D_1 \leftarrow D_0$ transitions, generally calculated to be on the order of $f = 10^{-4}$ as shown in Chapter 4.[185,195] The low oscillator strength was first explained by Pople and Longuet-Higgins,[338] and is a consequence of the Coulson-Rushbrooke orbital-pairing theorem.[342] As shown in Figure 5.1, electronic transitions into and out of the singly-occupied molecular orbital bring about near degenerate configurations which interact to yield two electronic states. The sign of the coulomb integral ensures that transitions to the higher electronic state are reinforced by the configuration interaction, while those to the lower state tend to cancel. This effect has been shown to manifest in carbon chains[343] as well as aromatic radicals.[185,192,201].

Modelling, based on the abundance of carbon in the ISM, suggests an oscillator strength on the order $f = 10^{-2}$ for PAH DIB carriers.[140] Indeed, for $D_1 \leftarrow D_0$ transitions with $f = 10^{-4}$ to be observed, column densities of these molecules, and their share of the interstellar carbon budget, would have to be significantly higher than assumed by existing models.[140]

The $D_2 \leftarrow D_0$ and higher transitions of PAH radical cations can be largely dismissed as DIB candidates as the absorption bands are generally broader than recorded DIBs, on account of the short-lived nature of the excited states. This is demonstrated in Chapters 6 and 7, as well as in previous studies. For example, Sukhorukov *et. al.* reported the gas phase spectral width for the $D_2 \leftarrow D_0$ transitions of naphthalenium radical cation as $36\,\mathrm{cm}^{-1}$, and that of anthracenium radical cation as $94\,\mathrm{cm}^{-1}$.[206] The average full-with-at-half-maximum (FWHM) of confirmed DIBs observed in HD 183143 is 1.40 Å ($5\,\mathrm{cm}^{-1}$ at 500 nm). The broadest DIB in this spectrum, centered on 4428.83 Å, has a FWHM of 22.56 Å, or $115\,\mathrm{cm}^{-1}$.[145] The $D_1 \leftarrow D_0$ transitions of PAH radical cations lie in the infrared region, of less relevance to DIBs. These transitions will also be discussed in Chapter 6.

The group of Maier investigated higher electronic states of polyacetylene cations on the expectation that they would exhibit large oscillator strengths, and to test whether the origin bands of these transitions were broadened by intramolecular processes to such an extent that they would not be relevant to the DIB problem.[344] They found that the bands were still narrow enough to be considered DIB candidates, being broadened by $1-10\,\mathrm{cm}^{-1}$.

This chapter reports on double-resonance spectra of higher-lying electronic transitions of the resonance stabilized aromatic radicals 1-naphthylmethyl (1-NpMe), 2-naphthylmethyl (2-NpMe), 1-phenylpropargyl (1-PPr) and 9-anthracenylmethyl (9-AnMe), pictured in Figure 5.2. It is found that these molecules exhibit strong $D_n \leftarrow D_0$ transitions in the near ultraviolet region. TD-DFT and *ab-initio* calculations are utilized to investigate the nature

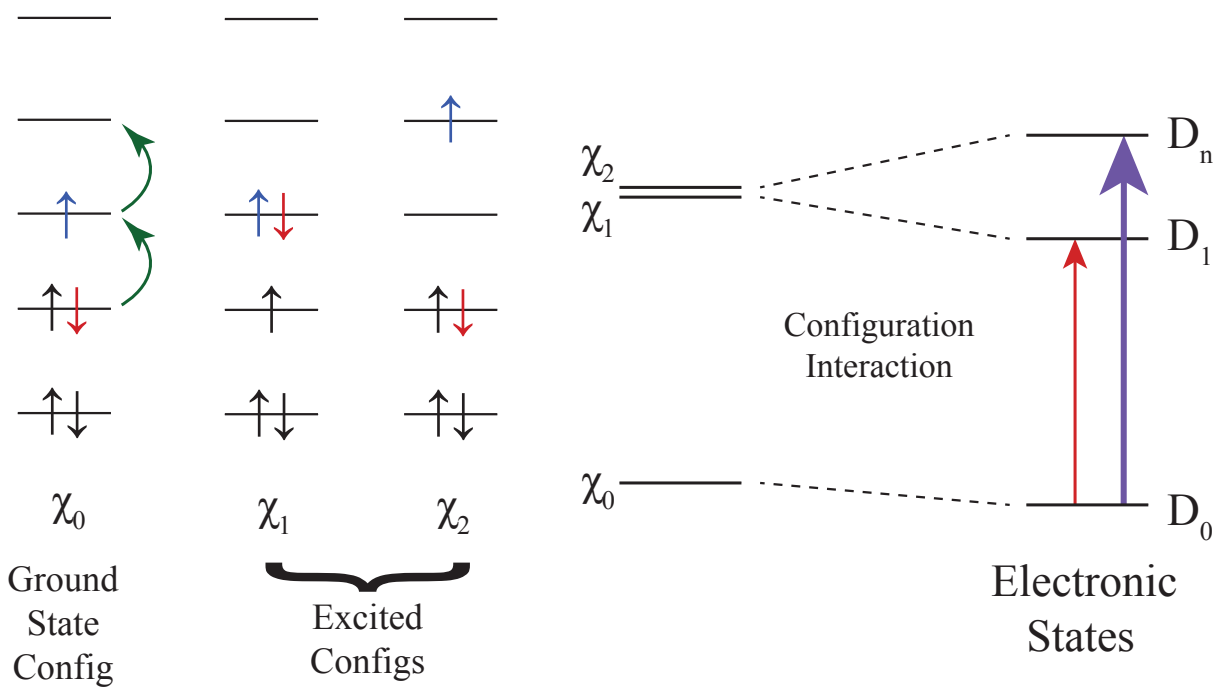

Figure 5.1: Longuet-Higgins model of configuration interaction in odd-alternant resonance-stabilized hydrocarbon radicals.[338] Two one-electron excitations bring about degenerate configurations which interact to yield two excited states. The transition to the higher energy state is strengthened by the configuration interaction, while the lower energy transition is weakened.

of the transitions, and show that the strong transitions observed are generally $D_3 \leftarrow D_0$. All transitions are found to be significantly lifetime-broadened, making these transitions largely irrelevant to the search for DIB carriers, even for larger species which are expected to exhibit $D_3 \leftarrow D_0$ in the visible region.

The 1-PPr spectrum discussed in this chapter was recorded by Gabrielle V.G. Woodhouse as part of her undergraduate honours thesis,[341] after having previously assisted the author in the recording of the 1-NpMe and 2-NpMe spectra. In this chapter these spectra are re-evaluated in light of additional theoretical results and the 9-AnMe data recorded using the R2C2PI after internal conversion technique, which exploits the long lived R2C2PI signal observed in the ionisation-lifetime scan in Chapter 4.

5.3 Experimental Methods

The REMPI-TOF apparatus used for these experiments was outlined in detail in Chapter 3. Higher-energy transitions than $D_1 \leftarrow D_0$ are potentially difficult to measure by R2C2PI due to short excited-state lifetimes, which also precludes laser-induced fluorescence as a spectroscopic technique. As such, for 1-NpMe, 2-NpMe and 1-PPr we opted for a double

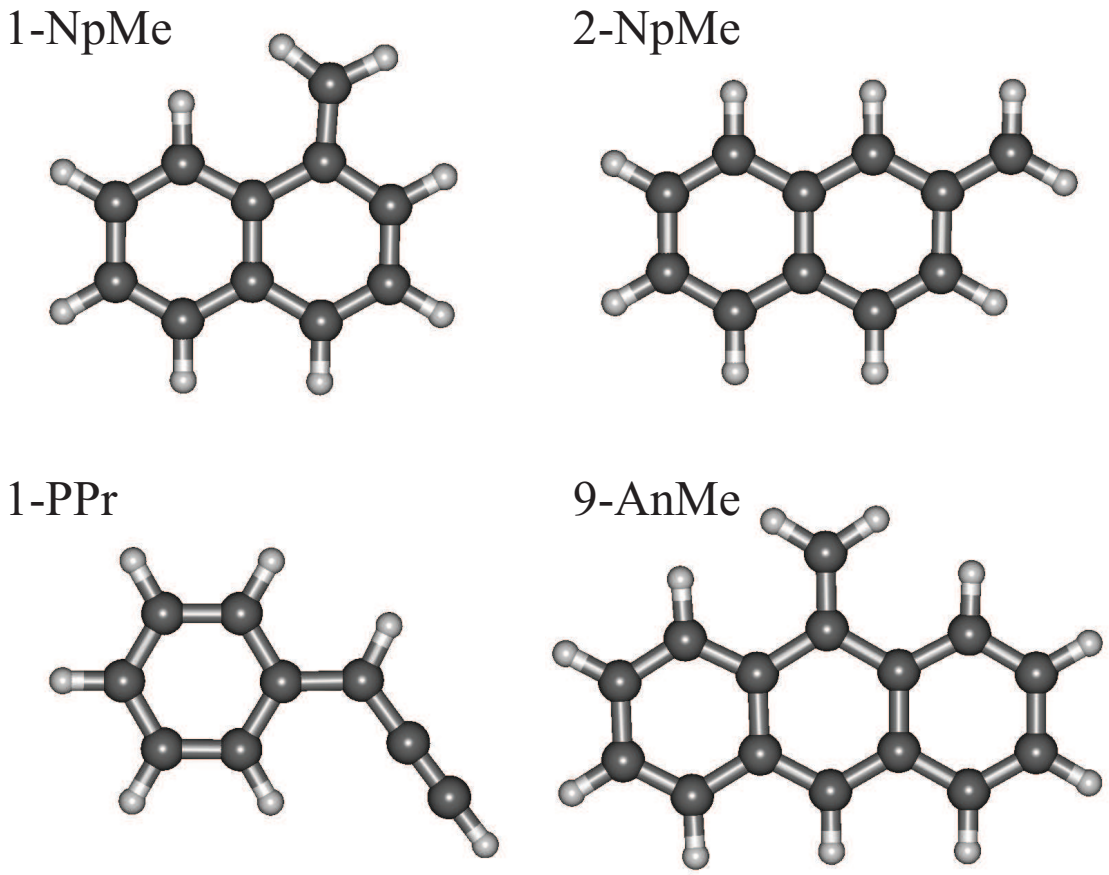

Figure 5.2: Structures of radicals for which $D_n \leftarrow D_0$ spectra have been obtained

resonance method, while for 9-AnMe a fortuitous coincidence between the photon energy of the 193 nm excimer laser and the ionization energy of the radical made delayed R2C2PI after internal conversion possible.

5.3.1 Double-Resonance Spectroscopy

Spectra due to the $D_n \leftarrow D_0$ transitions of 1-NpMe, 2-NpMe and 1-PPr were obtained through double-resonance depletion of R2C2PI signal. First, the known $D_1 \leftarrow D_0$ spectra were reproduced by R2C2PI as outlined in Chapter 3 and utilised in Chapter 4 as well as previous studies.[183,185,193,194,199–203] A preceding (probe) tunable laser was introduced to photo-excite radicals from the ground state into a higher excited state, D_n, ~ 100 ns prior to a pump laser resonant with the $D_1 \leftarrow D_0$ origin band. When the probe laser was resonant with a transition to a higher excited state the $D_1 \leftarrow D_0$ R2C2PI signal was diminished due to depletion of the common D_0 ground state. This process is illustrated in Figure 5.3.

This technique is a different application of the hole-burning technique used in Chapter 4. It has been proven to be an effective tool for recording the excitation spectra of short lived states. For example, Gasser *et. al.* used a similar double-resonance scheme to record the vibronic structure of Rydberg States of the Allyl Radical.[345]

Due to the relatively high stability of the ion peaks being depleted, no shot-to-shot subtraction was used in this study. Results were recorded unaveraged as well as averaged over 7, 15 and 32 shots to improve signal to noise while ensuring no artefacts or errors were introduced. The figures shown were typically recorded with 7 or 15 shot averaging.

Laser power was then reduced and the scans were repeated to identify the effects of power-broadening. This process was repeated at decreasing laser power to ensure the FWHM of the lorenzian component of the observed bands was consistent for subsequent power settings, ensuring no power broadening effects remained.

5.3.2 R2C2PI After Internal Conversion

In Chapter 4, while probing the D_1 lifetime of 9-AnMe in the R2C2PI experiment, we found that non-negligible two-laser signal was obtained for hundreds of nanoseconds after excitation to D_1, despite its few nanoseconds lifetime. In that case the photon energy of the ionization source, a 193 nm ArF excimer laser, was similar to the ionisation energy of 9-AnMe, ensuring good Franck-Condon factors for ionization, even after internal conversion to D_0, as shown in Figure 5.3. As this signal is independent of excited-state lifetime it is used here to probe higher-energy short-lived excited states. A delay was employed to eliminate signal instability due to timing jitter between the two pulsed lasers. As with the double-resonance spectroscopy, no shot-by-shot subtraction was necessary and the spectra was recorded both unaveraged and averaged. Effects of power broadening were eliminated in the same manner used when obtaining the double-resonance spectra.

5.4 Theoretical Methods

Ground state geometries of the benzyl, 1-PPr, 1-NpMe, 2-NpMe, and 9-AnMe radicals were obtained at B3LYP/6-311++G(d,p) level,[231,232,330] using the GAUSSIAN09 package.[221]

Semi-empirical vertical excitation energies were then calculated using time dependant density functional theory (TD-DFT), again using the TD-B3LYP and TD-M06 functionals.

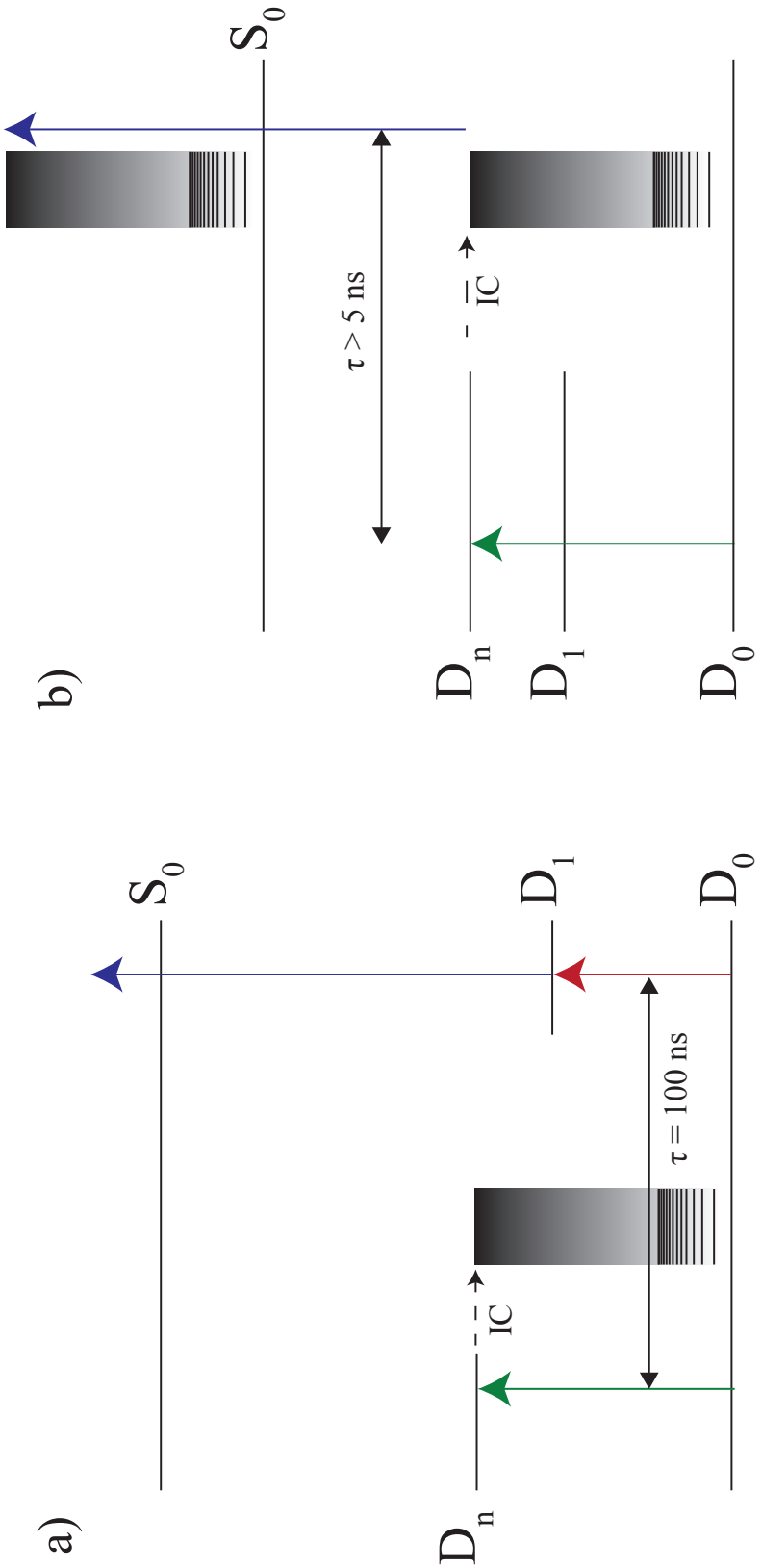

Figure 5.3: (a) Double Resonance: R2C2PI signal is initially obtained by exciting the molecule to D_1, then ionizing the excited molecule. A depletion laser is then introduced 100 ns in advance of the R2C2PI laser pulses. When the depletion laser is resonant with an excited state, D_n, the radical rapidly undergoes internal conversion to a highly vibrationally excited state of D_0. As similar vibrational states of the cation are energetically inaccessible upon absorption of the second photon, there is little Franck-Condon overlap and thus molecules excited to D_n are ionized inefficiently. This results in a reduction in ion flux and a depletion of the $D_1 \leftarrow D_0$ signal. (b) R2C2PI after Internal Conversion: When the excitation laser is resonant with an excited state, D_n, the molecule rapidly undergoes internal conversion to a highly vibrationally excited state of D_0. Similar highly vibrationally excited states of the cation are energetically accessible upon absorption of the ionization photon, since it is near resonant with the ionization energy, and as such there is good Franck-Condon overlap. Molecules excited to D_n lead to ions being formed, even with delayed photoionization. Resonant signal is observed as a significant increase in ion flux at the appropriate m/z.

These calculation were undertaken in GAUSSIAN09[221] utilizing the 6-311++G(d,p) basis set. These are the same calculations used in Chapter 4.

Excited states were also calculated using the extended multi-configuration quasi-degenerate perturbation theory (X-MCQDPT2) programme[346] of the FIREFLY package, which is partially based on the GAMESS (US) source code.[222,347] These *ab-initio* results were provided by Prof. Timothy Schmidt of The School of Chemistry at UNSW. Basis sets of triple-zeta valence quality were augmented with two sets of d-orbitals. Calculations on benzyl with an additional set of f-functions yielded improved results, but the additional cost was not considered necessary for the purposes of the present work. Orbitals were calculated at the ROHF level, and an active space comprising 5 electrons in 5 π-type orbitals was chosen for the X-MCQDPT2 calculation.

5.5 Results

5.5.1 Naphthylmethyl Radicals

Double-resonance ion-depletion spectra of the 1-NpMe and 2-NpMe radicals are displayed in Figure 5.4. Both spectra were obtained by depleting ion flux generated by resonant ionization through the origin bands of their $D_1 \leftarrow D_0$ excitation spectra.[183] Both radicals display a pronounced hump at lower energy, which may be fit to a lorentzian function. The band of 1-NpMe is centered at 27993 cm^{-1} (3.47 eV) with a FWHM of 292 cm^{-1}, whereas the 2-NpMe band is centered at 27478 cm^{-1} (3.41 eV) with FWHM 290 cm^{-1}. Additional depletion signal observed to higher energy than the fitted lorentzian is attributed to unresolved vibrational structure built onto the electronic origin.

5.5.2 1-Phenylpropargyl Radical

This spectrum was recorded by Gabrielle V. G. Woodhouse as part of her undergraduate honours thesis.[341] Figure 5.4 displays the double-resonance ion-depletion spectrum of 1-PPr radical, obtained by depleting the ion flux generated by resonant ionization through the origin band of its $D_1 \leftarrow D_0$ excitation spectrum.[193,282] The observed band is fit to a lorentzian function centered on 32437 cm^{-1} (4.02 eV) with FWHM 149 cm^{-1}. As with 1-NpMe and 2-NpMe, unresolved vibrational structure is observed to higher energy than the electronic origin band.

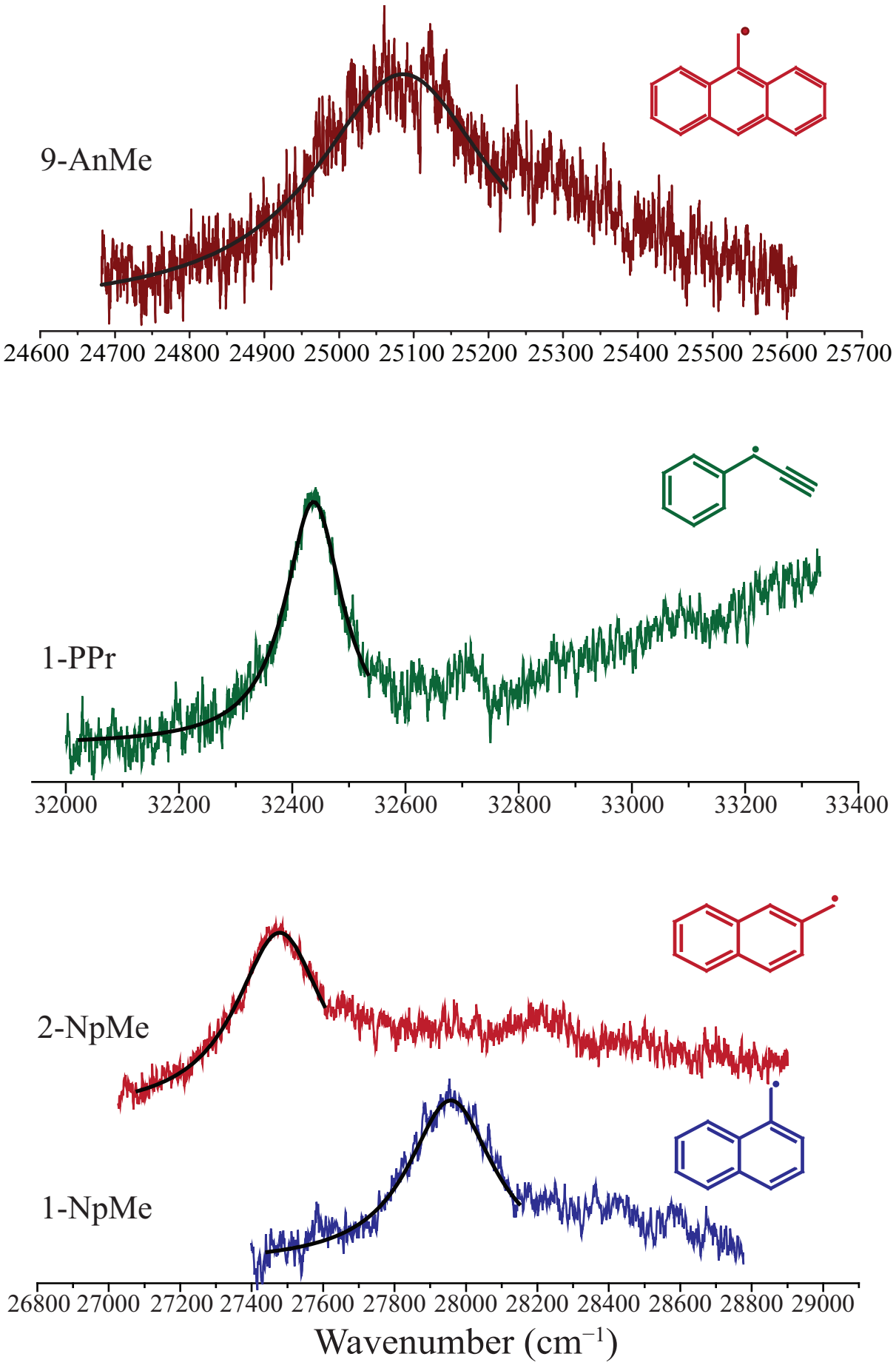

Figure 5.4: Excitation spectra of $D_n \leftarrow D_0$ transitions of neutral resonance-stabilized radicals. The spectra of 1-NpMe, 2-NpMe and 1-PPr were recorded *via* double-resonance ion-depletion spectroscopy, while the spectrum of 9-AnMe was measured *via* delayed R2C2PI after internal conversion. The 1-PPr spectrum was provided by Gabrielle V. G. Woodhouse.[341]

The original detection of this band was assisted by CASPT2/6-311G(d)[9,9] calculations, also performed by Gabrielle V. G. Woodhouse, which calculated the $D_3 \leftarrow D_0$ transition energy of 33858 cm^{-1} with oscillator strength 0.016.[341]

5.5.3 9-Anthracenylmethyl Radical

The delayed R2C2PI after internal conversion spectrum of 9-AnMe is displayed in Figure 5.4. The origin band was fit to a lorentzian function centered on 25063 cm^{-1} (3.17 eV) with a FWHM of 326 cm^{-1}. As expected, this spectrum also features unresolved vibrational structure to the blue of the origin features, observed as a departure from the lorentzian profile of the initial peak.

5.5.4 Calculated Vertical Excitation Energies

5.5.4.1 TD-DFT Vertical Excitation Energies

Vertical excitation energies and oscillator strengths were calculated at the TD-B3LYP/6-311++G(d,p) and TD-M06/6-311++G(d,p) level of theory. The gas-phase energies for the observed transitions to higher-excited states of 1-NpMe, 2-NpMe and 1-PPr, as well as previously published gas-phase data on the higher-excited states of benzyl,[186] were plotted against TD-DFT vertical excitation energies. The observed higher excited state transitions were tentatively assigned to calculated transitions, based on the assumption that the observed higher exited states would have oscillator strength greater than $f = 10^{-2}$. The plots, based on these assignments, are displayed in Figures 5.5 and 5.6.

It was shown in Chapter 4, and its accompanying publication,[185] that fitting semi-empirical TD-DFT calculations to experimental data can be a low-cost method of predicting the $D_1 \leftarrow D_0$ transition energy of hydrocarbon radicals. This technique was used to guide the initial search for the strong higher transition of 9-AnMe reported in this chapter.

The data in Figures 5.5 and 5.6 show two distinct trends exist for the plotted transitions, the previously identified trend in $D_1 \leftarrow D_0$ transitions[185] and an apparently linear trend in the energies of the observed strong higher excited states. It was hypothesised that this trend could be extrapolated to predict the higher excited states of larger aromatic RSRs. The linear fit had the form $T_{exp} = 0.980 T_{TD-B3LYP} + 0.310$ for TD-B3LYP and $T_{exp} = 1.047 T_{TD-M06} + 0.019$ for TD-M06.

Table 5.1: $D_n \leftarrow D_0$ vertical electronic transition energies, $T_{TD-B3LYP}$, and oscillator strengths, f, calculated at the TD-B3LYP/6-311++G(d,p) level of theory. The symmetry of the transition moment is given as $\Gamma_{\mu_{n0}}$. Oscillator strengths of strong transitions ($f > 10^{-2}$) are given in red.

n	$\Gamma_{\mu_{n0}}$	$T_{TD-B3LYP}$ (eV)	f	$\Gamma_{\mu_{n0}}$	$T_{TD-B3LYP}$ (eV)	f
	1-PPr			1-NpMe		
1	A'	3.01	0.0222	A'	2.50	0.0004
2	A'	3.13	0.0056	A'	3.01	0.0006
3	A''	3.36	0.0000	A'	3.30	0.1023
4	A'	3.77	0.0127	A'	3.60	0.0635
5	A'	4.16	0.2546	A'	3.63	0.0068
6	A''	4.24	0.0000	A''	4.14	0.0039
7	A'	4.37	0.1055	A'	4.17	0.0020
8	A''	4.54	0.0004	A''	4.46	0.0019
	2-NpMe			9-AnMe		
1	A'	2.43	0.0020	A_1	1.95	0.0003
2	A'	3.11	0.0389	A_1	2.76	0.0889
3	A'	3.15	0.0172	B_2	2.80	0.0006
4	A'	3.41	0.0046	A_1	3.13	0.0032
5	A'	3.94	0.0001	B_2	3.20	0.0013
6	A'	4.15	0.1629	B_2	3.39	0.1319
7	A''	4.23	0.0014	B_2	3.63	0.0696
8	A''	4.51	0.0042	B_2	3.87	0.0009

Table 5.2: $D_n \leftarrow D_0$ vertical electronic transition energies, T_{TD-M06}, and oscillator strengths, f, calculated at the TD-M06/6-311++G(d,p) level of theory. The symmetry of the transition moment is given as $\Gamma_{\mu_{n0}}$.

n	$\Gamma_{\mu_{n0}}$	T_{TD-M06} (eV)	f	$\Gamma_{\mu_{n0}}$	T_{TD-M06} (eV)	f
	1-PPr			1-NpMe		
1	A'	3.02	0.0223	A'	2.53	0.0006
2	A'	3.17	0.0039	A'	3.02	0.0003
3	A''	3.38	0.0000	A'	3.36	0.1033
4	A''	3.70	0.0000	A''	3.46	0.0019
5	A'	3.82	0.0144	A'	3.61	0.0136
6	A''	3.96	0.0006	A'	3.65	0.0672
7	A''	4.03	0.0022	A''	3.69	0.0011
8	A'	4.14	0.2169	A''	3.76	0.0000
	2-NpMe			9-AnMe		
1	A'	2.48	0.0025	A_1	2.05	0.0004
2	A'	3.11	0.0006	B_2	2.83	0.0008
3	A'	3.20	0.0589	A_1	2.85	0.0912
4	A'	3.41	0.0060	A_1	3.18	0.0058
5	A''	3.52	0.0007	B_2	3.25	0.0015
6	A''	3.78	0.0002	B_1	3.28	0.0023
7	A''	3.79	0.0021	B_1	3.47	0.0017
8	A'	3.93	0.0001	A_2	3.51	0.0000

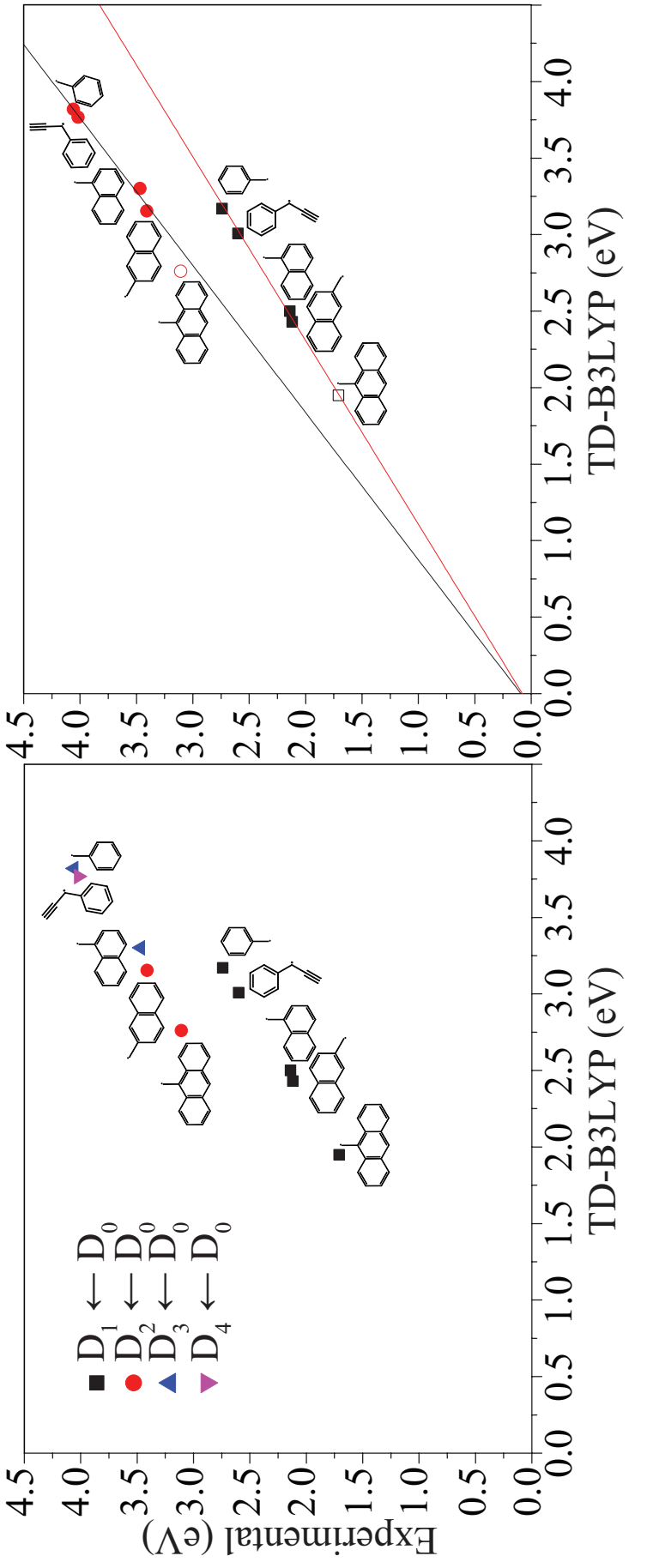

Figure 5.5: Plot of calculated TD-B3LYP vertical excitation energies against observed transitions; Includes excited states of benzyl, 1-PPr, 1-NpMe, 2-NpMe and 9-AnMe. 9-AnMe data was not available at time of initial calculation and is excluded from linear fit but shown for reference

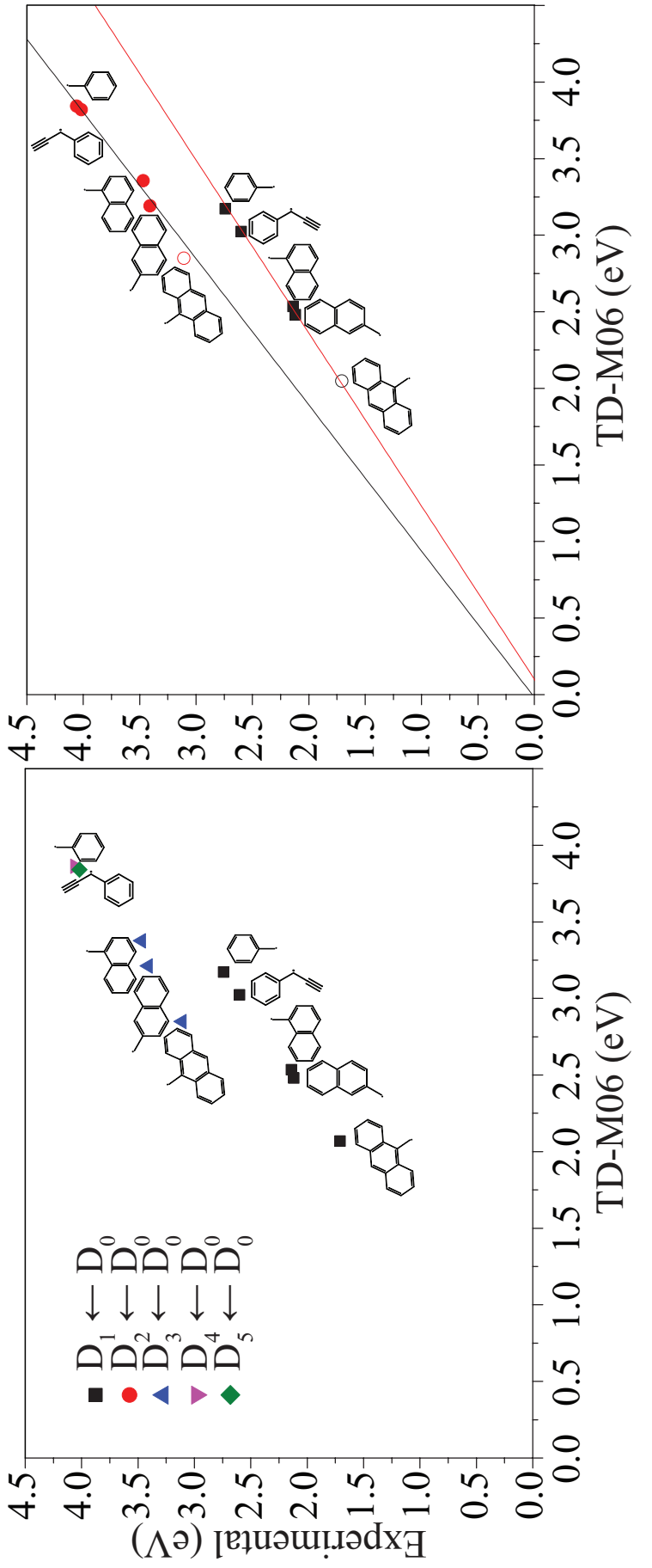

Figure 5.6: Plot of calculated TD-M06 vertical excitation energies against observed transitions; Includes excited states of benzyl, 1-PPr, 1-NpMe, 2-NpMe and 9-AnMe. 9-AnMe data was not available at time of initial calculation and is excluded from linear fit but shown for reference

Table 5.3: TD-B3LYP/6-311++G(d,p) calculated excitation energies of lowest strong ($f > 10^{-2}$) electronic transition. Scaled values obtained by linear fit to experimental data for benzyl, 1-NpMe and 2-NpMe (See Figure 5.5). 9-AnMe experimental results not used in fit, as this transition was discovered after initial calculations.

Molecule	trans.	$\Gamma_{\mu_{n0}}$	T_{B3LYP}	T_{scaled}	Expt.	Δ_E
benzyl	$D_3 \leftarrow D_0$	B_2	3.82	4.05	4.06[186]	-0.01
1-PPr	$D_4 \leftarrow D_0$	A'	3.77	4.00	4.02	-0.02
1-NpMe	$D_3 \leftarrow D_0$	A'	3.30	3.55	3.47	0.08
2-NpMe	$D_2 \leftarrow D_0$	A'	3.11	3.36	3.41	0.05
9-AnMe	$D_2 \leftarrow D_0$	A_1	2.76	3.02	3.11†	-0.09

Table 5.4: TD-M06/6-311++G(d,p) calculated excitation energies of lowest strong ($f > 10^{-2}$) electronic transition. Scaled values obtained by linear fit to experimental data for benzyl, 1-NpMe and 2-NpMe (See Figure 5.6). 9-AnMe experimental results not used in fit, as this transition was discovered after initial calculations.

Molecule	trans.	$\Gamma_{\mu_{n0}}$	T_{M06}	T_{scaled}	Expt.	Δ_E
benzyl	$D_4 \leftarrow D_0$	B_2	3.84	4.06	4.06[186]	0.00
1-PPr	$D_5 \leftarrow D_0$	A'	3.82	4.02	4.02	0.00
1-NpMe	$D_3 \leftarrow D_0$	A'	3.36	3.54	3.47	0.07
2-NpMe	$D_3 \leftarrow D_0$	A'	3.20	3.37	3.41	-0.04
9-AnMe	$D_3 \leftarrow D_0$	A_1	2.85	3.00	3.11†	-0.11

Table 5.5: Vertical excitation energies in cm^{-1} and (eV), and occilator strengths for observed higher excited state of 9-AnMe.

Method	T_v	f	Transition
TD-B3LYP	22264 (2.76)	0.0889	$D_2 \leftarrow D_0$
Scaled TD-B3LYP[a]	24324 (3.02)	0.0889	$D_2 \leftarrow D_0$
TD-M06	22992 (2.85)	0.0913	$D_3 \leftarrow D_0$
Scaled TD-M06[b]	24279 (3.01)	0.0913	$D_3 \leftarrow D_0$

a See Figure 5.5 and Table 5.3
b See Figure 5.6 and Table 5.4

The extrapolated trend was used to predict the excitation energy of the first transition of 9-AnMe with oscillator strength greater than $f = 10^{-2}$. TD-B3LYP assigns this transition as $D_2 \leftarrow D_0$ and TD-M06 as $D_3 \leftarrow D_0$. The scaled and unscaled energies are displayed in Table 5.5.

The observed transition energy for this higher excited state of 9-AnMe is 0.09 eV greater than the value extrapolated from TD-B3LYP and 0.11 eV above value extrapolated from TD-M06. However, this error is still small enough that these calculations proved to be a useful guide to the experiments. Data from larger molecules would be required to determine if this error is due to the trend becoming non-linear.

Including 9-AnMe in the linear fits gives corrected TD-DFT equations $T_{exp} = 0.911 T_{TD-B3LYP} +$

Table 5.6: TD-B3LYP/6-311++G(d,p) calculated excitation energies of lowest strong ($f > 10^{-2}$) electronic transition. Scaled values obtained by linear fit to experimental data for benzyl, 1-NpMe and 2-NpMe (See Figure 5.5). 9-AnMe results used in fit

Molecule	trans.	$\Gamma_{\mu_{n0}}$	T_{B3LYP}	T_{scaled}	Expt.	Δ_E
benzyl	$D_3 \leftarrow D_0$	B_2	3.82	4.04	4.06[186]	-0.02
1-PPr	$D_4 \leftarrow D_0$	A'	3.77	3.99	4.02	-0.03
1-NpMe	$D_3 \leftarrow D_0$	A'	3.30	3.57	3.47	0.10
2-NpMe	$D_2 \leftarrow D_0$	A'	3.11	3.39	3.41	-0.02
9-AnMe	$D_2 \leftarrow D_0$	A_1	2.76	3.08	3.11	-0.03

Table 5.7: TD-M06/6-311++G(d,p) calculated excitation energies of lowest strong ($f > 10^{-2}$) electronic transition. Scaled values obtained by linear fit to experimental data for benzyl, 1-NpMe and 2-NpMe (See Figure 5.6). 9-AnMe results used in fit

Molecule	trans.	$\Gamma_{\mu_{n0}}$	T_{M06}	T_{scaled}	Expt.	Δ_E
benzyl	$D_4 \leftarrow D_0$	B_2	3.84	4.04	4.06[186]	0.02
1-PPr	$D_5 \leftarrow D_0$	A'	3.82	4.00	4.02	0.02
1-NpMe	$D_3 \leftarrow D_0$	A'	3.36	3.56	3.47	0.09
2-NpMe	$D_3 \leftarrow D_0$	A'	3.20	3.41	3.41	0.00
9-AnMe	$D_3 \leftarrow D_0$	A_1	2.85	3.07	3.11	-0.04

0.561 with an R^2 value of 0.982 for TD-B3LYP and $T_{exp} = 0.958T_{TD-M06} + 0.341$ with an R^2 value of 0.985 for TD-M06. The recalculated corrected results are shown in Tables 5.6 and 5.7, with the maximum observed error 0.10 eV.

TD-B3LYP and TD-M06 disagree significantly in their numerical assignment of these states, due to minor inconsistency in the results for weaker unobserved states. This does not effect the nature or configuration of the observed states. However, the vastly different treatment of the weak $D_1 \leftarrow D_0$ transitions and the strong $D_n \leftarrow D_0$ transitions makes these methods unsuitable for assigning and calculating multiple higher-excited states, as will be done in Chapters 6 and 7. In the hopes of developing a method that treats the excited-states equally, and to better determine the ordering of the observed higher-excited states for accurate assignment, *ab-initio* X-MCQDPT2 techniques were used.

5.5.4.2 *Ab-initio* Excitation Energies

The vertical excitation energies and transition moments were calculated by Professor Timothy Schmidt using the X-MCQDPT2 method.

Table 5.8: Vertical excitation energies, in cm^{-1}, (and transition moments , in ea_0, shown in brackets) for benzyl radical calculated by the X-MCQDPT2 method and various basis sets.

State	Exp.[a]	tzv(2df,p)	tzv(2d,p)	tzv(d,p)
D_1	22002	22450 (0.11)	22434 (0.10)	23133 (0.10)
D_2	22850	23459 (0.06)	23379 (0.05)	23673 (0.06)
D_3	32760	32898 (0.58)	32965 (0.58)	34412 (0.59)
D_4	39200	38820 (0.13)	38691 (0.11)	39526 (0.12)

a Origin transition[186,190–192,348]

Table 5.9: Vertical excitation energies, in cm^{-1}, (and transition moments , in ea_0) for various radicals calculated by the X-MCQDPT2 method.

	Radical							
	1-NpMe		2-NpMe		1-PPr		9-AnMe	
State	Exp.[a]	tzv(2d,p)	Exp.[a]	tzv(2d,p)	Exp.[a]	tzv(2d,p)	Exp.[a]	tzv(2d,p)
D_1	17240[b]	16895 (0.10)	17134[b]	16270 (0.13)	21006[c]	19236 (0.21)	13757[d]	12906 (0.09)
D_2		21102 (0.08)		22374 (0.15)		21063 (0.15)		18084 (0.26)
D_3	27993	29447 (1.36)	27478[e]	26208 (0.73)	32437	31100 (0.42)	25063	22454 (1.78)
D_4		29616 (1.27)		29516 (0.05)		37002 (0.14)		26496 (1.38)

a Origin transition *b* Reference[183] *c* Reference[193] *d* Reference[185] *e* Assignment uncertain

Initially, the vertical excitation energies were computed for four electronically excited states of the benzyl radical, given in Table 5.8. The correlation between experimental and calculated values for these states show a clear linear trend for all basis sets when fitted with a fixed intercept at the origin (see Figure 5.7).

The transition moments obtained with the various basis sets were found to be consistent, with the strongest transition emphatically determined to be the $D_3 \leftarrow D_0$ with all bases. The level of theory chosen to calculate the larger radicals was the X-MCQDPT2/tzv(2d,p) level, which exhibited a slope (intercept) of 0.95 (1710). What is important for the present purposes, is that the correlation between calculated and measured state is clear. This is illustrated in Figure 5.7, where it can be seen that the two highest-quality basis sets yielded results close to the line $x = y$.

The calculated vertical excitation energies for the 1-NpMe, 2-NpMe, 1-PPr and 9-AnMe radicals are given in Table 5.9. For all radicals, the $D_3 \leftarrow D_0$ transition is calculated to be strong, with the $D_4 \leftarrow D_0$ transition also calculated to be strong for 1-NpMe and 9-AnMe. Discussion of these calculations, in the context of the observed spectra, is given below. Due to the relative success of this technique in assigning higher excited states, it was adopted by the author for use on higher excited states of radical cations in Chapters 6 and 7.

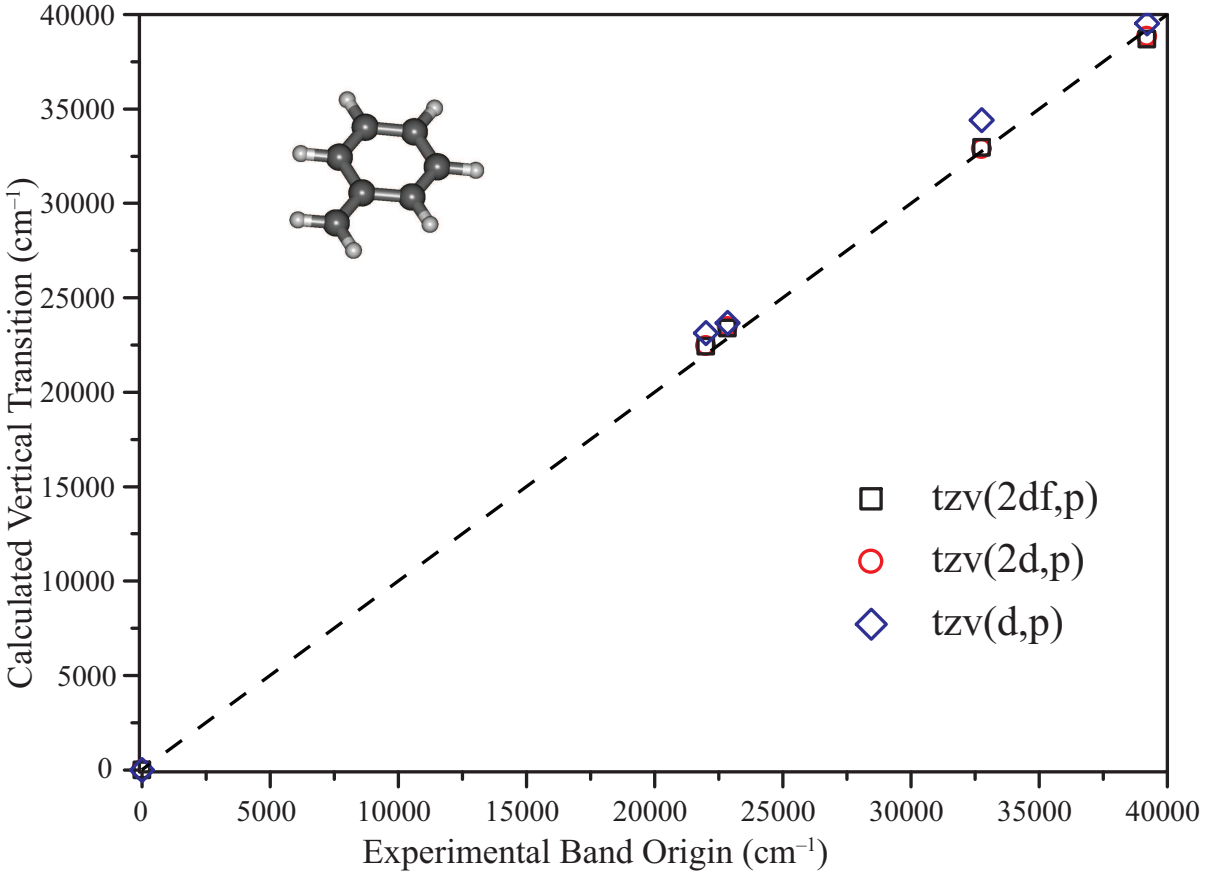

Figure 5.7: Calculated vertical transition energies of benzyl radical, in cm^{-1}, compared to experimental band origins, for different basis sets at the [5,5] X-MCQDPT2 level of theory. The function $x = y$ is given as dashed line.

5.6 Discussion

5.6.1 Comparison with Matrix Spectra

Matrix isolation spectra of 1-NpMe and 2-NpMe have been observed in a 6 K neon matrix by Nagy, Fulara and Maier.[271] They attributed a band at 28011 cm^{-1} to the $3^2A' \leftarrow X^2A''$ transition of 1-NpMe. This is just 18 cm^{-1} to the blue of our observed band, and well within its observed width. Nagy *et al.* reported the $6^2A' \leftarrow X^2A''$ transition of 2-NpMe to lie at 27293 cm^{-1}, similarly close to the band located by us at 27478 cm^{-1}, featuring a shift of 185 cm^{-1} to the red of our observed band. Again, the observed matrix band was found to be within the FWHM of the gas-phase band (290 cm^{-1}). A search was undertaken to locate the weaker band, attributed by Nagy *et al.* to the $2^2A' \leftarrow X^2A''$ transition, at 21177 cm^{-1}, but no depletion signal was observed in this region. The observed FWHMs of the gas-phase bands are both about 290 cm^{-1}, which appears, *prima facie*, to be similar to the matrix spectra. However, the spectra obtained by Nagy *et al.* exhibit resolved bands,

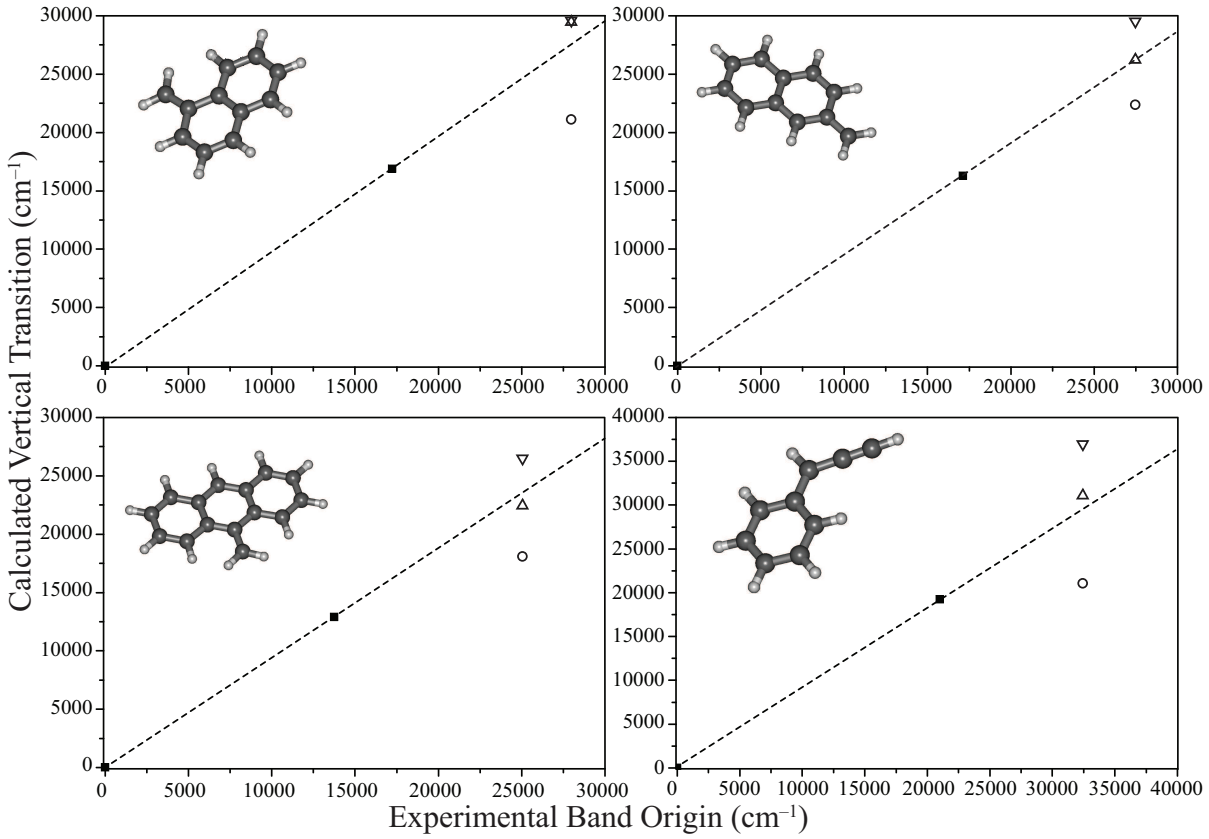

Figure 5.8: Calculated vertical transition energies (X-MCQDPT2/tzv(2d,p)), in cm^{-1}, compared to experimental band origins, for different radicals. Dashed lines are drawn through the origin and the previously determined lowest energy transition ($D_1 - \blacksquare$), with the calculated higher transitions, $D_n \leftarrow D_0$, $n > 1$, plotted at the experimentally determined band energy. Key: $D_2 - \bigcirc$, $D_3 - \triangle$, $D_4 - \nabla$

whereas the presently obtained spectra do not show regions of zero depletion between the spectroscopic features, possibly pointing to residual saturation of weaker features. It is worth noting that the excited state symmetries reported by Nagy *et al.* are incorrect, possibly due confusion between the symmetries of the transitions (which are A') and the excited states (which should be A'').[271]

5.6.2 Comparison with *Ab-initio* Calculations

Figure 5.8 shows the calculated vertical transitions for the radicals shown in Figure 5.2. For all four radicals, the $D_1 \leftarrow D_0$ transition is known and served as a point of reference.[183,185,193] A dashed line is drawn through the origin, and the point corresponding to the $D_1 \leftarrow D_0$ transition, and is extrapolated to high energy. For the benzyl radical, a very good linear correlation was observed between calculated vertical transitions and experimental band origins at the X-MCQDPT2/vtz(2d,p) level (Figure 5.7). As this fit has a

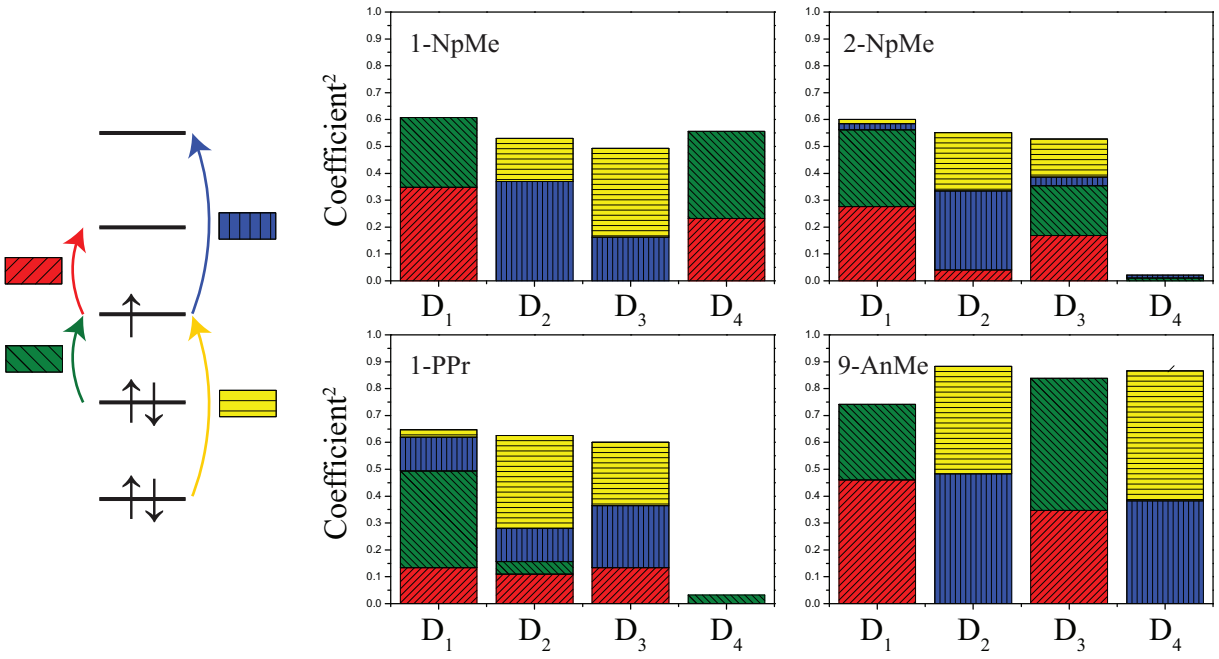

Figure 5.9: Pictorial representation of the nature of the excited states calculated by CAS-CI.

fixed intercept at the origin, the linear extrapolation indicated by the dashed line in Figure 5.8 should intercept the observed state at the experimental energy.

In Figure 5.8, it is seen that reasonable agreement is obtained for the calculated transition energies of both the D_3 ($4^2A''$) and D_4 ($5^2A''$) states of the 1-NpMe radical with the observed transition at 27993 cm^{-1}. And, as seen in Table 5.9, both of these transitions are calculated to be strong. As such, for this radical, the assignment of the observed band remains uncertain.

However, for 2-NpMe, there is unambiguous agreement between the calculated properties of the $D_3 \leftarrow D_0$ ($4^2A'' \leftarrow X^2A''$) transition and the observed band. Its position agrees with the extrapolation from the $D_1 \leftarrow D_0$ transition (Figure 5.8) and it is the strongest transition calculated (Table 5.9). Similarly for 1-PPr and 9-AnMe, the calculated band positions and strengths agree with the designation $D_3 \leftarrow D_0$, respectively $4^2A'' \leftarrow X^2A''$ and $3^2B_1 \leftarrow X^2B_1$.

5.6.3 Comparison to Longuet-Higgins Model

The squared coefficients of excited configurations, corresponding to low-energy single electron excitations, describing the excited states of the radicals are shown in Figure 5.9. The states were calculated at the CAS-CI level, with the same ROHF orbitals used for the X-MCQDPT2 calculations. Since the radicals derive from cyclic systems, the fully-occupied

orbitals shown on the left of Figure 5.9 are close in energy, and thus we must take account of two sets of transitions, degenerate at the Hückel level, to describe low-lying states.

The character of the excited states of 1-NpMe follows the Longuet-Higgins model. The leading configurations of the D_1 state are given by the excitations into and out of the singly occupied orbital respectively from, and to, the next lowest, and next highest energy orbital. These configurations make up 60 % of the state. The state calculated as D_4 is also dominated by these transitions, but whereas both coefficients of D_1 are positive, the D_4 state combines the configurations with opposite sign. Similarly, the D_2 and D_3 states are described by even and odd combinations of the excitations into, and out, of the singly occupied orbital respectively from, and to, the second highest fully occupied orbital and second lowest vacant orbital.

In contrast to 1-NpMe, the description of the excited states of 2-NpMe is less straightforward. While the D_1 and D_2 states are similarly described to 1-NpMe, the D_3 state as calculated contains significant character from all excitations drawn in Figure 5.9. This may be due to significant mixing between the higher energy states. The D_4 state, as calculated, contains little character from the one-electron excitations under consideration, which is consistent with its low calculated oscillator strength.

The 1-PPr radical exhibits a somewhat more complicated D_1 state, but it is still primarily described by the same four one-electron excitations. It is worth noting that the $D_1 \leftarrow D_0$ transition of 1-PPr is calculated to be a strong transition.

The states calculated as D_2 and D_3 exhibit the pairing shown by 1-NpMe, with the oscillator strength largely carried by $D_3 \leftarrow D_0$. As with 2-NpMe, the D_4 state is not well described by the electronic excitations under consideration.

Lastly, 9-AnMe, with C_{2v} symmetry, is more highly constrained in which excitations may contribute to a given electronically excited state. As such, D_1 and D_3, both being of B_1 symmetry, form a pair of states of low and high transition strength respectively (from D_0). They are both primarily described by the two lowest energy one-electron excitations. The states D_2 and D_4 form another pair, of A_2 symmetry, described by the other pair of one-electron excitations. As with D_1 and D_3, D_2 and D_4 the transitions are respectively weak and strong from D_0.

Table 5.10: Excited state energies (in cm^{-1}) and lifetimes. $D_2 \leftarrow D_0$ values estimated from X-MCQDPT2/tzv(2d,p)[5,5] values provided by Prof. Timothy Schmidt, used for determining energy gap $\Delta E_{D_3-D_2}$. Tabulated FWHM is for $D_3 \leftarrow D_0$ transitions recorded in this chapter.

Molecule	$D_1 \leftarrow D_0$	τ_{D_1} (ns)	$D_2 \leftarrow D_0$	$D_3 \leftarrow D_0$	$\Delta E_{D_3-D_2}$	FWHM	τ_{D_3} (fs)
1-PPr	21006	300	21063	32437	11374	149	36
1-NpMe	17240	20	21102	27993	6891	292	18
2-NpMe	17134	20	22374	27478	5104	290	18
9-AnMe	13757	4	18084	25063	6979	326	16

5.6.4 Astronomical Relevance

The broadest DIB so far reported, centered on 4428.83 Å as observed in HD 183143, has a FWHM of 115 cm^{-1}.[145] All bands reported in this chapter are significantly broader than this DIB. The transitions observed in this chapter are also significantly broader than the $D_2 \leftarrow D_0$ spectra of radical cations of similar size – naphthalenium and anthracenium are reported to have gas-phase FWHMs of 25 cm^{-1} and 94 cm^{-1}, respectively.[205,206]

The lorentzian profile of the observed bands suggests lifetime broadening. The lifetime of a state, Δt, can be directly calculated from the FWHM of the associated band, ΔE, by the Heisenberg relation

$$\Delta t = \hbar/\Delta E. \tag{5.1}$$

The widths of the observed transitions, and the lifetimes of their corresponding higher excited state, are listed in Table 5.10. A trend is observed of decreasing lifetime as the molecule (and its chromophore) increases in size and decreases in transition energy. This is consistent with the energy-gap law.[349,350]

As the energy-gap between the states decreases, so does the lifetime of the state. This trend is also observed for the D_1 states of these molecules (Table 5.10).[183,185,193]

A simplified form of the energy gap law may be written

$$\tau \propto e^{(\frac{\gamma}{\hbar\omega}\Delta E)} \tag{5.2}$$

where γ is a term that can be expressed in molecular parameters and ω is related to the available vibrational modes, relating to the wavefunction overlap and density of states.[351]

Figure 5.10 shows that plotting time against ΔE gives an exponential fit of the form $\tau = 1.06 \times 10^{-13} e^{\Delta E/1414}$. Plotting τ on a logarithmic scale shows that D_1 and D_3 actually follow two slightly different trends, as seen in Figure 5.11. This anomaly can be explained,

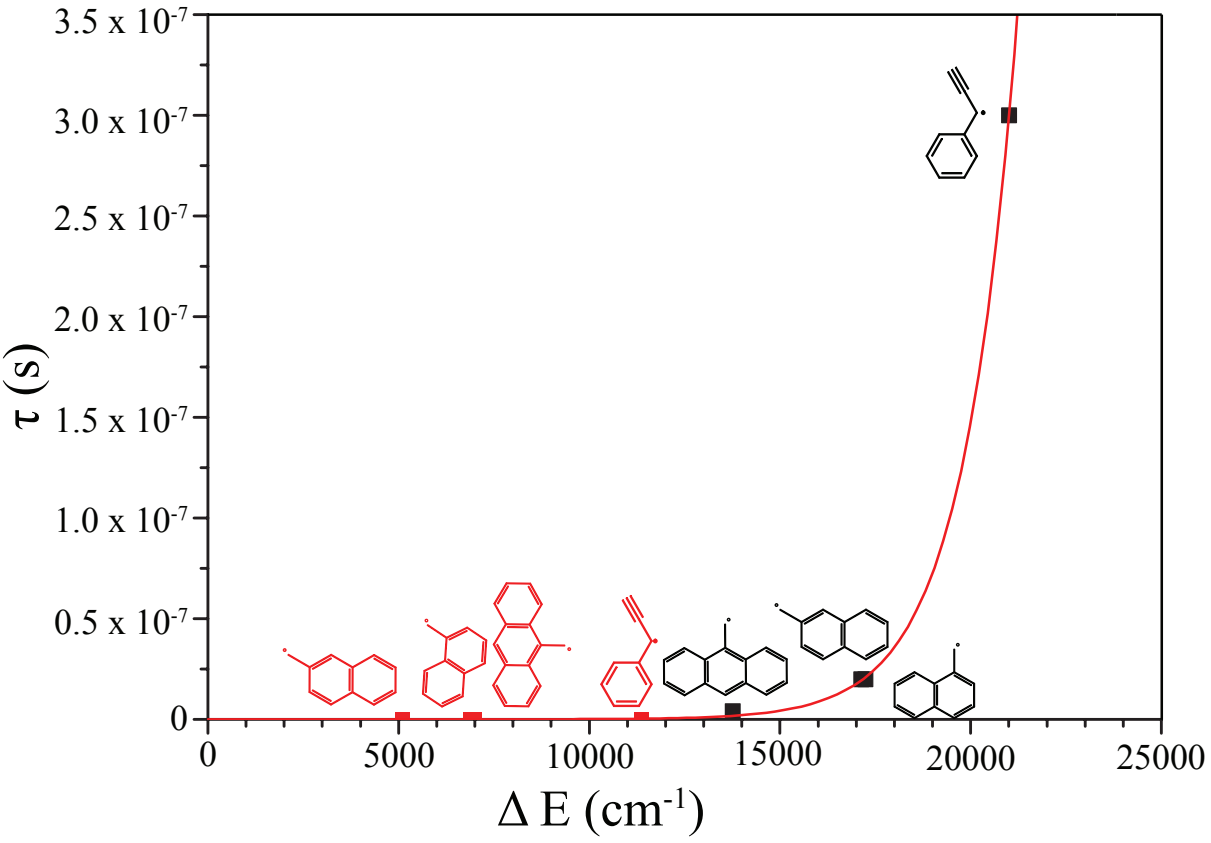

Figure 5.10: Plot of energy gap against state lifetime for D_1 (black) and D_3 (red) states of 1-PyMe, 1-NpMe, 2-NpMe and 9-AnMe.

as D_3 will also have some decay directly to D_1 and D_0, which would further suppress the lifetime of that state.

These observed trends of decreasing lifetime with increasing chromophore size suggests that the visible strong transitions of still larger radicals of the same type will be even broader than those reported in this chapter, and significantly broader than any observed DIB. It can therefore be concluded that transitions to higher excited states of cold aromatic hydrocarbon RSRs are not responsible for the DIBs. As these strong transitions are the most likely to be observed, neutral PAH RSRs can be largely put aside as potential DIB carriers.

5.7 Conclusions

The spectra of $D_n \leftarrow D_0$ transitions of the 1-Npme, 2-NpMe, and 1-PPr radicals were obtained by double resonance spectroscopy, and that of 9-AnMe was obtained by R2C2PI spectroscopy with delayed ionization. From a comparison of calculated vertical transition

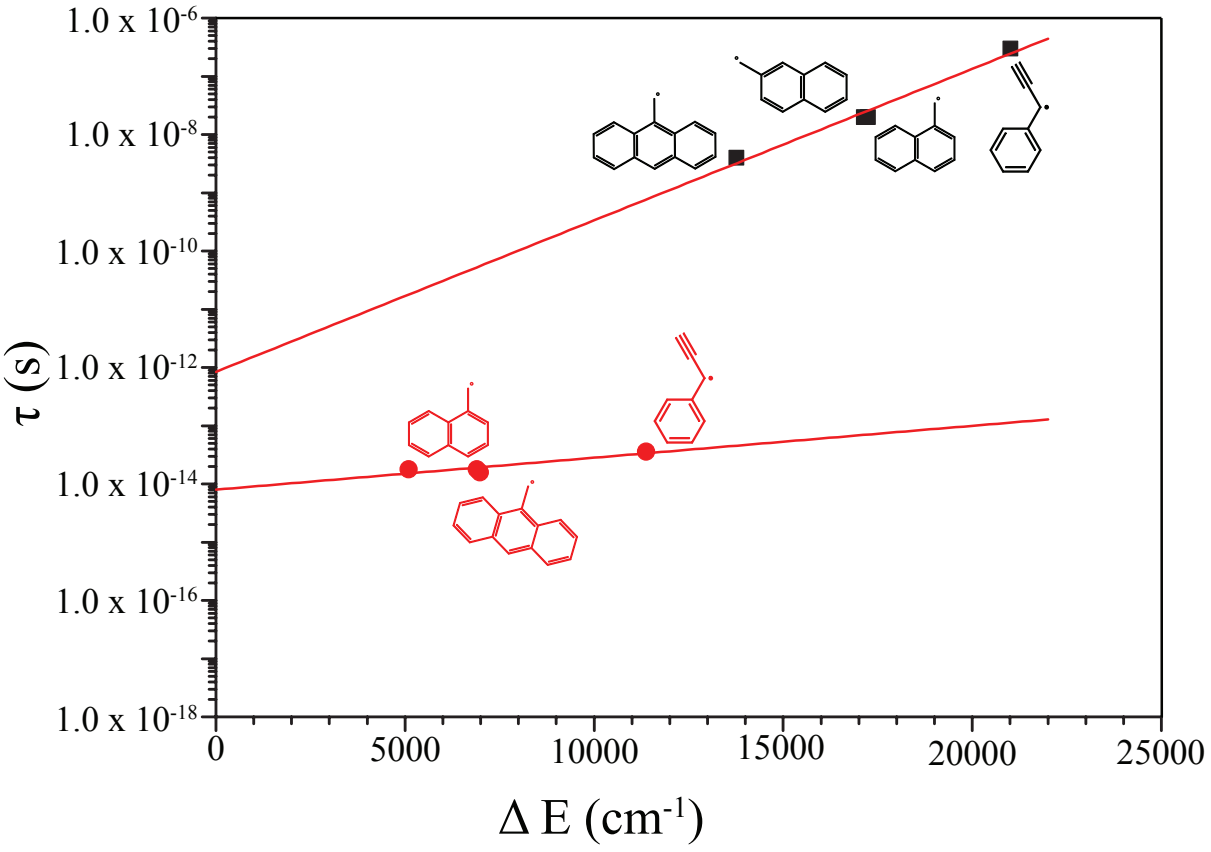

Figure 5.11: Plot of energy gap against state lifetime for D_1 (black) and D_3 (red) states of 1-PyMe, 1-NpMe, 2-NpMe and 9-AnMe

energies at the X-MCQDPT2/vtz(2d,p) level and observed bands, it was concluded that the observed transitions were to the D_3 states of 2-NpMe, 1-PPr and 9-AnMe, and to either or both of the D_3 and D_4 states of the 1-NpMe radical. These states were found to be largely consistent with configurational mixing according to the Longuet-Higgins model, but with complications arising for the higher excited-states of molecules of lower symmetry. The observed widths of these bands, which increased with decreasing transition energy, indicated severe lifetime broadening which from a phenomenological standpoint rules out larger examples of this class of radical as carriers of the diffuse interstellar bands.

Chapter 6

Transitions of Radical Cations: 9-MethylAnthracenium$^+$ ($C_{15}H_{12}$)

6.1 Author's Note

The photodissociation experiments reported in this chapter and Chapter 7 were undertaken by the author while working with the Bieske Research Group from the School of Chemistry at The University of Melbourne. The author would like to acknowledge J. A. Sanelli and V. Dryza for assistance in learning to operate the photodissociation spectrometer. J. A. Sanelli also assisted in the recording of the reported spectra.

6.2 Introduction

Sonnentrucker *et. al.* present evidence that the carriers of the λ5797 Å and λ6613 Å DIBs have IEs above 10 eV.[149] As such, if these bands were carried by PAH species, they must be in a cationic state. Indeed, due to the harsh ionising radiation of the interstellar medium, it is likely that many unassigned interstellar transitions are carried by positively charged hydrocarbon molecules. Many cations have already been observed in the ISM, as seen in Table 1.1.

The ionization energies of RSRs are rather low, in the $6-7$ eV range, and in the interstellar medium such species might be expected to exist in the cationic form.[352] In the cationic form, only one of the transitions depicted in Figure 5.1 is available. As such, these closed-shell cations of resonance-stabilized radicals tend to have $S_1 \leftarrow S_0$ transitions at a slightly

higher energy than the radical $D_1 \leftarrow D_0$ transition, with significantly stronger transition moments. These closed-shell cations will be discussed in Chapter 7.

Ionisation of a neutral closed-shell PAH results in a radical-cation, and these can be resonance stabilised in the same manner as neutral RSRs. Being cations, these molecules have high second-IEs and would be stable in the harsh radiation environment of the interstellar medium due to the energy required to remove a second electron. PAH radical cations have been previously observed in the gas-phase through cavity ring down,[206,353] and photodissociation spectroscopy.[205,354,355] Radical-cations are experimentally easier to produce than closed shell cations as they can be formed by ionising atmospherically stable closed-shell PAHs such as naphthalene, anthracane and pyrene, requiring no atomic rearrangement or bond fission.

Small PAH radical cations tend to have weak NIR $D_1 \leftarrow D_0$ transitions and very strong, broad, visible $D_2 \leftarrow D_0$ transition. For example Sukhorukov *et. al.* reports the gas-phase $D_2 \leftarrow D_0$ transition of the naphthalenium$^+$ radical cation has energy 14909 cm^{-1} and a FWHM of 36 cm^{-1}.[206] Sukhorukov *et. al.* also report the anthracenium$^+$ $D_2 \leftarrow D_0$ transition has energy 14109 cm^{-1} and a FWHM of 94 cm^{-1}.[206]

While generally these strong $D_2 \leftarrow D_0$ transitions are considered too broad to be carriers of the DIBs, as discussed in Chapter 1, they have been suggested as carriers of some of the broader DIBs. In particular, the naphthalenium$^+$ cation (Np$^+$) was suggested as a possible carrier of the broad λ6488 Å and λ6707 Å DIBs.[178,180] However, subsequent astronomical observations have largely disproved this hypothesis.[181,182] It had also been suggested that a species related to the pyrenium$^+$ radical cation (Py$^+$) may be responsible for the 4430 Å DIB, based on matrix isolation spectra.[179] However, subsequent gas-phase measurements have eliminated Py$^+$ as a potential carrier of this DIB.[356]

A comparison of the argon-tagged photodissociation spectra of Np$^+$[205] and the methylnaphthalenium$^+$ radical cations (1-MeNp$^+$ and 2-MeNp$^+$) have been reported in a paper by Friha *et. al.*[324] These spectra show that the electronic and vibronic structure of these molecules are very similar. The 1-MeNp$^+$ and 2-MeNp$^+$ transitions observed are slightly red-shifted compared to the corresponding Np$^+$ bands. The bands also appear broader due to unresolved methyl-rotor structure, which has been simulated well by Friha *et. al.*[324]

Electronic spectra of the related anthracenium$^+$ radical cation (An$^+$) has been previously published. The $D_2 \leftarrow D_0$ transition of An$^+$ has been observed in the gas-phase using cavity ring-down spectroscopy by Sukhorukov *et. al.*[206] Several states of An$^+$ have also been observed through photoelectron spectroscopy[357,358] and matrix isolation techniques.[358]

The experiments reported in this chapter were originally motivated by a search for the 9-anthracenylmethylium$^+$ (9-AnMe$^+$) closed-shell cation, which is the ionised form of the 9-AnMe radical, which was observed in Chapters 4 and 5. However, limitations in the resolution of the quadrupole mass-filters did not allow the 9-AnMe$^+$ spectrum to be observed due to the abundance of 9-methylanthracenium (9-MeAn$^+$) radical cation, which is the ionised form of the 9-methylanthracene (9-MeAn) parent. As 9-MeAn$^+$ is an interesting molecule in its own right, the spectrum was recorded and is assigned in this chapter with reference to *ab-initio* and TD-B3LYP levels of theory. Several of the observed electronic transitions have not been previously observed or assigned either for 9-AnMe$^+$ or the spectroscopically similar An$^+$. Additionally, the vibronic structure of the NIR $D_1 \leftarrow D_0$ transition has not been previously reported or assigned in either 9-MeAn$^+$ or An$^+$.

6.2.1 Experimental Methods

The argon tagged spectrum of the 9-MeAn$^+$ radical cation was recorded using the photodissociation spectrometer previously described in Chapter 3. As in Chapters 4 and 5, commercially available 9-MeAn was heated in argon behind the pulsed nozzle, seeding the argon with 9-MeAn. An electrospray source was used to create weakly bound 9-MeAn$^+ \cdots$ Ar van der Waals clusters which were then cooled in the free-jet expansion and skimmed before being guided into the first quadrupole mass filter by ion optics.

The first quadrupole mass filter (preceding the octapole photodissociation region) was set to the 232 m/z of the 9-MeAn$^+ \cdots$ Ar cluster, while the second mass filter was set to the 192 m/z of the bare 9-MeAn$^+$ radical cation. When the 9-MeAn$^+ \cdots$ Ar clusters absorb photons and fragment, signal is observed by the increased observation of 9-MeAn$^+$. Wavelength calibration was provided by an Ocean Optics spectrograph. Tunable dissociation photons were provided by an OPOTek Vibrant optical parametric oscillator (OPO) pumped by the 3rd harmonic of a Nd:YAG laser. The spectrum was recorded from 8000 cm^{-1} to 44444 cm^{-1}. There is a region missing around 25000 cm^{-1}where the OPOTek Vibrant does not provide good power.

Laser power was recorded and all spectra shown are power-corrected. However, conditions may have fluctuated between scans, and the relative intensities observed for transitions in different scanning regions should be considered only approximate.

It is important to note that excitation energies obtained in this manner are not true gas-phase values, with the weakly bonded argon red-shifting the spectrum slightly. This shift has been shown to be small for PAH radical cations.[205,324] For example, complexing with

a single argon atom was shown by Pino *et. al.* to redshift the $D_2 \leftarrow D_0$ origin of Np^+ by $43\,cm^{-1}$,[205] and Friha *et. al* show 1-MeNp$^+$ and 2-MeNp$^+$ red-shifted by $10\,cm^{-1}$ and $19\,cm^{-1}$ respectively.[324] However, while small, these solvent shift effects must be accounted for if photodissociation spectra is to be compared to astronomical spectra.

6.3 Theoretical Methods

The computational methods used in this chapter are described in detail in Chapter 2 and are similar to those carried out in Chapters 4 and 5. The quantum chemical calculations of ground and excited-state geometries and vibrational frequencies were carried out with B3LYP and TD-B3LYP respectively,[231,232] using the 6-311++G(d,p) basis set.

Vertical excitation energies and intensities for the 20 lowest-energy calculated electronic doublet states (including the ground state) were calculated at the X-MCQDPT2 levels of theory.[346] The *ab-initio* X-MCQDPT2 calculations were performed with an active space of 9 electrons in 9 orbitals, in conjunction with the tzv(2d,p) basis set. These are similar to the calculations performed in Chapters 5.

The B3LYP and TD-B3LYP calculations were carried out using the GAUSSIAN09[221] suites of software, wheras the X-MCQDPT2 calculations were performed in the FIREFLY package.[222,347]

6.4 Assignment of the Argon-Tagged 9-MeAn$^+$ Photodissociation Spectrum

6.4.1 Electronic Spectrum

The argon tagged 9-MeAn$^+$ photodissociation spectrum is displayed in Figure 6.1. The spectrum features a weak electronic transition in the NIR, featuring well resolved vibrational structure, three very strong electronic transitions (one in the visible and two others in the UV), and numerous other transitions of varying structure, width and intensity. Based on changes in band profile and intensity, seven suspected electronic origin bands are observed, and these are labelled in Figure 6.2. As expected, the visible and near-UV regions bear a strong resemblance to the previously recorded spectrum of the An$^+$ radical cation.[358]

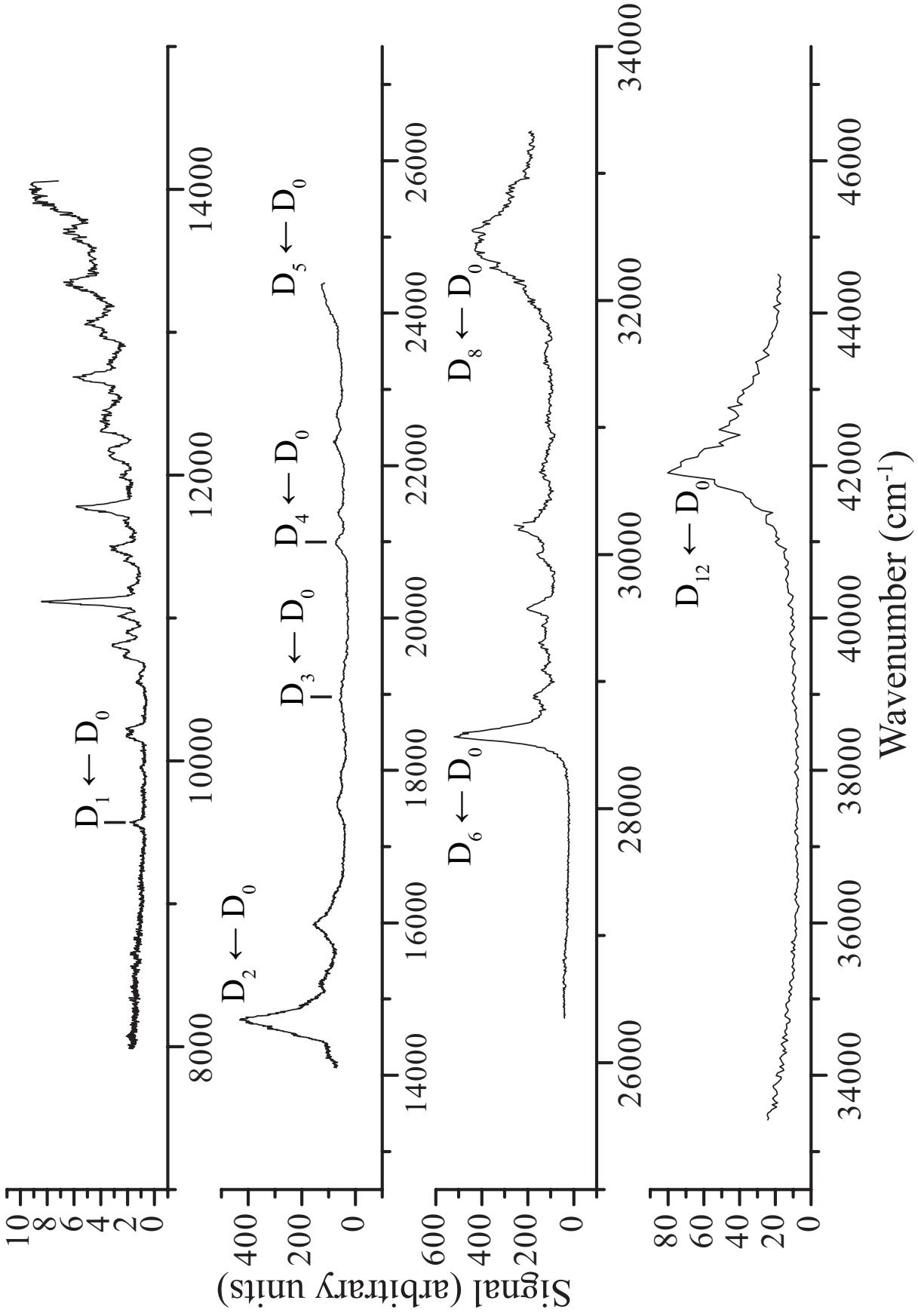

Figure 6.1: Photodissociation spectrum of argon-tagged 9-MeAn$^+$ radical cation.

Table 6.1: *Ab-initio* vertical excitation energies (T_v in cm^{-1}) and transition dipole moments (μ^2 in $Debye^2$) calculated at the X-MCQDPT2[9,9]/tzv(2d,p) level of theory.

Transition	T_v	μ^2	Transition	T_v	μ^2
$D_1 \leftarrow D_0$	8408	0.003	$D_{11} \leftarrow D_0$	35457	0.001
$D_2 \leftarrow D_0$	12064	0.474	$D_{12} \leftarrow D_0$	35613	0.017
$D_3 \leftarrow D_0$	16375	0.048	$D_{13} \leftarrow D_0$	37001	0.005
$D_4 \leftarrow D_0$	18368	0.030	$D_{14} \leftarrow D_0$	39803	1.545
$D_5 \leftarrow D_0$	20668	0.129	$D_{15} \leftarrow D_0$	40091	0.000
$D_6 \leftarrow D_0$	26478	0.552	$D_{16} \leftarrow D_0$	41548	0.000
$D_7 \leftarrow D_0$	28714	0.013	$D_{17} \leftarrow D_0$	42254	0.008
$D_8 \leftarrow D_0$	29163	0.468	$D_{18} \leftarrow D_0$	42564	0.028
$D_9 \leftarrow D_0$	29771	0.014	$D_{19} \leftarrow D_0$	42865	0.007
$D_{10} \leftarrow D_0$	34861	0.003			

The *ab-initio* X-MCQDPT2 calculated excitation energies and transition dipole moments are tabulated in Table 6.1. It can be seen that this calculation predicts a very weak $D_1 \leftarrow D_0$ transition in the IR ($8408\,cm^{-1}$) and a much stronger $D_2 \leftarrow D_0$ transition at the red edge of the visible spectrum ($12064\,cm^{-1}$). It should be noted that these calculations are for free, gas-phase 9-$MeAn^+$, and it is assumed that any shift caused by the weakly bound argon atom is small relative to the errors of the calculation. This is a plausible assumption, given the relatively small solvent shifts, on the order of tens of wavenumbers, observed in previous argon-tagging experiments for similar molecules.[205,207,324] Based on the results observed in Chapter 5, the errors in the X-MCQDPT2 calculation are likely to be in the order of one or two thousands of wavenumbers.

The lowest energy band in the spectrum, with energy $9564\,cm^{-1}$ and FWHM of $42\,cm^{-1}$, is initially assigned as the $D_1 \leftarrow D_0$ electronic origin. The very large lorentzian band with energy $14714\,cm^{-1}$ and width $300\,cm^{-1}$ is assigned to the $D_2 \leftarrow D_0$ electronic origin transition.

To aid in the assignment of the higher energy transitions, the $D_1 \leftarrow D_0$ and $D_2 \leftarrow D_0$ transition energies were plotted against the calculated X-MCQDPT2 transition energies for the two lowest states. A linear scaling factor of 1.19 ($T_{scaled} = 1.19T_v$) was then determined by linear fit with a fixed origin intercept. This was used to obtain scaled calculated X-MCQDPT2 energies, T_{scaled}, which are used in the simulated spectrum shown in Figure 6.2.

The assignment is further assisted by creating a stick spectrum from the scaled X-MCQDPT2 energies and the square of the calculated transition dipole moments. This stick spectrum is compared to the 9-$MeAn^+ \cdots Ar$ photodissociation in figure 6.2. By assuming that the

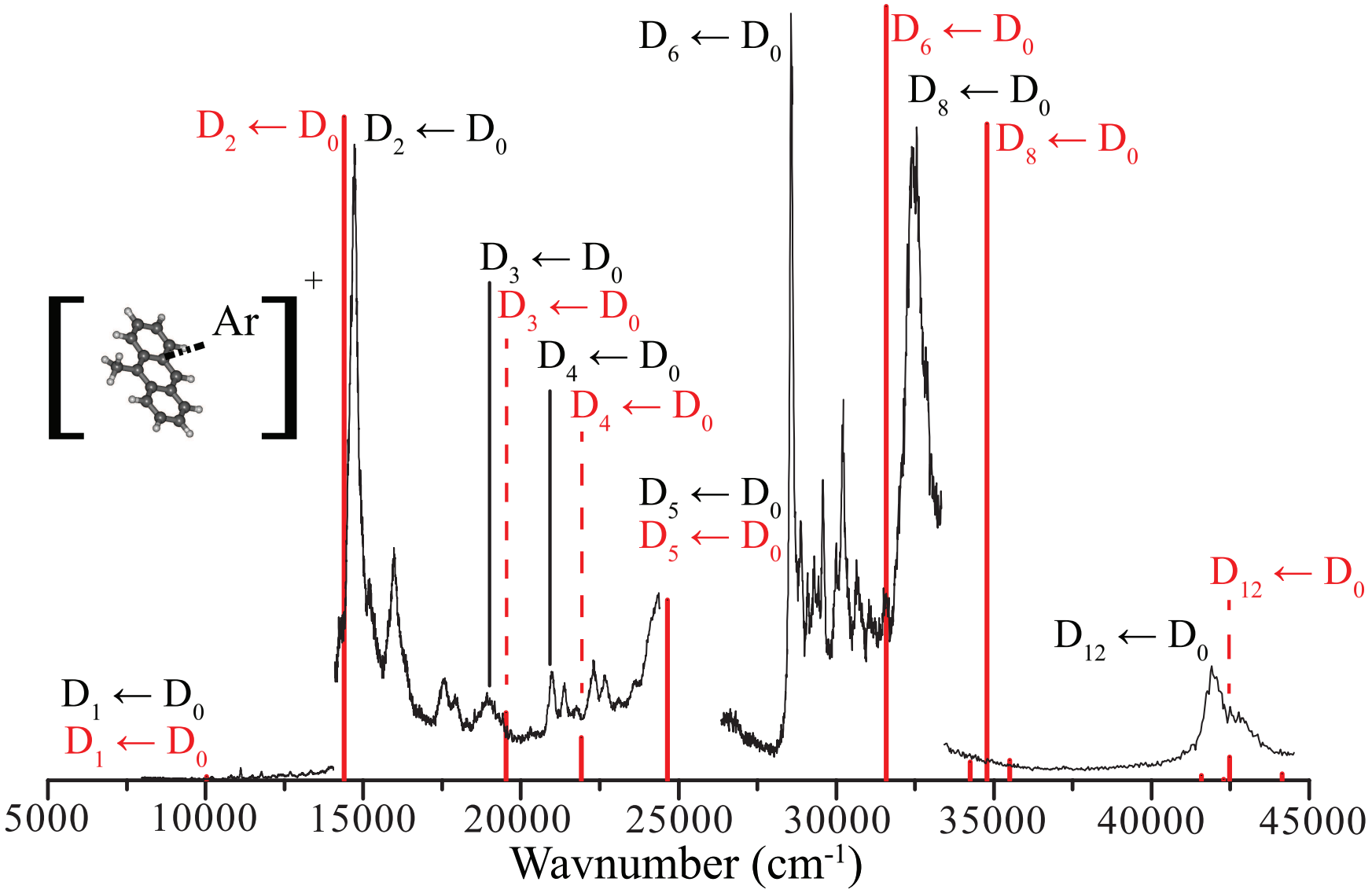

Figure 6.2: Black: Photodissociation spectrum of argon tagged 9-MeAn+ radical cation. Red: Scaled X-MCQDPT2[9,9]/tzv(2d,p) stick spectrum, based on corrected vertical excitation energies and transition dipole moments.

Table 6.2: Origin transition energies (T_0 in cm^{-1}) and intensities (relative to the $D_1 \leftarrow D_0$ origin band) of argon tagged 9-MeAn. T_v is calculated at the X-MCQDPT2[9,9]/tzv(2d,p) level of theory and ignores geometry change, zero point energy and red shift induced by the weakly bonded argon atom. T_{scaled} is empirically fit to the line $T_{scaled} = 1.19T_v$. Calculated transition dipole (μ^2) has units of Debye^2. † - Estimated peak position, band cut off by limits of scan range.

Transition	Experimental T_0	Intensity	T_v	T_{scaled}	μ^2
$D_1 \leftarrow D_0$	9564	1	8408	10029	0.003
$D_2 \leftarrow D_0$	14714	413	12064	14390	0.474
$D_3 \leftarrow D_0$	18948	18	16375	19532	0.048
$D_4 \leftarrow D_0$	20991	59	18368	21909	0.030
$D_5 \leftarrow D_0$	24500†	122	20668	24653	0.129
$D_6 \leftarrow D_0$	28577	616	26478	31583	0.552
$D_8 \leftarrow D_0$	32473	605	29163	34785	0.468
$D_{12} \leftarrow D_0$	41986	79	35613	42479	0.017

observed strong high energy transitions should have strong calculated intensities the assignment is undertaken. It can be seen that there is good agreement between the stick spectrum and several likely origin transitions. All of the assignments are tabulated in Table 6.2 and are shown on Figure 6.2.

In the visible, the simulated spectrum suggests the previously assigned $D_2 \leftarrow D_0$ band will be followed by three closely spaced weaker transitions, and are assigned to the bands at 18948 cm^{-1}, 20991 cm^{-1} and ~24500 cm^{-1}. The assignment of $D_3 \leftarrow D_0$ origin transition is somewhat tentative, as it lies close to vibronic transitions of the $D_2 \leftarrow D_0$ state with similar intensities. The band at 18948 cm^{-1} was chosen for its broader band profile compared to the adjacent bands.

The two large bands in the near-UV region of the spectrum have relative intensities that agree well with the predicted intensities for the $D_6 \leftarrow D_0$ and $D_8 \leftarrow D_0$ transitions, and these peaks are also predicted to have similar energies to the assigned origin bands. $D_7 \leftarrow D_0$ is predicted to have low intensity, and due to the large amount of vibronic structure observed in the $D_6 \leftarrow D_0$ state, the $D_7 \leftarrow D_0$ origin transition cannot be assigned with any confidence. The band centered on 41986 cm^{-1} is assigned as $D_{12} \leftarrow D_0$, this being the band in this region that best fits the observed intensity. However, the band may also be due to the origin transitions of $D_{10} \leftarrow D_0$, $D_{11} \leftarrow D_0$ or $D_{13} \leftarrow D_0$ all of which are predicted to absorb in this region, and it is possible that several of these transitions are responsible for the observed structure.

6.4.2 $D_1 \leftarrow D_0$ Vibronic Spectrum

The electronic transitions assigned as $D_2 \leftarrow D_0$, $D_3 \leftarrow D_0$ and $D_6 \leftarrow D_0$ in Figure 6.1 feature some semi-resolved vibronic structure, with the $D_6 \leftarrow D_0$ especially rich in vibronic features. The equivalent transitions of many of these bands have been observed previously in the An^+ radical cation.[358] The observed 9-MeAn$^+ \cdots$Ar transitions are redshifted by $\sim$500 cm^{-1} compared to the equivalent gas-phase transitions in An^+,[358] with this redshift due to both the methyl substitution and the attached argon. The structure of the NIR $D_1 \leftarrow D_0$ transition has not been previously reported or assigned for either 9-MeAn$^+$ or An^+, and as such has been a focus of this study.

TD-B3LYP harmonic vibrational frequencies were calculated for the D_1 state. These frequencies are numbered and tabulated in Table 6.3. The modes have been labelled in C_1 symmetry, however depending on the position of the methyl rotor C_s symmetry can also be valid. It can be seen in Table 6.3 that the internal rotation mode of the methyl-group, ν_{75} has been calculated as having an imaginary frequency. This is due to the orientation of the methyl group not being in a minimum geometry. The potential energy curve for this rotation will feature a six-fold symmetry within this internal rotational co-ordinate and results in many close lying energy transitions. As mentioned previously, similar methyl-rotor transitions have been discussed previously by Friha *et. al.*[324] While similar FC calculations would allow the methyl-rotor transitions to be simulated for the $D_1 \leftarrow D_0$ of 9-MeAn$^+$, there is no evidence of any resolved methyl-rotor structure in the observed spectra. As such, beyond an understanding that these transitions are responsible for broadening of the observed features, the methyl-rotor structure is ignored in this vibronic assignment.

Whereas the $D_1 \leftarrow D_0$ electronic origin band of An^+ is symmetry forbidden, this transition is slightly allowed for the lower symmetry 9-MeAn$^+$. The small band at 9564 cm^{-1} is assigned to this origin. The remaining vibronic assignments are referenced to this band.

It is apparent from Table 6.3 that multiple possible assignments exist for many of the observed transitions. An FC simulation was undertaken in Gaussian09 allowing the Franck-Condon intensities to guide the assignments. This stick spectrum is displayed as the red bars in Figure 6.3.

Most of the peaks with significant predicted Franck-Condon activity align well with observed vibronic bands. This agreement is further enhanced when this stick spectrum is also built upon the 1549 cm^{-1}(blue) and 3119 cm^{-1}(green) vibronic 'false -origins'. Based on the Franck-Condon spectrum, these 'false-origins' are assigned to one and two quanta

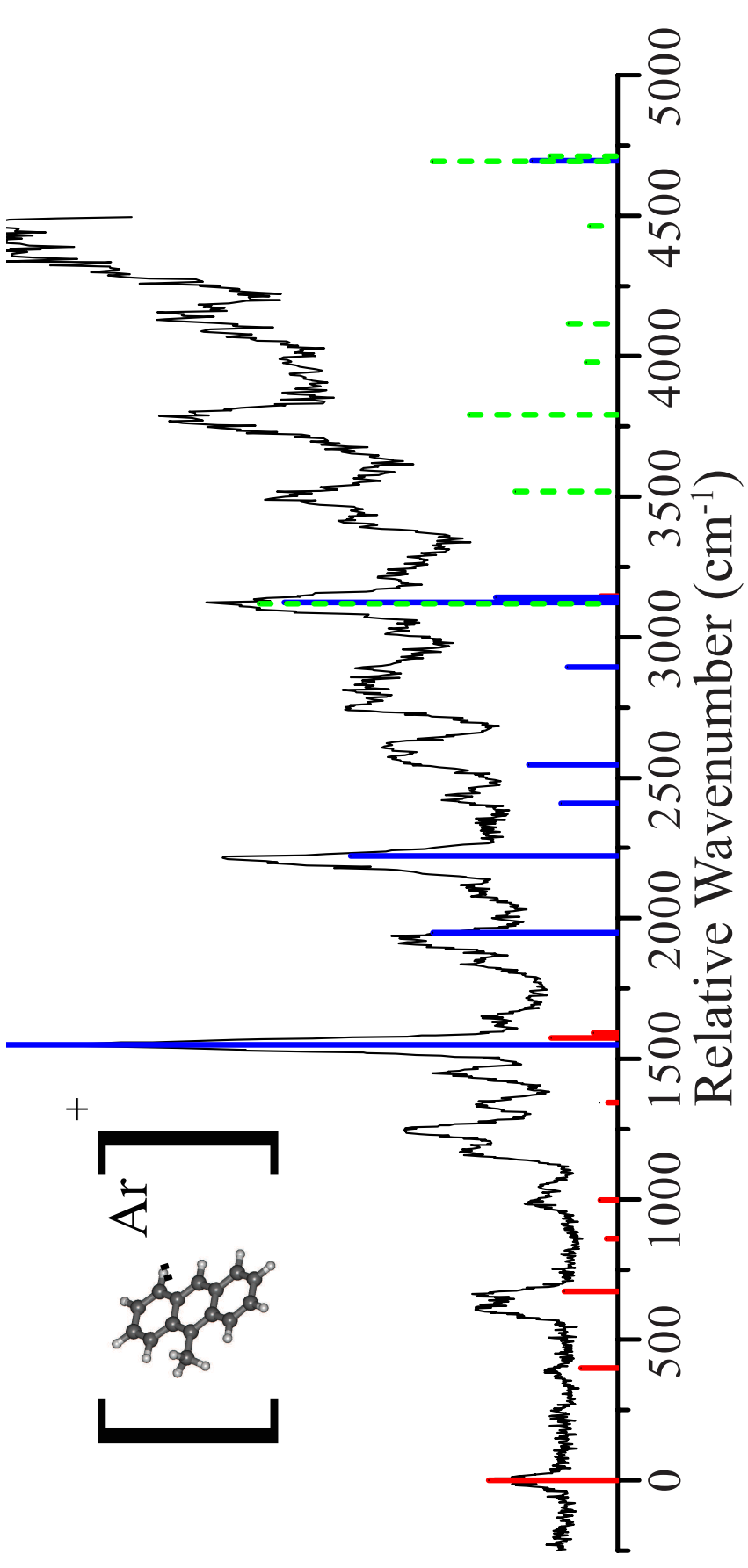

Figure 6.3: Black: $D_1 \leftarrow D_0$ Photodissociation spectrum of argon tagged 9-MeAn$^+$ radical cation. Red: TD-B3LYP/6-311++G(d,p) stick spectrum relative to the $D_1 \leftarrow D_0$ electronic origin. Blue: TD-B3LYP/6-311++G(d,p) stick spectrum relative to the 1549 cm^{-1} false origin. Green: TD-B3LYP/6-311++G(d,p) stick spectrum relative to the 3119 cm^{-1} false origin. Effect of weakly bound argon not included in calculation.

Table 6.3: 9-MeAn$^+$ D_1 excited state harmonic frequencies calculated at the TD-B3LYP/6-311++G(d,p) level of theory. The imaginary frequency is the mode responsible for rotation of the methyl-rotor. Normal mode frequency (Freq.) is in cm^{-1}. The modes have been numbered in the C_1 point-group, and as such all modes have A symmetry.

Mode	Freq.	Mode	Freq.	Mode	Freq.	Mode	Freq.
1	3229	21	1477	41	1005	61	518
2	3229	22	1458	42	997	62	485
3	3207	23	1452	43	994	63	464
4	3207	24	1419	44	992	64	432
5	3196	25	1416	45	978	65	423
6	3196	26	1393	46	916	66	399
7	3190	27	1367	47	906	67	368
8	3188	28	1358	48	864	68	367
9	3186	29	1315	49	859	69	257
10	3143	30	1265	50	852	70	251
11	3118	31	1244	51	804	71	218
12	3036	32	1209	52	776	72	128
13	1770	33	1208	53	770	73	89
14	1602	34	1193	54	747	74	74
15	1593	35	1188	55	738	75	-37
16	1574	36	1130	56	672		
17	1539	37	1071	57	623		
18	1525	38	1049	58	605		
19	1488	39	1040	59	562		
20	1481	40	1005	60	549		

of ν_{16} respectively. The intensity of these bands are strongly enhanced by *pseudo*-Jahn-Teller vibronic coupling of ν_{16} to the strong $D_2 \leftarrow D_0$ transition, and this coupling will be explored later in the chapter. The Franck-Condon transitions can also be observed on the two close lying bands assigned as ν_{56} (based on the Franck-Condon spectrum) and ν_{57} (based on its calculated excited state frequency and proximity to ν_{56}).

These bands provide the basis for the assignments tabulated in Table 6.4. These assignments are labelled on the $D_1 \leftarrow D_0$ photodissociation spectrum of argon tagged 9-MeAn$^+$ in Figure 6.4.

While the Franck-Condon simulation proves extremely useful in determining which transitions are responsible for the observed bands, the intensity pattern does not resemble the observed spectrum. The intensity pattern of the transitions built on the ν_{16} false origin agree reasonably well with that predicted by the Franck-Condon simulation. However, the intensity of bands built on the electronic origin, particularly ν_{16}, are significantly underestimated. This is due to vibronic coupling to the much stronger $D_2 \leftarrow D_0$ transition. While

Table 6.4: Assignment of $D_1 \leftarrow D_0$ vibronic bands of 9-MeAn$^+$. Calculated D_1 excited state harmonic frequencies are calculated at the TD-B3LYP/6-311++G(d,p) level of theory. Frequency is in cm^{-1}. † - Estimated frequency of unresolved band or sholder.

Transition	Observed	Calculated	Δ_{c-o}
ν_0	0	0	0
ν_{70}	231	251	20
ν_{66}	388	399	11
ν_{57}	617	623	6
ν_{56}	661	672	11
$\nu_{57}\nu_{66}$	992	1022	30
$\nu_{56}\nu_{66}$	1045	1071	26
$2\nu_{57}$	1174	1246	72
$\nu_{57}\nu_{56}$	1244	1295	51
$2\nu_{56}$	1335	1344	9
ν_{23}	1449	1452	3
ν_{16}	1549	1574	25
ν_{15}	1639	1593	-46
$\nu_{16}\nu_{70}$	1845	1825	-20
$\nu_{16}\nu_{66}$	1920	1973	53
$\nu_{16}\nu_{57}$	2175 †	2197	22
$\nu_{16}\nu_{56}$	2209	2246	37
$\nu_{16}\nu_{49}$	2440	2433	-7
$\nu_{16}\nu_{57}\nu_{66}$	2567	2596	29
$\nu_{16}\nu_{56}\nu_{66}$	2611	2645	34
$\nu_{16}2\nu_{57}$	2770 †	2820	50
$\nu_{16}\nu_{57}\nu_{56}$	2820 †	2869	49
$\nu_{16}2\nu_{56}$	2890 †	2918	28
$\nu_{16}\nu_{23}$	3020	3026	6
$2\nu_{16}$	3119	3148	29
$2\nu_{16}\nu_{70}$	3415	3399	-16
$2\nu_{16}\nu_{66}$	3500	3547	47
$2\nu_{16}\nu_{57}$	3715 †	3771	56
$2\nu_{16}\nu_{56}$	3775	3820	45

normally this coupling could be demonstrated through an FCHT simulation, the Herzberg-Teller theorem discussed in Chapter 2 assumes that the energy gap to the inducing mode is much greater than the vibrational energy level of the modes. As the $D_2 \leftarrow D_0$ origin has a relative frequency of just 5146 cm^{-1} and the ν_{16} false origin has a relative frequency of 1549 cm^{-1}, this is demonstrably untrue. The observed intensity pattern is instead modelled by *pseudo*-Jahn-Teller coupling.

To allow more accurate fitting of the observed intensities, a simple Vibronic calculator was developed by Prof. Timothy Schmidt. This was then used by the author to create the stick spectrum displayed in Figure 6.4. Inputs include calculated Franck-Condon intensities, the

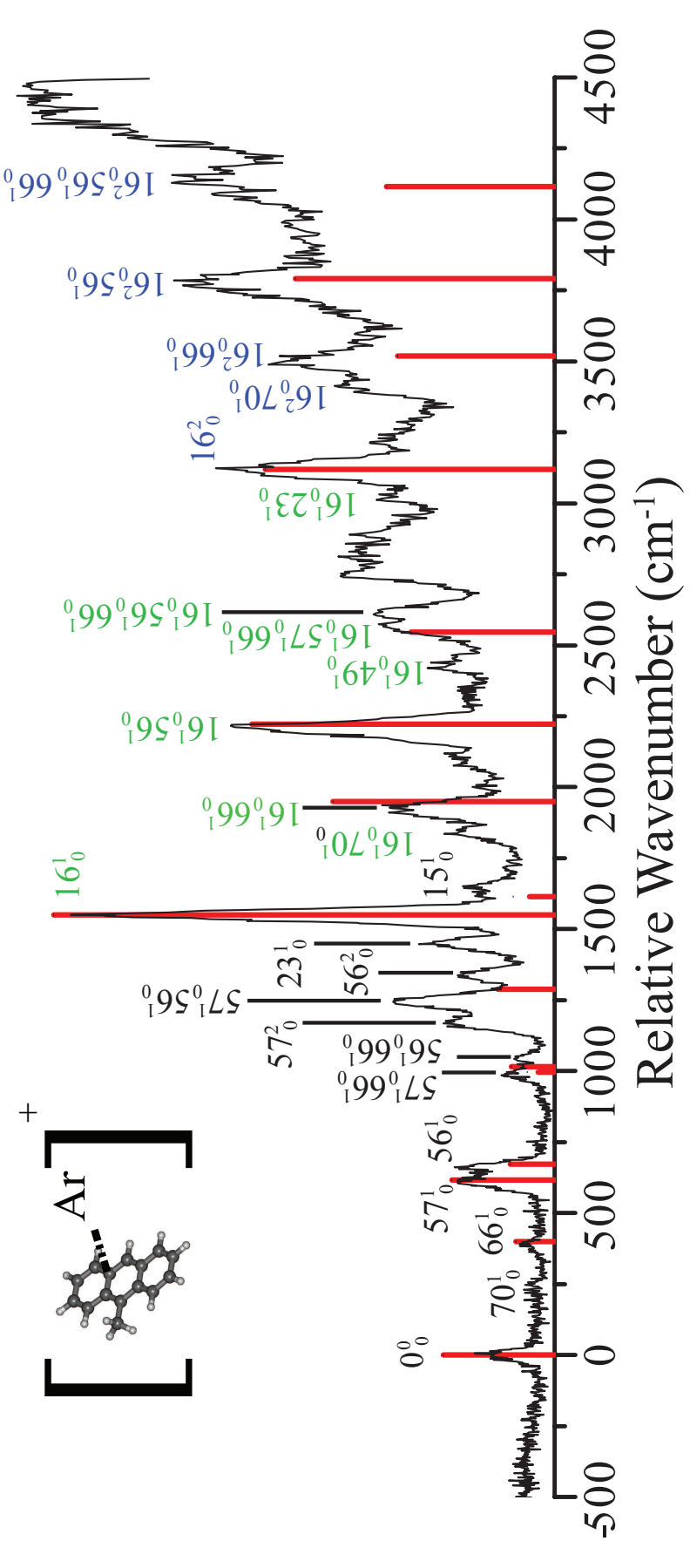

Figure 6.4: Black: $D_1 \leftarrow D_0$ Photodissociation spectrum of argon tagged 9-MeAn$^+$ radical cation. Assignments from Table 6.4 shown, green labeled tranitions are built onto ν_{16} blue labeled transitions are built onto $2\nu_{16}$. Assignments of small, or unresolved, transitions not all shown, See Table 6.4 for full list of assignments. Red: Fitted vibronic stick spectrum.

experimentally determined relative frequency and intensity of the $D_2 \leftarrow D_0$ transition and the position of the 617 cm^{-1}, 1549 cm^{-1} and 3119 cm^{-1} false origins. Coupling constants for the three false origins were fit to the observed intensities. The included stick spectra have coupling constants of 200 cm^{-1}, 350 cm^{-1} and 150 cm^{-1} for the 617 cm^{-1}, 1549 cm^{-1} and 3119 cm^{-1} respectively.

The intensity of the vibronic transitions is given by the equation

$$I_{vibronic} = I_{FC} \times \left(\frac{C}{(E_{D_2 \leftarrow D_0} - E_\mu)} \right)^2 \times I_{D_2 \leftarrow D_0} \tag{6.1}$$

where I_{FC} is the calculated Franck-Condon intensity (relative to the false origin), C is a fitted coupling for each false origin with units cm^{-1}, $E_{D_2 \leftarrow D_0}$ is the relative energy of the inducing $D_2 \leftarrow D_0$ transition, $I_{D_2 \leftarrow D_0}$ is the relative intensity of the inducing $D_2 \leftarrow D_0$ transition and E_μ is the relative energy of the transition being calculated. This equation is based on first-order perturbation theory.

To better understand this observed vibronic coupling, the symmetry of the molecule is approximated in order to better describe the vibrations and electronic transitions involved. If the methyl-group of 9-$MeAn^+$ is considered a featureless sphere, this molecule can be estimated as having C_{2v} symmetry. In C_{2v} both $D_1 \leftarrow D_0$ ($1^2A_2 \leftarrow X^2B_1$) and $D_2 \leftarrow D_0$ ($2^2A_2 \leftarrow X^2B_1$) can be considered as B_2 transitions. These B_2 transitions will be coupled by vibrations of a_1 symmetry. It can be seen from the observed fitted spectrum that the ν_{16} vibrational mode couples especially strongly to the $D_2 \leftarrow D_0$ transition. In C_{2v}, the ν_{16} vibration has a_1 symmetry and it is therefore able to vibronically couple to the stronger $D_2 \leftarrow D_0$ transition, gaining intensity from this transition.

Comparison with the spectroscopically similar D_{2h} symmetric An^+ is complicated by differing definitions of the spacial axis in the two symmetry groups. The $D_1 \leftarrow D_0$ ($1^2B_{3g} \leftarrow X^2B_{2g}$) transition of the D_{2h} An^+ has B_{1g} symmetry. To couple this weak transition to the strong B_{2u} $D_2 \leftarrow D_0$ ($1^2A_u \leftarrow X^2B_{2g}$) transition, a vibrational mode would be required to have b_{3u} symmetry. This corresponds to a vibrational normal mode vector along the short x axis of An^+. In the C_{2v} model of 9-$MeAn^+$ this axis is redefined as the z axis, and the required b_{3u} vibration would be identified as an a_1 vibration, such as ν_{16}. It can therefore be seen that this vibration would be effective at vibronically coupling the $D_1 \leftarrow D_0$ transition to the $D_2 \leftarrow D_0$ in both 9-$MeAn^+$ and An^+. Therefore, it is suggested that the $1^2B_{3g} \leftarrow X^2B_{2g}$ vibonic spectrum of An^+ will resemble the $D_1 \leftarrow D_0$ 9-$MeAn^+$ spectrum observed in this study, as would be expected. The primary difference

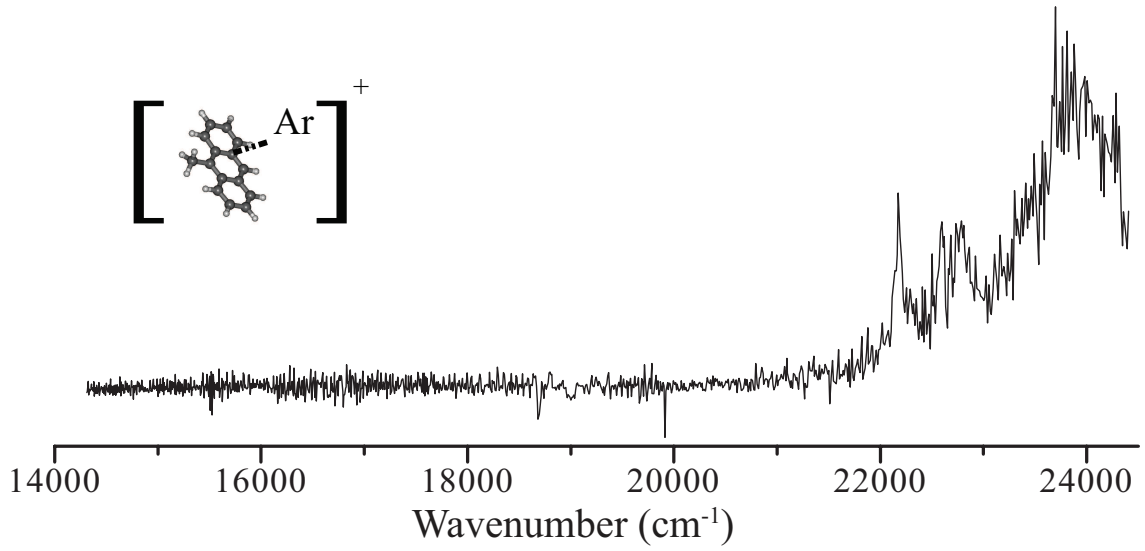

Figure 6.5: Photodissociation spectrum of argon tagged 9-MeAn$^+$ radical cation, monitored at the m/z 178 mass-channel of An$^+$, suggesting loss of either CH_2 and argon or CH_3 and argon (uncertainty due to limitation in mass resolution)

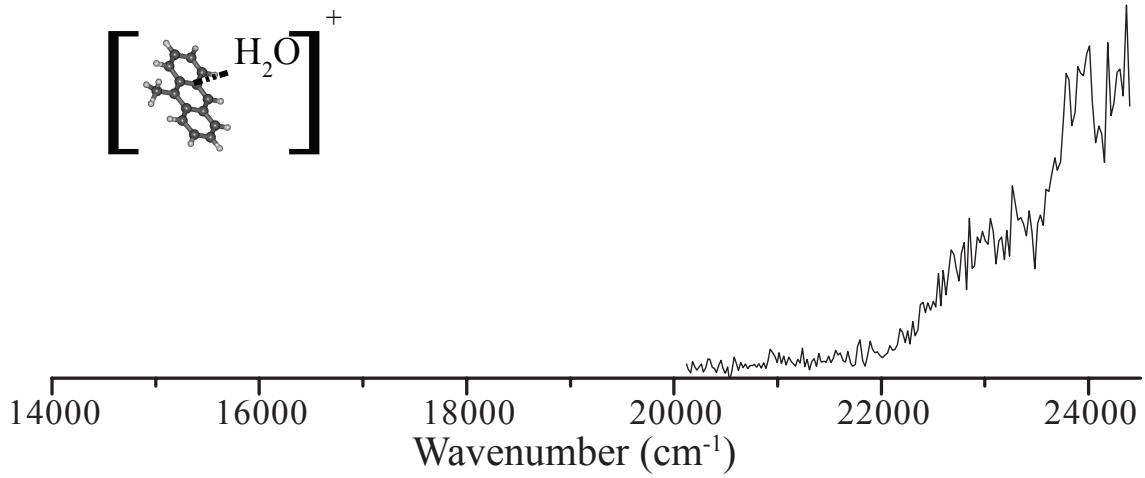

Figure 6.6: Photodissociation spectrum of H_2O tagged 9-MeAn$^+$ radical cation, monitored at the m/z 178 mass-channel of An$^+$, suggesting loss of methanol (CH_3OH) or CH_3 and H_2O

would likely be the absence of the electronic origin band, and the Franck-Condon structure built upon it, in An$^+$.

6.5 Photofragmentation of 9-MeAn$^+$

At high visible photon energies photo-dissociation signal of 9-MeAn$^+ \cdots$ Ar and MeAn$^+ \cdots H_2O$ was observed when monitoring the m/z 178 An$^+$ mass channel. These spectra are shown in Figures 6.5 and 6.6.

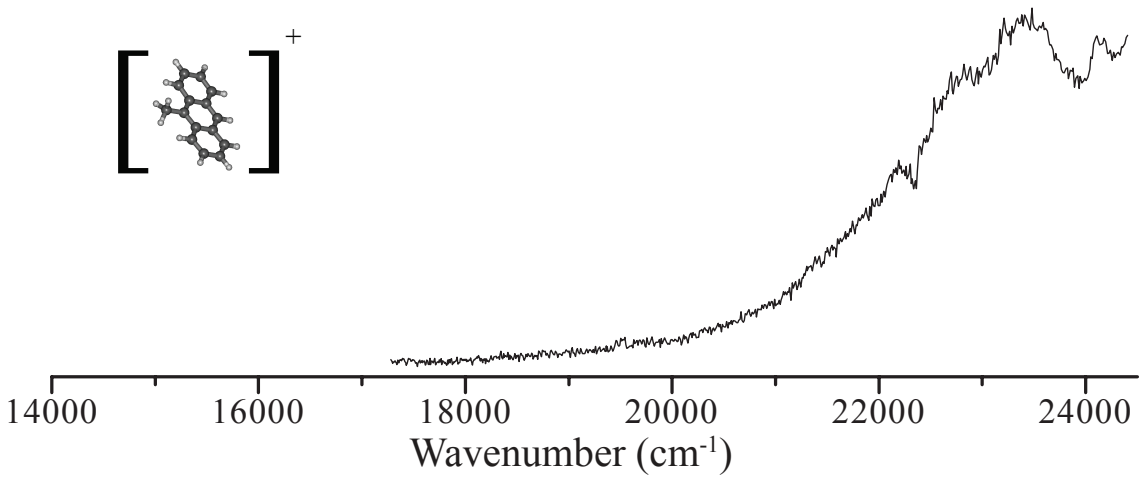

Figure 6.7: Photodissociation spectrum of 9-MeAn$^+$ radical cation, monitored at the m/z 178 mass-channel of An$^+$, suggesting loss of CH_2

For the argon-tagged spectrum (Figure 6.5) photodissociation signal is observed with an onset of 21600 cm^{-1}, suggesting a new photodissociation pathway opening at approximately 253 kJ/mol. Further calculations or experiments would be required to determine if this pathway results in the loss of CH_2/argon or CH_3/argon as this is below the resolution of the quadrupole mass filter in this range. As a result, the mechanism responsible for this new photo-dissociation pathway cannot be determined purely from the reported spectrum.

The water-tagged spectrum has a slightly higher onset of 22000 cm^{-1} suggesting a new photodissociation pathway opening at approximately 263 kJ/mol. This is very similar and the possible errors in fitting this onset have not been fully explored. It is possible that this reaction pathway may results in the loss of methanol (CH_3OH). However, this again cannot be determined due to the limitation in mass resolution.

Photodissociation of the bare cation at similar energies was also observed, with a much lower onset of 20500 cm^{-1} as shown in Figure 6.7. However, as bare cations are inadequately cooled by the electrospray source,[359] the spectrum does not provide a reliable value for the onset of dissociation.

Consideration of the relative energies of the proposed products allows for some speculation regarding the identity of the observed products. The BDE of 260 kJ/mol is significantly lower than the bond energy expected for a ground-state breaking of the PAH–CH_3 bond, the channel that would result in the loss of CH_3/argon. For example, the BDE of the methyl bond in toluene is 433 kJ/mol.[360] This large BDE is unsurprising as this would result in the creation of a σ-radical. As such, a mechanism leading to the formation of An$^+$ may be accessible at lower energies than the simple bond-fission leading to the creation of a σ-radical. However, such a mechanism would likely require an energetically accessible

transition state. Theoretical modelling of possible reaction pathways, possibly supported by additional experiments, would be required to obtain firm conclusions. The theoretical and experimental exploration of possible mechanisms for either CH_2 or CH_3 loss from electronically excited 9-MeAn$^+$ remain an avenue of future research.

6.6 Astronomical Relevance

It has been previously stated that the $D_2 \leftarrow D_0$ transitions of PAH radical cations have been largely dismissed as carriers of the DIBs due to their width. This is especially true for radical cations containing methyl rotors,[324] as this further broadens the observed bands. $D_1 \leftarrow D_0$ transitions, while in the NIR, are in a region potentially relevant to the DIBs. However, most PAH radical cations have weak $D_1 \leftarrow D_0$ transitions and even stronger transitions would likely feature vibronic features leading to non-origin-dominated spectra, contrary to the non-correlated nature of most DIBs.[146] Higher energy strong transitions of PAH radical-cations are likely to be broad, and are also are likely to have UV absorptions. As such, resonance-stabilised PAH radical cations do not make good candidates as carriers of the DIBs

6.7 Conclusions

The argon tagged spectrum of 9-MeAn$^+$ was recorded for the range from 8000 cm^{-1} to 44444 cm^{-1}. This included the spectra of seven distinct electronic transitions, which were assigned with the assistance of X-MCQDPT2[9,9]/tzv(2d,p) energies and intensities.

The vibronic spectrum of the $D_1 \leftarrow D_0$ electronic transition was assigned with a combination of TD-B3LYP/6-311++G(d,p) calculations and a simple vibronic analysis. While most observed transitions had some predicted Franck-Condon intensity, the intensity pattern could only be fully explained by invoking a *pseudo*-Jahn-Teller coupling with the energetically similar, and much stronger, $D_2 \leftarrow D_0$ transition.

Photodissociation of 9-MeAn$^+$ to produce An$^+$ was observed at energies above approximately 22000 cm^{-1}. This was observed with bare 9-MeAn$^+$, as well as when the molecule was tagged with argon or H_2O.

The $D_2 \leftarrow D_0$ transitions of most resonance-stabilised PAH radical cations are too broad to be carriers of most DIBs, and this is especially true for species with methyl-rotors.[324]

As all other electronic transitions are unlikely to produce the relevant spectral features, due to either excitation energy or intensity, most small resonance-stabilised PAH radical cations can be dismissed as potential carriers of the DIBs.

Chapter 7

The Phenalenyl Motif: 1H-Phenalene, 1H-Phenalenium Radical Cation and the Phenalenyl Radical

7.1 Introduction

The phenalenyl motif, the smallest polycyclic subunit of graphene, is a D_{3h} arrangement of 13 carbon atoms consisting of three conjoined six-membered rings bound at a central

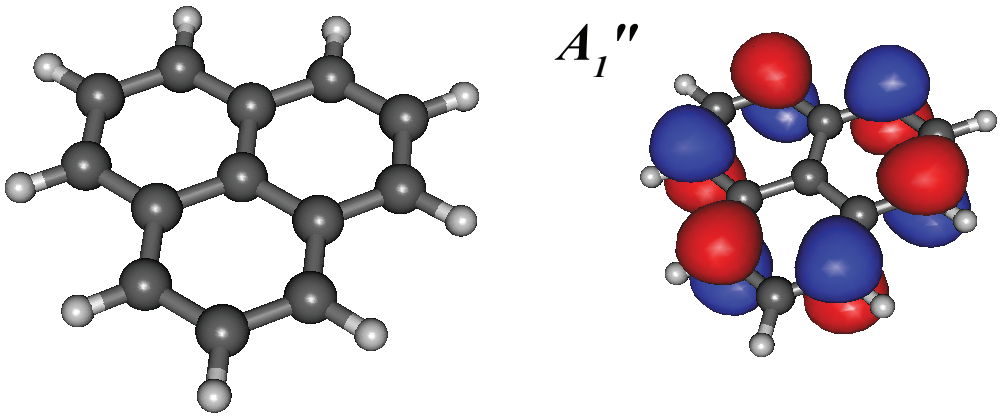

Figure 7.1: Structure and ROHF SOMO orbital of the phenalenyl radical ($C_{13}H_9$). The phenalenyl motif is a D_{3h} arrangement of 13 carbon atoms consisting of three conjoined six-membered rings bound at a central carbon atom. The SOMO of the phenalenyl radical has A_1'' symmetry

carbon atom such as seen in the phenalenyl radical, the structure of which is shown in Figure 7.1. Phenalenyl (also known as perinaphthenyl) occurs in three resonance stabilized oxidation states, forming a stable neutral radical species as well as stable closed-shell anion and cation species.

The stability of these phenalenyl species is a result of their structure. Phenalenyl, as well as its anion and cation, are all observed to have well-defined perimeter ring currents, traditionally a sign of aromaticity on the magnetic criterion.[361,362] It is this behaviour that has resulted in phenalenyl being described as a "magnetic chameleon."[362]

The phenalenyl radical motif is so stabilised by its resonance structure that 2,5,8-tri-tert-butyl-phenalenyl, where the radical sites are protected by adjacent tert-butyl groups, can be generated and observed at room temperature.[363,364] The stability and delocalisation of all three redox states of phenalenyl make it an excellent building block for single molecule molecular conductors.[365,366]

The source of this stability comes from interaction between the two possible odd-alternant peripheral molecular orbitals and the center molecular orbital, which result in the radical electron remaining on the peripheral carbons.[201] Figure 7.2 shows that the perimeter orbitals can be represented as cosine and sine waves multiplied by the unhybridised p-orbitals. One of these exhibits nodes on the atoms bonded to the central carbon while the other has anti-nodes in these positions. The orbital with antinodes adjacent the central carbon interacts with the central p-orbital, giving new molecular orbitals: one stable, one unstable.[201] It can be seen in Fgure 7.2 that the radical electron remains on the peripheral α carbons. Removing this electron will still give a stabilised species due to the interaction between the peripheral and center orbitals. It is this stabilising effect that allows for the three stable redox states of phenalenyl. This is confirmed with higher level theory. The ROHF calculation of the radical orbital is shown in Figure 7.1 showing electron density on the α carbons.

This stability makes the phenalenyl-based radical and cation good candadites for interstellar molecules. Indeed, positively charged π-stacked phenalenyl clusters have been suggested as possible carriers of the broad interstellar extended red emission (ERE), and these clusters have been theoretically examined by the group of Martin Head-Gordon of the Lawrence Berkeley National Laboratory, Berkeley, California.[367–370]

The phenalenylide$^-$ anion and phenalenylium$^+$ cation are also of significant interest due to their highly symmetric closed-shell nature. The anionic species has been observed through photodetachment spectroscopy by Gygax *et. al.*,[371] who observed a broad peak at 420 nm,

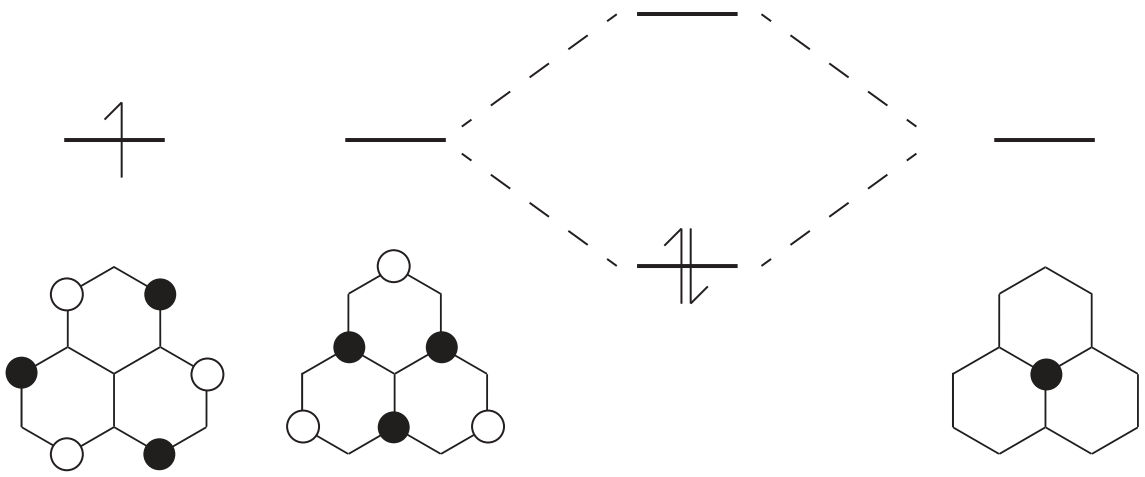

Figure 7.2: The antiaromatic periphery orbitals (left) differ in phase. Only one can interact with the central p orbital (right). This interaction produces new orbitals, one of which stabilizes the structure. Thus, the radical electron remains on the periphery. By subtracting the radical electron it can be seen that the cation will also be stable.

featuring a shoulder at 530 nm. Because of its apparent stability, and suspected astronomical significance, the excitation spectrum of the phenalenium closed-shell cation was unsuccessfully investigated by the author. These molecules, and their heteroatomic analogues, will be discussed later in this chapter.

Chapter 1 introduced the hypothesis that aromatic molecules, whose existence in the ISM are suggested by observed vibrational emission bands,[130,130] may be responsible for some or all of the DIBs. This hypothesis has been extensively examined experimentally by observing cold PAH molecules in simulated astronomical conditions of a low collisional environment, such as a that provided by a supersonic expansion. This hypothesis has been further explored in the previous chapters.

The transition energy of the first electronic transitions for a class of PAH can be inferred by a crude Hückel picture of the electronic orbitals. It can be seen in Figure 1.8 that the excitation energy of the transition to the first electronic excited state of a closed-shell neutral PAH can be expected to be approximately twice the energy of of an open shell neutral species with a similar chromophore. This basic picture is reflected in the closed shell neutral PAH 1H-phenalene and its radical cation. While the carbon arrangement of these C_s symmetric molecules reflect that of the phenalenyl radical, the peripheral π-conjugation is broken by the sp^3 hybridised carbon in the 1-position. This results in a chromophore reminiscent of 1-vinylnaphthalene. The spectrum of these molecules, and their possible relevance to the formation and thermochemistry of the phenylenyl based molecules, are discussed later in this chapter.

The simple molecular orbital picture is further complicated in the D_{3h} phenalenyl radical as well as its closed shell cation and anion. These molecules have degenerate E'' frontier orbitals, similar in energy to non-degenerate A_2'' orbitals, which in the radical represent the HOMO and LUMO, energetically equidistant below and above an A_1'' SOMO as seen in Figure 7.3. As a result, the excited state of phenalenyl is degenerate. The Jahn-Teller theorem states that a non-linear molecule in a degenerate electronic energy state is unstable[372]. Therefore, a distortion along a vibrational normal mode leads to an initial lowering in energy of one of the states, causing them to split. This results in significant theoretical challenges, which will be briefly discussed in a later section.

Previously published work, based on work undertaken for the author's undergraduate honours thesis,[220] experimentally and theoretically examined the first excited state of the free-phenalenyl radical.[201] In this chapter, further theoretical analysis of the phenalenyl radical will be explored.

Hydrogen or proton addition to phenalenyl can form phenalene molecules. The most stable phenalene isomer, 1H-phenalene, and its cation have been experimentally measured as part of this work. These molecules, interesting in their own right, will be discussed in light of theory and the recorded spectra.

The excitation spectrum of the phenalenylium closed-shell cation has yet to be recorded in the gas-phase. This species, of astronomical and theoretical interest, will be discussed later in this chapter.

7.2 Theoretical Methods

The computational methods used in this chapter are described in detail in Chapter 2 and are similar to those carried out in Chapters 4 and 5. The quantum chemical calculations of ground and excited-state geometries and vibrational frequencies were carried out with B3LYP and TD-B3LYP respectively,[231,232] and the 6-311++G(d,p) basis set.

The excitation energies were obtained both at the TD-B3LYP/6-311++G(d,p)[231,232,330,373] and X-MCQDPT2[346] levels of theory. The *ab-initio* X-MCQDPT2 calculations were performed with an active space of 7 electrons in 7 orbitals for radical species and 6 electrons in 7 orbitals for the closed shell neutral and cation species, in conjunction with the tzv(2d,p) basis set. These are similar to the calculations performed in Chapters 5 and 6.

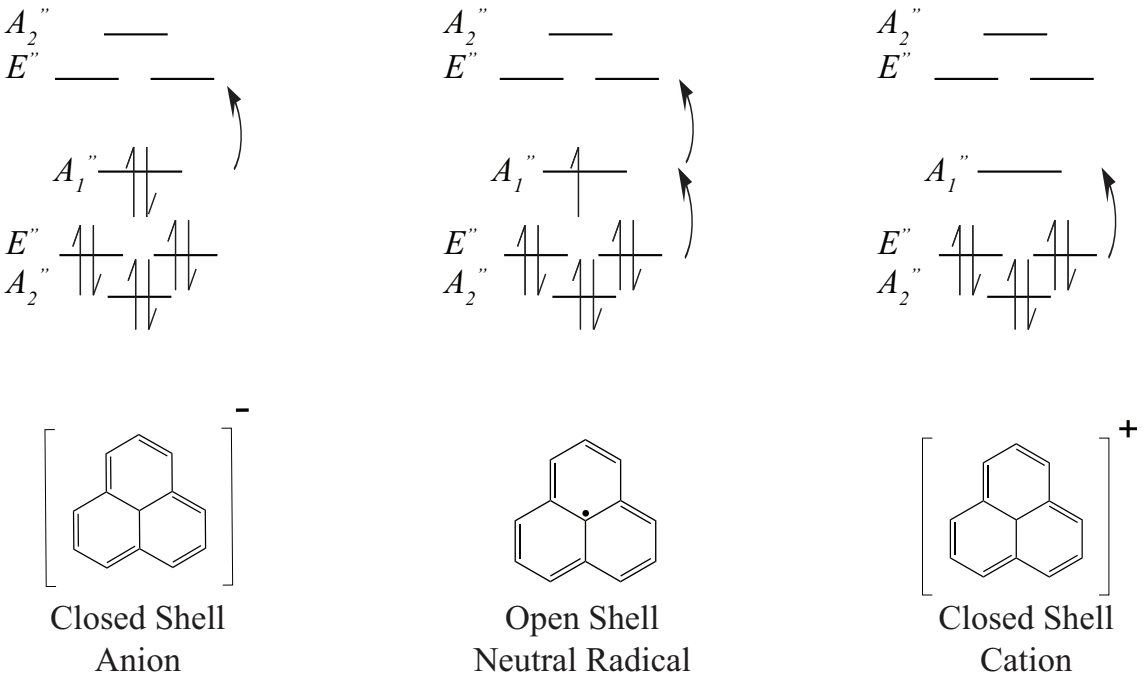

Figure 7.3: Frontier orbitals produced by basic molecular orbital picture of phenalenyl with various charges, as predicted by the Hückel model. PAHs can be divided into classes based on mulitplicity and charge. The single electron transitions likely to contribute to the first electronic excited state are indicated by the black curled arrows

Excited-state potential energy surfaces of 1H-phenalene were constructed by computing single point TD-B3LYP excited-state energies at geometries distorted by application of the appropriate excited-state vibrational coordinates. The calculated points were then fit with a cubic spline, allowing the variational calculation of (anharmonic) vibrational states. This is the same method of calculating anharmonic excited state frequencies used in the assignment of 9-AnMe in Chapter 4.

The B3LYP and TD-B3LYP calculations were carried out using the GAUSSIAN09[221] suites of software, whereas the X-MCQDPT2 calculations were performed in the FIREFLY package.[222,347]

7.3 The Phenalenyl Radical

Previously published work, based on the author's undergraduate honours thesis,[220] experimentally and theoretically examined the first excited state of the free-phenalenyl radical, recording the $D_1 \leftarrow D_0$ ($1^2E'' \leftarrow X^2A_1''$) excitation spectrum.[201] This spectrum is reproduced in Figure 7.4

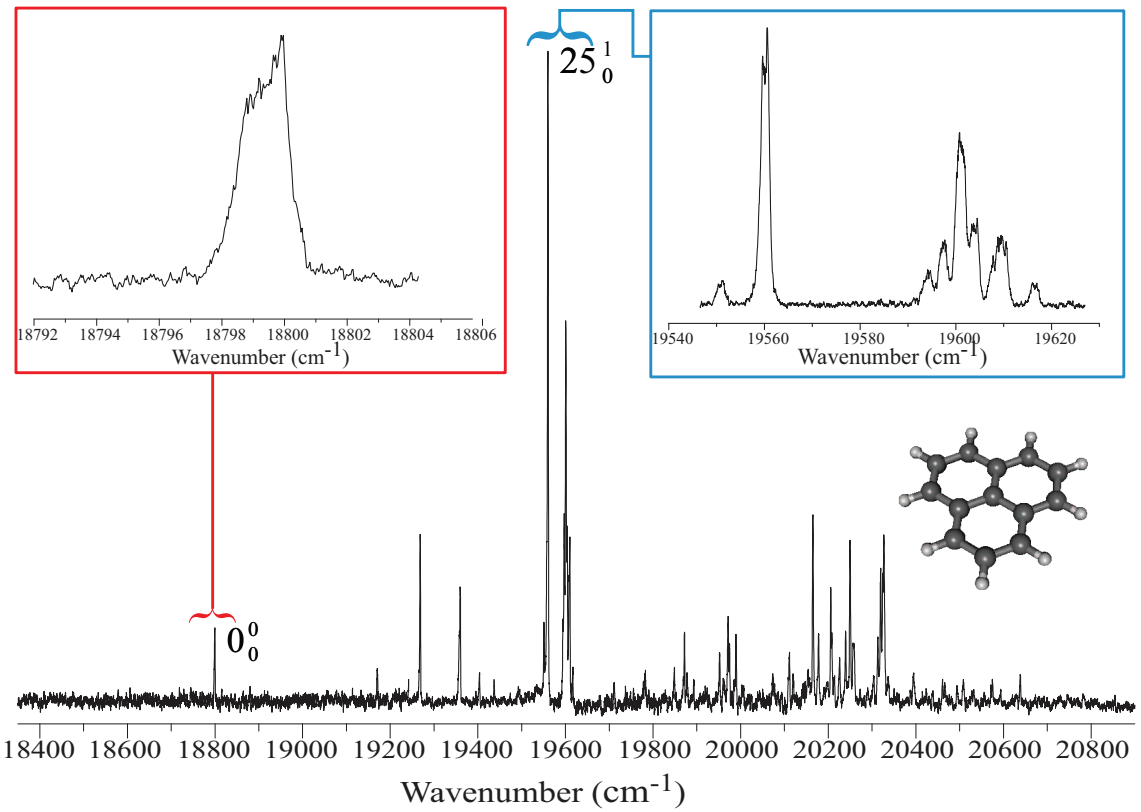

Figure 7.4: R2C2PI spectrum of the $1^2E'' \leftarrow X^2A_1''$ ($D_1 \leftarrow D_0$) transition of the phenalenyl radical. From O'Connor *et. al.* 2011.[201]

This spectrum was dominated by a single, strong, vibronically enhanced mode, a spectroscopic signature considerably different from that of the $D_1 \leftarrow D_0$ transitions of PAH RSRs discussed in previous chapters. The intensity of this vibronic band is enhanced by strong *pseudo*-Jahn-Teller coupling between the observed $1^2E'' \leftarrow X^2A_1''$ transition and the as yet unobserved, strong, $2^2E'' \leftarrow X^2A_1''$ transition. This vibronic coupling was further confirmed through dispersed fluorescence of the dominant band, with the molecule either emitting to two-quanta of the same mode or back to the origin mode. This dispersed fluorescence (DF) emission spectrum is reproduced in Figure 7.5.

In chapter 5 we discovered that the strong higher excited states of RSRs, generally $D_3 \leftarrow D_0$, are generally significantly lifetime-broadened. It was also hypothesised that this broadening was due, in part, to the small energy gap to a weak $D_2 \leftarrow D_0$ transition. In phenalenyl, the lowest energy weak electronic transitions are degenerate ($1^2E'' \leftarrow X^2A_1''$), as are the lowest energy strong electronic transitions($2^2E'' \leftarrow X^2A_1''$). It is likely that the weak $1^2E'' \leftarrow X^2A_1''$ transitions will have a broadening effect on the strong $2^2E'' \leftarrow X^2A_1''$ transition, however the extent of this broadening is unknown.

The search, via double-resonance depletion, for this strong higher-excited state was unsuccesful. However, during this search R2C2PI signal was observed on the m/z 166 mass

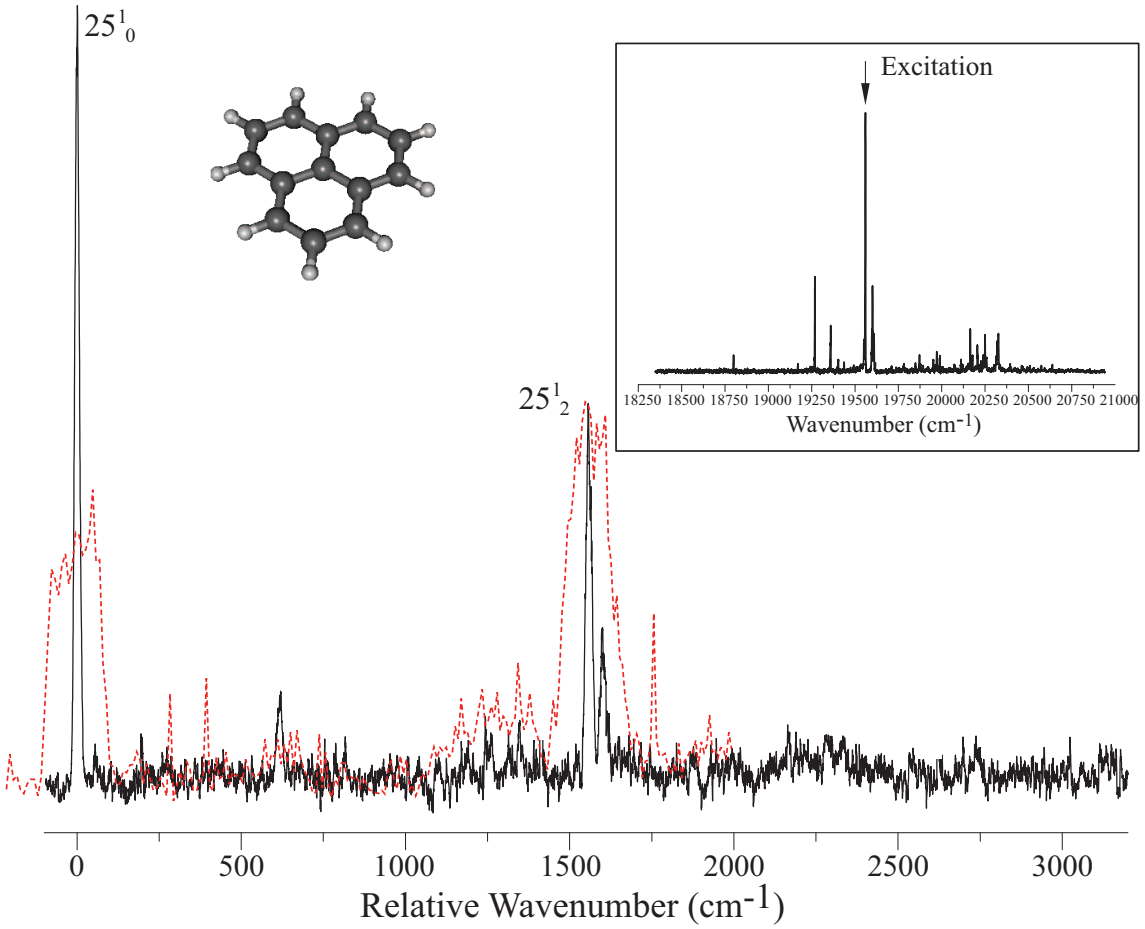

Figure 7.5: DF emission spectrum from excitation of the 25^1_0 band of the phenalenyl radical. The red dashed line is from a gated spectrometer, showing the true relative intensities of the peaks, minus the laser scatter observed at the excitation wavelength. From O'Connor *et. al.* 2011.[201]

channel, corresponding to the 1H-phenalene parent molecule. This spectrum was recorded and is discussed in the next section.

The computational methods used in previous chapters may provide a guide for further experimental studies into the $2^2E'' \leftarrow {}^2A_1''$ electronic transition.

7.3.1 Theoretical Results

TD-B3LYP and X-MCQDPT2 vertical transition energies and intensities of phenalenyl were calculated for the four lowest excited states, and these are shown in Table 7.1. Using the empirical correction developed in Chapter 4, the corrected TD-B3LYP value for the $1^2E'' \leftarrow X^2A_1''$ ($D_1 \leftarrow D_0$) transition of phenalenyl is calculated the be 19569 cm^{-1} (2.43 eV), overestimating the transition energy by 770 cm^{-1} (0.09 eV). The $2^2E'' \leftarrow X^2A_1''$ transition energy can also be estimated, using the empirical correction developed in Chapter 5, as 32825 cm^{-1} (4.07 eV).

X-MCQDPT has also been shown in Chapters 5 and 6 to provide a reliable estimate of the energies of higher excited states. In the previous chapters, a constant scaling factor for all states in this calculation was assumed. Based on the observed $1^2E'' \leftarrow X^2A_1''$ origin of phenalenyl (18879 cm^{-1}), and the X-MCQDPT2[7,7]/tzv(2df,p) calculated value (18399 cm^{-1}), a scaling factor of 1.026 is determined. This gives an estimated $2^2E'' \leftarrow X^2A_1''$ transition energy of 29961 cm^{-1} (3.71 eV).

The corrected TD-B3LYP and scaled X-MCQDPT2 values differ by 2864 cm^{-1}(0.35 eV). These values may offer a guide to future experiments. However, as these calculations place this state well into the ultraviolet, the $2^2E'' \leftarrow X^2A_1''$ state of the phenalenyl radical can now be dismissed as a potential DIB carrier.

Both TD-B3LYP and X-MCQDPT2 show two transitions of symmetry $^2A_2'' \leftarrow {}^2A_1''$ of energies between the two $^2E'' \leftarrow {}^2A_1''$ transitions, both of which have a calculated electric transition dipole moment near zero. These dark states are likely to further reduce the lifetime of the $2^2E''$ state.

7.3.2 Conclusions and Future Work

The phenalenyl radical demonstrates that vibronic bands in weak $D_1 \leftarrow D_0$ electronic state can have significant intensity, thanks to those modes coupling to strong higher excited states. Molecules featuring similarly intense Herzberg-Teller and *pseudo*-Jahn-Teller transitions are of significant theoretical interest and, due to their intensity, may yet be relevant to interstellar spectroscopy.

The methods used in this study are unsuitable for the calculation of the adiabatic and zero-point transition energies of the phenalenyl radical, as the excited state equilibrium geometry occurs at a conical intersection. As a result, optimisation of this state to a minimum distorts the molecule into a C_{2v} geometry which does not represent the true equilibrium geometry of the molecule in this state. The difficulties in performing excited state calculations on phenylenyl, which has a Jahn-Teller/pseudo-Jahn-Teller excited state, were explored in detail in the author's undergraduate honours thesis,[220] and subsequent paper.[201]

Future work remaining on the phenalenyl radical includes a detailed assignment of the molecule based on calculated excited state frequencies and simulated intensities of the *pseudo*-Jahn-Teller e' transitions. This work will be undertaken in collaboration with Prof. John F. Stanton of the University of Texas, Austin.

Table 7.1: $D_n \leftarrow D_0$ vertical electronic transition energies (eV) and squared transition dipole moments μ^2 (Debye^2), of the phenalenyl radical calculated at the TD-B3LYP/6-311++G(d,p) and X-MCQDPT2[7,7]/tzv(2df,p) levels of theory.

Transition	Symmetry	$T_{TD-B3LYP}$	$\mu^2_{TD-B3LYP}$	$T_{X-MCQDPT2}$	$\mu^2_{X-MCQDPT2}$
$D_1 \leftarrow D_0$	$1^2E'' \leftarrow 1^2A_1''$	2.7892	0.00111	2.2812	0.00110
$D_2 \leftarrow D_0$	$1^2A_2'' \leftarrow 1^2A_1''$	3.0132	0.00000	2.5120	0.00000
$D_3 \leftarrow D_0$	$2^2A_2'' \leftarrow 1^2A_1''$	3.2935	0.00000	3.2450	0.00000
$D_4 \leftarrow D_0$	$2^2E'' \leftarrow 1^2A_1''$	3.8547	0.30883	3.6202	0.37099

Table 7.2: Bond dissociation energy (BDE) for the 1-position hydrogen of 1H-phenalene. All data provided by Dr Bun Chan of the Radom group of the School of Chemistry at The University of Sydney.

BDE(C13H10)	vibrationless	0 K	298 K
B3LYP/6-31G(d)	275	243.3	248.5
B3LYP/6-311++G(3df,3pd)	271.2	239.6	244.8
G3X(MP2)-RAD	286.8	255.1	260.3
G4(MP2)-6X	310	278.3	283.5
CCSD(T)-F12b/VDZ	288.4	256.7	261.9

7.4 1H-phenalene

1H-phenalene is the precursor molecule used in the discharge production of the phenalenyl radical. However, it is also an interesting species in its own right. 1H-phenalene, like many other small neutral PAHs, has been detected as an atmospheric combustion product, recorded in 2003 with a concentrations of 8.07 ng/m^3 in the Xigu District of Lanzhou City, China.[374]

If the phenalenyl radical is an astronomical molecule, as has been suggested,[201,370] then attack by hydrogen atoms (which are abundant in the ISM) could lead to the formation of phenalene species. Of the possible phenalene molecules 1H-phenalene is the most stable, calculated with B3LYP/6311+G(2d,p) to be 199 kJmol^{-1} more stable than the second most stable structure (in which the extra hydrogen is bonded to the centre carbon).[375]

The hydrogens bonded to the sp^3 carbon of 1H-phenalene are weakly bound, with the published enthalpy of dissociation as 272 kJmol^{-1} by Gerst and Rüchardt in 1992.[376] This is in good agreement with theoretical values provided by Dr Bun Chan, shown in Table 7.2, considering the high temperature of the experimental conditions.

The low BDE is unsurprising, as this dissociation forms the highly resonance-stabilised phenalenyl radical. This has led to detailed theoretical studies by Vianello and Maksić on substituted phenalene species as the basis of highly powerful organic superacids.[375]

Phenalenyl is also the smallest scale model system of open-shell graphene nano-particles. Addition of hydrogen to graphene forms defects. Hydrogen defects in graphene have been shown to modify the electronic and magnetic properties.[377] Chemisorption of hydrogen on graphene fragments are also believed to catalyse the formation of interstellar H_2 molecules.[378] The mass-resolved $D_1 \leftarrow D_0$ excitation spectrum of 1H-phenalene, and its theoretical analysis and assignment is reported in this section.

7.4.1 Experimental Methods

As 1H-phenalene is not commercially available, it was synthesised from commercially available perinaphthenone, reduced with diisobutylaluminum hydride in a one step process by Katie Cergol of the Payne group of the School of Chemistry at The University of Sydney. The sample was placed in a heated sample container near the pulsed nozzle of a PDN.

As the sample was stable in an inert atmosphere, no discharge was needed to observe 1H-phenalene. It was seeded into an argon atmosphere by heating the sample chamber to approximately 390 K, with the temperature monitored by a T-type thermocouple. A General Valve Series 9 pulsed nozzle, similar to those used as part of the PDN described in Chapter 3, was then used to inject the 1H-phenalene seeded argon into the source chamber of the REMPI-TOF chamber, also described in Chapter 3. The source chamber had an operating pressure on the order of 10^{-4} Torr. Supersonic expansion of the seeded argon into the vacuum rapidly cooled and isolated the 1H-phenalene molecules. The coolest part of the jet passed through a 2 mm skimmer into the differentially-pumped interrogation region, between the electrostatic grids of a time of flight mass spectrometer.

For higher excitation energies the R2PI technique, described in Chapter 3, was used to record the spectrum. Excitation and ionisation photons were both produced by one frequency doubled Nd:YAG pumped dye laser. However, when the excitation energy was below half the ionisation energy of 1H-phenalene, a second high energy ionisation laser was required to ionise the excited molecules. This R2C2PI technique is also used in Chapters 4 and 5.

206 nm photons were produced by the frequency doubled output of a second Nd:YAG pumped dye laser and used as the second ionisation source. To reduce the non-resonant ionisation, the UV ionisation beam was defocused. This had the added advantage of increasing the interaction volume between the two laser paths and the molecular beam, improving overall signal.

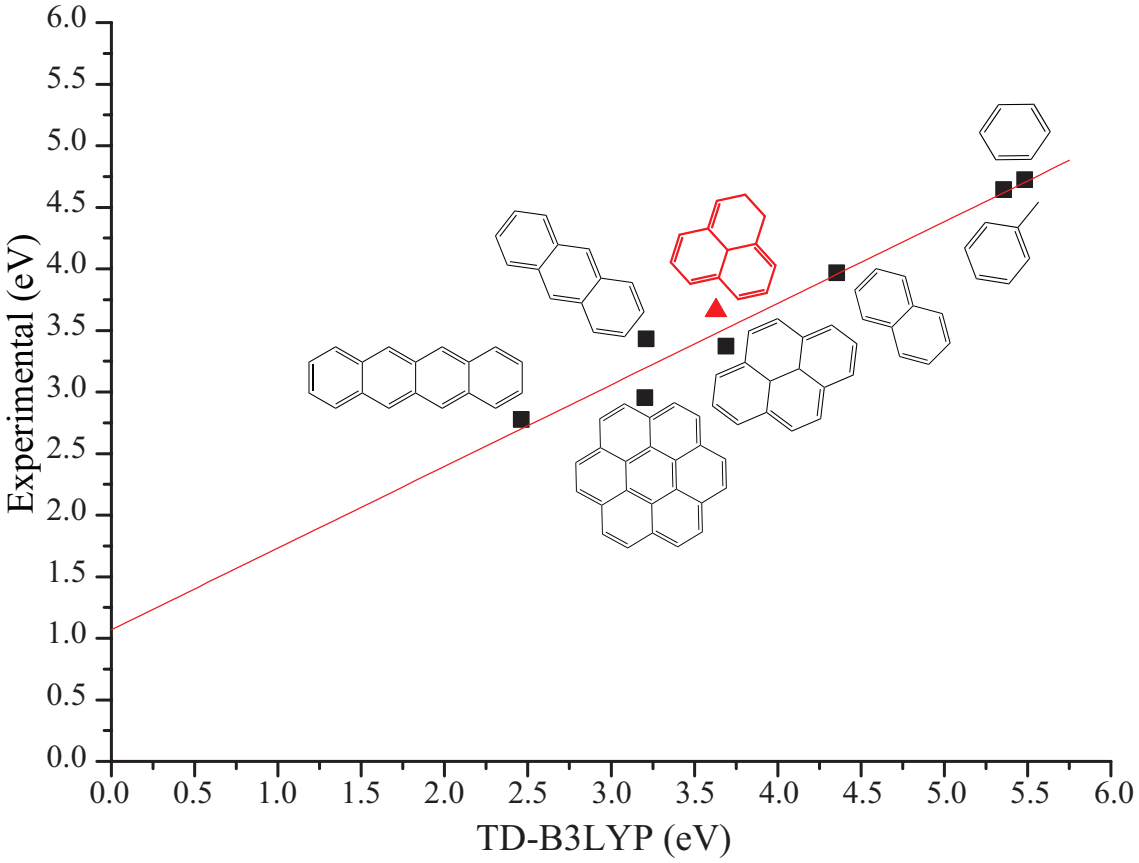

Figure 7.6: Correlation of experimental and TD-B3LYP/6-311++G(d,p) $S_1 \leftarrow S_0$ electronic excitation energies. Experimental values for benzene,[261] toluene,[189] naphthalene,[379] anthracene,[380,381] pyrene,[382] tetracene,[177] and coronene[383] are from literature. The line is a fit through the square black data points

7.4.2 Excitation Energies (TD-DFT and X-MCQDPT2)

TD-B3LYP vertical excitation energies and oscillator strengths of the eight lowest calculated singlet excited states are displayed in Table 7.4. It can be seen that, with the exception of the $S_8 \leftarrow S_0$ transition, the $S_1 \leftarrow S_0$ is predicted to be the strongest of the calculated transitions. This is expected, as the closed-shell 1H-phenalene's lowest possible energy single electron transition is non-degenerate, and this single electron transition is reported as the primary component of the $S_1 \leftarrow S_0$ transition. As such, the lowest energy electronic transition intensity is not susceptible to the Longuet-Higgins intensity splitting reported for the open-shell species observed in Chapters 4 and 5.

In earlier chapters, a linear correlation was observed between $D_1 \leftarrow D_0$ TD-DFT vertical excitation energies of PAH RSRs and experimentally obtained gas-phase transition energies. A similar approach was attempted for the $S_1 \leftarrow S_0$ transitions of neutral PAHs.

Table 7.3: TD-B3LYP $S_1 \leftarrow S_0$ transition energies of neutral closed shell PAHs, calculated with a 6-311++G(d,p) basis.

Mode	Formula	$T_{TD-B3LYP}$ (eV)	$T_{corrected}$ ‡ (eV)	Observed (cm^{-1})	ΔE (eV)
benzene	C_6H_6	5.48	4.70	4.72[261]†	0.02
toluene	C_7H_8	5.36	4.62	4.65[189]	0.03
naphthalene	$C_{10}H_8$	4.35	3.95	3.97[379]	0.01
anthracene	$C_{14}H_{10}$	3.21	3.20	3.43[380,381]	0.24
pyrene	$C_{16}H_{10}$	3.69	3.51	3.37[382]	-0.14
tetracene	$C_{18}H_{12}$	2.46	2.70	2.78[177]	0.08
coronene	$C_{24}H_{12}$	3.20	3.19	2.95[383]†	-0.24
1H-phenalene	$C_{13}H_{10}$	3.63	3.48	3.66	0.18

† - Estimated position of forbidden electronic origin transition ‡ - Corrected values from linear fit $T_{exp} = 0.663T_{TD-B3LYP} + 1.07$. See Figure 7.6

Table 7.4: $D_n \leftarrow D_0$ vertical electronic transition energies, T_v, and oscillator strengths, f, of 1H-phenalene calculated at the TD-B3LYP/6-311++G(d,p) level of theory. The symmetry of the transition moment is given as $\Gamma_{\mu_{n0}}$.

n	$\Gamma_{\mu_{n0}}$	T_v (eV)	f
1	A'	3.63	0.1538
2	A'	4.10	0.0093
3	A'	4.50	0.0009
4	A''	4.65	0.0004
5	A'	4.94	0.0995
6	A''	4.99	0.0000
7	A''	5.05	0.0013
8	A'	5.31	0.3135

The calculated TD-B3LYP/6-311++G(d,p) $S_1 \leftarrow S_0$ vertical excitation energies of benzene, toluene, naphthalene, anthracene, pyrene, tetracene and coronene are listed in Table 7.3, along with their literature experimental gas-phase $S_1 \leftarrow S_0$ energies. It is worth noting that benzene and coronene have forbidden $S_1 \leftarrow S_0$ origin bands. In these cases, the experimental origin positions are being estimated from the observed vibronic structure of these transitions, based on the estimates used in the literature to assign relative frequencies to the observed vibronic transitions.[261,383] Any error which may exist in these estimates is insignificant relative to the errors in the calculated excitation energy.

Figure 7.6 shows a plot of vertical TD-B3LYP excitation energies vs experimental $S_1 \leftarrow S_0$ energies. The line shows the best linear fit to the data, giving a corrected energy $T_{exp} = 0.663T_{TD-B3LYP} + 1.07$. The large intercept and shallow slope show that using uncorrected TD-B3LYP values for estimating the $S_1 \leftarrow S_0$ energy of neutral PAHs would be invalid.

It can be seen that the correlation, with an R^2 value of 0.96, is significantly more scattered than that seen for $D_1 \leftarrow D_0$ transitions of neutral radicals ($R^2 > 0.99$) , or even their

accompanying higher excited states ($R^2 = 0.98$). It was speculated in Chapter 4 that systems with non linear arrangements of aromatic rings, such as the 1-PyMe radical, may diverge from the linear trend due to the centre carbon atoms acting as perturbations to the external ring of sp^2 carbons. However, while this would explain the low observed values of the $S_1 \leftarrow S_0$ transitions of pyrene and coronene, it does not explain the unexpectedly high observed energy of anthracene.

The maximum divergence from the linear fit value is 0.24 eV, seen with both anthracene and coronene. While this does not provide sufficient accuracy to allow for accurate assignments of similar molecules, it does remain a useful guide to experiments.

The 1H-phenalene $S_1 \leftarrow S_0$ transition is predicted, by corrected TD-B3LYP, to have energy at 3.48 eV (28068cm^{-1}). The $S_1 \leftarrow S_0$ origin was observed at 3.66 eV (29527cm^{-1}), which is 0.18 eV above the predicted energy. The uncorrected vertical TD-B3LYP calculation estimates the 1H-phenalene origin remarkably well with a $T_{TD-B3LYP}$ value of 3.63 eV. This is a coincidence, as the $T_{exp} = 0.663T_{TD-B3LYP} + 1.07$ line crosses the $x = y$ line in this region.

7.4.3 1H-Phenalene Spectrum

The recorded 1H-phenalene spectrum is displayed in Figure 7.7. The lowest-frequency band in the spectrum was observed at 29527cm^{-1}. This band is also the strongest band in the spectrum and is assigned as the $S_1 \leftarrow S_0$ electronic origin band of 1H-phenalene. This band has a FWHM of 1.7 cm^{-1}. Other features of the observed spectrum include a number of low frequency vibrational modes, and a dense region of transitions centred about a strong mode with relative frequency 1380 cm^{-1}.

Due to the large number of assignments required, and the large number of assignments possible, the dense region centred about 1380 cm^{-1} will not be assigned during this work. However assignment of the relatively uncluttered low frequency region was attempted. This region is displayed, with assignments, in Figure 7.8.

In C_s symmetry, the observed $S_1 \leftarrow S_0$ electronic transition has total symmetry A' ($A' \leftarrow A'$). As such, vibrational transitions with total symmetry a' will be Franck-Condon allowed. Total symmetry a' can be the result of any combination of in-plane a' transitions or even-quanta of out-of-plane a'' transitions.

The lowest frequency vibrational band, with a relative frequency of 254 cm^{-1}, is significantly lower in energy than ν_{42}, the lowest frequency in-plane mode. As such, this band is

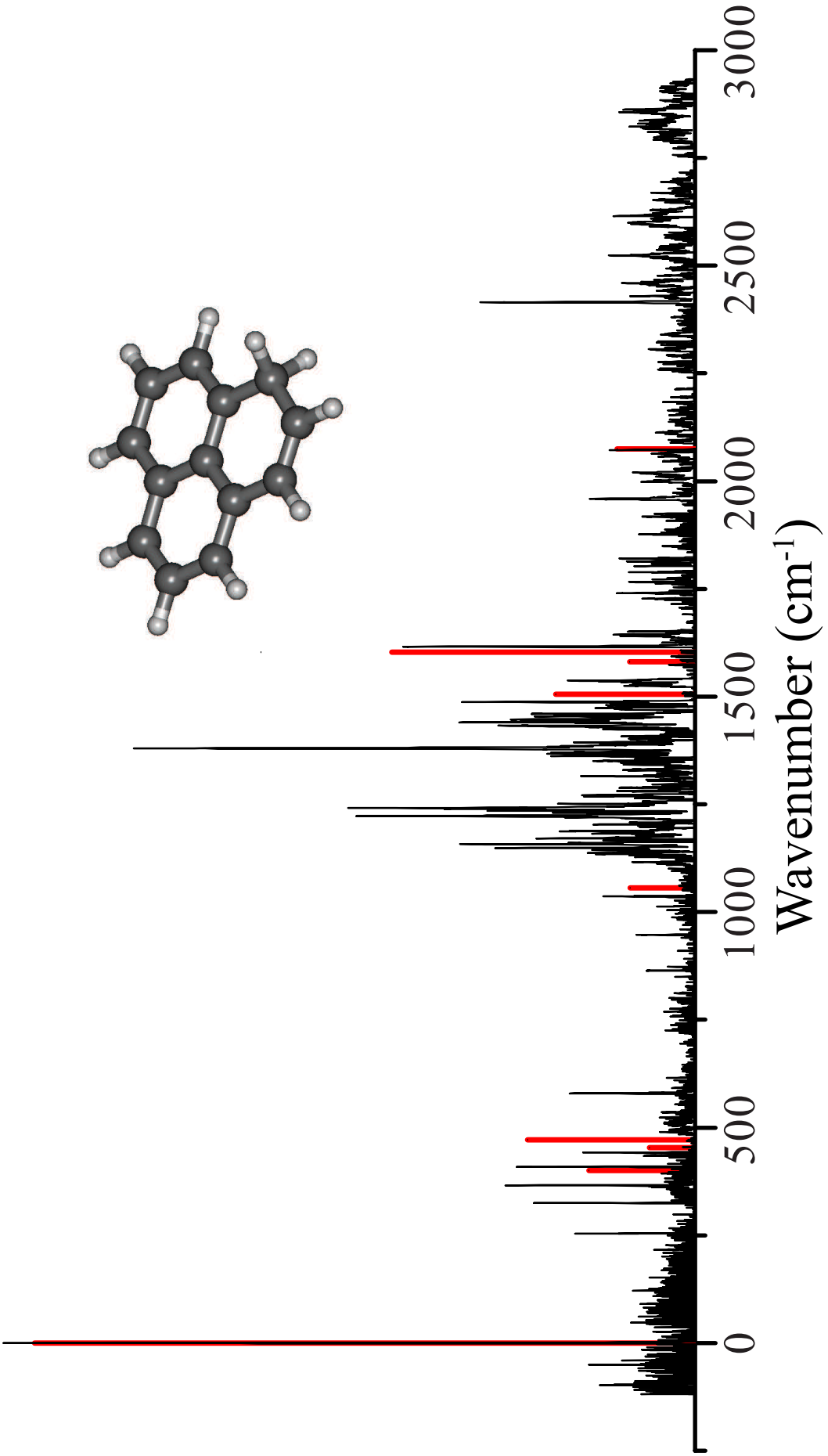

Figure 7.7: Combined REMPI-TOF and TD-B3LYP FCHT spectrum of 1H-phenalene (m/z 166)

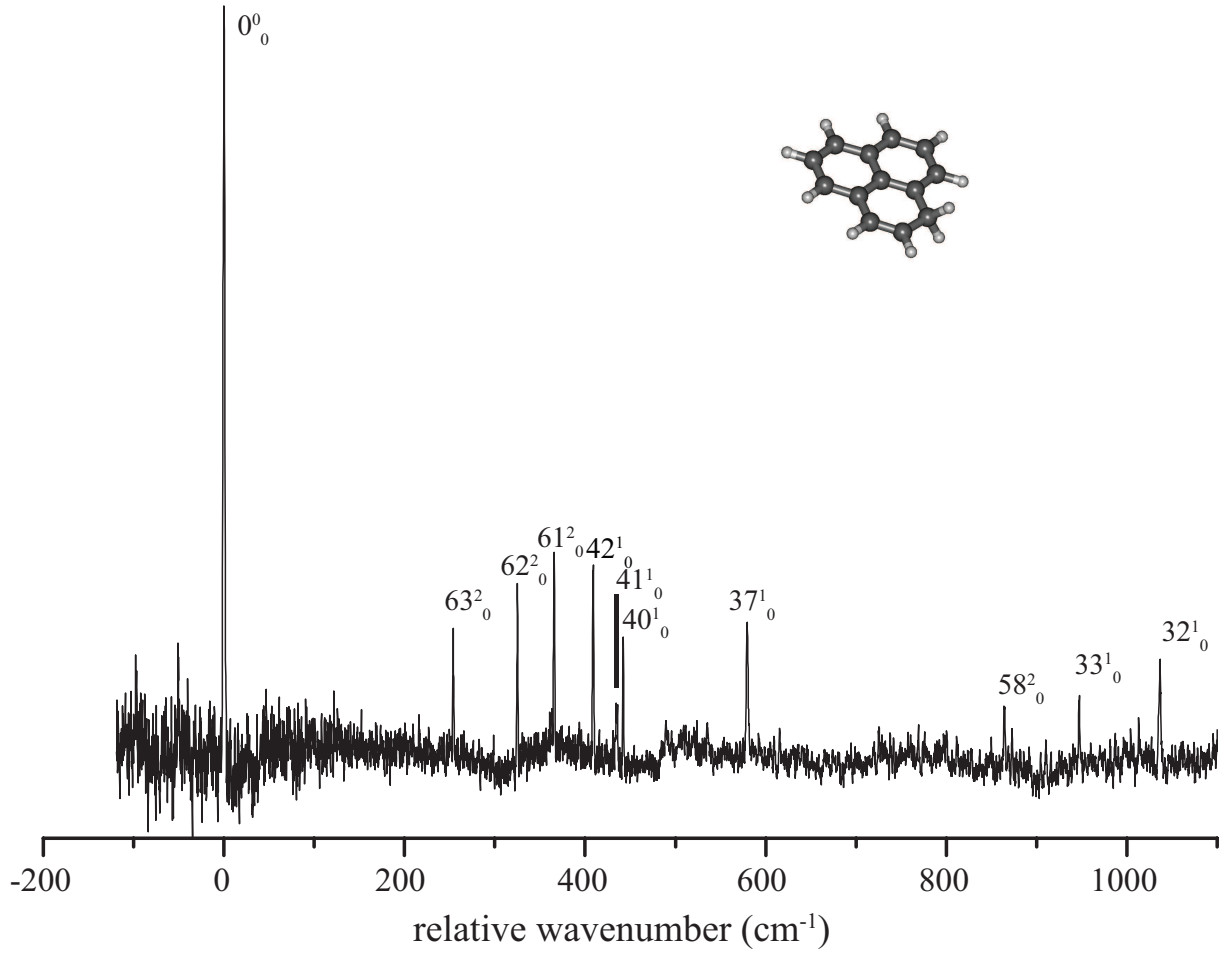

Figure 7.8: Assigned low frequency region of 1H-phenalene (m/z 166) spectrum

assigned to the 2nd-quanta excitation of the lowest frequency out-of-plane mode, ν_{63}, an out of plane torsion of the ring containing the sp_3 hybridised carbon. Table 7.5 shows that the observed frequency of this band is 22 cm^{-1} red of the calculated anharmonic excited-state transition energy, and 30 cm^{-1} blue of the harmonic value. This suggests that the calculation overestimates this vibrational modes anharmonicity. 2-quanta excitations of ν_{62} and ν_{61} are also assigned, and for these the anharmonic frequency calculation performs well, with the observed bands 9cm^{-1} and 15cm^{-1} blue of the calculated values respectively. $2\nu_{60}$ and $2\nu_{59}$ are predicted to have relative frequencies of 486 cm^{-1} and 626 cm^{-1} respectively. No peaks are observed in these regions, however noise around 486 cm^{-1} could possibly be hiding $2\nu_{60}$. Given the low signal-to-noise achieved for this experiment, small transitions are likely to be unobserved. A band with relative frequency 864 cm^{-1} is close in energy to the predicted energy for 2-quanta of ν_{58} and is assigned thus.

The peak observed with relative frequency 409 cm^{-1} is assigned to the lowest frequency

Table 7.5: Experimental and calculated relative frequencies, in cm^{-1}, for assigned low frequency vibrational bands of 1H-phenalene. All calculations performed at the TD-B3LYP/6-311++G(d,p) theory level. ΔE is the energy difference between the anharmonic and the experimental frequency in cm^{-1} (where anharmonic frequency isn't calculated, harmonic frequency was used).

Assignment	Experimental	Harmonic	Anharmonic	ΔE
$2\nu_{63}$	254	224	276	22
$2\nu_{62}$	325	304	316	-9
$2\nu_{61}$	366	384	351	-15
$2\nu_{58}$	864	886	884	-15
ν_{42}	409	401	398	-11
ν_{41}	435	420	420	-15
ν_{40}	442	453	447	5
ν_{37}	580	602	602	22
ν_{33}	947	964		17
ν_{32} †	1036	1031		-5
ν_{10}	1616	1603	1606	-13

† - Tentative assignment

in-plane a' mode ν_{42}, with a calculated anharmonic frequency of 398 cm^{-1}. Similar assignments are made for modes ν_{41}, ν_{40}, ν_{37}, ν_{33} and ν_{32}. It can be seen in table 7.5 that the in-plane a' modes are relatively harmonic. As such, relatively inexpensive harmonic frequencies were used for the assignment of a' modes ν_{33}, ν_{32}.

To attempt to assign the high intensity peaks at higher energies, TD-B3LYP/6-311++G(d,p) FC and FCHT simulations were calculated. These methods were shown to be able to successfully simulate radical spectra in Chapter 2, however success was limited with this closed-shell molecule.

The FC, FCHT and anharmonic calculations all suggest that ν_{10} should be strong, and this is assigned to the strong band observed at 1616 cm^{-1}.

The band at 1036 cm^{-1} is closest in energy to the calculated harmonic frequency of ν_{32}. However, ν_{31} is predicted to be more intense in the FCHT simulation. The original assignment of ν_{32} is tentatively retained, due to the generally poor agreement between simulated and observed intensities.

None of the simulations predict a strong transition at 1380 cm^{-1}. Due to the congestion in this region, combination bands are required to explain the sheer number of peaks. As such, energetically, there are many possible assignments in this region. For now, this transition remains unassigned.

Table 7.6: Theoretic IEs, provided by Dr Bun Chan

Method	kJ/mol	eV
B3LYP/6-31G(d)	661.9	6.86
B3LYP/6-311++G(3df,3pd)	688.1	7.13
G3X(MP2)-RAD	729.7	7.56
G4(MP2)-6X	734	7.61
CCSD(T)-F12b/A'VDZ	717.9	7.44

Experiment brackets result between 7.47 eV and 7.43 eV

7.4.4 Ionisation Energy

While recording the spectrum using R2PI, no bands were observed below 30107 cm^{-1} (ν_{37} - relative frequency 580 cm^{-1}). When the second, 206 nm, ionisation laser was introduced lower frequency bands could be observed.

The most likely reason for this behaviour is that 29970 cm^{-1} photons (the energy of ν_{40}, the next highest energy band) do not have enough energy to ionise the 1H-phenalene molecule from the state of the same energy. This gives upper and lower bounds for the ionisation energy (IE) of 1H-phenalene of 7.47 eV and 7.43 eV respectively.

Troy *et. al.*[200] demonstrated a simple method for accurately calculating the IE of RSRs. For the molecules examined, vertical IEs calculated with the B3LYP/6-311++G(3df,3pd) and G3X(MP2)-RAD level of theory bracket the experimental result for a range of RSRs tested. It is of interest to learn if this method is also valid for closed-shell molecules such as 1H-phenalene.

Dr Bun Chan calculated the IE of 1H-phenalene as part of this work. His values are tabulated in Table 7.6. Here it can be shown that, as with Troy *et. al.* B3LYP/6-311++G(3df,3pd) and G3X(MP2)-RAD bracket the experimental result, with the higher level CCSD(T)-F12b/A'VDZ result of 7.44 eV falling within the experimental range.

7.4.5 Astronomical Relevance

The $S_1 \leftarrow S_0$ transition of 1H-phenalene is observed in the UV region, significantly too high in energy to be a carrier of the DIBs, which are observed in the visible and NIR regions of the spectrum.[144,145] Additionally, while having a strong origin, the strong vibrational bands would likely be visible in any spectra where the origin could be observed, and therefore this 1H-phenalene also violates the non-correlation criteria for the DIBs.[146]

As mentioned previously, 1H-phenalene can be considered the smallest model system for edge addition of hydrogen to radical graphene fragments, creating defects in their outer pi-orbital structure. H-addition to peripheral sp^2 carbons of sufficiently larger open shell graphene fragments will have visible spectra. Given the relatively small FWHM of 1H-phenalene, it is likely that larger edge H-defected graphene fragments will have widths appropriate to the DIBs. Whether or not these larger molecules are origin dominated remains to be seen.

However, spectroscopically, these H-defected graphene fragments are unlikely to differ significantly from other large neutral closed-shell PAHs. The $S_1 \leftarrow S_0$ transition of tetracene is observed in the visible and has a strong origin with a 20 ns lifetime, but it also has a second strong vibronic peak 314 cm^{-1}above the origin transition.[384] The largest PAH observed in the gas-phase, Hexa-*peri*-hexabenzocoronene ($C_{42}H_{18}$),[176] also had spectral properties, width and frequency, relevant to the DIBs. Comparison to astronomical spectra eliminated these molecules as potential carriers.

Hexa-*peri*-hexabenzocoronene has the same D_{6h} symmetry as benzene. As such, the origin band of the $S_1 \leftarrow S_0$ transition of this molecule is forbidden, and only vibronic structure was observed. An experimental study of a closed-shell molecule of a lower symmetry with a similar sized chromophore to Hexa-*peri*-hexabenzocoronene may be an interesting direction for future work, to determine if such species are likely to have strong origin dominated $S_1 \leftarrow S_0$ transitions.

7.5 Phenalenylium$^+$ Closed-Shell Cation

As mentioned in previous chapters, the $D_1 \leftarrow D_0$ transitions of PAH RSRs are generally very weak, much weaker than the $f = 10^{-2}$ assumed in previous models for proposed DIB generating PAHs.[140] Chapter 5 discusses how this is caused by the electronic structure of odd-alternate hydrocarbon radicals, which results in a splitting of intensity between a weak $D_1 \leftarrow D_0$ transition and a stronger high-energy transition.[338,342]

For closed-shell cations, the lowest-energy electronic transition is often, but not always, dominated by the single-electron transition from the HOMO to the LUMO (which is the same as the transition from the HOMO to the SOMO in the radical). As a result, only one electronic transition is formed from. As the intensity is not shared amongst multiple transitions, these $S_1 \leftarrow S_0$ transitions are often strong, visible, bands of narrow width. It has been shown that the UV flux of certain DIBs would require molecules to have IEs of

10 eV or more.[149] Neutral RSRs have relatively low ionisation energies (∼6 eV),[200] and as such these species are likely to exist in their ionised forms.

The $S_1 \leftarrow S_0$ transitions of several closed-shell protonated PAHs have been observed,[208,209,385,386] as many of these species will dissociate on excitation to form a PAH radical cation and a hydrogen atom.[208,209,385,386] This photodissociation has been used as the basis for the recording of action spectra.[208,209,385,386] Previous experimental studies have shown that the $S_1 \leftarrow S_0$ transitions of small closed shell cations have long Franck-Condon progressions.[207] However, theoretical simulations suggest that larger closed-shell cations will trend towards a more origin dominated vibronic structure.[352]

An experimental search for the $1^1E' \leftarrow X^1{A_1}'$ transition of the phenalenylium$^+$ closed-shell cation by argon-tagged photo-fragmentation spectroscopy was unsuccessful. This was because the quadrupole mass filters of the apparatus used were unable to differentiate between phenalenylium$^+$ (m/z 165) and the significantly more abundant ionised form of the parent molecule, 1H-phenalenium$^+$ (m/z 166) (the spectrum of which is presented later in this chapter). Phenalenylium$^+$ remains theoretically and astronomically interesting. This section includes theoretical results aimed at estimating the $1^1E' \leftarrow X^1{A_1}'$ excitation energy of phenalenylium$^+$. Theoretical results are also presented for two phenalenyl structures with a carbon substituted with nitrogen. These heteroatomic species are stable and isoelectronic with the phenalenylide$^-$ anion.

7.5.1 Theoretical Results

TD-B3LYP and X-MCQDPT2 vertical transition energies and intensities of phenalenylium$^+$ were calculated for the four lowest excited states, and these are shown in Table 7.7. It can be seen from this table that the strong E' transition of interest is predicted to be a transition to the second excited state. The transition to the lower-energy dark state has a transition dipole moment symmetry of ${A_2}'$, and is dominated by the single-electron transition from the highest occupied ${A_2}''$ molecular orbital to the ${A_1}''$ LUMO. The simple Huckel model predicts the highest occupied ${A_2}''$ and E'' orbitals to be degenerate in the phenalenylium$^+$ closed-shell cation. This degeneracy is split very slightly by higher-level theory, with the ordering changing based on the level of theory.

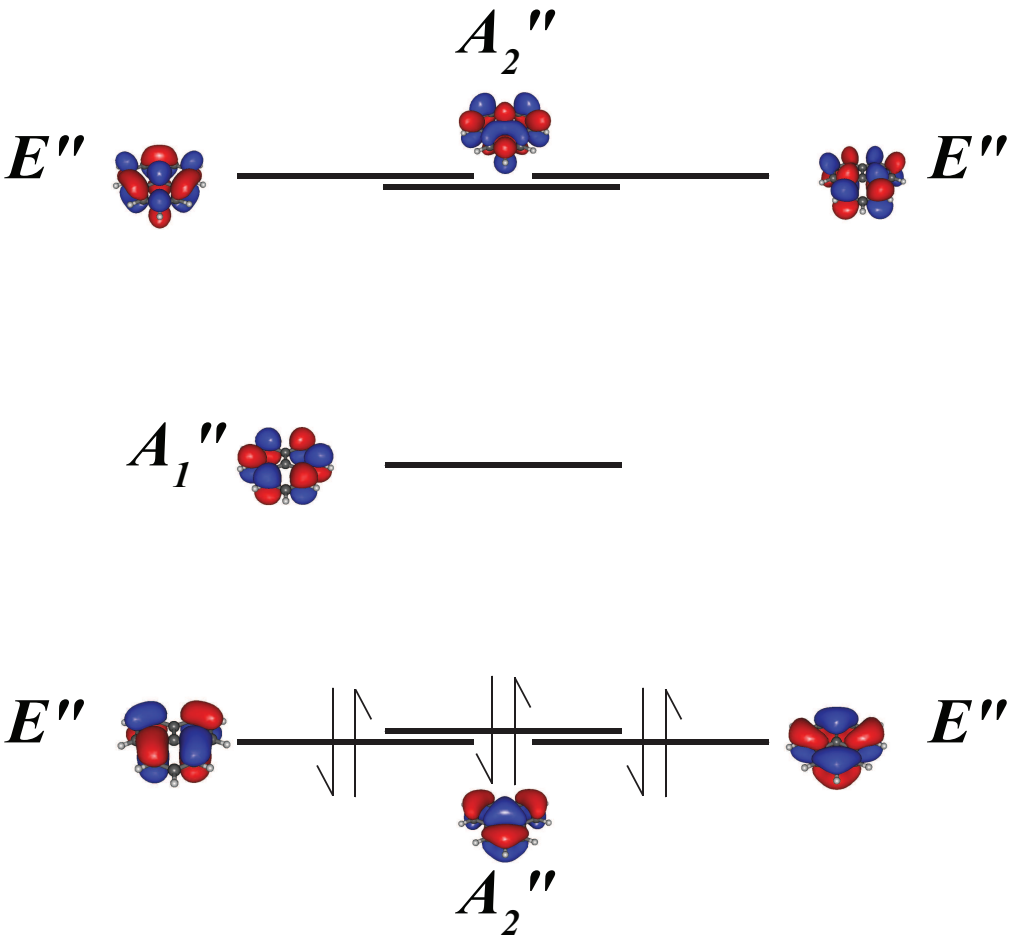

Figure 7.9: Frontier RHF orbitals of the phenalenylium$^+$ closed-shell cation. The occupied A_2'' and E'' orbitals are near-degenerate

Table 7.7: $S_n \leftarrow S_0$ vertical electronic transition energies (eV) and squared transition dipole moments μ^2 (Debye^2), of the phenalenylium$^+$ closed-shell cation calculated at the TD-B3LYP/6-311++G(d,p) and X-MCQDPT2[7,7]/tzv(2df,p).

	TD-B3LYP/6311++G(d,p)			X-MCQDPT2[7,7]/tzv(2df,p)		
Transition	Γ_μ	T_v	μ^2	Γ_μ	T_v	μ^2
$S_1 \leftarrow S_0$	A_2'	2.74	0.0000	A_2'	2.02	0.0000
$S_2 \leftarrow S_0$	E'	3.53	2.1141	E'	2.78	2.5707
$S_3 \leftarrow S_0$	E''	4.73	0.0000	E'	4.79	0.6773
$S_4 \leftarrow S_0$	E'	5.43	0.0143	E'	5.04	0.4236

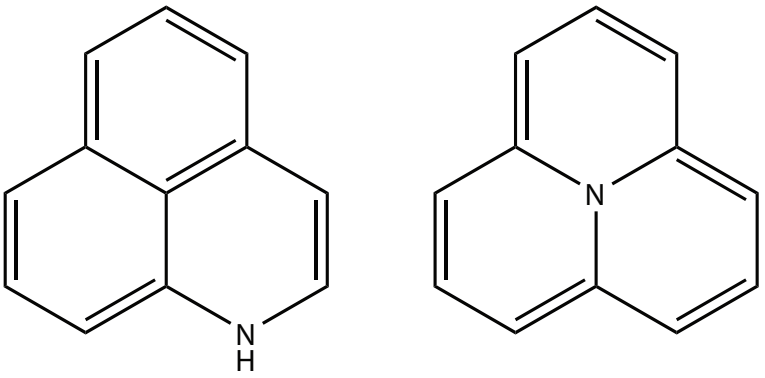

Figure 7.10: Structure of Nitrogen containing heteromolecules: 1H-azaphenalene (left) and 9b-azaphenalene (right)

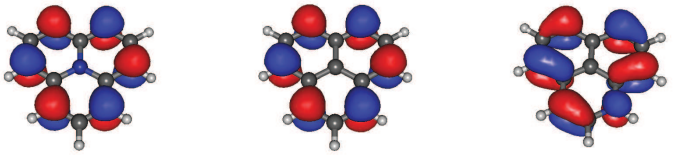

Figure 7.11: RHF orbitals of the HOMO of : 9b-azaphenalene (left), the phenalenylide$^-$ closed-shell anion (centre) and 1H-azaphenalene (right). Calculated with a 6-311++G(d,p) basis set in GAUSSIAN09

7.5.2 Nitrogen containing phenalenyl molecules

Heteroatomic substitution of nitrogen into the structure of the phenalenyl radical gives two stable species, 1H-azaphenalene and 9b-azaphenalene. These structures are shown in Figure 7.10. Nitrogen containing PAHs (PANHs) have been widely suggested as carriers of interstellar spectra.[387–390]

TD-B3LYP/6-311++G(d,p) calculations show the 1H-azaphenalene isomer, which is commercially available, to be 108 kJ/mol lower in energy than 9b-azaphenalene. While arguably less interesting from a theoretical standpoint, if 1H-azaphenalene has visible transitions, recording its gas-phase spectrum would be of significant astronomical interest and a priority for future experimental studies.

9b-azaphenalene maintains the phenalenyl radical's D_{3h} structure and is isoelectronic with the phenalenylide$^-$ closed-shell anion. As such, it is a highly resonance-stabilised species. The synthesis of 9b-azaphenalene has been known for some time.[391] π-stacked dimers of 9b-azaphenalene, and its boron doped equivalent 9b-borophenalene, have recently been the subject of high-level quantum chemistry calculations in a paper by Tian *et. al.* which suggested that molecules based on these motifs may be ingredients for the development of molecular spin-electronic (or "spintronics") devices.[392,393]

Table 7.8: $S_n \leftarrow S_0$ vertical electronic transition energies (eV) and oscillator strength calculated at the TD-B3LYP/6-311++G(d,p) level of theory.

	phenalenyl			phenalenylide$^-$		
Transition	Γ_μ	$T_{TD-B3LYP}$	f	Γ_μ	$T_{TD-B3LYP}$	f
$S_1 \leftarrow S_0$	E'	2.79	0.0005	A_2'	2.60	0.0000
$S_2 \leftarrow S_0$	A_2'	3.01	0.0000	E'	3.43	0.1877
$S_3 \leftarrow S_0$	A_2'	3.29	0.0000	A_1''	3.54	0.0000
$S_4 \leftarrow S_0$	E'	2.03	0.1884	E''	3.93	0.0000
	9b-azaphenalene			1H-azaphenalene		
Transition	Γ_μ	$T_{TD-B3LYP}$	f	Γ_μ	$T_{TD-B3LYP}$	f
$S_1 \leftarrow S_0$	A_2'	1.24	0.0000	A'	3.20	0.0235
$S_2 \leftarrow S_0$	E'	3.32	0.1567	A'	3.74	0.1238
$S_3 \leftarrow S_0$	A_1''	4.25	0.0000	A'	4.01	0.1226
$S_4 \leftarrow S_0$	E''	4.87	0.0143	A''	4.48	0.0002

Comparison of the spectral properties of the 1H-azaphenalene and 9b-azaphenalene allows the effect of symmetry in aromatic molecules to be observed. TD-B3LYP/6-311++G(d,p) energies and oscillator strengths for phenalenyl, phenalenide$^-$, 1H-azaphenalene and 9b-azaphenalene are tabulated in Table 7.8. They show that phenalenylide$^-$ and 9b-azaphenalene are predicted to have very similar electronic properties, with the difference in nuclear charge resulting in a 0.11 eV (887 cm^{-1}) red-shift of the strong E' transition in 9b-azaphenalene.

The C_s 1H-azaphenalene has significantly different predicted spectroscopic properties. The $S_1 \leftarrow S_0$ transition of 9b-azaphenalene/phenalenylide$^-$ is calculated to be the dark $A_2{}'$ ($1^1A_2{}' \leftarrow X^1A_1{}'$) transition, which is symmetry forbidden.

1H-azaphenalene's $S_1 \leftarrow S_0$ transition ($1^1A' \leftarrow X^1A'$) has total symmetry of A', and as such is symmetry allowed. This transition is calculated to have significant oscillator strength (f=0.0235).

Conceptually, this can be further understood from the RHF HOMO's displayed in Figure 7.11. For all three species, the $S_1 \leftarrow S_0$ transition is dominated by the single-electron transition from the A_1'' HOMO ($A_1{}''$ in the D_{3h} species) to the A_2'' LUMO ($A_2{}''$ in the D_{3h} species). In 9b-azaphenalene and phenalenylide$^-$ the wavefunctions of the $A_1{}''$ HOMO have very little overlap with the corresponding wavefunction of the $A_2{}''$ LUMO (similar to the phenalenylium$^+$ unoccupied $A_2{}''$ orbital in Figure 7.9). The presence of the electronegative nitrogen atom on the peripheral ring distorts the HOMO (and LUMO) of 1H-azaphenalene. This gives significant overlap between the wavefunctions of the A'' HOMO and LUMO.

TD-B3LYP predicts both azaphenalene species to have strong transitions in the near UV. Using the correction factor for the $S_1 \leftarrow S_0$ transitions of closed-shell neutral PAHs in

the previous section, 1H-azaphenalene is predicted to absorb at approximately 3.19 eV (25729 cm^{-1}, 389 nm). While this transition energy is slightly high for the DIBs, the accuracy of this correction of TD-B3LYP for PANHs is uncertain, and these molecules may still be of interstellar interest, as may larger nitrogen substituted graphene fragments.

7.6 1H-Phenalenium Radical Cation

During the unsuccessful attempt to observe the $1^1E'' \leftarrow {}^1A_1'$ transition of the phenalenylium$^+$ closed shell cation ($C_{13}H_9^+$) the 1H-phenalenium$^+$ radical cation ($C_{13}H_{10}^+$) was observed.

The same arguments suggesting the potential for hydrogen attack of the unpaired electron of phenalenyl (or larger open-shell graphene fragments) in the ISM are equally valid for proton addition. Protons have a high relative abundance in the ISM, and charged particles are likely to be formed due to the high flux of ionising radiation present. An additional route to production would be hydrogen attack of closed-shell cationic graphene fragments.

1H-phenalene has been previously observed in a 77 K freon matrix by Bally *et. al.*[270] The argon tagged 1H-phenalenium$^+$ spectrum reported in this chapter reproduces all the features observed in the matrix (within the limits of our spectrum). This results in minor corrections to the assignments of Bally *et. al.*[270] as any features observed in the photofragmentation spectrum must be assigned to cationic species. Indeed, all transitions reported in this section are assigned to the 1H-phenalenium$^+$ radical cation.

7.6.1 Experimental Methods

The argon-tagged spectrum of the 1H-phenalenium$^+$ radical cation was recorded using the photofragmentation spectrometer previously described in Chapters 3 and 6.

As previously reported in this chapter, 1H-phenalene was synthesised from commercially available perinaphthenone, reduced with diisobutylaluminum hydride in a one step process by Katie Cergol of the Payne group of the School of Chemistry at The University of Sydney. This parent sample was heated in argon behind the pulsed nozzle, seeding the argon with 1H-phenalene. An electrospray source was used to create 1H-phenalenium$^+ \cdots$Ar clusters which were then cooled in the free jet expansion and skimmed before being guided into the first quadrupole mass filter by ion optics.

Table 7.9: 1H-phenalenium$^+$ vertical electronic transition energies (eV) and squared transition dipole moments μ^2 (Debye^2), calculated at the TD-B3LYP/6-311++G(d,p) and X-MCQDPT2[7,7]/tzv(2df,p).

Transition	Symmetry	$T_{TD-B3LYP}$	$\mu^2_{TD-B3LYP}$	$T_{X-MCQDPT2}$	$\mu^2_{X-MCQDPT2}$
$D_1 \leftarrow D_0$	$2^2A'' \leftarrow 1^2A''$	1.61	0.0010	1.08	0.0034
$D_2 \leftarrow D_0$	$3^2A'' \leftarrow 1^2A''$	1.92	0.1476	1.49	0.2895
$D_3 \leftarrow D_0$	$4^2A'' \leftarrow 1^2A''$	2.66	0.0414	2.26	0.0425
$D_4 \leftarrow D_0$	$5^2A'' \leftarrow 1^2A''$	3.15	0.3320	2.58	0.4272
$D_5 \leftarrow D_0$	$6^2A'' \leftarrow 1^2A''$	3.56	0.0023	3.50	0.0081

The first mass filter (preceding the photofragmentation region) was set to the m/z 206 of the 1H-phenalenium$^+ \cdots$Ar cluster, while the second mass filter was set to the m/z 166 of the bare 1H-phenalenium$^+$ radical cation. When the 1H-phenalenium$^+ \cdots$/Ar cluster absorbs photons and fragments, signal is observed by the increased observation of 1H-phenalenium$^+$. Laser power was recorded and all spectra shown are power-corrected, with the exception of the low power scan of the $D_4 \leftarrow D_0$ region shown in figure 7.14. Due to limited sample and low signal-to-noise, only the "visible" region of the OPOTEK VIBRANT 355 OPO was scanned. Observation at higher energies using Sum-Frequency-Mixing was attempted. However, signal was not observed despite the fact that the high energy tail of the peak assigned to the $D_4 \leftarrow D_0$ transition being in this region. Repeated scans suggested signal in the region of the peak assigned to the phenalenylium$^+$ closed-shell cation by Bally *et. al.*,[270] but signal-to-noise was insufficient to confirm observation. Even if this peak was observed, this work cannot determine if the band was due to 1H-phenalenium$^+$ or phenalenylium$^+$ due to the limit of resolution of the quadrupole mass filters at high masses, m/z 165 and m/z 166 being indistinguishable in this experiment (unlike the REMPI-TOF experiments which have isotopic resolution in the m/z regime of all species observed in this work).

7.6.2 Theoretical Results

Calculated vertical excitation energies and squared transition dipole moments of the 1H-phenalenium$^+$ radical cation are shown in Table 7.9. It has been shown in Chapter 5 that X-MCQDPT2 treats the lower and higher excited states of RSRs equally and that a linear fit through the origin and the observed states will approximate the transition energy of higher excited states with a scaling factor. To determine this scaling factor, it was assumed the three largest observed bands correspond to $D_2 \leftarrow D_0$, $D_3 \leftarrow D_0$ and $D_4 \leftarrow D_0$. This gives a a relatively small scaling factor of 1.133. This assumes the energy shift from argon

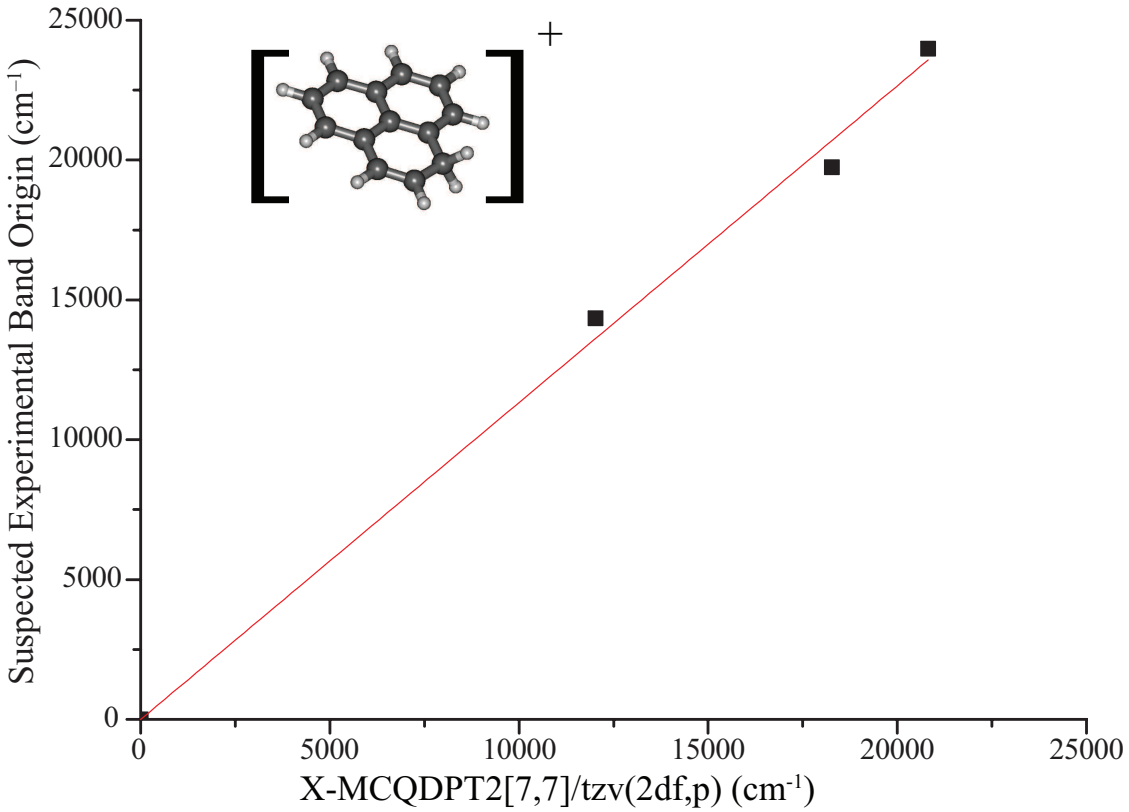

Figure 7.12: X-MCQDPT2[7,7]/tzv(2df,p) vertical electronic transition energies of 1H-phenaenium$^+$ vs experimental energies of suspected origin bands of argon tagged 1H-phenalenium$^+$ radical cation. Red line has slope 1.133 and has a fixed [0,0] intercept. All transitions are $A'' \leftarrow A''$

tagging is relatively small compared to the differences in predicted energy, which would be expected based on past studies.[207,318]

This scaling factor is used to plot a stick spectrum of the region of interest, allowing predicted intensity to act as an additional aid to assignment. This stick spectrum is superimposed on the argon-tagged photofragmentation spectrum of 1H-phenalenium$^+$ in Figure 7.13.

7.6.3 Argon-Tagged 1H-phenalenium Radical Cation Spectrum

The resonant photodissociation spectrum of the 1H-phenalenium$^+ \cdots$Ar complex is shown in Figure 7.13. The increased noise at the low-energy end of the spectrum is an artifact of power-correction.

The first transition is observed as a broad strong band, which begins before the lower limit of our scan, centred on $\sim$14358 cm^{-1} with FWHM $\sim$1120 cm^{-1}. The high energy end of this band appears to be convoluted by unresolved vibrational transitions (such as

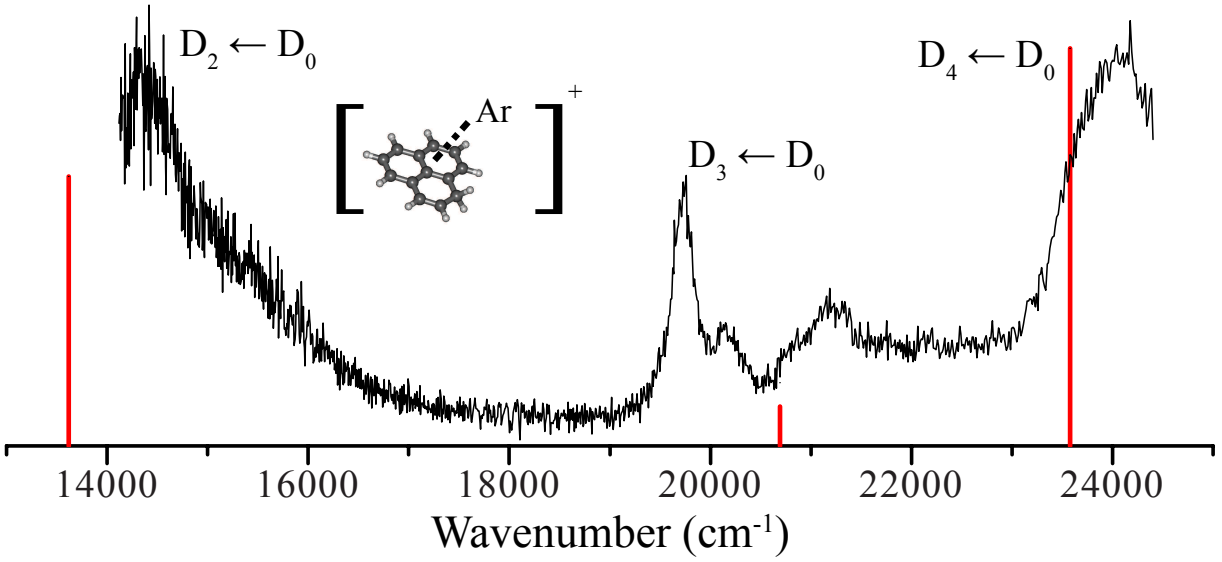

Figure 7.13: Black: Argon-tagged photofragmentation spectrum of 1H-phenalenium$^+$ radical cation; Red: X-MCQDPT2[7,7]/tzv(2df,p) stick spectrum (red) for the 1H-phenalenium$^+$ radical cation. Calculated transition energies are scaled by 1.13. All transitions are $A'' \leftarrow A''$

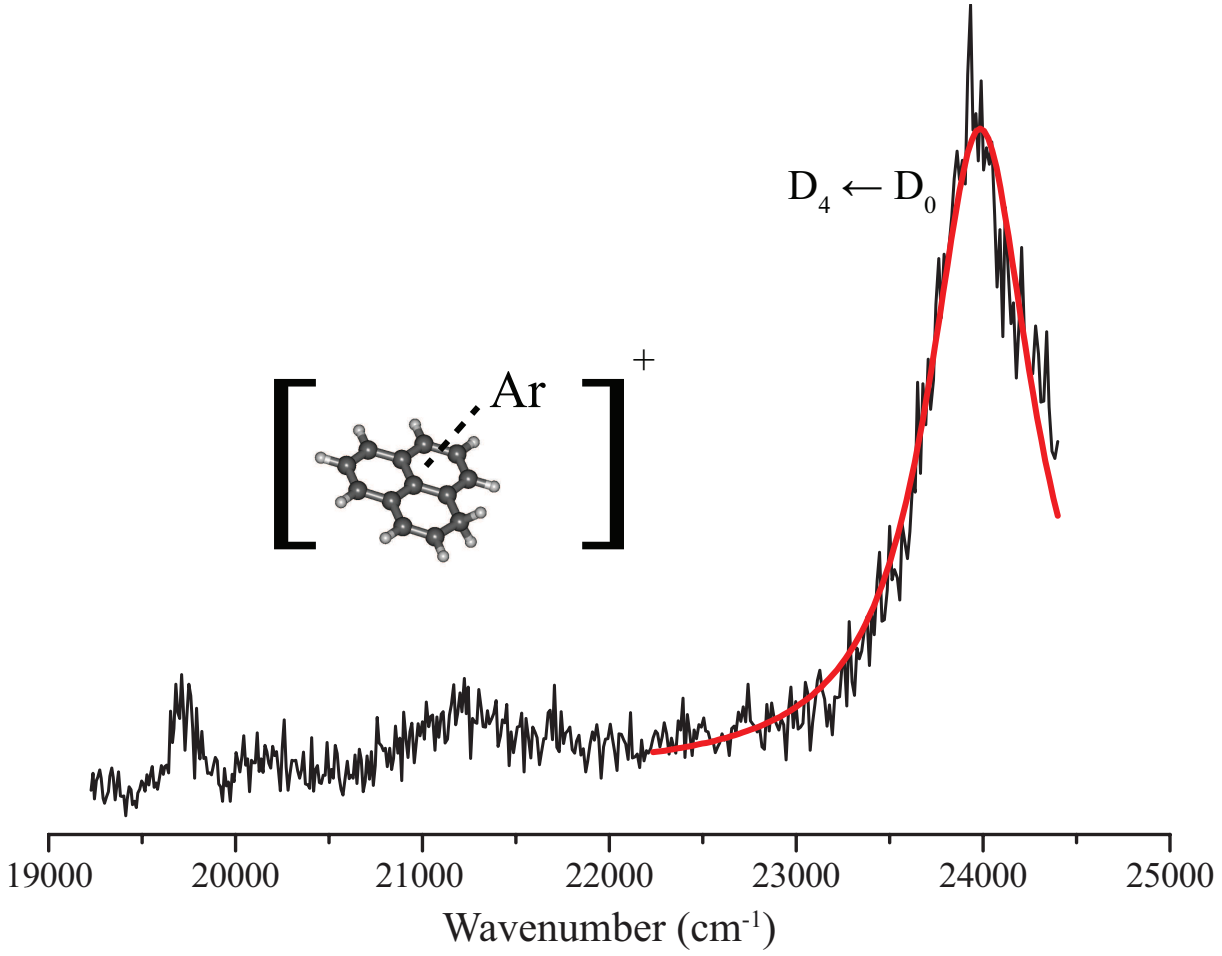

Figure 7.14: Black: Low power argon-tagged photofragmentation spectrum of 1H-phenalenium$^+$ radical cation; Red: lorenzian fit to band centered 23985 cm^{-1}, width 680 cm^{-1}

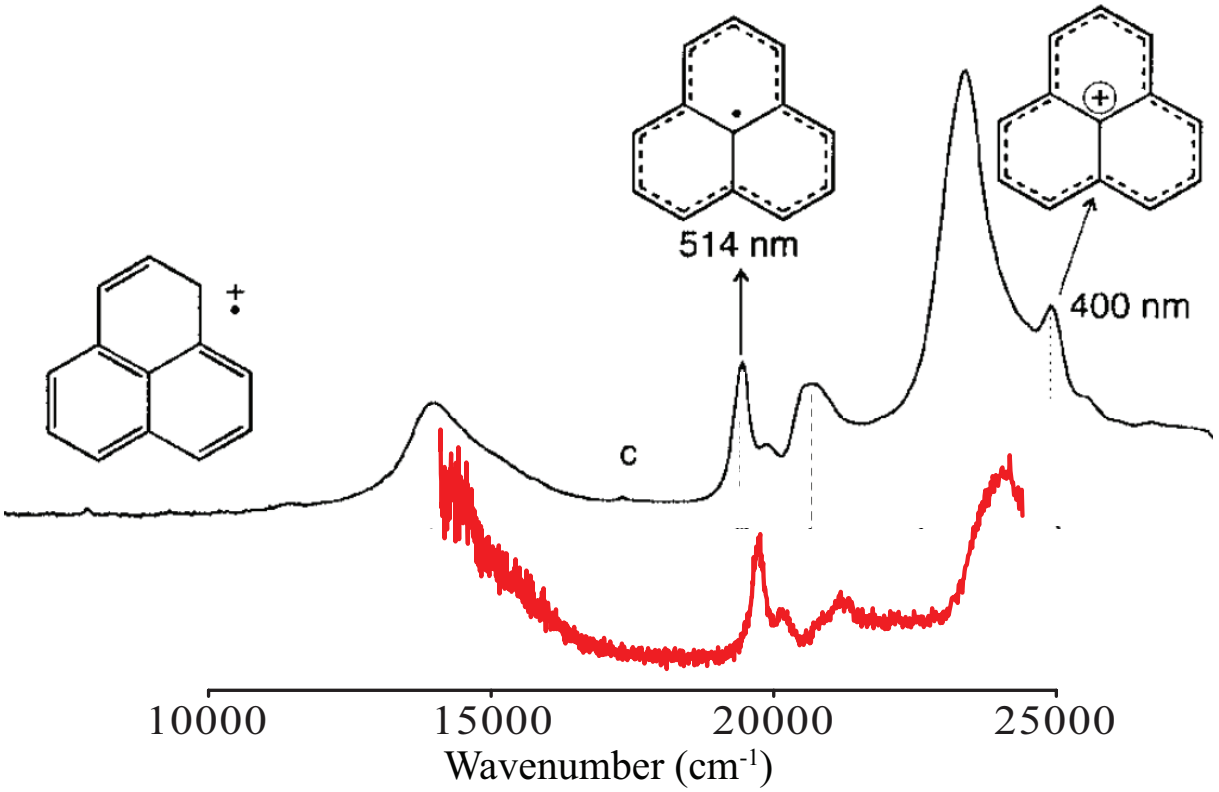

Figure 7.15: Comparison between the matrix spectrum recorded and assigned by Bally *et.al.* 2000 (black) and the argon-tagged spectrum of 1H-phenalenium$^+$ recorded in this work (red). As all bands in the red argon-tagged spectrum must be cationic spiecies, the transition assigned to the phenalenyl radical is instead likely due to phenalenium$^+$

the spectra observed in Chapter 5). This is similar to the band observed, and assigned as $D_2 \leftarrow D_0$, by Bally *et. al.*,[270] as seen in Figure 7.15.

The next transition observed has a lorentzian band profile centred about 19735 cm^{-1} with width 287 cm^{-1}. Figure 7.15 shows that this feature was assigned by Bally *et. al.*[270] as being carried by the phanelenyl radical. This is an understandable assignment. The strongest vibronic band (ν_{25}) of the $1^2E'' \leftarrow 1^2A_1''$ ($D_1 \leftarrow D_0$) state of the phenalenyl radical had been previously observed in the matrix in this region by Cofino *et. al.*[269] and has since been since recorded by the author to have a gas-phase frequency of 19560 cm^{-1}.[201] However, as neutral species such as phenalenyl cannot be detected by the photofragmentation spectrometer used to record the spectrum in Figure 7.13, the carrier of this band must be a catiotic species with m/z of approximately 166. Given this, the transition is reassigned as the electronic origin of the $D_3 \leftarrow D_0$ transition of the 1H-phenalenium$^+$ radical cation. The argument could be made that this feature is the $1^1E'' \leftarrow X^1A_1{}'$ transition of the phenalenylium$^+$ closed-shell cation. However, this is unlikely as the intensity of this peak correlates well with the other observed transitions, when compared to the spectrum of Bally *et. al.*[270] and between repeated scans in this work. Additionally, the observed band

Table 7.10: Experimentally derived argon tagged 1H-phenalenium$^+$ origin energies and lifetimes

State	Energy (cm^{-1})	Width (cm^{-1})	Lifetime (fs)
$D_2 \leftarrow D_0$	14357	990	5.4
$D_3 \leftarrow D_0$	19735	287	19
$D_4 \leftarrow D_0$	23985	680	7.8

is significantly lower in energy than the calculations earlier in this paper suggest for the $1^1E'' \leftarrow X^1A_1{}'$ transition energy of the phenalenylium$^+$ closed-shell cation. The smaller features at slightly higher energy, assigned by Bally *et. al.*[270] as the electronic origin of the $D_3 \leftarrow D_0$ transition of the 1H-phenalenium$^+$ radical cation are instead assumed to be vibronic features of the same state.

The remaining feature is a large band at the high energy end of the scanned region. Laser power in this region is significantly higher than for the rest of the scan. As such, to eliminate power broadening effects, a low-power scan was performed of this region. This allowed a lorentzian to be fit centred on 23985 cm^{-1} with a width of 680 cm^{-1}. This peak is assigned as the $D_4 \leftarrow D_0$ transition of the 1H-phenalenium$^+$ radical cation, as shown in Figure 7.13.

The experimentally determined energies, widths and lifetimes for the observed states are listed in Table 7.10. Unlike the 9-MeAn$^+$ radical cation in Chapter 6, there is no methyl-rotor to potentially broaden the band profile of 1H-phenalenium$^+$, allowing accurate estimation of the lifetime of the state via the Heisenberg relationship.

$$\delta E = \frac{\hbar}{\delta \tau} \tag{7.1}$$

These lifetimes are tabulated in Table 7.10

Figure 7.16 shows that a plot of the tabulated lifetimes *vs* the energy gap approximately follow the expected log/linear relationship, however some deviation is observed.

While there is significant difference in the lifetimes of the states observed, all transitions are significantly broader than any observed DIB. This is unsurprising, as it is consistent with all previously observed visible transitions or PAH resonance stabilised radical cations.

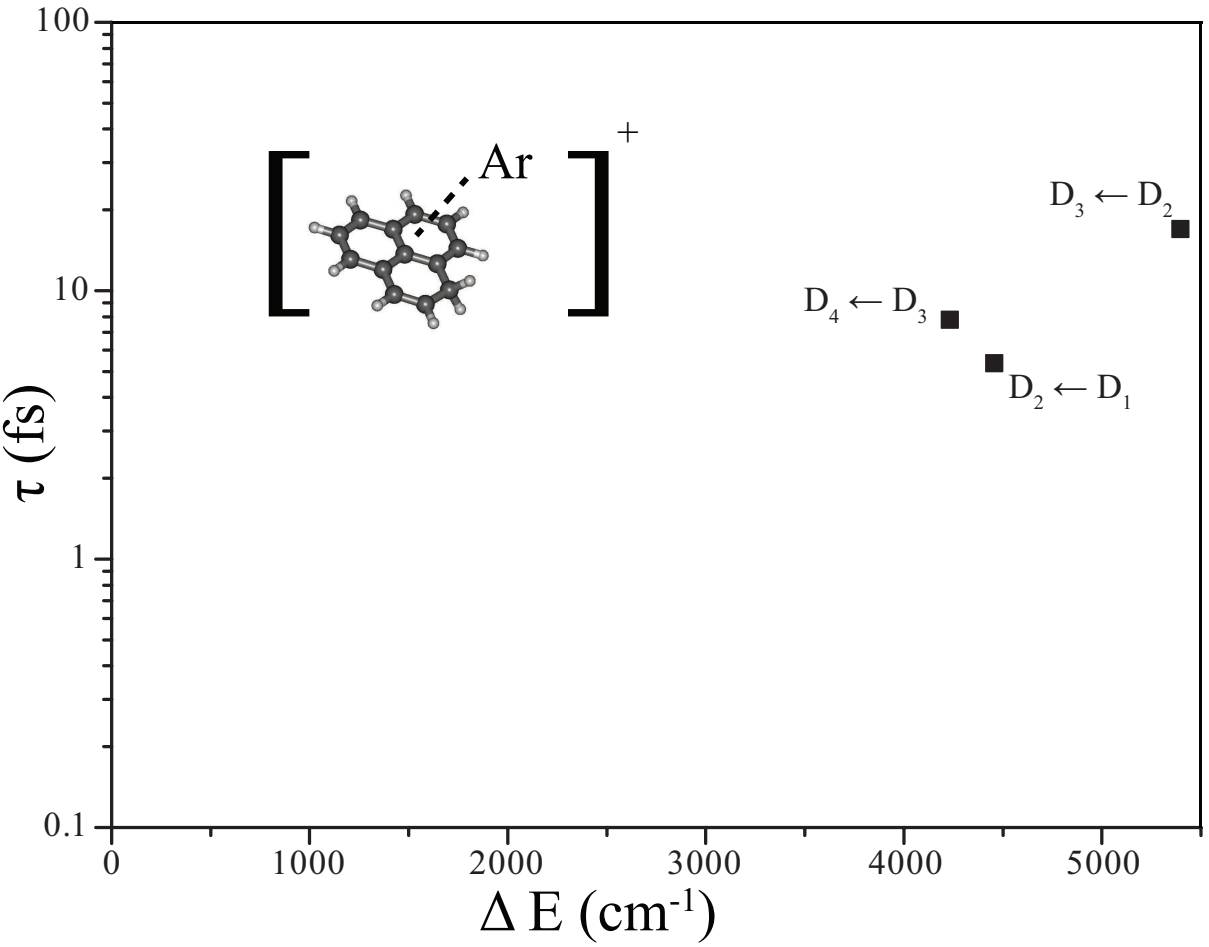

Figure 7.16: Plot of state lifetime τ versus energy gap to next lowest state. Unobserved D_1 energy estimated by X-MCQDPT2[7,7]/tzv(2df,p)

7.7 Conclusions

Initial attempts to detect the $2^2E'' \leftarrow 1^2A_1''$ state of the phenalenyl radical have been unsuccessful. However, new theoretical guidance developed through the course of this work greatly increase the possibility of future observation of this state. Observation of this state will greatly benefit future studies into the *pseudo*-Jahn-Teller coupling of the $1^2E'' \leftarrow 1^2A_1''$ and $2^2E'' \leftarrow 1^2A_1''$ transitions of phenalenyl and allow for more accurate vibronic assignment of the vibrational modes of the $1^2E''$ state. Consistent corrected calculations of the $2^2E'' \leftarrow 1^2A_1''$ transition energy unfortunately dismiss this transition as a possible carrier of the DIBs, being too high in energy.

Excitation spectra have been recorded for 1H-phenalene and its radical cation. The 1H-phenalene spectra showed its lowest energy transition in the UV, and it has been conclusively demonstrated in previous works that the first electronic transitions of neutral closed

shell PAH molecules of this size are not sensible candidates as carriers of the DIBs. However larger molecules of this type remain potentially interesting, particularly molecules of lower symmetry with strongly allowed $D_1 \leftarrow D_0$ electronic origin transitions.

The argon tagged spectrum of 1H-phenalenium$^+$ was recorded and assigned for transitions to three electronic excited states. While the lifetimes and intensities of these states varied considerably, all of the observed absorption bands were too broad to be relevant to the DIB problem. This is a feature of this class of molecule. The previous assignment of 1H-phenalenium$^+$ by Bally *et. al.*[270] was corrected, as the presence of observed bands in the argon-tagged photodissociation spectrum requires the carrier of these bands to be cationic. The primary goal of the photodissociation experiment was the unsuccessful attempt to observe the $S_1 \leftarrow S_0$ transition of the phenalenylium$^+$ closed shell cation. Calculations on this molecule and several heteroatomic species were discussed in the previous section. Symmetric and non-symmetric closed-shell molecules such as these remain a high priority for further study.

The spectroscopy and stability of species based on the phenalenyl motif provide an insight into the properties of a wide range of stable aromatic molecules, including every class of PAH discussed in this study, with a wide range of symmetries. Continued spectroscopic and theoretical studies are required so that a greater understanding of the exotic excited states of these molecules, and how they interact, may be reached.

Chapter 8

Future Work and Conclusions

This work has examined electronic transitions of several classes of aromatic molecules. Small closed-shell neutral PAHs have their lowest-energy electronic absorption in the UV spectrum. There has been little gas-phase spectra recorded for larger PAHs, and the visible transitions of the large PAHs that have been observed, such as tetracene ($C_{18}H_{12}$)[177] and Hexa-*peri*-hexabenzocoronene ($C_{42}H_{18}$),[176] have not corresponded to observed DIBs. However, there is insufficient data to conclusively rule out all large neutral PAHs as possible DIB carriers on the basis of the features investigated in this study. However, any assignment due to this class must also suggest a mechanism by which some large neutral PAHs carry the DIBs, while others do not.

Defected graphene fragments are another form of closed-shell PAH potentially worth further investigation. Chapter 7 examined the $S_1 \leftarrow S_0$ jet-cooled excitation spectrum of the smallest scale model system of hydrogen-edge-defected graphene nano-particles, revealing a complex vibronic spectrum. Trends in the behavior of this class of molecules could not be established as only one species has been observed, and the recording of the $S_1 \leftarrow S_0$ spectrum of a larger neutral closed-shell hydrogen-defected graphene structures would make an interesting avenue of future research.

The hypothesis that the DIBs may be carried by the $D_1 \leftarrow D_0$ transitions of BBRs produced by the photofragmentation of HACs,[183,184] predicted to exist in the ISM,[5] was further explored in Chapter 4. This study found that, like the previously studied benzyl and napthylmethyl radicals,[183,187–192,327] the $D_1 \leftarrow D_0$ transitions of the larger 9-AnMe and 1-PyMe radicals were weak, with a calculated oscillator strength on the order of $f = 10^{-4}$, making these transitions unlikely to be observed in the ISM given anticipated

column densities.[140] No trend of increasing oscillator strength was observed with increasing chromophore size. Additionally, increased chromophore size led to an increase in the Herzberg-Teller enhancement of vibronic transition intensities. These trends eliminate the $D_1 \leftarrow D_0$ transitions of BBRs as carriers of the DIBs.

While these transitions are in general representative of the $D_1 \leftarrow D_0$ transitions of aromatic RSRs, Tables 5.1 and 5.2 both identify the $D_1 \leftarrow D_0$ transition of the combined aromatic-olefinic 1-PPr radical as having an oscillator strength of $f = 0.022$. This corresponds to fluorescence experiments carried out by Reilly *et. al.*, in which 1-PPr was observed to be one of the brightest emitting species produced in a high-voltage discharge of benzene.[193,266] Despite this encouraging data, 1-PPr has not yet been observed in the DIBs or any other interstellar source. As a guide to future experimental studies, the author recommends that the oscillator strengths of the $D_1 \leftarrow D_0$ transitions of larger aromatic-olefinic chromophores should be calculated. If these radicals are calculated to have strong visible $D_1 \leftarrow D_0$ transitions they should be considered for future gas-phase experiments.

One possible issue with these RSRs is the existence of strong broad features corresponding to transitions to higher excited states, however the non-observation of such correlated features may be explained by observed ultraviolet extinction.[394] By similar logic, the $D_1 \leftarrow D_0$ transitions of neutral PAH RSRs dominated by very strong Herzberg-Teller/*pseudo*-Jahn-Tellar vibronic transitions, as seen in the spectrum of the phenalenyl radical,[201] may also warrant further study.

Chapter 5 examined strong transitions of PAH RSRs to higher excited states. All states observed contained significant lifetime broadening. A clear trend was also observed that larger chromophores produce broader transitions. As such, larger PAH RSRs with strong visible transitions to higher excited states would be even broader. While other classes of molecules possess strong transitions to higher excited state with FWHMs relevant to the DIBs,[344] the transitions of neutral PAH RSRs to these strong states can be eliminated as possible carriers of the DIBs.

Chapter 5 also demonstrated the R2C2PI after internal conversion technique. As discussed in Chapters 4 and 5, this was due to a chance match of the IE of 9-AnMe with the output of an ArF excimer laser, producing 193 nm photons. An interesting future project would be to attempt to generalise this technique as a means of recording the spectra of other short-lived excited states. This would require a source of tunable VUV photons, capable of producing photon energies in the range of the single-photon ionisation energy of the chemical species being examined. An example of such an experiment would first involve obtaining a single photon photoionisation efficiency (PIE) curve. The ionisation wavelength can then be set

to just below ionisation threshold energy. The excitation laser can then be scanned through the transition of interest allowing R2C2PI after internal conversion signal to be recorded in the same manner as regular R2C2PI spectra.

Chapter 6 and 7 both presented argon-tagged spectra of resonance stabilised radical cations. The band widths of 9-MeAn$^+$ were broadened by unresolved methyl-rotor structure. This behaviour has been seen before for similar molecules.[324] However, even without this structure, the visible $D_2 \leftarrow D_0$ transitions of PAH radical cations are still generally too lifetime-broadened for them to be plausible DIB carriers.

Transitions to several electronic excited states of the PAH radical cations observed were assigned with the assistance of intensities and empirically scaled energies calculated by the *ab initio* X-MCQDPT2 method, demonstrating the value of this technique. The highly vibronic $D_1 \leftarrow D_0$ transition of 9-MeAn$^+$ was fit and assigned using a combination of Franck-Condon simulations and a simple vibronic coupling calculation. These assignments were confirmed by symmetry arguments.

The $S_1 \leftarrow S_0$ transitions of some closed shell PAH cations have now been observed in jet cooled conditions.[207–209] The smaller molecules show large Franck-Condon progressions which eliminate these molecules as potential carriers of the DIBs, although Franck-Condon simulations have suggested the $S_1 \leftarrow S_0$ transitions of larger closed-shell PAH cations may have more origin dominated spectra.[352] More experimental spectra are required to conclusively determine if closed-shell cations may play a role in the DIBs.

8.1 DFT and TD-DFT Techniques

One of the continuing elements of this work has been the demonstrated practical usefulness of semi-empirical hybrid DFT techniques to the understanding of the jet-cooled spectra of aromatic molecules. The usefulness of these methods in the geometry optimisation of molecular species has long been demonstrated, to the extent that it represents a serious challenge to find recent studies featuring geometry optimisations of polyatomic molecules in which these method were not used.

TD-B3LYP was also used extensively for the calculation of excited state harmonic vibrational frequencies. While these methods are relatively expensive, as shown in Table 2.1, the accuracy with which they predict the energy of excited state harmonic vibrational frequencies has been worth the expense. TD-B3LYP methods were also successfully used

to create potential energy surfaces of anharmonic modes, such as the low frequency out of plane modes of 9-AnMe in Chapter 4, allowing transitions carried by these vibrations to be assigned.

The linear correlation between experimental electronic excitation energies and calculated TD-DFT vertical excitation energies provided an inexpensive means of predicting the electronic excitation energies of aromatic species. It was shown that this trend was different for different excited states, but consistent for electronically similar states. The extent to which these techniques may be applicable to other organic molecules is worth further examination.

8.2 Oxygen and Nitrogen Heterocycles

Chapter 7 introduced the concept of heteroatomic substitution. It was demonstrated that these substitutions can have a significant effect on the electronic transitions of aromatic molecules. Oxygen and nitrogen are both common in the ISM.[139,395] While there is not the same observed shortfall in interstellar abundance that is observed with carbon,[140] oxygen and nitrogen containing species are likely to have a role in interstellar chemistry,[396] as they do in terrestrial organic chemistry. There has been jet-cooled spectra of nitrogen heterocycles for some time.[323,397,398] Several nitrogen heterocyclic cations have recently been observed by the Bieske group at The University of Melbourne.[313,317,318] However, little work has been done on the visible transitions of larger aromatic molecules containing oxygen and nitrogen heterocycles, and this represents another potential avenue of research.

By introducing heteroatoms, the number of plausible isomers for a small to moderate sized PAH increase dramatically. REMPI-TOF techniques can have trouble distinguishing between chemical isomers, although double-resonance techniques and theory have been successfully used to deconvolve these spectra in the past.[183,193,194] An additional form of optical action spectra, based on the double resonance depletion of rotational spectra, is suggested.

8.3 Microwave-Optical Double-Resonance - Applications to Optical Action Spectroscopy

One of the strengths of microwave spectroscopy is that it allows for unambiguous assignment of molecules, as the rotational spectrum provides information on the molecular structure. These techniques, coupled with jet-cooled molecules formed in a PDN,[284] have resulted in the assignment of numerous astronomical molecules.[6–8,98,100–104]

The bulk of these assignments were made on the basis of jet-cooled spectra recorded through cavity enhanced fourier transform microwave (FTM) spectroscopy.[399] This is a mature technique that has proven extremely successful in identifying reaction intermediates. By assigning rotational constants, the vibrationally averaged ground-state geometry of the chemical species can be determined and the entire rotational spectrum, including all lines not yet observed, can then be accurately simulated. Recently, chirped-pulse broadband FTM techniques have also been developed. While the absence of cavity enhancement results in significantly lower single-pulse signal, this technique allows large regions of the spectrum to observed. This allows long accumulation times without the need for scanning, and can lead to the simultaneous detection of the many species formed in complex discharges.[400]

Microwave-microwave double-resonance techniques are common in FTM spectroscopy. The benefits of combining FTM and double-resonance techniques were demonstrated in the detection of nitrosyl-O-hydroxide (HOON) reported by Crabree *et. al.*[99] As the author assisted in these experiments, this paper is reproduced in Appendix A. HOON is a minority discharge product of the reaction forming nitrous acid (HONO) from nitric oxide (NO) and the hydroxyl radical (OH). HOON, an isomer of HONO, is produced with an abundance of roughly 3% in these reactions.[99]

Optical spectra of minority discharge products that are isomers of more abundant products, such as HOON, are difficult to measure with existing methods due to competing signal and noise produced by the dominant isomers. A potential method of recording the optical spectra of isomers, and unambiguously assigning their carriers, is through microwave-optical double-resonance.

Early applications of microwave-optical double-resonance have focused on obtaining rotational spectra of known optical transitions. One early previous application of microwave-optical double-resonance was in a paper by Field *et. al.* which detected microwave absorptions of BaO by its effect on photoluminescence produced by optical excitation of the

$A^1\Sigma^* \leftarrow X^1\Sigma$ transition.[401] Optical excitation can also be observed by a loss of FTM signal. This has been demonstrated by McCarthy and co-workers at the Harvard-Smithsonian Center for Astrophysics using chirped-pulse broadband FTM, in research yet to be published.[402] This is an excellent method for quickly recording the microwave spectrum of an observed visible transition. However, it does not lend itself to recording the optical spectrum of a molecule already identified through microwave spectroscopy, as the FTM signal is accumulated over a long acquisition times, preventing the laser from being scanned. This does not preclude this technique from being useful in the identification of the carriers of the DIBs, as the optical absorption frequencies of these bands are already known. It is therefore possible to use this broadband double-resonance technique to record a difference spectrum while pre-exciting a chemically rich discharge at DIB wavelength. If the carrier of this DIB is then formed in the discharge, depletions in the FTM spectrum will be apparent. The drawback of this technique is that there are now over 500 DIBs and observing all of them for each attempted discharge would be arduous. However, by combining this technique with a wavemeter calibrated OPO, or some other broadly tunable laser, it may be possible to automate the process somewhat.

The author proposes that optical spectra could be obtained by scanning a pre-excitation laser while monitoring single rotational lines observed as FTM signal in cavity enhanced FTM. This is the optical analogue of the microwave-microwave techniques used in Crabtree *et. al.*[99] An immediately apparent issue with the suggested technique is that in order to obtain strong observable depletion, the majority of the discharge product being observed in the jet expansion must be pre-excited by the laser. While this represents a clear engineering challenge, the author submits that this may be accomplished by pre-excitation of the molecular beam with a co-axial continuous wave tunable laser, eliminating temporal and spacial overlap issues. This technique would also prove useful for obtaining the electronic spectra of molecules of potential atmospheric importance, such as HOON, that are formed as minority isomers in discharge experiments.

8.4 Epilogue

Bill Klemperer is quoted as having said "there is no better way to lose a scientific reputation than to speculate on the carrier for the diffuse bands".[159,174] For many, the temptation to ignore this sage advice seems too much to bear. This is fortunate, as speculation remains an essential ingredient in the continuing process of trial-and-error that is currently

driving spectroscopic research of the DIBs. The techniques and tools available to the modern spectroscopist are vast and ever growing, and the spectra of many as-yet unobserved chemical species remain unobserved simply because no-one has yet attempted to record their spectra. The difficulty, as it always has been, remains knowing what to look for.

Through this work and many others, several classes of aromatic and non-aromatic species have been eliminated as potential carriers of the DIBs. And yet, the diversity of organic species, assuming the carriers of the DIBs are indeed organic, makes the list of potential carriers daunting. Tielens recently commented that "Solving the DIB problem will require the close cooperation of astronomers, molecular physicists, astrochemists, and spectroscopists – each contributing their pieces of the puzzle." [403] How long the identity of the DIB carriers will remains a mystery is unknown. But when the carriers are eventually identified, it will be due to the combined effort, inspiration and ultimately luck of a broad scientific community.

Appendix A

Appendix A: Papers Featuring Contributions from the Author

The following papers include a collaborative contribution from the author during his candidature. To view papers, please click on URL to visit publishers page. In all cases, that contribution included:

- The recording of spectra.
- Proof reading of drafts.
- Discussions with the primary author of that paper on the analysis, results and conclusions of that paper.

Troy, T. P. and Chalyavi, N. and Menon, A. S. and O'Connor, G. D. and Fuckel, B. and Nauta, K. and Radom, L. and Schmidt, T. W.: "The spectroscopy and thermochemistry of phenylallyl radical chromophores". *Chem. Sci.*, 9(2), 1755-1765 (2011)[200] `http://dx.doi.org/10.1039/C1SC00247C`

Crabtree, K. N. and Talipov, M. R. and Martinez, O. and O'Connor, G. D. and Khursan, S. L. and McCarthy, M. C.: "Detection and Structure of HOON: Microwave Spectroscopy Reveals an O–O Bond Exceeding 1.9 Å". *Science*, 6164(342), 1354-1357 (2013)[99] `http://www.sciencemag.org/content/342/6164/1354.abstract`

Krechkivska, O. and Wilcox C. and O'Connor G. D. and Nauta K. and Kable S. H. and Schmidt T. W. "Ionization Energies of Three Resonance-Stabilized Radicals: Cyclohexadienyl (dn, n = 0, 1, 6, 7), 1-Phenylpropargyl, and Methylcyclohexadienyl". *J. Phys. Chem. A*, 44(118), 10252-10258 (2014)[280] `http://dx.doi.org/10.1021/jp508985s`

Bibliography

[1] P. Marigo, L. Girardi, M. A. T. Groenewegen, and A. Weiss. Evolution of Planetary Nebulae. *Astron. Astrophys.*, 378(3):958–985, 2001.

[2] J. A. Cardelli, D. M. Meyer, M. Jura, and Savage B. D. The Abundance of Interstellar Carbon. *Astrophys. J.*, 467:334–340, 1996.

[3] R. Terzieva and E. Herbst. The Sensitivity of Gas-Phase Chemical Models of Interstellar Clouds to C and O Elemental Abundances and to a New Formation Mechanism for Ammonia. *Astrophys. J.*, 501(1, Part 1):207–220, 1998.

[4] Y. H. Le Teuff, T. J. Millar, and A. J. Markwick. The UMIST Database for Astrochemistry 1999. *Astron. Astrophys. Supp. Ser.*, 146(1):157–168, 2000.

[5] S. Kwok. The Synthesis of Organic and Inorganic Compounds in Evolved Stars. *Nature*, 430(7003):985–991, 2004.

[6] H. S. P. Müller, S. Thorwirth, D. A. Roth, and G. Winnewisser. The Cologne Database for Molecular Spectroscopy, CDMS. *Astron. Astrophys.*, 370(3):L49–L52, 2001.

[7] H. S. P. Müller, F. Schlöder, J. Stutzki, and G. Winnewisser. The Cologne Database for Molecular Spectroscopy, CDMS: a Useful Tool for Astronomers and Spectroscopists. *J. Mol. Struct.*, 742(1):215–227, 2005.

[8] The Cologne Database for Molecular Spectroscopy - Molecules in Space. URL `http://www.astro.uni-koeln.de/cdms/molecules`.

[9] F. H. Shu, F. C. Adams, and S. Lizano. Star Formation in Molecular Clouds-Observation and Theory. *Annu. Rev. Astron. Astr.*, 25:23–81, 1987.

[10] N. J. Evans, L. E. Allen, G. A. Blake, A. C. A. Boogert, T. Bourke, P. M. Harvey, J. E. Kessler, D. W. Koerner, C. W. Lee, L. G. Mundy, P. C. Myers, D. L. Padgett, K. Pontoppidan, A. I. Sargent, K. R. Stapelfeldt, E. F. van Dishoeck, C. H. Young, and K. E. Young. From Molecular Cores to Planet Forming Disks: An SIRTF Legacy Program. *Publ. Astron. Soc. Pac.*, 115(810):pp. 965–980, 2003.

[11] J. S. Carr and J. R. Najita. Organic Molecules and Water in the Planet Formation Region of Young Circumstellar Disks. *Science*, 319(5869):1504–1506, 2008.

[12] M. R. Swain, G. Tinetti, G. Vasisht, P. Deroo, C. Griffith, J. Bouwman, P. Chen, Y. Yung, A. Burrows, L. R. Brown, J. Matthews, J. F. Rowe, R. Kuschnig, and D. Angerhausen. Water, Methane, and Carbon Dioxide Present in the Dayside Spectrum of the Exoplanet HD 209458b. *Astrophys. J.*, 704(2):1616, 2009.

[13] M. R. Swain, P. Deroo, C. A. Griffith, G. Tinetti, A. Thatte, G. Vasisht, P. Chen, J. Bouwman, I. J. Crossfield, D.l Angerhausen, C. Afonso, and T. Henning. A Ground-Based Near-Infrared Emission Spectrum of the Exoplanet HD 189733b. *Nature*, 463(7281):637–639, 2010.

[14] J. L Bean, E. M. R. Kempton, and D. Homeier. A Ground-Based Transmission Spectrum of the Super-Earth Exoplanet GJ 1214b. *Nature*, 468(7324):669–672, 2010.

[15] S. Kwok, K. Volk, and B. J. Hrivnak. Chemical Evolution of Carbonaceous Materials in the Last Stages of Stellar Evolution. *Astron. Astrophys.*, 350:L35–L38, 1999.

[16] R. I. Kaiser. Experimental Investigation on the Formation of Carbon Bearing Molecules in the Interstellar Medium via Neutral-Neutral Reactions. *Chem. Rev.*, 102(5):1309–1358, 2002.

[17] J. Cernicharo, A. M. Heras, A.G.G.M. Tielens, J.R. Pardo, F. Herpin, M. Guelin, and L.B.F.M. Waters. Infrared Space Observatory's Discovery of C_4H_2, C_6H_2, and Benzene in CRL 618. *Astrophys. J.*, 546(2, Part 2):L123–L126, 2001.

[18] M. Livio, I. N. Reid, and W. B. Sparks. *Astrophysics of Life: Proceedings of the Space Telescope Science Institute Symposium, held in Baltimore, Maryland May 6-9, 2002*, volume 16. Cambridge University Press, 2005.

[19] S. Kwok. Organic Nanoparticles as a Component of the Interstellar Medium. In *The Diffuse Interstellar Bands*, volume 9 of *Proc. Int. Astron. U.*, pages 213–215, 5 2013.

[20] P. Ehrenfreund and S. B. Charnley. Organic Molecules in the Interstellar Medium, Comets, and Meteorites: A Voyage from Dark Clouds to the Early Earth. *Annu. Rev. Astron. Astrophys.*, 38(1):427–483, 2000.

[21] S. Kwok. Organic Matter in Space: from Star Dust to the Solar System. *Astrophys. Space Sci.*, 319(1):5–21, 2009.

[22] P. Ehrenfreund and J. Cami. Cosmic Carbon Chemistry: from the Interstellar Medium to the Early Earth. *Cold Spring Harb Perspect. Bio.*, 2(12):a002097, 2010.

[23] Chyba, C. F. and Thomas, P. J. and Brookshaw, L. and Sagan, C. Cometary Delivery of Organic Molecules to the Early Earth. *Science*, 249(4967):366–373, 1990.

[24] C. F. Chyba and C. Sagan. Endogenous production, exogenous delivery and impact-shock synthesis of organic molecules: an inventory for the origins of life. *Nature*, 355: 125–132, 1992.

[25] C. F. Chyba and C. Sagan. Comets as a Source of Prebiotic Organic Molecules for the Early Earth. In P. J. Thomas, C. F. Chyba, and C. P. McKay, editors, *Comets and the Origin and Evolution of Life*, pages 147–173. Springer New York, 1997.

[26] I. Newton. *Opticks: Or a Treatise of the Reflections, Refractions, Inflections and Colours of Light*. Digireads.com Publishing, digital edition, 2011. Based on 4th edition, published in 1730 by the Royal Society, London. Original edition published in 1704 by the Royal Society, London.

[27] W. H. Wollaston. A Method of Examining Refractive and Dispersive Powers, by Prismatic Reflection. *Philos. T. R. Soc.*, 92:365–380, 1802.

[28] J. Fraunhofer. Bestimmung des Brechungs- und des Farben-Zerstreuungs - Vermögens verschiedener Glasarten, in Bezug auf die Vervollkommnung achromatischer Fernröhre. *Denkschriften der Königlichen Akademie der Wissenschaften zu München*, pages 193–226, 1815.

[29] J. B. Hearnshaw. *The Analysis of Starlight: One Hundred and Fifty Years of Astronomical Spectroscopy*. CUP Archive, 1990.

[30] J. Fraunhofer. Kurzer Bericht von den Resultaten neuerer Versuche über die Gesetze des Lichtes, und die Theorie derselben. *Ann. Phys. (Berlin)*, 74(8):337–378, 1823.

[31] G. Kirchhoff. Ueber die Fraunhofer'schen Linien. *Annalen der Physik*, 185(1):148–150, 1860.

[32] G. Kirchhoff. Ueber das Verh altniss zwischen dem Emissionsverm ogen und dem Absorptionsverm ogen der K orper f—:ur W arme und Licht. *Annalen der Physik*, 185(2):275–301, 1860.

[33] G. Kirchhoff and R. Bunsen. Chemische Analyse durch Spectralbeobachtungen. *Annalen der Physik*, 186(6):161–189, 1860.

[34] D. L. Lambert. Quantitative stellar spectroscopy with large optical telescopes. *Phys. Scripta*, 1993(T47):186, 1993.

[35] D. F. Gray. *The Observation and Analysis of Stellar Photospheres*. Cambridge University Press, 2005.

[36] W. Swan. Ueber die prismatischen Spectra der Flammen von Kohlenwasserstoffverbindungen. *Annalen der Physik*, 176, 1857.

[37] W. Huggins. Further Observations on the Spectra of Some of the Stars and Nebulae, with an Attempt to Determine Therefrom Whether These Bodies are Moving towards or from the Earth, Also Observations on the Spectra of the Sun and of Comet II., 1868. *Phil. Trans. Roy. Soc. London*, 158:529–564, 1868.

[38] R. S. Mulliken. Electronic States and Band Spectrum Structure in Diatomic Molecules. IV. Hund's Theory; Second Positive Nitrogen and Swan Bands; Alternating Intensities. *Phys. Rev.*, 29:637–649, May 1927.

[39] R. C. Johnson. The Structure and Origin of the Swan Band Spectrum of Carbon. *Philosophical Transactions of the Royal Society of London A: Mathematical, Physical and Engineering Sciences*, 226(636-646):157–230, 1927.

[40] J. D. Shea. The Structure of the Swan Bands. *Phys. Rev.*, 30(6):825, 1927.

[41] W. E. Pretty. The Swan Band Spectrum of Carbon. *Proc. Phys. Soc. (London)*, 40 (1):71, 1927.

[42] R. S. Mulliken. The Assignment of Quantum Numbers for Electrons in Molecules. I. *Phys. Rev.*, 32:186–222, Aug 1928.

[43] F. H. Chaffee Jr and B. L. Lutz. The Detection of Interstellar Diatomic Carbon Toward Zeta Ophiuchi. *Astrophys. J.*, 221:L91–L93, 1978.

[44] LM Hobbs. Interstellar C_2 Molecules Toward Zeta Persei. *Astrophys. J.*, 232:L175–L177, 1979.

[45] E. F. van Dishoeck and T. de Zeeuw. Observations of Interstellar C_2 Toward χ Oph, HD 154368, 147889 and 149404. *Mon. Not. R. Astron. Soc.*, 206(2):383–406, 1984.

[46] R. Gredel. Interstellar C_2 Absorption Lines Towards CH^+ Forming Regions. *Astron. Astrophy.*, 351:657–668, 1999.

[47] B. H. Andrew. Radio Observations of some Minor and Major Planets . *Icarus*, 22 (4):454 – 458, 1974.

[48] F. C. Gillett. Further Observations of the 8-13 Micron Spectrum of Titan. *Astrophys. J.*, 201:L41–L43, 1975.

[49] I. De Pater and S. T. Massie. Models of the Millimeter-Centimeter Spectra of the Giant Planets. *Icarus*, 62(1):143 – 171, 1985.

[50] I. De Pater and M. Richmond. Neptune's Microwave Spectrum from 1 mm to 20 cm. *Icarus*, 80(1):1 – 13, 1989.

[51] T. Owen. The Spectra of Jupiter and Saturn in the Photographic Infrared. *Icarus*, 10(3):355 – 364, 1969.

[52] V. M. Slipher. Spectrographic Studies of the Planets,(George Darwin Lecture). *Mon. Not. R. Astron. Soc.*, 93:657, 1933.

[53] A. Adel and V. M. Slipher. Concerning the Carbon Dioxide Content of the Atmosphere of the Planet Venus. *Phys. Rev.*, 46:240–240, Aug 1934.

[54] C. Ponnamperuma. The Organic Chemistry and Biology of the Atmosphere of the Planet Jupiter. *Icarus*, 29(2):321–328, 1976.

[55] B. N. Khare, C. Sagan, E. T. Arakawa, F. Suits, T. A. Callcott, and M. W. Williams. Optical Constants of Organic Tholins Produced in a Simulated Titanian Atmosphere: From Soft X-ray to Microwave Frequencies. *Icarus*, 60(1):127–137, 1984.

[56] C. Sagan, W. R. Thompson, and B. N. Khare. Titan: A Laboratory for Prebiological Organic Chemistry. *Accounts Chem. Res.*, 25(7):286–292, 1992.

[57] R. Hanel, B. Conrath, D. Gautier, P. Gierasch, S. Kumar, V. Kunde, P. Lowman, W. Maguire, J. Pearl, J. Pirraglia, C. Ponnamperuma, and R. Samuelson. The Voyager Infrared Spectroscopy and Radiometry Investigation. *Space Sci. Rev.*, 21 (2):129–157, 1977.

[58] A. L. Broadfoot, B. R. Sandel, D. E. Shemansky, S. K. Atreya, T. M. Donahue, H. W. Moos, J. L. Bertaux, J. E. Blamont, J. M. Ajello, D. F. Strobel, J. C. McConnell, A. Dalgarno, R. Goody, M. B. McElroy, and Y. L. Yung. Ultraviolet Spectrometer Experiment for the Voyager Mission. *Space Sci. Rev.*, 21(2):183–205, 1977.

[59] R. H. Brown, K. H. Baines, G. Bellucci, J. P. Bibring, B. J. Buratti, F. Capaccioni, P. Cerroni, R. N. Clark, A. Coradini, D. P. Cruikshank, P. Drossart, V. Formisano, R. Jaumann, Y. Langevin, D. L. Matson, T. B. Mccord, V. Mennella, E. Miller, R. M. Nelson, P. D. Nicholson, B. Sicardy, and C. Sotin. The Cassini Visual and Infrared Mapping Spectrometer (VIMS) Investigation. In *The Cassini-Huygens Mission*, pages 111–168. Springer, 2004.

[60] L. W. Esposito, C. A. Barth, J. E. Colwell, G. M. Lawrence, W. E. McClintock, A. I. F. Stewart, H. Uwe Keller, A. Korth, H. Lauche, M. C. Festou, A. L. Lane, C. J. Hansen, J. N. Maki, R. A. West, H. Jahn, R. Reulke, K. Warlich, D. E. Shemansky, and Y. L. Yung. The Cassini Ultraviolet Imaging Spectrograph Investigation. In C. T. Russell, editor, *The Cassini-Huygens Mission*, pages 299–361. Springer, 2004.

[61] J. H. Hoffman, R. R. Hodges, T. M. Donahue, and M. B. McElroy. Composition of the Venus Lower Atmosphere from the Pioneer Venus Mass Spectrometer. *J. Geophys. Res. - Space.*, 85(A13):7882–7890, 1980.

[62] H. B. Niemann, S. K. Atreya, G. R. Carignan, T. M. Donahue, J. A. Haberman, D. N. Harpold, R. E. Hartle, D. M. Hunten, W. T. Kasprzak, P. R. Mahaffy, T. C. Owen, N. W. Spencer, and S. H. Way. The Galileo Probe Mass Spectrometer: Composition of Jupiter's Atmosphere. *Science*, 272(5263):846–849, 1996.

[63] J. H. Waite, W. S. Lewis, W. T. Kasprzak, V. G. Anicich, B. P. Block, T. E. Cravens, G. G. Fletcher, W. H. Ip, J. G. Luhmann, R. L. McNutt, H. B. Niemann, J. K. Parejko, J. E. Richards, R. L. Thorpe, E. M. Walter, and R. V. Yelle. The Cassini Ion and Neutral Mass Spectrometer (INMS) Investigation. In C. T. Russell, editor, *The Cassini-Huygens Mission*, pages 113–231. Springer, 2004.

[64] J. H. Waite, H. Niemann, R. V. Yelle, W. T. Kasprzak, T. E. Cravens, J. G. Luhmann, R. L. McNutt, W. H. Ip, D. Gell, V. De La Haye, I. Müller-Wordag, B. Magee, N. Borggren, S. Ledvina, G. Fletcher, E. Walter, R. Miller, S. Scherer, R. Thorpe, J. Xu, B. Block, and K. Arnett. Ion Neutral Mass Spectrometer Results from the First Flyby of Titan. *Science*, 308(5724):982–986, 2005.

[65] J. H. Waite, M. R. Combi, W. H. Ip, T. E. Cravens, R. L. McNutt, W. Kasprzak, R. Yelle, J. Luhmann, H.o Niemann, D. Gell, B. Magee, G. Fletcher, J. Lunine, and W. L. Tseng. Cassini Ion and Neutral Mass Spectrometer: Enceladus Plume Composition and Structure. *Science*, 311(5766):1419–1422, 2006.

[66] J. Cui, R. V. Yelle, V. Vuitton, J. H. Waite Jr., W. T. Kasprzak, D. A. Gell, H. B. Niemann, I. C. F. Müller-Wodarg, N. Borggren, G. G. Fletcher, E. L. Patrick, E. Raaen, and B. A. Magee. Analysis of Titan's Neutral Upper Atmosphere from Cassini Ion Neutral Mass Spectrometer Measurements. *Icarus*, 200(2):581 – 615, 2009.

[67] H. B. Niemann, S. K. Atreya, J. E. Demick, D. Gautier, J. A. Haberman, D. N. Harpold, W. T. Kasprzak, J. I. Lunine, T. C. Owen, and F. Raulin. Composition of Titan's Lower Atmosphere and Simple Surface Volatiles as Measured by the Cassini-Huygens Probe Gas Chromatograph Mass Spectrometer Experiment. *J. Geophys. Res. - Planet*, 115(E12):E12006, 2010.

[68] G. P. Kuiper. Titan: a Satellite with an Atmosphere. *Astrophys. J.*, 100:378, 1944.

[69] D. F. Strobel and D. E. Shemansky. EUV Emission from Titan's Upper Atmosphere: Voyager 1 Encounter. *J. Geophys. Res. - Space.*, 87(A3):1361–1368, 1982.

[70] A. Coustenis, B. Bézard, and D. Gautier. Titan's Atmosphere from Voyager Infrared Observations: I. The Gas Composition of Titan's Equatorial Region. *Icarus*, 80(1): 54 – 76, 1989.

[71] A. Coustenis, B. Bézard, and D. Gautier. Titan's Atmosphere from Voyager Infrared Observations: II. The CH_3D Abundance and DH Ratio from the 900-1200 cm^{-1} Spectral Region. *Icarus*, 82(1):67 – 80, 1989.

[72] A. Coustenis, B. Bézard, D. Gautier, A. Marten, and R. Samuelson. Titan's Atmosphere from Voyager Infrared Observations: III. Vertical Distributions of Hydrocarbons and Nitriles near Titan's North Pole. *Icarus*, 89(1):152 – 167, 1991.

[73] B. Letourneur and A. Coustenis. Titan's Atmospheric Structure from Voyager 2 Infrared Spectra. *Planet. Space Sci.*, 41(8):593 – 602, 1993.

[74] A. Coustenis and B. Bézard. Titan's Atmosphere from Voyager Infrared Observations: IV. Latitudinal Variations of Temperature and Composition. *Icarus*, 115(1): 126 – 140, 1995.

[75] R. Courtin, D. Gautier, and C. P. McKay. Titan's Thermal Emission Spectrum: Reanalysis of the Voyager Infrared Measurements. *Icarus*, 114(1):144 – 162, 1995.

[76] A. Coustenis, B. Schmitt, R.K. Khanna, and F. Trotta. Plausible Condensates in Titan's Stratosphere from Voyager Infrared Spectra. *Planet. Space Sci.*, 47(10–11): 1305 – 1329, 1999.

[77] R. H. Brown, J. P. Lebreton, and J. H. Waite. *Titan from Cassini-Huygens*. Springer Science & Business Media, 2009.

[78] A. Coustenis, D. E. Jennings, C. A. Nixon, R. K. Achterberg, P. Lavvas, S. Vinatier, N. A. Teanby, G. L. Bjoraker, R. C. Carlson, L. Piani, G. Bampasidis, F. M. Flasar, and P .N. Romani. Titan Trace Gaseous Composition from {CIRS} at the end of the Cassini–Huygens Prime Mission. *Icarus*, 207(1):461 – 476, 2010.

[79] J. H. Waite, D. T. Young, T. E. Cravens, A. J. Coates, F. J. Crary, B. Magee, and J. Westlake. The Process of Tholin Formation in Titan's Upper Atmosphere. *Science*, 316(5826):870–875, 2007.

[80] V. Vuitton, R. V. Yelle, and J. Cui. Formation and Distribution of Benzene on Titan. *J. Geophys. Res. - Planet*, 113(E5), 2008.

[81] C. Sagan, B. N. Khare, W. R. Thompson, G. D. McDonald, M. R. Wing, J. L. Bada, T. Vo-Dinh, and E. T. Arakawa. Polycyclic Aromatic Hydrocarbons in the Atmospheres of Titan and Jupiter. *Astrophys. J.*, 414:399–405, 1993.

[82] A. Ricca, C. W. Bauschlicher Jr., and E. L. O. Bakes. A Computational Study of the Mechanisms for the Incorporation of a Nitrogen Atom into Polycyclic Aromatic Hydrocarbons in the Titan Haze. *Icarus*, 154(2):516 – 521, 2001.

[83] E. H. Wilson and S. K. Atreya. Chemical Sources of Haze Formation in Titan's Atmosphere. *Planet. Space Sci.*, 51(14):1017–1033, 2003.

[84] E. H. Wilson, S. K. Atreya, and A. Coustenis. Mechanisms for the Formation of Benzene in the Atmosphere of Titan. *J. Geophys. Res. - Planet*, 108(E2), 2003.

[85] H. Imanaka, B. N. Khare, J. E. Elsila, E. L. O. Bakes, C. P. McKay, D. P. Cruikshank, S. Sugita, T. Matsui, and R. N. Zare. Laboratory Experiments of Titan Tholin Formed in Cold Plasma at Various Pressures: Implications for Nitrogen-Containing Polycyclic Aromatic Compounds in Titan Gaze. *Icarus*, 168(2):344 – 366, 2004.

[86] F. Goulay, C. Rebrion-Rowe, L. Biennier, S. D. Le Picard, A. Canosa, and B. R. Rowe. Reaction of Anthracene with CH Radicals: An Experimental Study of the Kinetics between 58 and 470 K. *J. Phys. Chem. A*, 110(9):3132–3137, 2006.

[87] S. Soorkia, C. A. Taatjes, D. L. Osborn, T. M. Selby, A. J. Trevitt, K. R. Wilson, and S. R. Leone. Direct Detection of Pyridine Formation by the Reaction of CH (CD) with Pyrrole: a Ring Expansion Reaction. *Phys. Chem. Chem. Phys.*, 12:8750–8758, 2010.

[88] C. A. Soorkia, S. Taatjes, K. R. Wilson, and S. R. Leone. Reaction of the C_2H Radical with 1-Butyne (C_4H_6): Low-Temperature Kinetics and Isomer-Specific Product Detection. *J. Phys. Chem. A*, 114(9):3340–3354, 2010.

[89] A. J. Trevitt, F. Goulay, C. A. Taatjes, D. L. Osborn, and S. R. Leone. Reactions of the CN Radical with Benzene and Toluene: Product Detection and Low-Temperature Kinetics. *J. Phys. Chem. A*, 114(4):1749–1755, 2010.

[90] A. K. Y. Lam, C. Li, G. Khairallah, B. B. Kirk, S. J. Blanksby, A. J. Trevitt, U. Wille, R. A. J. O'Hair, and G. da Silva. Gas-phase Reactions of Aryl Radicals with 2-Butyne: Experimental and Theoretical Investigation Employing the N-Methyl-pyridinium-4-yl Radical Cation. *Phys. Chem. Chem. Phys.*, 14:2417–2426, 2012.

[91] R. Delaunay, M. Gatchell, P. Rousseau, A. Domaracka, S. Maclot, Y. Wang, M. H. Stockett, T. Chen, L. Adoui, M. Alcamí, F. Martín, H. Zettergren, H.and Cederquist, and B.A. Huber. Molecular Growth Inside of Polycyclic Aromatic Hydrocarbon Clusters Induced by Ion Collisions. *J. Phys. Chem. Lett.*, 6(9):1536–1542, 2015.

[92] C. J. Grillmair, A. Burrows, D. Charbonneau, L. Armus, J. Stauffer, V. Meadows, J. van Cleve, K. von Braun, and D. Levine. Strong Water Absorption in the Dayside Emission Spectrum of the Planet HD 189733b. *Nature*, 456(7223):767–769, 2008.

[93] L. Schaefer and B. Fegley. Chemistry of Silicate Atmospheres of Evaporating Super-Earths. *Astrophys. J. Lett.*, 703(2):L113, 2009.

[94] T. Castan and K. Menou. Atmospheres of Hot Super-Earths. *Astrophys. J. Lett.*, 743(2):L36, 2011.

[95] A. Heger, S. E. Woosley, C. L. Fryer, and N. Langer. Massive Star Evolution Through the Ages. In Hillebrandt, W. and Leibundgut, B., editor, *From Twilight To Highlight: The Physics Of Supernovae*, ESO Astrophysics Symposia, pages 3–12, 2003.

[96] A. Heger, C. L. Fryer, S. E. Woosley, N. Langer, and D. H. Hartmann. How Massive Single Stars End Their Life. *Astrophys. J.*, 591(1):288–300, 2003.

[97] T. W. Schmidt and R. G. Sharp. The Optical Spectroscopy of Extraterrestrial Molecules. *Aust. J. Chem.*, 58:69–81, 2005.

[98] P. Thaddeus and M. C. McCarthy. Carbon Chains and Rings in the Laboratory and in Space. *Spectrochim. Acta A.*, 57(4, Sp. Iss. SI):757–774, 2001.

[99] K. N. Crabtree, M. R. Talipov, O. Martinez, G. D. O'Connor, S. L. Khursan, and M. C. McCarthy. Detection and Structure of HOON: Microwave Spectroscopy Reveals an O–O Bond Exceeding 1.9 Å. *Science*, 342(6164):1354–1357, 2013.

[100] M. C. McCarthy, W. Chen, M. J. Travers, and P. Thaddeus. Microwave Spectra of 11 Polyyne Carbon Chains. *Astrophys. J. Supp. Ser.*, 129(2):611, 2000.

[101] M. C. McCarthy, M. J. Travers, A. Kovacs, Wei Chen, Stewart E. Novick, C. A. Gottlieb, and P. Thaddeus. Detection and Characterization of the Cumulene Carbenes H_2C_5 and H_2C_6. *Science*, 275(5299):518–520, 1997.

[102] M. C. McCarthy and P. Thaddeus. High-Resolution Rotational Spectroscopy of NNOH+, DCS+, Ar $\cdots$ D_3+, Ar $\cdots$ DCO+, and Ar $\cdots$ HN_2+. *J. Mol. Spectrosc.*, 263(1):71–77, 2010.

[103] A. L. Cooksy, J. K. G. Watson, C. A. Gottlieb, and P. Thaddeus. The Rotational Spectrum Of The Carbon Chain Radical HCCCO. *Astrophys. J.*, 386(1, Part 2): L27–L30, 1992.

[104] M. C. McCarthy, M. J. Travers, P. Kalmus, C. A. Gottlieb, and P. Thaddeus. Laboratory Detection of the C_9H Radical. *Astrophys. J.*, 467(2, Part 2):L125–L127, 1996.

[105] M. B. Bell, P. A. Feldman, S. Kwok, and H. E. Matthews. Detection Of $HC_{11}N$ In IRC+10-DEGREES 216. *Nature*, 295(5848):389–391, 1982.

[106] M. Guélin, N. Brouillet, J. Cernicharo, F. Combes, and A. Wooten. Unveiling the Chemistry of Hot Protostellar Cores with ALMA. *Astrophys. Space. Sci.*, 313(1-3): 45–51, 2008.

[107] L. I. Cleeves, E. A. Bergin, T. J. Bethell, N. Calvet, J. K. J. Fogel, J. Sauter, and S. Wolf. Transition Disk Chemistry and Future Prospects with ALMA. *Astrophys. J. Lett.*, page L2, 2011.

[108] J. K. Jørgensen, C. Favre, S. E. Bisschop, T. L. Bourke, E. F. van D., and M. Schmalzl. Detection of the Simplest Sugar, Glycolaldehyde, in a Solar-type Protostar with ALMA. *Astrophys. J. Lett.*, 757(1):L4, 2012.

[109] S. Johnston, M. Bailes, N. Bartel, C. Baugh, M. Bietenholz, C. Blake, R. Braun, J. Brown, S. Chatterjee, J. Darling, A. Deller, R. Dodson, P. G. Edwards, R. Ekers, S. Ellingsen, I. Feain, B. M. Gaensler, M. Haverkorn, G. Hobbs, A. Hopkins, C. Jackson, C. James, G. Joncas, V. Kaspi, V. Kilborn, B. Koribalski, R. Kothes, T. L. Landecker, E. Lenc, J. Lovell, J. P. Macquart, R. Manchester, D. Matthews, N. M. McClure-Griffiths, R. Norris, U. L. Pen, C. Phillips, C. Power, R. Protheroe, E. Sadler, B. Schmidt, I. Stairs, L. Staveley-Smith, J. Stil, R. Taylor, S. Tingay, A. Tzioumis, M. Walker, J. Wall, and M. Wolleben. Science with the Australian Square Kilometre Array Pathfinder. *Pub. Astron. Soc. Aust.*, 24(4):174–188, 2007.

[110] P. F. Bernath, K. H. Hinkle, and J. J. Keady. Detection Of C_5 In The Circumstellar Shell Of IRC+10216. *Science*, 244(4904):562–564, 1989.

[111] K. W. Hinkle, J. J. Keady, and P. F. Bernath. Detection Of C_3 In The Circumstellar Shell Of IRC+10216. *Science*, 241(4871):1319–1322, 1988.

[112] E. Dwek, R. G. Arendt, D. J. Fixsen, T. J. Sodroski, N. Odegard, J. L. Weiland, W. T. Reach, M. G. Hauser, T. Kelsall, S. H. Moseley, R. F. Silverberg, R. A. Shafer, J. Ballester, D. Bazell, and R. Isaacman. Detection and Characterization of Cold Interstellar Dust and Polycyclic Aromatic Hydrocarbon Emission, from COBE observations. *Astrophys. J.*, 475(2, Part 1):565–579, 1997.

[113] J. Cami, J. Bernard-Salas, E. Peeters, and S. E. Malek. Detection of C_{60} and C_{70} in a Young Planetary Nebula. *Science*, 329(5996):1180–1182, 2010.

[114] K. Sellgren, M. W. Werner, J. G. Ingalls, J. D. T. Smith, T. M. Carleton, and C. Joblin. C_{60} in Reflection Nebulae. *Astrophys.l J. Lett.*, 722(1):L54, 2010.

[115] D. A. Garcia-Hernández, S. Iglesias-Groth, J. A. Acosta-Pulido, A. Manchado, P. García-Lario, L. Stanghellini, E. Villaver, R. A. Shaw, and F. Cataldo. The Formation of Fullerenes: Clues from New C_{60}, C_{70}, and (Possible) Planar C_24 Detections in Magellanic Cloud Planetary Nebulae. *Astrophys. J. Lett.*, 737(2):L30, 2011.

[116] Y. Zhang and S. Kwok. Detection of C_{60} in the Protoplanetary Nebula IRAS 01005+7910. *Astrophys. J.*, 730(2):126, 2011.

[117] P. W. Merrill. Note on the Spectrum of UV Aurigæ. *Publ. Astron. Soc. Pac.*, 38 (223):175–176, June 1929.

[118] R. F. Sanford. Two Bands in Spectra of Class N. *Publ. Astron. Soc. Pac.*, 38(223): 177–179, June 1929.

[119] B. Kleman. Laboratory Excitation of the Blue-Green Bands Observed in the Spectra of N-Type Stars. *Astrophys. J.*, 123:162, 1956.

[120] A. E. Douglas. Laboratory Studies of the λ 4050 Group of Cometary Spectra. *Astrophys. J.*, 114:466, 1951.

[121] L. Gausset, G. Herzberg, A. Lagerqvist, and B. Rosen. Analysis of the 4050 Å Group of the C_3 Molecule. *Astrophys. J.*, 142:45, 1965.

[122] W. Weltner Jr and D. McLeod Jr. Spectroscopy of Carbon Vapor Condensed in Rare-Gas Matrices at 4 K. III. *J. Chem. Phys.*, 45(8):3096–3105, 1966.

[123] D. L. Michalopoulos, M. E. Geusic, P. R. R. Langridge-Smith, and R. E. Smalley. Visible Spectroscopy of Jet-Cooled SiC_2: Geometry and Electronic Structure. *J. Chem. Phys.*, 80(8):3556–3560, 1984.

[124] H. S. P. Müller, J. Cernicharo, M. Agúndez, L. Decin, P. Encrenaz, J. C. Pearson, D. Teyssier, and L. B. F. M. Waters. Spectroscopic Parameters for Silacyclopropynylidene, SiC2, from Extensive Astronomical Observations Toward {CW} Leo (IRC +10216) with the Herschel Satellite. *J. Mol. Spec.*, 271(1):50 – 55, 2012.

[125] M. Steglich and J. P. Maier. Electronic Transitions of Jet-cooled SiC_2, Si_2C_n (n=1-3), Si_3C_n (n = 1,2), and SiC_6H_4 between 250 and 710 nm. *Astrophys. J.*, 801(2):119, 2015.

[126] M. Cohen, C. M. Anderson, A. Cowley, G. V. Coyne, W. Fawley, T. R. Gull, E. A. Harlan, G. H. Herbig, .F Holden, H. S. Hudson, R. O. Jakoubek, H. M. Johnson, K. M. Merrill, H. S. Schiffer, B. T. Soifer, and B. Zuckerman. The Peculiar Object HD 44179/'The Red Rectangle'. *Astrophys. J.*, 196:179–189, 1975.

[127] R. J. Glinski, P. D. Michaels, C. M. Anderson, T. W. Schmidt, R. G. Sharp, M. L. Sitko, L. S. Bernstein, and H. Van Winckel. Current Assessment of the Red Rectangle Band Problem. *Astrophys. Space Sci.*, 323(4):337–344, 2009.

[128] G. Lagache. The Large-Scale Anomalous Microwave Emission Revisited by WMAP. *Astron. Astrophys.*, 405(3):813–819, 2003.

[129] R. A. Watson, R. Rebolo, J. A. Rubiño-Martín, S. Hildebrandt, C. M. Gutiérrez, S. Fernández-Cerezo, R. J. Hoyland, and E. S. Battistelli. Detection of Anomalous Microwave Emission in the Perseus Molecular Cloud with the COSMOSOMAS Experiment. *Astrophys. J. Lett.*, 624(2):L89, 2005.

[130] A. Léger and J. L. Puget. Identification of the 'Unidentified' IR Emission Features of Interstellar Dust ? *Astron. Astrophys.*, 137(1):L5–L8, 1984.

[131] L. J. Allamandola, A. G. G. M. Tielens, and J. R. Barker. Polycyclic Aromatic Hydrocarbons and the Unidentified Infrared Emission Bands - Auto Exhaust Along the Milky Way. *Astrophys. J.*, 290:L25–L28, 1985.

[132] P J. Sarre. The Diffuse Interstellar Bands: A Major Problem in Astronomical Spectroscopy. *J. Molec. Spectrosc.*, 238(1):1 – 10, 2006.

[133] T. P. Snow. Diffuse Interstellar Bands: Past and Present. In *The Diffuse Interstellar Bands*, volume 9 of *Proc. IAU*, pages 3–12 (2014), 5 2013.

[134] M. L. Heger. The Occurrence of Stationary D Lines of Sodium in the Spectroscopic Binaries, β Scorpii and δ Orionis. *Lick Obs. Bull.*, 10:59–63, 1919.

[135] M. L. Heger. Further Study of the Sodium Lines in Class B Stars. *Lick Obs. Bull.*, 10(337):141–145, 1922.

[136] P.W. Merrill. title. *Publ. Astron. Soc. Pac.*, 1934.

[137] B. J. McCall and R. E. Griffin. On the Discovery of the Diffuse Interstellar Bands. *P. R. Soc. Lond. A Mat.*, 469(2151), 2013.

[138] L. S. Bernstein, F. O. Clark, and D. K. Lynch. H_2 Molecular Clusters with Embedded Molecules and Atoms as the Source of the Diffuse Interstellar Bands. *The Astrophysical Journal*, 768(1):84, 2013.

[139] T. P. Snow and B. J. McCall. Diffuse Atomic and Molecular Clouds. *Annu. Rev. Astron. Astr.*, 44(1):367–414, 2006.

[140] T. P. Snow and A. N. Witt. The Interstellar Carbon Budget and the Role of Carbon in Dust and Large Molecules. *Science*, 270(5241):pp. 1455–1460, 1995.

[141] P. Jenniskens and F.-X. Désert. A Survey of the Diffuse Interstellar Bands (3800-8680 Å). *Astron. Astrophys. Suppl. Ser.*, 106:39–78, 1994.

[142] P. Jenniskens, I. Porceddu, P. Benvenuti, and F.-X. Désert. Diffuse Interstellar Bands: Resolved Rotational Band Structure at 5850 Å. *Astron. Astrophys.*, 313: 649–656, 1996.

[143] J. Krelowski, C. Sneden, and D. Hiltgen. A Survey of Weak Diffuse Interstellar Bands in Selected Ranges Between 5600 and 7000 Å. *Planet. Space Sci.*, 43:1195–1203, 1995.

[144] L. M. Hobbs, D. G. York, T. P. Snow, T. Oka, J. A. Thorburn, M. Bishof, S. D. Friedman, B. J. McCall, B. Rachford, P. Sonnentrucker, and D. E. Welty. A Catalog of Diffuse Interstellar Bands in the Spectrum of HD 204827. *Astrophys. J.*, 680(2): 1256, 2008.

[145] L. M. Hobbs, D. G. York, J. A. Thorburn, T. P. Snow, M. Bishof, S. D. Friedman, B. J. McCall, T. Oka, B. Rachford, P. Sonnentrucker, and D. E. Welty. Studies of the Diffuse Interstellar Bands. III. HD 183143. *Astrophys. J.*, 705(1):32, 2009.

[146] B. J. McCall, M. M. Drosback, J.A. Thorburn, D. G. York, S. D. Friedman, L. M. Hobbs, B. L. Rachford, T. P. Snow, P. Sonnentrucker, and D. E. Welty. Studies of the Diffuse Interstellar Bands. IV. The Nearly Perfect Correlation Between 6196.0 and 6613.6. *Astrophys. J.*, 708(2):1628, 2010.

[147] T. Oka, D. E. Welty, S. Johnson, D. G. York, J. Dahlstrom, and L. M. Hobbs. Anomalous Diffuse Interstellar Bands in the Spectrum of Herschel 36. II. Analysis of Radiatively Excited CH+, CH, and Diffuse Interstellar Bands. *Astrophys. J.*, 773 (1):42, 2013.

[148] L. S. Bernstein, F. O. Clark, D. K. Lynch, and G. A. Galazutdinov. Analysis of Narrow and Broad Profiles Observed for the λ6614 Diffuse Interstellar Band. *Astrophys. J.*, 801(1):6, 2015.

[149] P. Sonnentrucker, J. Cami, P. Ehrenfreund, and B. H. Foing. The Diffuse Interstellar Bands at 5797, 6379 and 6613 Angstroms. Ionization Properties of the Carriers. *Astron. Astrophys.*, 327:1215–1221, 1997.

[150] A. E. Douglas. Origin of Diffuse Interstellar Lines. *Nature*, 269:130–132, 1977.

[151] J. P. Maier. Electronic Spectroscopy of Carbon Chains. *Chem. Soc. Rev.*, 26:21–28, 1997.

[152] E. B. Jochnowitz and J. P. Maier. Electronic Spectroscopy of Carbon Chains. *Mol. Phys.*, 106(16-18):2093–2106, 2008.

[153] R. Nagarajan and J. P. Maier. Electronic Spectra of Carbon Chains and Derivatives. *Int. Rev. Phys. Chem.*, 29(3):521–554, 2010.

[154] C. A. Rice and J. P. Maier. Electronic Spectroscopy of Carbon Chains and Rings of Astrophysical Interest. *J. Phys. Chem. A*, 117(27):5559–5566, 2013.

[155] M. Tulej, D. A. Kirkwood, M. Pachkov, and J. P. Maier. Gas-Phase Electronic Transitions of Carbon Chain Anions Coinciding with Diffuse Interstellar Bands. *Astrophys. J. Lett.*, 506:L69–L73, October 1998.

[156] F. Güthe, M. Tulej, M. V. Pachkov, and J. P. Maier. Photodetachment Spectrum of l-C3H2-: The Role of Dipole Bound States for Electron Attachment in Interstellar Clouds. *Astrophys. J.*, 555(1):466, 2001.

[157] J. P. Maier, G. A. H. Walker, D. A. Bohlender, F. J. Mazzotti, R. Raghunandan, J. Fulara, I. Garkusha, and A. Nagy. Identification of H2CCC as a Diffuse Interstellar Band Carrier. *Astrophys. J.*, 726(1):41, 2011.

[158] B. J. McCall, J. Thorburn, L. M. Hobbs, T. Oka, and D. G. York. Rejection of the C_7^- Diffuse Interstellar Band Hypothesis. *Astrophys. J. Lett.*, 559(1):L49, 2001.

[159] T. Oka and B. J. McCall. Disclosing Identities in Diffuse Interstellar Bands. *Science*, 331:293–294, 2011.

[160] A. K. Geim and K. S. Novoselov. The Rise of Graphene. *Nat. Mater.*, 6:183–191, 2007.

[161] M. Baba, Y. Kowaka, U. Nagashima, T.i Ishimoto, H. Goto, and N. Nakayama. Geometrical Structure of Benzene and Naphthalene: Ultrahigh-Resolution Laser Spectroscopy and Ab Initio Calculation. *J. Chem. Phys.*, 135(5):054305, 2011.

[162] D. N. Congreve, J. Lee, N. J. Thompson, E. Hontz, S. R. Yost, P. D. Reusswig, M. E. Bahlke, S. Reineke, T. Van Voorhis, and M. A. Baldo. External Quantum Efficiency Above 100% in a Singlet-Exciton-Fission–Based Organic Photovoltaic Cell. *Science*, 340(6130):334–337, 2013.

[163] B. Ehrler, M. W. B. Wilson, A. Rao, R. H. Friend, and N. C. Greenham. Singlet Exciton Fission-Sensitized Infrared Quantum Dot Solar Cells. *Nano Lett.*, 12(2): 1053–1057, 2012.

[164] H. Richter and J. B. Howard. Formation of Polycyclic Aromatic Hydrocarbons and their Growth to Soot - A Review of Chemical Reaction Pathways. *Prog. Energy Combust. Sci.*, 26:565–608, 2000.

[165] C. S. McEnally, L. D. Pfefferle, B. Atakan, and K. Kohse-Höinghaus. Studies of Aromatic Hydrocarbon Formation Mechanisms in Flames: Progress Towards Closing the Fuel Gap. *Prog. Energy Combust. Sci.*, 32:247–294, 2006.

[166] B. Donn and K. S. K. Swamy. Extinction by Interstellar Grains, Mie Particles and Polycyclic Aromatic Molecules. *Physica*, 41(1):144 – 150, 1969.

[167] F. Salama and L. J. Allamandola. Neutral and Ionized Polycyclic Aromatic Hydrocarbons, Diffuse Interstellar Bands and the Ultraviolet Extinction Curve. *J. Chem. Soc., Faraday Trans.*, 89:2277–2284, 1993.

[168] S. Kwok and Y. Zhang. Mixed Aromatic-Aliphatic Organic Nanoparticles as Carriers of Unidentified Infrared Emission Features. *Nature*, 479:80–83, November 2011.

[169] A. Li and B. T. Draine. The Carriers of the Interstellar Unidentified Infrared Emission Features: Aromatic or Aliphatic? *Astrophys. J. Lett.*, 760(2):L35, 2012.

[170] H. W. W. Spoon, A. F. M. Moorwood, D. Lutz, A. G. G. M. Tielens, R. Siebenmorgen, and J. V. Keane. Mid-Infrared Spectral Evidence for a Luminous Dust Enshrouded Source in Arp. *Astron. Astrophys.*, 414(3):873–883, 2004.

[171] A. Léger and L. d'Hendecourt. Polycyclic Aromatic Hydrocarbons and the Diffuse Interstellar Bands. *Astron. Astrophys.*, 146(1):81–85, 1985.

[172] G. P. Van der Zwet and L. J. Allamandola. Polycyclic Aromatic Hydrocarbons and the Diffuse Interstellar Bands. *Astron. Astrophys.*, 146(1):76–80, 1985.

[173] N. L.J. Cox. The PAH-DIB Hypothesis. *EAS Publications*, 46:349–354, 1 2011.

[174] G. H. Herbig. The Diffuse Interstellar Bands. *Annu. Rev. Astron. Astr.*, 33(1):19–73, 1995.

[175] D. L. Kokkin, N. J. Reilly, T. P. Troy, K. Nauta, and T. W. Schmidt. Gas Phase Spectra of All-Benzenoid Polycyclic Aromatic Hydrocarbons: Triphenylene. *J. Chem. Phys.*, 126(8):084304, 2007.

[176] D. L. Kokkin, T. P. Troy, M. Nakajima, K. Nauta, T. D. Varberg, G. F. Metha, N. T. Lucas, and T. W. Schmidt. The Optical Spectrum of a Large Isolated Polycyclic Aromatic Hydrocarbon: Hexa-peri-hexabenzocoronene, $C_{42}H_{18}$. *Astrophys. J.*, 681: L49, 2008.

[177] H. G. Loehmannsroeben, D. Bahatt, and U. Even. Spectroscopy of Jet-Cooled Tetracene Derivatives in the First Excited Singlet State. *Journal Phys. Chem.*, 94 (10):4025–4029, 1990.

[178] F. Salama and L. J. Allamandola. The Ultraviolet and Visible Spectrum of the Polycyclic Aromatic Hydrocarbon $C_{10}H_8^+$ - Possible Contributions to the Diffuse Interstellar Bands and to the Ultraviolet-Visible Extinction. *Astrophys. J.*, 395:301–306, August 1992.

[179] F. Salama and L.J. Allamandola. Is a Pyrene-like Molecular Ion the cause of the 4,430 ÅDiffuse Interstellar Absorption Band? *Nature*, 358:42, 1992.

[180] S. Iglesias-Groth, A. Manchado, D. A. García-Hernández, J. I. González Hernández, and D. L. Lambert. Evidence for the Naphthalene Cation in a Region of the Interstellar Medium with Anomalous Microwave Emission. *Astrophys. J. Lett.*, 685(1): L55–L58, 2008.

[181] G. Galazutdinov, B.C. Lee, I.O. Song, M. Kazmierczak, and J. Krełowski. A Search for Interstellar Naphthalene and Anthracene Cations. *Mon. Not. R. Astron. Soc.*, 412(2):1259–1264, 2011.

[182] J. M. Searles, J. D. Destree, T. P. Snow, F. Salama, D. G. York, and J. Dahlstrom. Searching for Naphthalene Cation Absorption in the Interstellar Medium. *Astrophys. J.*, 732(1):50, 2011.

[183] N. Chalyavi, T. P. Troy, M. Nakajima, B. A Gibson, K. Nauta, R. G. Sharp, S. H. Kable, and T. W. Schmidt. Excitation and Emission Spectra of Jet-Cooled Naphthylmethyl Radicals. *J. Phys. Chem. A*, 115(27):7959–7965, 2011.

[184] T. P. Troy. *The Jet-Cooled Spectroscopy of Resonance-Stabilized Radical Chromophores*. PhD thesis, School of Chemistry, The University of Sydney, 2011.

[185] G. D. O'Connor, G. B. Bacskay, G. V. G. Woodhouse, T. P. Troy, K. Nauta, and T. W. Schmidt. Excitation Spectra of Large Jet-Cooled Polycyclic Aromatic Hydrocarbon Radicals: 9-Anthracenylmethyl ($C_{15}H_{11}$) and 1-Pyrenylmethyl ($C_{17}H_{11}$). *J. Phys. Chem. A*, 117(50):13899–13907, 2013.

[186] G. Porter and F. J. Wright. Primary Photochemical Processes in Aromatic Molecules. Part 3. Absorption Spectra of Benzyl, Anilino, Phenoxy and Related Free Radicals. *Trans. Faraday Soc.*, 51:1469–1474, 1955.

[187] M. Heaven, L. Dimauro, and T. A. Miller. Laser-Induced Fluorescence Spectra of Free-Jet Cooled Organic Free Radicals. Vinoxy, Cyclopentadienyl, and Benzyl. *Chem. Phys. Lett.*, 95:347 – 351, 1983.

[188] T-Y. D. Lin, X-Q. T., T. M. Cerny, J. M. Williamson, D. W. Cullin, and T. A. Miller. High-Resolution Fluorescence Excitation Spectra of Jet-Cooled Benzyl and P-Methylbenzyl Radicals. *Chem. Phys.*, 167:203 – 214, 1992.

[189] J. I. Selco and P. G. Carrick. Jet Cooled Emission Spectra of Toluene and the Benzyl Radical. *J. Mol. Specrosc.*, 137(1):13 – 23, 1989.

[190] M. Fukushima and K. Obi. Jet Spectroscopy and Excited State Dynamics of Benzyl and Substituted Benzyl Radicals. *J. Chem. Phys.*, 93(12):8488–8497, 1990.

[191] H. S. Im and E. R. Bernstein. Mass Resolved Excitation Spectroscopy of Radicals: Benzyl and Phenylnitrene. *J. Chem. Phys.*, 95(9):6326–6329, 1991.

[192] M. Fukushima and K. Obi. Jet Spectroscopy of Benzyl and Benzyl-alpha-d[sub 2]. *J. Chem. Phys.*, 96(6):4224–4232, 1992.

[193] N. J. Reilly, D. L. Kokkin, M. Nakajima, K. Nauta, S. H. Kable, and T. W. Schmidt. Spectroscopic Observation of the Resonance-Stabilized 1-Phenylpropargyl Radical. *J. Am. Chem. Soc.*, 130(10):3137–3142, 2008.

[194] N. J. Reilly, M. Nakajima, T. P. Troy, N. Chalyavi, K. A Duncan, K. Nauta, S. H. Kable, and T. W. Schmidt. Spectroscopic Identification of the Resonance-Stabilized cis-and trans-1-Vinylpropargyl Radicals. *J. Am. Chem. Soc.*, 131(37):13423–13429, 2009.

[195] J. A. Sebree, V. V. Kislov, A. M. Mebel, and T. S. Zwier. Spectroscopic and Thermochemical Consequences of Site-Specific H-Atom Addition to Naphthalene. *J. Phys. Chem. A*, 114(21):6255–6262, 2010.

[196] J. A. Sebree, V. V. Kislov, A. M. Mebel, and T. S. Zwier. Isomer Specific Spectroscopy of $C_{10}H_n$, n = 8-12: Exploring pathways to naphthalene in Titan's atmosphere. *Faraday Discuss.*, 147:231–249, 2010.

[197] J. A. Sebree, N.l M. Kidwell, E. G. Buchanan, M. Z. Zgierski, and T. S. Zwier. Spectroscopy and Ionization Thresholds of π-Isoelectronic 1-Phenylallyl and Benzylallenyl Resonance Stabilized Radicals. *Chem. Sci.*, 2:1746–1754, 2011.

[198] N. M. Kidwell, D. N. Mehta-Hurt, J. A. Korn, E. L. Sibert, and T. S. Zwier. Ground and Excited State Infrared Spectroscopy of Jet-Cooled Radicals: Exploring the Photophysics of Trihydronaphthyl and Inden-2-ylmethyl. *J. Chem. Phys.*, 140(21):214302, 2014.

[199] N. Chalyavi, G. B. Bacskay, A. S. Menon, T. P. Troy, N. J. L. K. Davis, L. Radom, S. A. Reid, and T. W. Schmidt. Spectroscopy and Thermochemistry of a Jet-Cooled Open-Shell Polyene: 1,4-Pentadienyl Radical. *J. Chem. Phys.*, 135(12), 2011.

[200] T. P. Troy, N. Chalyavi, A. S. Menon, G. D. O'Connor, B. Fückel, K. Nauta, L. Radom, and T. W. Schmidt. The Spectroscopy and Thermochemistry of Phenylallyl Radical Chromophores. *Chem. Sci.*, 2:1755–1765, 2011.

[201] G. D. O'Connor, T. P. Troy, D. A. Roberts, N. Chalyavi, B. Fückel, M. J. Crossley, K. Nauta, J. F. Stanton, and T. W. Schmidt. Spectroscopy of the Free Phenalenyl Radical. *J. Am. Chem. Soc*, 133(37):14554–14557, 2011.

[202] N. Chalyavi, T. P. Troy, G. B. Bacskay, K. Nauta, S. H. Kable, S. A. Reid, and T. W. Schmidt. Excitation Spectra of the Jet-Cooled 4-Phenylbenzyl and 4-(4'-Methylphenyl) Benzyl Radicals. *J. Phys. Chem. A*, 116(44):10780–10785, 2012.

[203] T. P. Troy, M. Nakajima, N. Chalyavi, K. Nauta, S. H. Kable, and T. W. Schmidt. Hydroxyl Addition to Aromatic Alkenes: Resonance-Stabilized Radical Intermediates. *J. Phys. Chem. A*, 116(30):7906–7915, 2012.

[204] T. Pino, Y. Carpentier, G. Féraud, H. Friha, D. L. Kokkin, T.P. Troy, N. Chalyavi, Ph. Bréchignac, and T. W. Schmidt. Electronic Spectroscopy of PAHs. *EAS Publications Series*, 46:355–371, 1 2011.

[205] T. Pino, N. Boudin, and P. Bréchignac. Electronic Absorption Spectrum of Cold Naphthalene Cation in the Gas Phase by Photodissociation of its Van der Waals Complexes. *J. Chem. Phys.*, 111(16):7337–7347, 1999.

[206] O. Sukhorukov, A. Staicu, E. Diegel, G. Rouillé, Th. Henning, and F. Huisken. $D_2 \leftarrow D_0$ Transition of the Anthracene Cation Observed by Cavity Ring-Down Absorption Spectroscopy in a Supersonic Jet. *Chem. Phys. Lett.*, 386(4–6):259 – 264, 2004.

[207] V. Dryza, N. Chalyavi, J. A. Sanelli, and E. J. Bieske. Electronic Absorptions of the Benzylium Cation. *J. Chem. Phys.*, 137(20):204304, 2012.

[208] O. Krechkivska, Y. Liu, K. L. K. Lee, K. Nauta, S. H. Kable, and T. W. Schmidt. Triple-Resonance Spectroscopy Reveals the Excitation Spectrum of Very Cold, Isomer-Specific Protonated Naphthalene. *J. Phys. Chem. Lett.*, 4(21):3728–3732, 2013.

[209] C. A. Rice, F.-X. Hardy, O. Gause, and J. P. Maier. $(1)^1$A' $\leftarrow$ X ^{1}A' Electronic Transition of Protonated Coronene at 15 K. *J. Phys. Chem. Lett.*, 5(6):942–945, 2014.

[210] J. Franck and E.G. Dymond. Elementary Processes of Photochemical Reactions. *Trans. Faraday Soc.*, 21(February):536–542, 1926.

[211] E. Condon. A Theory of Intensity Distribution in Band Systems. *Phys. Rev.*, 28: 1182–1201, Dec 1926.

[212] G. Herzberg and E. Teller. Schwingungsstruktur der Elektronenübergänge bei mehratomigen Molekülen. *Z. Phys. Chem. B*, 21(5-6):410, 1933.

[213] N. Bohr. I. On the Constitution of Atoms and Molecules. *Philos. Mag. 6*, 26(151): 1–25, 1913.

[214] N. Bohr. XXXVII. On the Constitution of Atoms and Molecules. *Philos. Mag.*, 26 (153):476–502, 1913.

[215] E. Rutherford. The Scattering of α and β Particles by Matter and the Structure of the Atom. *Philos. Mag.*, 21:669, 1911.

[216] M. Planck. Zur Theorie der Wärmestrahlung. *Ann. d. Phys.*, 336(4):758–768, 1910.

[217] E. Schrödinger. An Undulatory Theory of the Mechanics of Atoms and Molecules. *Phys. Rev.*, 28:1049–1070, Dec 1926.

[218] P. W. Atkins and R. S. Friedman. *Molecular Quantum Mechanics*. Oxford university press, 2011.

[219] M. Born and R. Oppenheimer. Quantum Theory of Molecules. *Annalen der Physik*, 84(20):0457–0484, 1927.

[220] G. D. O'Connor. Gas Phase Spectroscopy of the Phenalenyl Radical, 2010.

[221] M. J. Frisch, G. W. Trucks, H. B. Schlegel, G. E. Scuseria, M. A. Robb, J. R. Cheeseman, G. Scalmani, V. Barone, B. Mennucci, G. A. Petersson, H. Nakatsuji, M. Caricato, X. Li, H. P. Hratchian, A. F. Izmaylov, J. Bloino, G. Zheng, J. L. Sonnenberg, M. Hada, M. Ehara, K. Toyota, R. Fukuda, J. Hasegawa, M. Ishida, T. Nakajima, Y. Honda, O. Kitao, H. Nakai, T. Vreven, J. A. Montgomery, Jr., J. E. Peralta, F. Ogliaro, M. Bearpark, J. J. Heyd, E. Brothers, K. N. Kudin, V. N. Staroverov, R. Kobayashi, J. Normand, K. Raghavachari, A. Rendell, J. C. Burant, S. S. Iyengar, J. Tomasi, M. Cossi, N. Rega, J. M. Millam, M. Klene, J. E. Knox, J. B. Cross,

V. Bakken, C. Adamo, J. Jaramillo, R. Gomperts, R. E. Stratmann, O. Yazyev, A. J. Austin, R. Cammi, C. Pomelli, J. W. Ochterski, R. L. Martin, K. Morokuma, V. G. Zakrzewski, G. A. Voth, P. Salvador, J. J. Dannenberg, S. Dapprich, A. D. Daniels, O. Farkas, J. B. Foresman, J. V. Ortiz, J. Cioslowski, and D. J. Fox. Gaussian09 Revision A.1, 2009. Gaussian Inc. Wallingford CT.

[222] A. A. Granovsky. Firefly version 8.0.0, http://classic.chem.msu.su/gran/firefly/index.html.

[223] R. G. Parr, D. P. Craig, and I. G. Ross. Molecular Orbital Calculations of the Lower Excited Electronic Levels of Benzene, Configuration Interaction Included. *J. Chem. Phys.*, 18(12):1561–1563, 1950.

[224] C. C. J. Roothaan. Self-Consistent Field Theory for Open Shells of Electronic Systems. *Rev. Mod. Phys.*, 32:179–185, 1960.

[225] F. Jensen. *Introduction to Computational Chemistry.* John Wiley and Sons Ltd., 2004.

[226] J. Simons and J. Nichols. *Quantum Mechanics in Chemistry.* Oxford University Press, 2nd edition, 1997.

[227] A. A. Granovsky. Extended Multi-Configuration Quasi-Degenerate Perturbation Theory: The New Approach to Multi-State Multi-Reference Perturbation Theory. *J. Chem. Phys.*, 134(21):214113/1–214113/14, 2011.

[228] R. K. Chaudhuri, K. F. Freed, G. Hose, P. Piecuch, K. Kowalski, M. Włoch, S. Chattopadhyay, D. Mukherjee, Z. Rolik, Á. Szabados, G. Tóth, and P. R. Surján. Comparison of Low-Order Multireference Many-Body Perturbation Theories. *J. Chem. Phys.*, 122(13):134105/1–134105/9, 2005.

[229] C. Møller and M. S. Plesset. Note on an Approximation Treatment for Many-Electron Systems. *Phys. Rev.*, 46:618–622, 1934.

[230] P. Hohenberg and W. Kohn. Inhomogeneous Electron Gas. *Phys. Rev.*, 136:B864–B871, 1964.

[231] C. Lee, W. Yang, and R. G. Parr. Development of the Colle-Salvetti Correlation-Energy Formula into a Functional of the Electron Censity. *Phys. Rev. B*, 37:785–789, 1988.

[232] A. D. Becke. A New Mixing of Hartree–Fock and Local Density Functional Theories. *J. Chem. Phys.*, 98(2):1372–1377, 1993.

[233] T. Yanai, D. P. Tew, and N. C. Handy. A New Hybrid Exchange–Correlation Functional using the Coulomb-Attenuating Method (CAM-B3LYP). *Chem. Phys. Lett.*, 393(1–3):51 – 57, 2004.

[234] Y. Zhao, N. E. Schultz, and D. G. Truhlar. Exchange-Correlation Functional with Broad Accuracy for Metallic and Nonmetallic Compounds, Kinetics, and Noncovalent Interactions. *J. Chem. Phys.*, 123(16):161103, 2005.

[235] M. Horbatsch and R. M. Dreizler. Time Dependent Thomas Fermi Approach to Atomic Collisions II. *Zeitschrift für Physik A Atoms and Nuclei*, 308(4):329–338, 1982.

[236] E. Runge and E. K. U. Gross. Density-Functional Theory for Time-Dependent Systems. *Phys. Rev. Lett.*, 52:997–1000, 1984.

[237] E. K. U. Gross and W. Kohn. Time-Dependent Density Functional Theory. *Adv. Quant. Chem*, 21:255–291, 1990.

[238] G. Onida, L. Reining, and A. Rubio. Electronic Excitations: Density-Functional versus Many-Body Green's-Function Approaches. *Rev. Mod. Phys.*, 74:601–659, Jun 2002.

[239] J. R. Chelikowsky, L. Kronik, and I. Vasiliev. Time-Dependent Density-Functional Calculations for the Optical Spectra of Molecules, Clusters, and Nanocrystals. *J. Phys. Condens. Mat.*, 15(35):R1517, 2003.

[240] A. Rosa, G. Ricciardi, O. Gritsenko, and E. J. Baerends. Excitation energies of metal complexes with time-dependent density functional theory. In *Principles and Applications of Density Functional Theory in Inorganic Chemistry I*, volume 112 of *Structure and Bonding*, pages 49–116. Springer Berlin Heidelberg, 2004.

[241] A. Dreuw and M. Head-Gordon. Single-Reference Ab-Initio Methods for the Calculation of Excited States of Large Molecules. *Chem. Rev.*, 105(11):4009–4037, 2005.

[242] V. Barone, R. Improta, and N. Rega. Quantum Mechanical Computations and Spectroscopy: From Small Rigid Molecules in the Gas Phase to Large Flexible Molecules in Solution. *Accounts Chem. Res.*, 41(5):605–616, 2008.

[243] D. Jacquemin, V. Wathelet, E. A. Perpéte, and C. Adamo. Extensive TD-DFT Benchmark: Singlet-Excited States of Organic Molecules. *J. Chem. Theory Comput.*, 5(9):2420–2435, 2009.

[244] M. E. Casida. Time-Dependent Density-Functional Theory for Molecules and Molecular Solids. *J. Mol. Struc. - THEOCHEM*, 914(1–3):3 – 18, 2009.

[245] M. van Faassen and K. Burke. Time-Dependent Density Functional Theory of High Excitations: To Infinity, and Beyond. *Phys. Chem. Chem. Phys.*, 11:4437–4450, 2009.

[246] D. Jacquemin, B. Mennucci, and C. Adamo. Excited-State Calculations with TD-DFT: From Benchmarks to Simulations in Complex Environments. *Phys. Chem. Chem. Phys.*, 13:16987–16998, 2011.

[247] M. A. L. Marques, N. T. Maitra, F. M. S. Nogueira, E. K. U. Gross, and A. Rubio. *Fundamentals of Time-Dependent Density Functional Theory*, volume 837. Springer Science & Business Media, 2012.

[248] C. Adamo and D. Jacquemin. The Calculations of Excited-State Properties with Time-Dependent Density Functional Theory. *Chem. Soc. Rev.*, 42:845–856, 2013.

[249] H. B. Schlegel. Optimization of Equilibrium Geometries and Transition Structures. *J. Comput. Chem.*, 3(2):214–218, 1982.

[250] X. Li and M. J. Frisch. Energy-Represented Direct Inversion in the Iterative Subspace within a Hybrid Geometry Optimization Method. *J.Chem. Theory and Computation*, 2(3):835–839, 2006.

[251] P. Pulay, F. Fogarasi, G.and Pang, and J. E. Boggs. Systematic *ab-initio* gradient calculation of molecular geometries, force constants, and dipole moment derivatives. *J. Am. Chem. Soc.*, 101(10):2550–2560, 1979.

[252] G. Fogarasi, X. Zhou, P. W. Taylor, and P. Pulay. The Calculation of Ab Initio Molecular Geometries: Efficient Optimization by Natural Internal Coordinates and Empirical Correction by Offset Forces. *J. Am. Chem. Soc.*, 114(21):8191–8201, 1992.

[253] P. Pulay and G. Fogarasi. Geometry Optimization in Redundant Internal Coordinates. *J. Chem. Phys.*, 96(4):2856–2860, 1992.

[254] J. Baker. Techniques for Geometry Optimization: A Comparison of Cartesian and Natural Internal Coordinates. *J. Comput. Chem.*, 14(9):1085–1100, 1993.

[255] C. Peng and H. B. Schlegel. Combining Synchronous Transit and Quasi-Newton Methods to Find Transition States. *Israel J. Chem.*, 33(4):449–454, 1993.

[256] C. Peng, P. Y Ayala, H. B. Schlegel, and M. J. Frisch. Using Redundant Internal Coordinates to Optimize Equilibrium Geometries and Transition States. *J. Comput. Chem.*, 17:49–56, 1996.

[257] Gaussian 09 Users Reference, 2009. URL `http://www.gaussian.com/`.

[258] S. Shekar. *Study of Gas-Phase Decomposition of Tetraethoxysilane.* PhD thesis, Department of Chemical Engineering and Biotechnology, University of Cambridge, 2009.

[259] A. Einstein and O. Stern. Einige Argumente für die Annahme einer molekularen Agitation beim absoluten Nullpunkt. *Annalen der Physik*, 345(3):551–560, 1913.

[260] W. Heisenberg. Über den anschaulichen Inhalt der quantentheoretischen Kinematik und Mechanik. *Zeitschrift für Physik*, 43(3-4):172–198, 1927.

[261] T. A. Stephenson, P. L. Radloff, and S. A. Rice. $^1B_{2u} \leftrightarrow {}^1A_{1g}$ Spectroscopy of Jet-Cooled Benzene: Single Vibronic Level Fluorescence Studies. *J. Chem. Phys.*, 81(3): 1060–1072, 1984.

[262] L. Barnes, S. Abdul-Al, and A.-R. Allouche. TDDFT Assessment of Functionals for Optical 0–0 Transitions in Small Radicals. *J. Phys. Chem. A*, 118(46):11033–11046, 2014.

[263] J. Friedrich and D. Haarer. Photochemical Hole Burning: A Spectroscopic Study of Relaxation Processes in Polymers and Glasses. *Angewandte Chemie International Edition in English*, 23(2):113–140, 1984.

[264] A. D. McNaught, A. Wilkinson, M. Nic, J. Jirat, B. Kosata, and A. Jenkins. *IUPAC. Compendium of Chemical Terminology (the "Gold Book").* Blackwell Scientific Publications, Oxford (1997), 2nd edition, 2006-.

[265] P. R. Bunker and P. Jensen. *Molecular Symmetry and Spectroscopy, 2nd Ed.* NRC Research Press, 2006.

[266] N. J. Reilly, M. Nakajima, T. P. Troy, D. L. Kokkin, N. Chalyavi, K. Duncan, K. Nauta, R. G. Sharp, T. W. Schmidt, and S. H. Kable. Two-Dimensional Fluorescence Spectroscopy for the Identification of Discharge Intermediates. *J. Phys: Conference Series*, 2009.

[267] T. A. Miller. Chemistry and Chemical Intermediates in Supersonic Free Jet Expansions. *Science*, 223(4636):545–553, 1984.

[268] E. L. Wehry and Gleb Mamantov. Matrix Isolation Spectroscopy. *Anal. Chem.*, 51 (6):643A–656A, 1979.

[269] W. P. Cofino, S. M. van Dam, D. A. Kamminga, G. P. Hoornweg, C. Gooijer, C. MacLean, and N. H. Velthorst. Jahn-Teller Effect in Highly Resolved Optical Spectra of the Phenalenyl Radical. *Mol. Phys.*, 51(3):537–550, 1984.

[270] T. Bally, Z. Zhu, J. Wirz, M. Fulscher, and J.Y. Hasegawa. Radical Cations of Perinaphthocyclopropanes. Conditions for the Observation of 1,3-Perinaphthadiyl Radical Cations. *J. Chem. Soc., Perkin Trans. 2*, pages 2311–2318, 2000.

[271] A. Nagy, J. Fulara, and J. P. Maier. Formation of Aromatic Structures from Chain Hydrocarbons in Electrical Discharges: Absorption and Fluorescence Study of $C_{11}H_9+$ and $C_{11}H_9\bullet$ Isomers in Neon Matrices. *J. Am. Chem. Soc.*, 133(49): 19796–19806, 2011.

[272] A. Barnes, W.J. Orville-Thomas, R. Gaufrès, and A. Müller. *Matrix Isolation Spectroscopy*. Nato Science Series C:. Springer Netherlands, 2012. ISBN 9789400985407.

[273] Katia M. Ferrière. The Interstellar Environment of our Galaxy. *Rev. Mod. Phys.*, 73:1031–1066, 2001.

[274] A. Kantrowitz and J. Grey. A High Intensity Source for the Molecular Beam. Part I. Theoretical. *Rev. Sci. Instrum.*, 22(5):328–332, 1951.

[275] G. B. Kistiakowsky and W. P. Slichter. A High Intensity Source for the Molecular Beam. Part II. Experimental. *Rev. Sci. Instrum.*, 22(5):333–337, 1951.

[276] D. H Levy. Laser Spectroscopy of Cold Gas-Phase Molecules. *Ann. Rev. Phys. Chem.*, 31(1):197–225, 1980.

[277] D. H. Levy. The Spectroscopy of Very Cold Gases. *Science*, 214(4518):263–269, 1981.

[278] T. P. Troy, M. Nakajima, N. Chalyavi, R. G. C. R. Clady, K. Nauta, S. H. Kable, and T. W. Schmidt. Identification of the Jet-Cooled 1-Indanyl Radical by Electronic Spectroscopy. *J. Phys. Chem. A*, 2009.

[279] R. Schlachta, G. Lask, S. H. Tsay, and V. E. Bondybey. Pulsed Discharge Source of Supersonically Cooled Transient Species. *Chem. Phys.*, 1991.

[280] O. Krechkivska, C. Wilcox, G. D. O'Connor, K. Nauta, S. H. Kable, and T. W. Schmidt. Ionization Energies of Three Resonance-Stabilized Radicals: Cyclohexadienyl (dn, n = 0, 1, 6, 7), 1-Phenylpropargyl, and Methylcyclohexadienyl. *J. Phys. Chem. A*, 118(44):10252–10258, 2014.

[281] H. L. Snyder, B. T. Smith, T. P. Parr, and R. M. Martin. Dissociative Excitation of Water by Metastable Argon . *Chem. Phys.*, 65(3):397 – 406, 1982.

[282] N. J. Reilly, M. Nakajima, T. P. Troy, N. Chalyavi, K. A. Duncan, K. Nauta, S. H. Kable, and T. W. Schmidt. Spectroscopic Identification of the Resonance-Stabilized *cis* and *trans*-1-Vinylpropargyl Radicals. *J. Am. Chem. Soc.*, 131:13423–13429, 2009.

[283] N. Reilly. *Flourescence Spectroscopy of Jet-Cooled Hydrocarbon Discharge Products.* PhD thesis, School of Chemistry, The University of Sydney, 2008.

[284] Y. Ohshima and Y. Endo. Structure of C_3S Studied by Pulsed-Discharge-Nozzle Fourier-Transform Microwave Apectroscopy. *J. Mol. Specrosc.*, 153:627 – 634, 1992.

[285] D. A. Wild and E. J. Bieske. Infrared Investigations of Negatively Charged Complexes and Clusters. *Int. Rev. Phys. Chem.*, 22(1):129–151, 2003.

[286] A. O'Keefe and D. A. G. Deacon. Cavity Ring Down Optical Spectrometer for Absorption Measurements using Pulsed Laser Sources. *Rev. Sci. Instrum.*, 59(12), 1988.

[287] T. P. Troy, M. Nakajima, N. Chalyavi, R. G. C. R. Clady, K. Nauta, S. H. Kable, and T. W. Schmidt. Identification of the Jet-Cooled 1-Indanyl Radical by Electronic Spectroscopy. *J. Phys. Chem. A*, 113:10279–10283, 2009.

[288] N. Chalyavi, T. P. Troy, G. B. Bacskay, K. Nauta, S. H. Kable, S. A. Reid, and T. W. Schmidt. Excitation Spectra of the Jet-Cooled 4-Phenylbenzyl and 4-(4'-Methylphenyl)benzyl Radicals. *J. Phys. Chem. A*, 116(44):10780–10785, 2012.

[289] W. C. Wiley and I. H. McLaren. Time-of-Flight Mass Spectrometer with Improved Resolution. *Rev. Sci. Instrum.*, 26(12):1150–1157, 1955.

[290] M. Guilhaus. Principles and instrumentation in time-of-flight mass spectrometry. *J. Mass Spectrom*, 30(11):1519–1532, 1995.

[291] D. Kokkin. *The Spectroscopy of Interstellar Molecules.* PhD thesis, School of Chemistry, The University of Sydney, 2009.

[292] V. Dryza and E. J. Bieske. Non-Covalent Interactions Between Metal Cations and Molecular Hydrogen: Spectroscopic Studies of M^+-H_2 Complexes. *Int. Rev. Phys. Chem.*, 32(4):559–587, 2013.

[293] D. A. Wild, Z. M. Loh, R. L. Wilson, and E. J. Bieske. Locating and Confirming the C-H Stretch Bands of the Halide-Acetylene Anion Complexes using Argon Predissociation Spectroscopy. *Chem. Phys. Lett.*, 369(5–6):684 – 690, 2003.

[294] Z. M. Loh, R. L. Wilson, D. A. Wild, E. J. Bieske, and A. Zehnacker. $Cl^-{-}C_6H_6$, $Br^-{-}C_6H_6$, and $I^-{-}C_6H_6$ Anion Complexes: Infrared Spectra and *Ab-Initio* Calculations. *J. Chem. Phys.*, 119(18):9559–9567, 2003.

[295] D. A. Wild, R. L. Wilson, Z. M. Loh, and E. J. Bieske. The Infrared Spectrum of the $F^-{-}H_2$ Anion Complex. *Chem. Phys. Lett.*, 393(4–6):517 – 520, 2004.

[296] D. A. Wild and E. J. Bieske. Infrared Spectrum of the $I^-{-}D_2$ Anion Complex. *J. Chem. Phys.*, 121(24):12276–12281, 2004.

[297] Z. M. Loh, R. L. Wilson, D. A. Wild, E. J. Bieske, and M. S. Gordon. Infrared Spectra and *ab-Initio* Calculations for the $Cl^-{-}(CH_4)_n$ $(n = 1-10)$ Anion Clusters. *J. Phys. Chem. A*, 109(38):8481–8486, 2005.

[298] R. L. Wilson, Z. M. Loh, D. A. Wild, C. D. Thompson, M. D. Schuder, J. M. Lisy, and E. J. Bieske. Infrared Spectra of the $Cl^-{-}C_2H_4$ and $Br^-{-}C_2H_4$ Anion Dimers. *Phys. Chem. Chem. Phys.*, 7:3419–3425, 2005.

[299] C. D. Thompson, C. Emmeluth, B. L. J. Poad, G. H. Weddle, and E. J. Bieske. Rotationally Resolved Infrared Spectrum of the $Li^+{-}D_2$ Cation Complex. *J. Chem. Phys.*, 125(4):044310, 2006.

[300] C. D. Thompson, B. L.J. Poad, C. Emmeluth, and E. Bieske. Infrared Spectra of $Cl^-{-}(C_6H_6)_m$ $m = 1, 2$. *Chem. Phys. Lett.*, 428(1–3):18 – 22, 2006.

[301] Z. M. Loh, R. L. Wilson, D. A. Wild, E. J. Bieske, J. M. Lisy, B. Njegic, and M. S. Gordon. Infrared Spectra and *Ab-Initio* Calculations for the $F^-{-}(CH_4)_n$ $(n = 1-8)$ Anion Clusters. *J. Phys. Chem. A*, 110(51):13736–13743, 2006.

[302] C. Emmeluth, B. L. J. Poad, C. D. Thompson, G. H. Weddle, and E. J. Bieske. Infrared Spectra of the $Li^+{-}(H_2)_n (n = 1-3)$ Cation Complexes. *J. Chem. Phys.*, 126(20):204309, 2007.

[303] C. Emmeluth, B. L. J. Poad, C. D. Thompson, and E. J. Bieske. Interactions Between the Chloride Anion and Aromatic Molecules - Infrared Spectra of the $Cl^--C_6H_5CH_3$, $Cl^--C_6H_5NH_2$ and $Cl^--C_6H_5OH$ Complexes. *J. Phys. Chem. A*, 111(31):7322–7328, 2007.

[304] C. Emmeluth, B. L. J. Poad, C. D. Thompson, G. Weddle, E. J. Bieske, A. A. Buchachenko, T. A. Grinev, and J. Kłos. The Al^+-H_2 Cation Complex: Rotationally Resolved Infrared Spectrum, Potential Energy Surface, and Rovibrational Calculations. *J. Chem. Physi.*, 127(16):164310, 2007.

[305] V. Dryza, B. L. J. Poad, and E. J. Bieske. Attachment of Molecular Hydrogen to an Isolated Boron Cation: An Infrared and *ab-initio* Study. *J. Am. Chem. Soc.*, 130 (39):12986–12991, 2008.

[306] B. L. J. Poad, P. J. Wearne, E. J. Bieske, A. A. Buchachenko, D. I. G. Bennett, J. Klos, and M. H. Alexander. The Na^+-H_2 Cation Complex: Rotationally Resolved Infrared Spectrum, Potential Energy Surface, and Rovibrational Calculations. *J. Chem. Phys.*, 129(18):4306, 2008.

[307] V. Dryza, B. L. J. Poad, and E. J. Bieske. Spectroscopic Study of the Benchmark Mn^+-H_2 Complex. *J. Phys. Chem. A*, 113(21):6044–6048, 2009.

[308] V. Dryza and E. J. Bieske. The Cr^+-D_2 Cation Complex: Accurate Experimental Dissociation Energy, Intermolecular Bond Length, and Vibrational Parameters. *J. Chem. Phys.*, 131(16):164303, 2009.

[309] D. A. Wild, K. T. Kuwata, C. K. Wong, J. D. Lobo, A. Deev, T. S. Schindler, M. Okumura, and E. J. Bieske. Infrared Spectra of Mass-Selected $Br^-(NH_3)_n$ and I^-NH_3 Clusters. *J. Phys. Chem. A*, 114(14):4762–4769, 2010.

[310] B. L. J. Poad, V. Dryza, J. Kłos, A. A. Buchachenko, and E. J. Bieske. Rotationally Resolved Infrared Spectrum of the Na^+-D_2 Complex: An Experimental and Theoretical Study. *J. Chem. Phys.*, 134(21):214302, 2011.

[311] V. Dryza and E. J. Bieske. Infrared Spectroscopy of the Ag^+-H_2 Complex: Exploring the Connection Between Vibrational Band-Shifts and Binding Energies. *J. Phys. Chem. Lett.*, 2(7):719–724, 2011.

[312] B. L. J. Poad, V. Dryza, A. A. Buchachenko, J. Kłos, and E. J. Bieske. Properties of the B^+-H_2 and B^+-D_2 Complexes: A Theoretical and Spectroscopic Study. *J. Chem. Phys.*, 137(12):124312, 2012.

[313] V. Dryza, J. A. Sanelli, E. G. Robertson, and E. J. Bieske. Electronic Spectra of Gas-Phase Polycyclic Aromatic Nitrogen Heterocycle Cations: Isoquinoline+ and Quinoline+. *J. Phys. Chem. A*, 116(17):4323–4329, 2012.

[314] V. Dryza, B. L. J. Poad, and E. J. Bieske. Attaching Molecular Hydrogen to Metal Cations: Perspectives from Gas-Phase Infrared Spectroscopy. *Phys. Chem. Chem. Phys.*, 14:14954–14965, 2012.

[315] N. Chalyavi, V. Dryza, J. A. Sanelli, and E. J. Bieske. Gas-Phase Electronic Spectroscopy of the Indene Cation ($C_9H_8^+$). *J. Chem. Phys.*, 138(22):224307, 2013.

[316] N. Chalyavi, J. A. Sanelli, V. Dryza, and E. J. Bieske. Electronic Spectroscopy of the 1,3-Cyclopentadiene Cation ($C_5H_6^+$). *J. Phys. Chem. A*, 117(44):11276–11281, 2013.

[317] C. S. Hansen, S. J. Blanksby, N. Chalyavi, E. J. Bieske, J. R. Reimers, and A. J. Trevitt. Ultraviolet Photodissociation Action Spectroscopy of the N-pyridinium Cation. *J. Chem. Phys.*, 142(1):014301, 2015.

[318] N. Chalyavi, K.J. Catani, J.A. Sanelli, V. Dryza, and E.J. Bieske. Gas-phase Electronic Spectrum of the Indole Radical Cation. *Mol. Phys.*, Preprint(0):1–9, 2015.

[319] W. Gaede. Die Diffusion der Gase durch Quecksilberdampf bei niederen Drucken und die Diffusionsluftpumpe. *Annalen der Physik*, 351(3):357–392, 1915.

[320] P. E. Miller and M. B. Denton. The Quadrupole Mass Filter: Basic Operating Concepts. *J. Chem. Ed.*, 63(7):617, 1986.

[321] J. F. O'Hanlon. *A User's Guide to Vacuum Technology.* John Wiley & Sons, 2005.

[322] D. F. Dyer. *The Pressure Distribution in a Liquid-Nitrogen Cold Trap.* Springer, 1971.

[323] Y. Huang, S. Guan, H. S. Kim, and A. G. Marshall. Ion Transport Through a Strong Magnetic Field Bradient by R.R.-Only Octupole Ion Guides. *Int. J. Mass Spectrom. Ion Processes*, 152(2–3):121 – 133, 1996.

[324] H. Friha, G. Féraud, T. Troy, C. Falvo, P. Parneix, P. Bréchignac, Z. Dhaouadi, T. W. Schmidt, and T. Pino. Visible Photodissociation Spectra of the 1- and 2-Methylnaphthalene Cations: Laser Spectroscopy and Theoretical Simulations. *J. Phys. Chem. A*, 117(50):13664–13672, 2013.

[325] C. Cossart-Magos and S. Leach. Determination of the Symmetry of the First Excited Electronic State of Benzyl by Rotational Contour Analysis of Vibronic Bands of the Emission Spectra of $C_6H_5CH_2$, $C_6H_5CD_2$, and $C_6D_5CD_2$. *J. Chem. Phys.*, 56(4): 1534–1545, 1972.

[326] C. Cossart-Magos and S. Leach. Two-mode Vibronic Interaction Between Neighboring 1^2A_2 and 2^2B_2 Excited Electronic States of the Benzyl Radical. *J. Chem. Phys.*, 64(10):4006–4019, 1976.

[327] G. C. Eiden and J. C. Weisshaar. Vibronic Coupling Mechanism in the $\tilde{A}^2A_2 - -\tilde{B}^2B_2$ Excited States of Benzyl Radical. *J. Chem. Phys.*, 104(22):8896–8912, 1996.

[328] A. S. Menon, G. P. F. Wood, D. Moran, and L. Radom. Bond Dissociation Energies and Radical Stabilization Energies: An Assessment of Contemporary Theoretical Procedures. *J. Phys. Chem. A*, 111(51):13638–13644, 2007.

[329] B. O. Roos. *Ab Initio Methods in Quantum Chemistry - II*, chapter 69 The complete active space self-consistent field method and its applications in electronic structure calculations, page 399. Adv. Chem. Phys. John Wiley & Sons Ltd., Chichester, England, 1987.

[330] R. Ditchfield, W. J. Hehre, and J. A. Pople. Self-Consistent Molecular Orbital Methods. 9. Extended Gaussian-Type Basis for Molecular-Orbital Studies of Organic Molecules. *J. Chem. Phys.*, 54:72, 1971.

[331] W. J. Hehre, R. F. Stewart, and J. A. Pople. Self-Consistent Molecular Orbital Methods. 1. Use of Gaussian Expansions of Slater-Type Atomic Orbitals. *J. Chem. Phys.*, 51:2657–64, 1969.

[332] H. J. Werner. Third-order Multireference Perturbation Theory: The CASPT3 Method. *Mol. Phys.*, 89:645, 1996.

[333] P. Celani and H. J. Werner. Multireference Perturbation Theory for Large Restricted and Selected Active Space Reference Wave Functions. *J. Chem. Phys.*, 112:5546, 2000.

[334] K. Andersson, P.-Å. Malmqvist, B. O. Roos, A. J. Sadlej, and K. Wolinski. Second-Order Perturbation Theory with a CASSCF Reference Function. *J. Phys. Chem.*, 94:5483, 1990.

[335] Dalton, a Molecular Electronic Structure Program, Release Dalton2011 (2011), see http://daltonprogram.org.

[336] MOLPRO, Version 2010.1, a Package of Ab Initio Programs, H.-J. Werner, P. J. Knowles, G. Knizia, F. R. Manby, M. Schütz, and others , see http://www.molpro.net.

[337] N. Chalyavi, G. B. Bacskay, A. S. Menon, T. P. Troy, N. J. L. K. Davis, L. Radom, S. A. Reid, and T. W. Schmidt. Spectroscopy and Thermochemistry of a Jet-Cooled Open-Shell Polyene: 1,4-Pentadienyl Radical. *J. Chem. Phys.*, 135:124306, 2011.

[338] H. C. Longuet-Higgins and J. A. Pople. The Electronic Spectra of Aromatic Molecules .4. Excited States of Odd Alternant Hydrocarbon Radicals and Ions. *Proc. Phys. Soc. Lond. A*, 68(7):591–600, 1955.

[339] E. Hückel. *Grundzuge der Theorie Ungesattigter und Aromatischer Verbindungen.* Verlag Chemie, G.m.b.H., Berlin, 1938.

[340] G. D. O'Connor, G. V.G. Woodhouse, T. P. Troy, and T. W. Schmidt. Double-Resonance Spectroscopy of Radicals: Higher Electronic Excited States of 1- and 2-naphthylmethyl, 1-phenylpropargyl and 9-anthracenylmethyl. *Mol. Phys.*, 113:2138–2147, 2015.

[341] G. V. G. Woodhouse. Closing in on Interstellar Molecules: The Spectroscopy of Higher Excited States of Resonance-Stabilised Radicals, 2010.

[342] C. A. Coulson and G. S. Rushbrooke. Note on the Method of Molecular Orbitals. *Proc. Cambridge Phil. Soc.*, 36:193–200, 1940.

[343] H. Ding, T. W. Schmidt, T. Pino, A. E. Boguslavskiy, F. Güthe, and J. P. Maier. Gas Phase Electronic Spectra of the Linear Carbon Chains $HC_{2n+1}H$(n=3–6,9). *J. Chem. Phys.*, 119(2):814–819, 2003.

[344] C. A. Rice, V. Rudnev, R. Dietsche, and J. P. Maier. Gas-phase Electronic Spectra of Polyacetylene Cations: Relevance of Higher Excited States. *Astronom. J.*, 140(1): 203, 2010.

[345] M. Gasser, J. A. Frey, J. M. Hostettler, A. Bach, and P. Chen. Vibronic Structure of the 3s and 3p Rydberg States of the Allyl Radical. *J. Phys. Chem. A*, 114(14): 4704–4711, 2010.

[346] A. A. Granovsky. Extended Multi-Configuration Quasi-Degenerate Perturbation Theory: The New Approach to Multi-State Multi-Reference Perturbation Theory. *J. Chem. Phys.*, 134(21):214113, 2011.

[347] M.W.Schmidt, K.K.Baldridge, J.A.Boatz, S.T.Elbert, M.S.Gordon, J.H.Jensen, S.Koseki, N.Matsunaga, K.A.Nguyen, S.Su, T.L.Windus, M.Dupuis, and J.A.Montgomery. General Atomic and Molecular Electronic Structure System. *J. Comput. Chem.*, 14:1347–1363, 1993.

[348] F. Bayrakceken and J. E. Nicholas. A Flash Photolytic Study of the Benzyl and α-Chlorobenzyl Radicals. *J. Chem. Soc. B*, pages 691–694, 1970.

[349] J. P. Byrne, E. F. McCoy, and I. G. Ross. Internal Conversion in Aromatic and N-Heteroaromatic Molecules. *Aust. J. Chem.*, 18(10):1589–1603, 1965.

[350] R. Englman and J. Jortner. The Energy Gap Law for Non-Radiative Decay in Large Molecules. *Journal of Luminescence*, 1–2(0):134 – 142, 1970.

[351] J. S. Wilson, N. Chawdhury, M. R. A. Al-Mandhary, M. Younus, M. S. Khan, P. R. Raithby, A. K ohler, and R. H. Friend. The Energy Gap Law for Triplet States in Pt-Containing Conjugated Polymers and Monomers. *J. Am. Chem. Soc.*, 123(38): 9412–9417, 2001.

[352] T. P. Troy, S. H. Kable, T. W. Schmidt, and S. A. Reid. On the Electronic Spectroscopy of Closed-Shell Cations Derived from Resonance-Stabilized Radicals: Insights from Theory and Franck-Condon Analysis. *Astron. Astrophys.*, 541:A8, 2012.

[353] D. Romanini, L. Biennier, F. Salama, A. Kachanov, L. J. Allamandola, and F. Stoeckel. Jet-Discharge Cavity Ring-Down Spectroscopy of Ionized Polycyclic Aromatic Hydrocarbons: Progress in Testing the {PAH} Hypothesis for the Fiffuse Interstellar Band Problem. *Chem. Phys. Lett.*, 303(1–2):165 – 170, 1999.

[354] P. Bréchignac and T. Pino. Electronic Spectra of Cold Gas Phase PAH Cations: Towards the Identification of the Diffuse Interstellar Bands Carriers. *Astron. Astrophys.*, 343:L49–L52, March 1999.

[355] F. Useli-Bacchitta, A. Bonnamy, G. Mulas, G. Malloci, D. Toublanc, and C. Joblin. Visible Photodissociation Spectroscopy of PAH Cations and Derivatives in the PIRENEA experiment. *Chemical Physics*, 371(1–3):16 – 23, 2010.

[356] L. Biennier, F. Salama, M. Gupta, and A. O'Keefe. Multiplex Integrated Cavity Output Spectroscopy of Cold {PAH} Cations. *Chem. Phys. Lett.*, 387(4–6):287 – 294, 2004.

[357] W. Schmidt. Photoelectron Spectra of Polynuclear Aromatics. V. Correlations with Ultraviolet Absorption Spectra in the Catacondensed Series. *J. Chem. Phys.*, 66(2): 828–845, 1977.

[358] J. Szczepanski, M. Vala, D. Talbi, O. Parisel, and Y. Ellinger. Electronic and Vibrational Spectra of Matrix Isolated Anthracene Radical Cations: Experimental and Theoretical Aspects. *J. Chem. Phys.*, 98(6):4494–4511, 1993.

[359] B. Klærke, Y. Toker, D. B. Rahbek, L. Hornekær, and L. H. Andersen. Formation and Stability of Hydrogenated PAHs in the Gas-Phase. *Astron. Astrophys.*, 549:A84, 2013.

[360] S. J. Blanksby and G. B. Ellison. Bond Dissociation Energies of Organic Molecules. *Accounts Chem. Res.*, 36(4):255–263, 2003.

[361] P. Lazzeretti. Assessment of Aromaticity via Molecular Response Properties. *Phys. Chem. Chem. Phys.*, 6:217–223, 2004.

[362] M. K. Cyrański, R. W. A. Havenith, M. A. Dobrowolski, B. R. Gray, T. M. Krygowski, P. W. Fowler, and L. W. Jenneskens. The Phenalenyl Motif - A Magnetic Chameleon. *Chem. Eur. J.*, 13(8):2201–2207, 2007.

[363] K. Goto, T. Kubo, K. Yamamoto, K. Nakasuji, K. Sato, D. Shiomi, T. Takui, M. Kubota, T. Kobayashi, K. Yakusi, and J. Ouyang. A Stable Netral Hydrocarbon Radical Synthesis, Crystal Structure and Physical Properties of 2,5,8-Tre-tert-bytylphenalenyl. *J. Am. Chem. Soc.*, 121(7):1619–1620, 1999.

[364] Y. Morita, T. Aoki, K. Fukui, S. Nakazawa, K. Tamaki, S. Suzuki, A. Fuyuhiro, K. Yamamoto, K. Sato, D. Shiomi, A. Naito, T. Takui, and K. Nakasuji. A New Trend in Phenalenyl Chemistry A Persistent Neutral Radical, 2,5,8-Tri-tert-butyl-1,3-diazaphenalenyl, and the Excited Triplet State of the Gable syn-Dimer in the Crystal of Column Motif. *Angew. Chem. Int. Ed.*, 41(10):1793–1796, 2002.

[365] A. Sarkar, F. S. Tham, and R. C. Haddon. Synthesis, Crystallization, Electrochemistry and Single Crystal X-ray Analysis of a Methoxy-Substituted Tris-phenalenyl Based Neutral Radical. *J. Mater. Chem.*, 21:1574–1581, 2011.

[366] T. Kubo. Phenalenyl-Based Open-Shell Polycyclic Aromatic Hydrocarbons. *Chem. Rec.*, 15(1):218–232, 2015.

[367] D. Small, V. Zaitsev, Y. Jung, S. V. Rosokha, M. Head-Gordon, and J. K. Kochi. Intermolecular Π to Π Bonding between Stacked Aromatic Dyads Experimental and

Theoretical Binding Energies and Near-IR Optical Transitions for Phenalenyl Radical/Radical versus Radical/Cation Dimerizations. *J. Am. Chem. Soc.*, 126(42): 13850–13858, 2004.

[368] D. Small, S. V. Rosokha, J. K. Kochi, and M. Head-Gordon. Characterizing the Dimerizations of Phenalenyl Radicals by *ab-Initio* Calculations and Spectroscopy : σ-Bond Formation versus Resonance π-Stabilization. *J. Phys. Chem. A*, 109(49): 11261–11267, 2005.

[369] V. Zaitsev, S. V. Rosokha, M. Head-Gordon, and J. K. Kochi. Steric Modulations in the Reversible Dimerizations of Phenalenyl Radicals via Unusually Weak Carbon-Centered π - and σ Bonds. *J. Org. Chem*, 71(2):520–526, 2006.

[370] Y. M. Rhee, T. J. Lee, M. S. Gudipati, L. J. Allamandola, and M. Head-Gordon. Charged Polycyclic Aromatic Hydrocarbon Clusters and the Galactic Extended Red Emission. *Proc. Natl. Acad. Sci. U.S.A.*, 104(13):5274–5278, 2007.

[371] R. Gygax, H. L. McPeters, and J. I. Brauman. Photodetachment of Electrons from Anions of High Symmetry. Electron Photodetachment Spectra of the Cyclooctatetraenyl and Perinaphthenyl Anions. *J. Am. Chem. Soc.*, 101(10):2567–2570, 1979.

[372] H. A. Jahn and E. Teller. Stability of Polyatomic Molecules in Degenerate Electronic States. I. Orbital Degeneracy. *P. Roy. Soc. Lond. A. Mat.*, 161(905):pp. 220–235, 1937.

[373] R. Bauernschmitt and R. Ahlrichs. Treatment of Electronic Excitations Within the Adiabatic Approximation of Time Dependent Density Functional Theory. *Chem. Phys. Lett.*, 256:454–64, 1996.

[374] H. Gao, M. Q Ma, L. Zhou, R. P. Jia, X. G. Chen, and Z. D. Hu. Interaction of DNA with Aromatic Hydrocarbons Fraction in Atmospheric Particulates of Xigu District of Lanzhou, China. *J. Environ. Sci.*, 19(8):948–954, 2007.

[375] R. Vianello and Z. B. Maksiċ. Towards Highly Powerful Neutral Organic Superacids - a DFT Study of Some Polycyano Derivatives of Planar Hydrocarbons. *Tetrahedron*, 61(39):9381–9390, 2005.

[376] M. Gerst and C. Rüchardt. Bimolekulare Radikalbildung durch H-Transfer, 2. H-Transferreaktionen mit Phenalen. *Chem. Ber.*, 126(4):1039–1045, 1993.

[377] A. H. Castro Neto, F. Guinea, N. M. R. Peres, K. S. Novoselov, and A. K. Geim. The Electronic Properties of Graphene. *Rev. Mod. Phys.*, 81:109–162, 2009.

[378] L. Hornekær, E. Rauls, W. Xu, Ž. Šljivančanin, R. Otero, I. Stensgaard, E. Lægsgaard, B. Hammer, and F. Besenbacher. Clustering of Chemisorbed H(D) Atoms on the Graphite (0001) Surface due to Preferential Sticking. *Phys. Rev. Lett.*, 97: 186102, Oct 2006.

[379] S. M. Beck, D. E. Powers, J. B. Hopkins, and R. E. Smalley. Jet Cooled Naphthalene - I - Absorption Spectra and Line Profiles. *J. Chem. Phys.*, 73(5):2019–2028, 1980.

[380] A. Amirav, C. Horwitz, and J. Jortner. Optical Selection Studies of Electronic Relaxation from he S_1 State of Jet-Cooled Anthracene Derivatives. *J. Chem. Phys.*, 88(5):3092–3110, 1988.

[381] A. Staicu, G. Rouillé, O. Sukhorukov, Th. Henning, and F. Huisken. Cavity Ring-Down Laser Absorption Spectroscopy of Jet-Cooled Anthracene. *Mol. Phys.*, 102 (16-17):1777–1783, 2004.

[382] E. A. Mangle and M. R. Topp. Excited-State Dynamics of Jet-Cooled Pyrene and some Molecular Complexes. *J. Phys. Chem.*, 90(5):802–807, 1986.

[383] G. Bermudez and I. Y. Chan. Excitation and Fluorescence Spectra of Coronene in a Jet. *J.Phys. Chem.*, 90(21):5029–5034, 1986.

[384] A. Amirav, U. Even, and J. Jortner. Energetics and Intramolecular Dynamics of the Isolated Ultracold Tetracene Molecule in its First Excited Singlet State. *J. Chem. Phys.*, 75(8):3770–3793, 1981.

[385] I. Alata, R. Omidyan, Michel Broquier, C. Dedonder, O. Dopfer, and C. Jouvet. Effect of Protonation on the Electronic Structure of Aromatic Molecules: NaphthaleneH(+). *Phys. Chem. Chem. Phys.*, 12(43):14456–14458, 2010.

[386] F. X. Hardy, O. Gause, C. A. Rice, and J. P. Maier. Absorptions in the Visible of Protonated Pyrene Collisionally Cooled to 15 K. *Astrophys. J. Lett.*, 778(2):L30, 2013.

[387] D. M. Hudgins, Jr. C. W. Bauschlicher, and L. J. Allamandola. Variations in the Peak Position of the 6.2 μm Interstellar Emission Feature: A Tracer of N in the Interstellar Polycyclic Aromatic Hydrocarbon Population. *Astrophys. J.*, 632(1):316, 2005.

[388] D. M. Hudgins and L. J. Allamandola. Steps toward Identifying PAHs: A Summary of Some Recent Results. In *Astrochemistry: Recent Successes and Current Challenges*, volume 1 of *P. Int. Astro. U.*, pages 443–454, 8 2005.

[389] M. L. Theis, A. Candian, A. G. G. M. Tielens, T. J. Lee, and R. C. Fortenberry. Electronically Excited States of PANH Anions. *Phys. Chem. Chem. Phys.*, preprint, 2015.

[390] J. A. Noble, C. Dedonder, and C. Jouvet. The Electronic Spectra of Protonated Nitrogen-Substituted Polycyclic Aromatic Hydrocarbon Molecules. *Astron. Astrophys.*, 577:A79, 2015.

[391] D. Farquhar, T. T. Gough, and D. Leaver. Heterocyclic Compounds with Bridgehead Nitrogen Atoms. Part V. Pyrido[2,1,6-de]quinolizines (cycl[3.3.3]azines). *J. Chem. Soc., Perkin Trans. 1*, pages 341–355, 1976.

[392] Y. H. Tian, B. G. Sumpter, S. Du, and J. Huang. Pancake π-π Bonding Goes Double: Unexpected 4e/All-Sites Bonding in Boron- and Nitrogen-Doped Phenalenyls. *J. Phys. Chem. Lett.*, 6(12):2318–2325, 2015.

[393] I. Ratera and J. Veciana. Playing with Organic Radicals as Building Blocks for Functional Molecular Materials. *Chem. Soc. Rev.*, 41:303–349, 2012.

[394] F. X. Désert, F. Boulanger, and J. L. Puget. Interstellar Dust Models for Extinction and Emission. *Astron. Astrophys.*, 237:215–236, 1990.

[395] I. Iben Jr and J. W. Truran. On the Surface Composition of Thermally Pulsing Stars of High Luminosity and on the Contribution of Such Stars to the Element Enrichment of the Interstellar Medium. *Astrophys. J.*, 220:980–995, 1978.

[396] Y. Le Page, V.and Keheyan, V. M. Bierbaum, and T. P. Snow. Chemical Constraints on Organic Cations in the Interstellar Medium. *J. Am. Chem. Soc.*, 119(35):8373–8374, 1997.

[397] M. Heaven, T. Sears, V. E. Bondybey, and Terry A. Miller. The Free Jet Cooled, Laser Induced Fluorescence Spectrum of *s y m* Triazine. *J. Chem. Phys.*, 75(11), 1981.

[398] N. J. Kim, G. Jeong, Y. Sam Kim, J. Sung, S. Keun Kim, and Y. D. Park. Resonant Two-Photon Ionization and Laser Induced Fluorescence Spectroscopy of Jet-Cooled Adenine. *J. Chem. Phy.*, 113(22):10051–10055, 2000.

[399] T. J. Balle and W. H. Flygare. Fabry–Perot Cavity Pulsed Fourier Transform Microwave Spectrometer with a Pulsed Nozzle Particle Source. *Rev. Sci. Instrum.*, 52 (1):33–45, 1981.

[400] G. G. Brown, B. C. Dian, K. O. Douglass, S. M. Geyer, S. T. Shipman, and B. H. Pate. A Broadband Fourier Transform Microwave Spectrometer Based on Chirped Pulse Excitation. *Rev. Sci. Instrum.*, 79(5):053103, 2008.

[401] R. W. Field, A. D. English, T. Tanaka, D. O. Harris, and D. A. Jennings. Microwave Optical Double Resonance Spectroscopy with a cw Dye Laser: BaO $X^1\Sigma$ and $A^1\Sigma^*$. *J. Chem. Phys.*, 59:2191–2203, 1973.

[402] M. C. McCarthy and co workers. Microwave Optical Double Reasonance. Personal Communication, 2013),.

[403] A. G. G. M. Tielens. Diffuse interstellar bands: The way forward. In *The Diffuse Interstellar Bands*, volume 9 of *Proceedings of the International Astronomical Union*, pages 399–411, 5 2013.